Subduction of the Tethys Oceans reconstructed from plate kinematics and mantle tomography

Edith Hafkenscheid

Subduction of the Tethys Oceans reconstructed from plate kinematics and mantle tomography

Subductie van de Tethys Oceanen gereconstrueerd uit plaatbewegingen en mantel-tomografie

(met een samenvatting in het Nederlands)

PROEFSCHRIFT

DOOR

Edith Hafkenscheid

GEBOREN OP 30 MAART 1974, TE LEIDERDORP

Promotoren: Prof. dr. M. J. R. Wortel
              Prof. dr. W. Spakman

Contents

Chapter 1

Introduction

1.1 The Tethys Oceans

The Tethys Oceans separated the African, Arabian and Indian continents from Eurasia in Mesozoic-Cenozoic times. When the Atlantic Ocean opened, the continents started to converge and the Tethys Oceans gradually began closing. The final continental collisions of Africa, Arabia and India with the southern margins of Eurasia resulted in the formation of the impressive Alpine-Himalayan mountain chain that extends from the Mediterranean region to the Indonesian archipelago (Figure 1.1). Whereas the subduction of the Tethys Oceans was dominated by the convergence of the continents, the process was complicated by the rifting of various intermediate fragments, back-arc spreading, and intra-oceanic subduction. The large orogenic belt of the Tethyan region is therefore an interesting but extremely complex domain of continental fragments, highly deformed suture zones and ophiolitic terranes. Although the large-scale evolution of the area is now relatively well constrained, the more detailed aspects are still poorly understood.
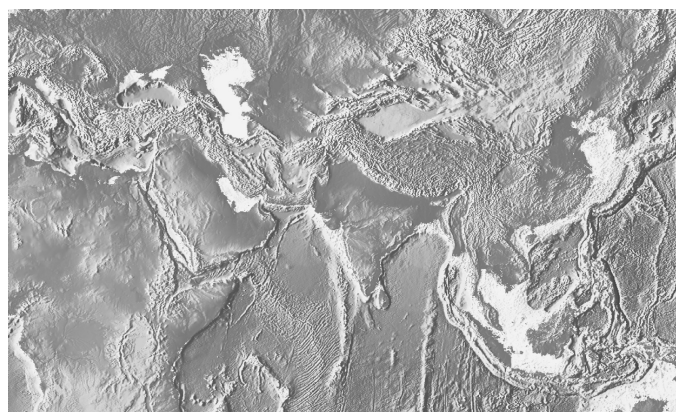
Figure 1.1: Topography of the Tethyan region, see Figure A.1 in the Appendix for a colour version.

1.2   Plate kinematics, mantle tomography, and subduction

Tectonic reconstructions of past plate motions form a framework for other geological, oceano-graphic and climatology studies. Especially the plate kinematics of large-scale reconstructions, as those for the complete Tethyan region, can be useful in this respect. Tectonic reconstructions are generally based upon many integrated sources of information that can be found near the Earth's surface, like paleomagnetic and paleobiogeographic data, fracture zones and magnetic anomalies on the ocean floor, stratigraphy, and the occurrence of volcanism. For the Tethyan region, the currently available data are not always well constrained and can be interpreted in different ways. As a result, the numerous reconstructions that have been presented for the Mesozoic-Cenozoic evolution of the Tethyan region still show significant differences. The Tethys Oceans subducted into the mantle, but disappeared without leaving enough clues at the surface to arrive at one single geodynamic scenario so far.

Seismic tomography is a technique to image the velocity structure of the Earth's interior. The cold material of subducted oceanic lithosphere, re-heating slowly within the mantle, will generally be imaged as positive velocity anomalies in these models. Also beneath the Tethyan region, tomographic images show large anomalous volumes in the present mantle that seem to represent remnants of the Tethys Oceans. Although care should be taken when interpreting seismic velocity anomalies, the positive anomalies associated with subducted oceanic lithosphere are largely due to temperature perturbations. We can therefore use the temperature-derivatives of the seismic velocities to convert these anomalies to thermal perturbations.

To test the tectonic reconstructions of the Tethyan region, we connect the near-surface geological information to the deep mantle structure by using the tomographic anomalous volumes. Therefore, we have to determine the total amount of convergence, thus the subducted lithospheric surface, from the plate kinematic models. The prediction of the present thermal volumes of these plates comprises the effects of age-dependent lithospheric cooling and that of the subduction process itself. To use the present positions and geometries of the seismic anomalies in our comparison, we have to acknowledge the complex behaviour of slabs descending into the mantle. Processes of importance are, for example, slab sinking throughout the mantle, slab thickening when entering the lower mantle, ridge subduction, and possible slab break-off after continental collisions. When comparing the spatial distributions of the predicted and tomographic volumes, the absolute plate motion, i.e. the motion of the plate with respect to the underlying mantle, becomes especially relevant.

1.3   Aim and approach

The aim of this research is to reconstruct the Mesozoic-Cenozoic subduction of the Tethys Oceans, by integrating plate tectonic reconstructions, mantle tomography, and elements of subduction dynamics.

As schematically illustrated in Figure 1.2, we therefore:

1. Calculate the surface of subducted lithosphere (Su) from plate tectonic reconstructions

2. Estimate the initial thermal volumes (Vi) of the subducted lithosphere calculated in 1

3. Predict the present thermal volumes (Vp) of the slabs from the volumes estimated in 2

4. Estimate the size of the anomalous volumes in seismic tomography (Vt) that may be related to subducted lithosphere

5. Compare the tomographic volumes (Vt) estimated in 4 with the present slab volumes (Vp) predicted in 3, and test the tectonic reconstructions and subduction scenarios

In the first three steps, we incorporate the effects of subduction-related processes for which the kinematic boundary conditions are implicitly given by the tectonic reconstructions. As different plate tectonic reconstructions will generally lead to different predictions of the slab thermal volumes, we expect that this approach will enable us to evaluate the quality of the reconstructions and subduction scenarios involved.
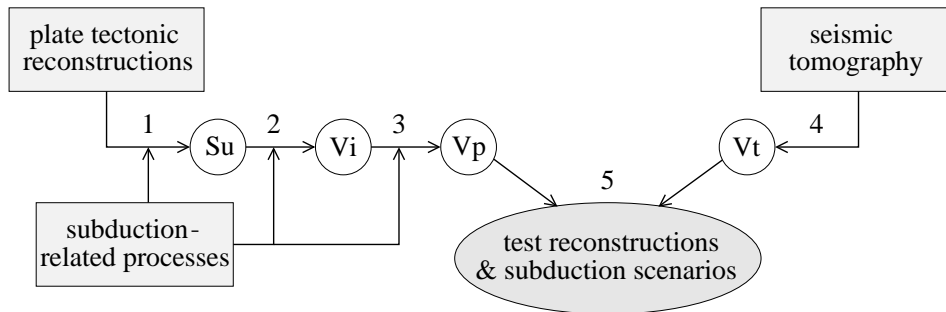
Figure 1.2: Schematic representation of our approach

1.4   This thesis

An overview of the Mesozoic-Cenozoic evolution of the Tethyan region is presented in **Chapter 2**. Herein, we will primarily focus on the large-scale plate motions as proposed by various tectonic reconstructions. The chapter is concluded with a summary of the aspects of the evolution that will be of importance for our analysis of Tethyan subduction.
In **Chapter 3**, we discuss the most important methods used in this study, namely (1) the interpretation of the positive velocity anomalies from seismic tomographic models in terms of temperature, (2) the calculation of the amount of convergence from plate tectonic reconstructions, and (3) the prediction of the present thermal structure of the subducted oceanic lithosphere. Because most Tethyan lithosphere started to subduct in Mesozoic times already,

and has almost completely disappeared today, we will develop a simplified method to approximate these slab volumes.

The large-scale history of subduction within the Tethyan region is explored in **Chapter 4** by analysing the bulk volumes of oceanic lithosphere subducted in the past 200 Ma. The total lithospheric surface subducted between the converging continents is calculated from the tectonic reconstruction of *Norton* (1999). The present thermal volumes predicted from these subducted plates are compared to the total volume of the relevant positive velocity anomalies underneath the Tethyan region, as determined from the tomographic model of *Bijwaard et al.* (1998).

More detailed aspects of the Tethyan evolution are investigated in **Chapter 5**. We incorporate other reconstructions (*Dercourt et al.*, 1993; *Şeng ör and Natal'in*, 1996; *Stampfli and Borel*, 2002, 2004) and analyse, among others, the effect of spreading ridge subduction, the Cenozoic continental collisions and possible subsequent slab break-off, and the role of oceanic back-arc basins. Each process will lead to a particular subdivision of the subducted lithosphere, of which the amounts, locations and timing of subduction can be compared to the volumes, positions and geometries of the separate tomographic anomalies. By evaluating the results for the different tectonic reconstructions, we will be able to present a preferred scenario for the subduction in the western and central Tethyan region.

Finally, in **Chapter 6** we address the subduction in the easternmost Tethyan region, namely the Indonesian archipelago. Because this region is characterised by ongoing subduction, we will directly model the present thermal structure of the subduction zones, instead of approximating the thermal volumes as in the previous chapters. The subduction zones models, based on the regional tectonic reconstructions of *Rangin et al.* (1990a,b) and *Lee and Lawver* (1995), will be converted into seismic velocity anomalies which can be compared directly to the tomographic images of the mantle structure.

Chapter 2

The Mesozoic-Cenozoic evolution of the Tethyan region

In this chapter, we review the tectonic evolution of the Tethyan region, the area marked today by the Alpine-Himalayan mountain chain that stretches from the Mediterranean to the Indonesian archipelago (Fig. 2.1). In Section 2.1, the main aspects of the present-day tectonics of this Tethyan region will be outlined. A discussion of the overall Mesozoic-Cenozoic evolution of the area, on the basis of a series of tectonic reconstructions, follows in Section 2.2. The chapter will be concluded in Section 2.3 with an overview of the aspects of the Tethyan evolution that will be investigated in this thesis.

2.1 Present-day tectonics

In the Eastern Mediterranean, the Hellenic trench forms the boundary between the African and Eurasian plates in the Aegean region (Fig. 2.1), and Arabia is in continental collision with Eurasia at the Bitlis suture in Turkey. The relative motion between the African and Eurasian plates is only small (<1 cm/yr), whereas the motion of Arabia to Eurasia is ∼2-3 cm/yr (*DeMets et al.*, 1994; *McClusky et al.*, 2000; *Sella et al.*, 2002). On the southern margin of the Eurasian plate, the Anatolian block of Turkey moves westward with ∼2.5 cm/yr relative to Eurasia (*McClusky et al.*, 2000). This motion is accommodated along the Bitlis suture and the North Anatolian Fault (e.g. *Morris and Tarling*, 1996). Faster movements, in a more southwestward direction, are recorded in the Aegean region as a result of additional extension in this area (*Jolivet*, 2001): Geodetic measurements indicate velocities with respect to Eurasia of ∼3 cm/yr for the Aegean (*McClusky et al.*, 2000). Both the Aegean region and Anatolian block are made up of several microcontinents and ophiolitic terranes (e.g. *Okay*, 2000; *Stampfli*, 2000; *Lips et al.*, 2001).
In the Middle East, the boundary between Arabia and Eurasia is formed by the Zagros suture zone, and the last remnant of Neo-Tethyan oceanic lithosphere is currently accommodated along the Makran trench south of Iran and Pakistan. GPS results indicate a distributed shortening across the Zagros mountains of ∼2-2.5 cm/yr (*McClusky et al.*, 2003). The Arabian

plate itself is rifting from the African plate through the spreading systems in the Red Sea and Gulf of Aden, their relative motion being ~0.5-1.5 cm/yr (*DeMets et al.*, 1994; *Sella et al.*, 2002; *McClusky et al.*, 2003). Large ophiolitic belts are found not only along the Bitlis and Zagros suture zones, but also in the Oman region on the eastern edge of the Arabian peninsula (e.g. *Knipper et al.*, 1986; *Robertson and Searle*, 1990).

The zone of continental collision between India and Eurasia is formed by the Indus-Tsangpo suture, extending along the margin of the Himalayan chain in Pakistan, northwest India, south Tibet and Myanmar. Although in collision, the present-day motion of India relative to Eurasia is ~3-4 cm/yr (*Sella et al.*, 2002; *DeMets et al.*, 1994). The Owen Fracture Zone and Carlsberg Ridge in the Indian Ocean form the boundary between the Indo-Australian and Africa-Arabian plates. The Arabian vs. Indo-Australian rate of motion along the Owen Fracture Zone is ~1-2 mm/yr (*Fournier et al.*, 2001). The relative motion between the Indo-Australian and African plates is ~2-2.5 cm/yr along the Carlsberg Ridge (*DeMets et al.*, 1994).

The complexity of the present-day tectonics in the Southeast Asian region is the result of the convergence and collision of the Eurasian, Indo-Australian and Philippine Sea plates (e.g. *Hamilton*, 1979). A major trench system curves around the rigid continental Sunda Block on the Eurasian plate. Along this Sunda-Java trench, Indian Ocean lithosphere of the Indo-Australian plate subducts northward beneath Indonesia at rates up to 8 cm/yr (*DeMets et al.*, 1994). The Australian continental shelf is in collision with the Eurasian continent along the extremely curved Banda arc, and the Halmahera trench is in frontal collision with the Sangihe trench in the Molucca Sea region (e.g. *Bowin et al.*, 1980; *Richardson and Blundell*, 1996; *Rangin et al.*, 1996). The Philippine and Eurasian plates are converging obliquely along the Philippine archipelago with a relative velocity of about 8 cm/yr (*DeMets et al.*, 1994).
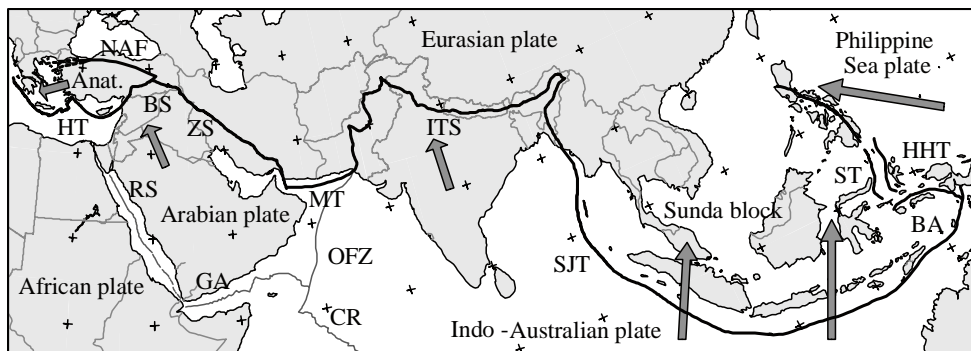
Figure 2.1: Tectonic framework of the Tethyan region, with Anat. = Anatolian Block. The arrows indicate present-day plate motions relative to Eurasia. Trenches and suture zones (black lines): Hellenic Trench (HT), North Anatolian Fault (NAF), Bitlis Suture (BS), Zagros Suture (ZS), Makran Trench (MT), Indus-Tsangpo Suture (ITS), Sunda-Java Trench (SJT), Sangihe Trench (ST), Halmahera Trench (HHT), and Banda Arc (BA). Other plate boundaries (grey lines): Red Sea (RS) and Gulf of Aden (GA) rifts, Owen Fracture Zone (OFZ), Carlsberg Ridge (CR).

2.2   Tethyan evolution according to various reconstructions

The Mesozoic-Cenozoic evolution of the Tethyan region will be reviewed on the basis of six different tectonic reconstructions, namely those of
1. *Van der Voo* (1993), referred to as **Van der Voo** in the following discussion, and giving an overview of the available paleomagnetic data from Carboniferous times onwards;
2. *Dercourt et al.* (1993), referred to as **Dercourt** hereafter, a reconstruction from the Early Triassic until present;
3. *Şengör and Natal'in* (1996), referred to as **Şengör**, a reconstruction from Late Triassic times onwards;
4. *Yang* (1998), referred to as **Yang**, a more general description of the eastern Tethyan evolution depicted in a Carboniferous-Triassic and Triassic-Tertiary configuration;
5. *Norton* (1999), referred to as **ExxonMobil**, a digitised reconstruction from the Early Ordovician until present;
6. *Stampfli and Borel* (2002, 2004), referred to as **Stampfli**, a reconstruction from the Early Ordovician to Late Cretaceous times.
Whereas the tectonic reconstructions of Van der Voo, Dercourt, Şengör, Yang, and ExxonMobil can be viewed upon as classical continental drift models, the recent plate tectonic reconstructions of Stampfli are constrained by dynamic plate boundaries. That is to say, oceanic surface has been added or removed to major continents and terranes in order to reconstruct the ancient plate boundaries through time.

Comparison of the rifting and accretion times of the several tectonic fragments is not straightforward, as they usually have different names and geometries in each reconstruction. For many continental fragments, only few or poor-quality data are available. The uncertainties generally increase going backwards in time, and are highly dependent on the tectonic fragment involved. Because of the uncertainties in the paleo-positions of the separate fragments, and in view of the more global approach of this research, we will concentrate here on the motions of the larger continental blocks in the reconstructions. Also the definition of the several oceanic basins varies from reconstruction to reconstruction: Oceans can be viewed upon as a single unit or as consisting of separate parts, and the direction of subduction is not always explicitly defined. Moreover, the reconstructions are usually given as a series of maps for which scale, projection, as well as the relative directions of motions of the fragments are missing. Therefore, the amount of convergence, which will be of interest for this study, is often hard to estimate. The reconstruction of ExxonMobil is totally digitised, and can thus be used to accurately determine the amount of convergence involved. Since we will primarily work with the reconstruction of ExxonMobil in later chapters, we will give special attention to this reconstruction in the discussion below.

2.2.1   Definition of tectonic fragments and terranes

In the discussion of the Tethyan evolution, many different continental fragments will come across. Each reconstruction usually has another interpretation of the geometries and names of the fragments involved. The names and present-day locations of the tectonic fragments of the Tethys region that are used in this section are illustrated in Figure 2.2. In this figure, both

the names and the shown accretion times, c.q. the moments at which the fragments accreted to Eurasia, are taken from the reconstruction of ExxonMobil. Summarised in Table 2.1 are the accretion times of the main tectonic fragments of Figure 2.2 as proposed by the different reconstructions discussed in this paper. In Table 2.2, the spreading and closure times of the oceanic basins in the Tethyan region, as proposed by the reviewed reconstructions, are shown. The fragments in Table 2.1 and Table 2.2 are often referred to differently in the various reconstructions. Therefore, an overview of the names of the fragments used in these tables, and the alternatives used in Figure 2.2 and other reconstructions, is given in Table 2.3. The several stages in the evolution of the Tethyan region according to the reconstructions of Stampfli and ExxonMobil are illustrated in Figures 2.3 to 2.8.

2.2.2 Definition of oceanic domains and suture zones

Throughout the Tethyan evolution, three large oceanic domains are generally recognised: First (see Figs. 2.3/2.4 and upper panels of 2.7/2.8), the **Paleo-Tethys** is the Paleozoic ocean south of the Hun Superterrane (see Table 2.3), and the Cimmerian blocks form the southern margin of the Paleo-Tethys. Closure of the Paleo-Tethys, associated with the collision of the Cimmerian blocks with Eurasia, is proposed before the end of the Triassic in most reconstructions. Secondly (see Figs. 2.4/2.5 and middle panels of 2.7/2.8), the **Neo-Tethys** is a Late Carboniferous-Permian (Dercourt, Şengör, Stampfli) or Late Triassic-Early Cretaceous (ExxonMobil, Van der Voo, Yang) ocean that separated the Cimmerian blocks from Gondwana. The eastern Mediterranean Sea is considered to be part of the Neo-Tethys as well. After final closure of the Paleo-Tethys, the Neo-Tethys started to subduct underneath Eurasia instead. The larger Arabian and Indian continents form the southern margin of the Neo-Tethys, thus closure of this ocean is associated with the continental collisions of Arabia and India with Eurasia. The third oceanic domain, although not strictly Tethyan, is the Indo-Australian oceanic lithosphere that was formed while India separated from Gondwana during Late Jurassic to Cretaceous times (see lower panels of 2.7/2.8).

Before the final closure of the Paleo-Tethys, slab roll-back is expected to have triggered, among others, the opening of various back-arc oceanic basins along the whole Eurasian margin in Permo-Triassic times. For example, in the reconstruction of Stampfli we can see that back-arc oceans like the **Meliata**, **Maliac**, **Pindos**, and **Karakya Oceans** opened, and stopped spreading, before the end of the Triassic (Figs. 2.3 and 2.4). Some of the back-arc basins must have closed together with the last remnants of the Paleo-Tethys. Other basins remained open even after the Paleo-Tethys closure, and have disappeared with the complex collision of the Cimmerian terranes later. The northward subduction of the Neo-Tethys also resulted in Mariana-type back-arc spreading and subsequent intra-oceanic subduction (see also Fig. 2.5). For example, the **Vardar Ocean** opened by the subduction of the Meliata Ocean underneath the Neo-Tethys (Stampfli), or as a branch of the Neo-Tethys directly (Şengör). In the reconstruction of Stampfli, the Neo-Tethys was subducting beneath the back-arc **Semail Ocean** in Cretaceous times. The Neo-Tethys, Semail Ocean and Vardar Ocean closed simultaneously during the Cretaceous.

A suture can be defined as the place where a former oceanic basin used to separate two con-
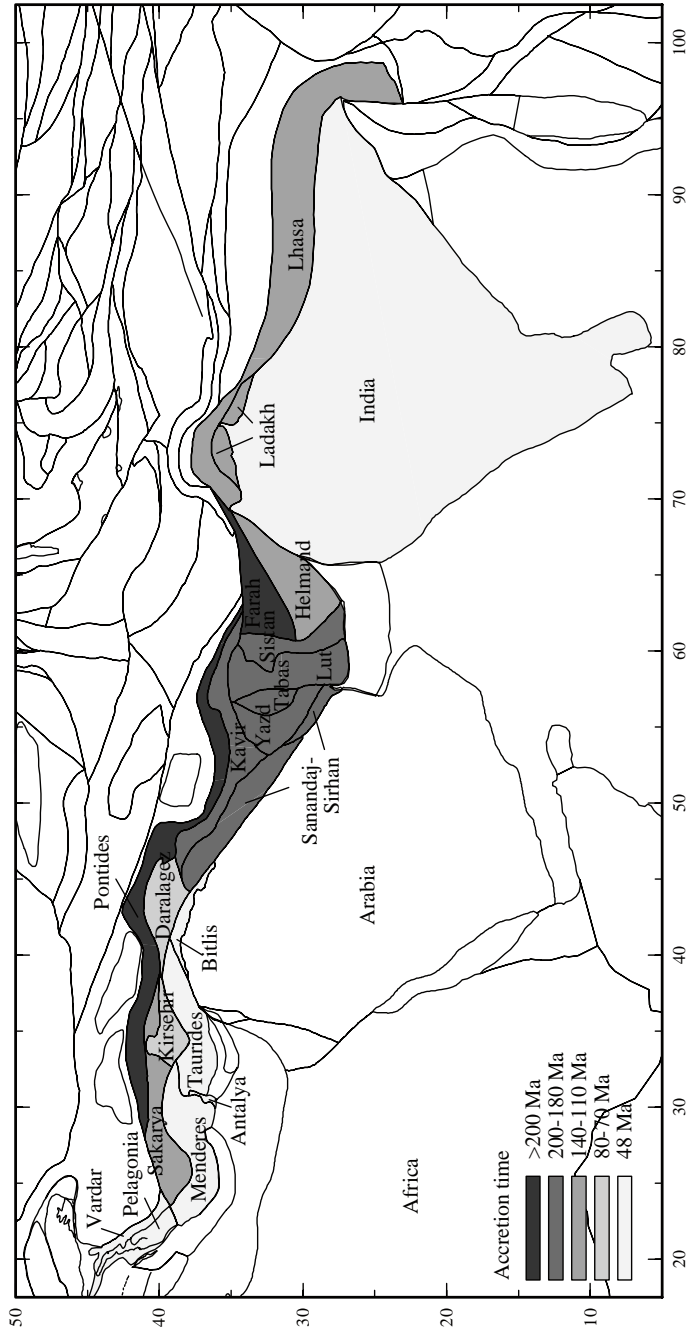
Figure 2.2: The tectonic fragments as discussed in this chapter, as well as their accretion times, according to the reconstruction of ExxonMobil (*Norton*, 1999). The collision of Arabia with Eurasia occurred around 22 Ma. Accreted at 48 Ma: Vardar, Pelagonia, Menderes, Antalya, Taurides, Bitlis area, and India. Accreted around 80-70 Ma: Kirşehir, Daralagez. Accreted between 140 and 110 Ma: Sakarya/Karakaya complex, Helmand, Ladakh-Kohistan arc, Lhasa. Accreted between 200 and 180 Ma: Sanandaj-Sirhan, Kavir area, Yazd, Tabas, Lut, Sistan. Accreted prior to 200 Ma: Pontides, Farah. The tectonic fragments north and east of the Pontides-Farah-Lhasa line (including the North Tibet, South China, Indochina, and Sibumasu block of Table 2.1) all accreted onto the Eurasian margin before 200 Ma, and are therefore not shown separately.

tinental fragments. Such a zone will form a stratigraphic, structural, metamorphic and magmatic boundary between both continental units. The larger suture zones within the Tethyan region include the **Izmir-Ankara(-Erzincan) suture**, separating the Menderes-Taurides-Kırşehir blocks from the Pontides. This suture probably contains the remnants of both the Paleo-Tethys and the Vardar oceanic basin. Suture zones in the Aegean region are likely to be connected to this Izmir-Ankara suture, but due to the more recent extension and collisional processes within the area it is difficult to identify these. More to the east, the **Bitlis suture zone** is the boundary between the Anatolide-Tauride block of Turkey and the Arabian plate, and has resulted from the Tertiary closure of the Neo-Tethys. The **Zagros suture** is the eastern continuation of the Bitlis suture zone, marking the boundary between the Arabian platform and the earlier accreted fragments in the Middle East. Remnants of the Semail Ocean must have been included here as well. Finally, the **Indus-Tsangpo suture** is associated with the closure of the Neo-Tethys between Greater India and the Helmand/Lhasa block.

2.2.3 Mesozoic-Cenozoic evolution

Pre-Jurassic ($>$ 200 Ma)

According to the reconstruction of ExxonMobil, the South China block starts its collision with Siberia around 225 Ma. Blocks like North Tibet, Indochina and Sibumasu are all part of South China, and thus Eurasia, before the end of the Triassic ($\sim$205 Ma). The Late Triassic accretion of Sibumasu onto Eurasia is associated with the closure of the northern part of the Paleo-Tethys. Amalgamation of the other Cimmerian terranes (see Table 2.3) with Eurasia, and the subsequent closure of the southern Paleo-Tethys, is proposed in Early Cretaceous times only. More to the west, also the Pontides already forms part of Eurasia before the Jurassic. The several blocks of Iran are positioned close to the Eurasian margin, but are not yet accreted to it. Moreover, South Tibet and Afghanistan are still part of the Gondwana margin, as are the Menderes-Taurides and Kırşehir blocks.

Like the reconstruction of ExxonMobil, the other reconstructions discussed here also assume North Tibet, Indochina and South China to be part of Eurasia by the Late Triassic. Only Van der Voo proposes accretion of Indochina and South China, and subsequent closure of the northern Paleo-Tethys, in the Early Jurassic. As for the closure of the southern part of the Paleo-Tethys, the reconstructions of Dercourt, Şengör and Van der Voo agree with ExxonMobil on a closing time *after* the Triassic. On the contrary, Stampfli and Yang assume a complete Paleo-Tethys closure by the Late Triassic: Stampfli proposes the Iran, Afghanistan, and South Tibet blocks to accrete onto Eurasia simultaneously with the pre-Jurassic collision of Sibumasu. Yang assumes that South Tibet is moving northward with the Neo-Tethys instead of the Paleo-Tethys, so that the Paleo-Tethys is already completely closed with the Sibumasu-Eurasia accretion. In the reconstruction of Stampfli, several back-arc oceans are formed in the western Tethyan region in pre-Jurassic times, e.g. the Meliata, Maliac and Pindos Oceans. However, spreading within these basins has already ceased before they start to subduct by the end of the Triassic. The ExxonMobil reconstruction does not explicitly define these oceans, but the rifting Mediterranean fragments are separated by intermediate basins as well.

Accretion times of Tethyan continental blocks

Timespan	Stampfli	Yang	Şengör	Dercourt	Van der Voo	ExxonMobil
Late Triassic	North Tibet South China ↓*) Afghanistan South Tibet	North Tibet South China Indochina Sibumasu	North Tibet South China Indochina	North Tibet South China Indochina Iran	North Tibet	North Tibet South China Indochina Pontides Sibumasu
Early Jurassic (~200)			Iran Pontides	Pontides	South China Indochina Sibumasu	Iran
Late Jurassic (~150)				Sibumasu	Iran Afghanistan South Tibet	
Early Cretaceous			Sibumasu Afghanistan South Tibet	Afghanistan South Tibet		Sakarya Afghanistan South Tibet
Late Cretaceous (~100)	Sakarya Kırşehir	South Tibet	Sakarya Kırşehir	Kırşehir		Kırşehir east Taurides
Early Tertiary (~50)	Taurides Menderes		Taurides Menderes	Taurides Menderes		west Taurides Menderes

Table 2.1: Approximate accretion times of the main tectonic blocks in the Tethyan region, c.q. the moments at which the blocks formed part of Eurasia, as proposed by the different reconstructions discussed in this chapter. Not all blocks are incorporated in all reconstructions. The shown reconstructions are from Stampfli = *Stampfli and Borel* (2002, 2004), Yang = *Yang* (1998), Şengör = *Şengör and Natal'in* (1996), Dercourt = *Dercourt et al.* (1993), Van der Voo = *Van der Voo* (1993), and ExxonMobil = *Norton* (1999). The Tertiary accretion times of the Arabian and Indian subcontinents are the same in all reconstructions, and are therefore not shown here. See Table 2.3 for comparison of the names of the blocks with the alternatives used in Figure 2.2 and other reconstructions. *) Including Indochina, Pontides, Sibumasu and Iran.

19

Opening and closure times of Tethyan oceanic basins

Timespan	Stampfli	Yang	Şengör	Dercourt	Van der Voo	ExxonMobil
Late Triassic	Closure Paleo-Tethys	Closure Paleo-Tethys	Closure northern Paleo-Tethys	Closure northern Paleo-Tethys	Closure northern Paleo-Tethys	Closure northern Paleo-Tethys
Early Jurassic			Spreading Kirşehir + Menderes	Spreading separating Kirşehir	Closure northern Paleo-Tethys	
Late Jurassic	Spreading Vardar Ocean		Spreading Vardar Ocean	Spreading separating Menderes	Closure southern Paleo-Tethys	Spreading separating Kirşehir
Early Cretaceous	Spreading Semail Ocean		Closure southern Paleo-Tethys	Closure southern Paleo-Tethys		Closure *) southern Paleo-Tethys
Late Cretaceous	Obduction Semail Ocean ridge	Closure northern Neo-Tethys	Obduction Neo-Tethys ridge	Obduction Neo-Tethys ridge		Obduction Neo-Tethys ridge
Tertiary	Closure Neo-Tethys	Closure southern Neo-Tethys	Closure Neo-Tethys	Closure Neo-Tethys	Closure Neo-Tethys	Closure Neo-Tethys

~200 ~150 ~100 ~50

Table 2.2: Approximate opening and closure times of the oceanic basins in the Tethyan region according to the reconstructions discussed in this chapter. The shown reconstructions are from Stampfli = *Stampfli and Borel* (2002, 2004), Yang = *Yang* (1998), Şengör = *Şengör and Natal'in* (1996), Dercourt = *Dercourt et al.* (1993), Van der Voo = *Van der Voo* (1993), and ExxonMobil = *Norton* (1999). See Table 2.3 for comparison of the names of the blocks with the alternatives used in Figure 2.2. *) Early Cretaceous separation of Menderes from Gondwana as well.

	Figure 2.2	Table 2.1/2.2	Alternatives
Hun Superterrane		North Tibet	Qiantang
		South China	Yangtze
		Indochina	Annamia
	Pontides	Pontides [1]	
	Sakarya	Sakarya	west-Pontides
		Sibumasu [2]	Mnt Victoria
	Helmand	Afghanistan	
Cimmerian blocks / Mega-Lhasa terrane	Yazd	Iran	
	Tabas		
	Lut		
	Sistan		
	Kavir		
	San/Sir [3]		
	Ladakh	South Tibet	
	Lhasa		
	Kirşehir	Kirşehir	
	Daralagez	east-Taurides	
	Taurides	west-Taurides	Menderes-Taurides
	Menderes	Menderes	

Table 2.3: Overview of the names of the various fragments as given in Table 2.1/2.2, and the alternatives as used in Figure 2.2 and other reconstructions. The North Tibet, South China, Indochina, and Pontides blocks belong to the Hun Superterrane. This terrane formed, together with the Kazakhstan block, the northern margin of the Paleo-Tethys. Iran, Afghanistan, South Tibet, and Sibumasu are usually referred to as the Cimmerian blocks or Mega-Lhasa terranes. They formed the southern margin of the Paleo-Tethys and northern margin of the Neo-Tethys. [1] With the Pontides, the whole sliver extending from the Aegean Sea to the Lesser Caucasus is addressed, thus including fragments like the southern Caucasus, Alborz and Kopet Dagh. [2] The Sibumasu terrane derives its name from the regions of Siam (Thailand or Shan-Thai block), Burma (Myanmar), Malaysia and Sumatra. [3] San/Sir = Sanandaj-Sirhan.

21

230 Ma - Ladinian

Figure 2.3: Triassic reconstruction of *Stampfli and Borel* (2004), see Fig. A.2 in the Appendix for a colour version.

Early Jurassic (∼200-160 Ma)

After the Late Triassic, seafloor spreading in the Central Atlantic induces the rotation of Gondwana relative to Eurasia. In the reconstruction of ExxonMobil, the Iranian blocks are amalgamated with Eurasia since the Late Triassic - Early Jurassic. Northward subducting oceanic lithosphere of the Neo-Tethys is now accommodated along an arc system south of the Pontides and Iran. More to the east, Afghanistan and South Tibet have rifted from the Gondwana margin. These terranes are drifting towards Eurasia while the oceanic lithosphere of the southern Paleo-Tethys is subducting further northward.

As discussed above, the northern part of the Paleo-Tethys is already closed in the Triassic according to the reconstructions of ExxonMobil, Dercourt and Şengör. In Early Jurassic, the
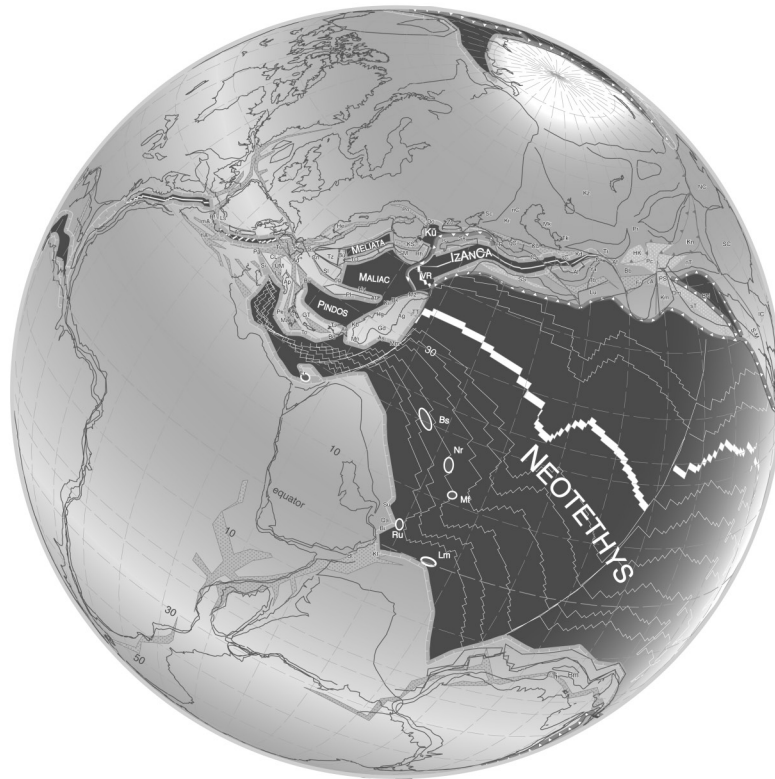
180 Ma - Toarcian-Aalenian

Figure 2.4: Jurassic reconstruction of *Stampfli and Borel* (2004), see Fig. A.3 in the Appendix for a colour version.

northern part of the Paleo-Tethys is closed in the reconstruction of Van der Voo as well. Like ExxonMobil, also Dercourt and Şengör propose collision of Iran and Pontides with Eurasia around the Late Triassic to Early Jurassic, indicating that the Neo-Tethys has started to subduct in the western Tethyan region. In these reconstructions, the southern Paleo-Tethys is still subducting in the eastern part of the area. According to Stampfli and Yang, the Paleo-Tethys is already totally closed by this time so that only the Neo-Tethys is subducting northward underneath Eurasia. In the reconstruction of Stampfli, the Vardar Ocean develops as an oceanic back-arc basin, caused by the subduction of the Meliata Ocean underneath the Neo-Tethys. The ocean opens within the Paleo-Tethys suture zone, thereby separating the
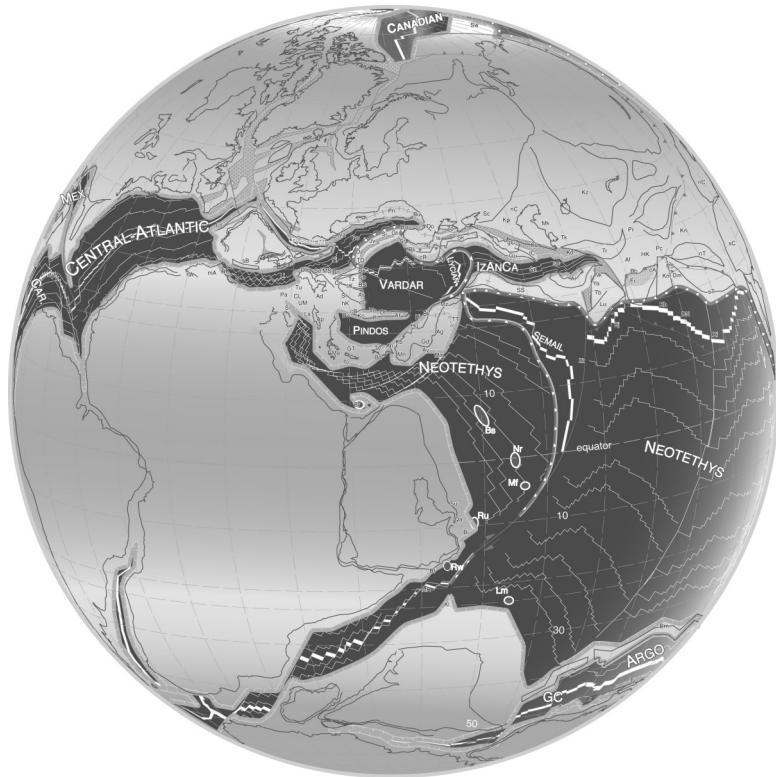
121Ma - Barremian-Aptian (an. M0)

Figure 2.5: Early Cretaceous reconstruction of *Stampfli and Borel* (2004), see Fig.A.4 in Appendix for a colour version.

Taurides-Menderes-Kirşehir block from the Pontides again. During the Jurassic, the Vardar Ocean consumes the Meliata and Maliac oceanic basins. In the reconstruction of Şengör, the Vardar Ocean is an Early Jurassic branch of the Neo-Tethys.

Late Jurassic to Early Cretaceous (∼160-100 Ma)

Spreading in the northern and southern Atlantic commences in the Early Cretaceous, increasing the motion of Africa relative to Eurasia. Furthermore, rifting between India and Gondwana initiates the opening of the Indian Ocean. In the reconstruction of ExxonMobil, Afghanistan and South Tibet collide into Eurasia around 140 Ma. After amalgamation of blocks like South Tibet and Iran, the region is left with only one single, long-stretched subduction zone along which the Neo-Tethys subducts northward underneath Eurasia. From 120
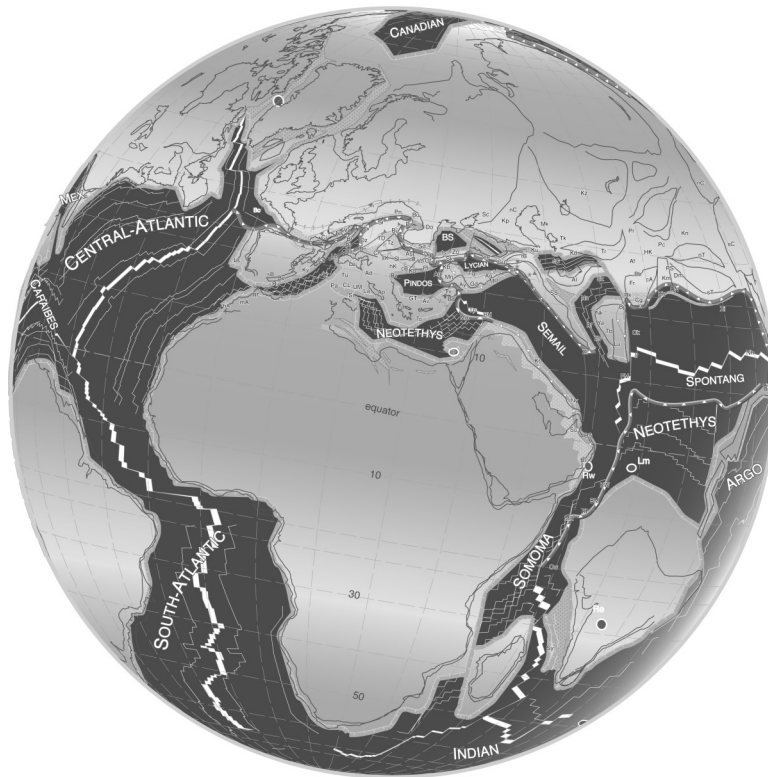
70 Ma - Early Maastrichtian (an. 31)

Figure 2.6: Late Cretaceous reconstruction of *Stampfli and Borel* (2004), see Fig. A.5 in Appendix for a colour version.

to 90 Ma, continental fragments like Kirşehir and Menderes-Taurides are separated from the Northeast African continent by active spreading.

In agreement with ExxonMobil, also Şengör and Dercourt propose that the Afghanistan and South Tibet blocks (the remaining parts of the Cimmerian terranes) are not yet accreted to Eurasia, and thus the Paleo-Tethys not yet closed, until the Early Cretaceous. Opposed to this, Van der Voo suggests that the Paleo-Tethys is completely closed in the Late Jurassic. As discussed above, ExxonMobil proposes rifting of Kirşehir and Menderes-Taurides around Late Jurassic - Early Cretaceous only, while Stampfli proposes the separation of Menderes-Taurides-Kirşehir already in the Early Jurassic. Also in the Late Jurassic reconstructions of Dercourt and Şengör, these blocks are positioned half-way between Gondwana and Eurasia. Compared to the ExxonMobil reconstruction, Dercourt, Şengör and Stampfli thus propose an

earlier rifting of Menderes-Taurides and Kirşehir. By the end of the Jurassic, the Vardar Ocean of Stampfli has totally replaced the Meliata Ocean, and subduction of the Vardar Ocean itself starts. Also according to Şengör, subduction of the Vardar branch starts around this time. For the Early Cretaceous, Stampfli proposes the development of the Semail and Spongtang back-arc oceans, overriding the complete Neo-Tethys, in the Middle East and Indian region, respectively.

Late Cretaceous (∼100-65 Ma)

In the Late Cretaceous, the Indian continent rifts from Gondwana and moves northward along a major transform fault. South of the continent, the present Indian Ocean of the Indo-Australian plate is formed. In the Mediterranean, separate smaller fragments are moving further northward towards their present-day positions. All major suture zones in Greece and Turkey are thought to have closed in Cretaceous or Early Cenozoic times. In the ExxonMobil reconstruction, the block formed of Kirşehir and the eastern Taurides collides into Eurasia, and the Pontides subduction zone closes accordingly, between 80 and 70 Ma. This zone is known today as the eastern part of the Izmir-Ankara(-Ercinzan) suture. Neo-Tethyan oceanic lithosphere is now subducting along the Izmir-Ankara arc south of Sakarya, and the Taurides arc south of Kirşehir and the eastern Taurides. Between 90 and 70 Ma, the ridge axis separating Arabia and India has an extension northeast of the Arabian platform that obducts onto the Arabian continental margin.

According to Dercourt and Şengör, the oceanic spreading ridge of the Neo-Tethys subducts underneath Eurasia in the Indian region, and obducts onto the Arabian margin in the Middle East, around Late Cretaceous times (∼90-80 Ma). In agreement with ExxonMobil, the Kirşehir blocks become attached to Eurasia around the Middle Cretaceous in these reconstructions. On the contrary, Stampfli proposes Neo-Tethyan ridge subduction in the western part of the region around 140 Ma being the trigger for the opening of the Semail Ocean (see above). Around 90-80 Ma, the Semail Ocean in this reconstruction has totally consumed the Neo-Tethys, and starts to subduct itself. The reconstruction of Stampfli suggests that most 'Neo-Tethys' ophiolites do not originate from the Neo-Tethys itself, but from its back-arc basins. In the Stampfli and Şengör reconstructions, spreading in the Vardar Ocean ceases by the Middle Cretaceous, and the basin itself subducts during the Late Cretaceous.

Tertiary (∼65-0 Ma)

The Cenozoic evolution of the Tethyan region is relatively well defined, and the several reconstructions only show minor differences for this timespan. In the Tertiary, the Menderes-Taurides and other Eastern Mediterranean blocks finally accrete onto Eurasia. In the ExxonMobil reconstruction, the Menderes-Taurides block collides with Eurasia around 48 Ma. Convergence between Africa and Eurasia is now accommodated along the Hellenic arc, and northward subduction of the last remnants of the Neo-Tethys starts around the Miocene when Cyprus accretes to Eurasia (∼13 Ma). Extension within the Aegean region since ∼10 Ma is associated with outward migration of the Hellenic arc.

The most recent Tertiary developments in the Middle East include the separation of Arabia from the African continent through the spreading in the Red Sea and Gulf of Aden since 30 Ma. Collision of the Arabian continent with Eurasia, and the formation of the Makran accretionary zone, occurs around 22 Ma. This results in further deformation of the fragments at the southern margin of Eurasia. The Iran subduction zone is closed, and is recognised as the Bitlis-Zagros suture zone today. The last remnants of the Neo-Tethys (or Semail Ocean) are now subducting along the southern margin of Makran only.

In the eastern part of the Tethyan region, the evolution is dominated by the first indentation of Greater India into Eurasia around 48 Ma. Although in continental collision, northward convergence between India and Eurasia continues. Due to the collision, the Iranian blocks start an anti-clockwise rotation towards their present-day position. Furthermore, the collision of India causes deformation of Afghanistan, South Tibet, and older continental blocks on the Eurasian margin.

In the Indonesian region, Indo-Australian oceanic lithosphere is actively subducting underneath the Indonesian archipelago. An accretionary sliver forms in the western Andaman, and Borneo rotates anti-clockwise, between 48 and 15 Ma. Around 10 Ma, the Andaman Sea opens due to the oblique plate convergence along the trench system. More to the east, the first continental fragments of the Australian plate arrive at the Eurasian Sunda Block in the Sulawesi and Banda arc region around 20 Ma. The Tertiary evolution of the Indonesian region will be discussed in more detail in Chapter 6 on the basis of the regional reconstructions of *Rangin et al.* (1990a,b) and *Lee and Lawver* (1995).
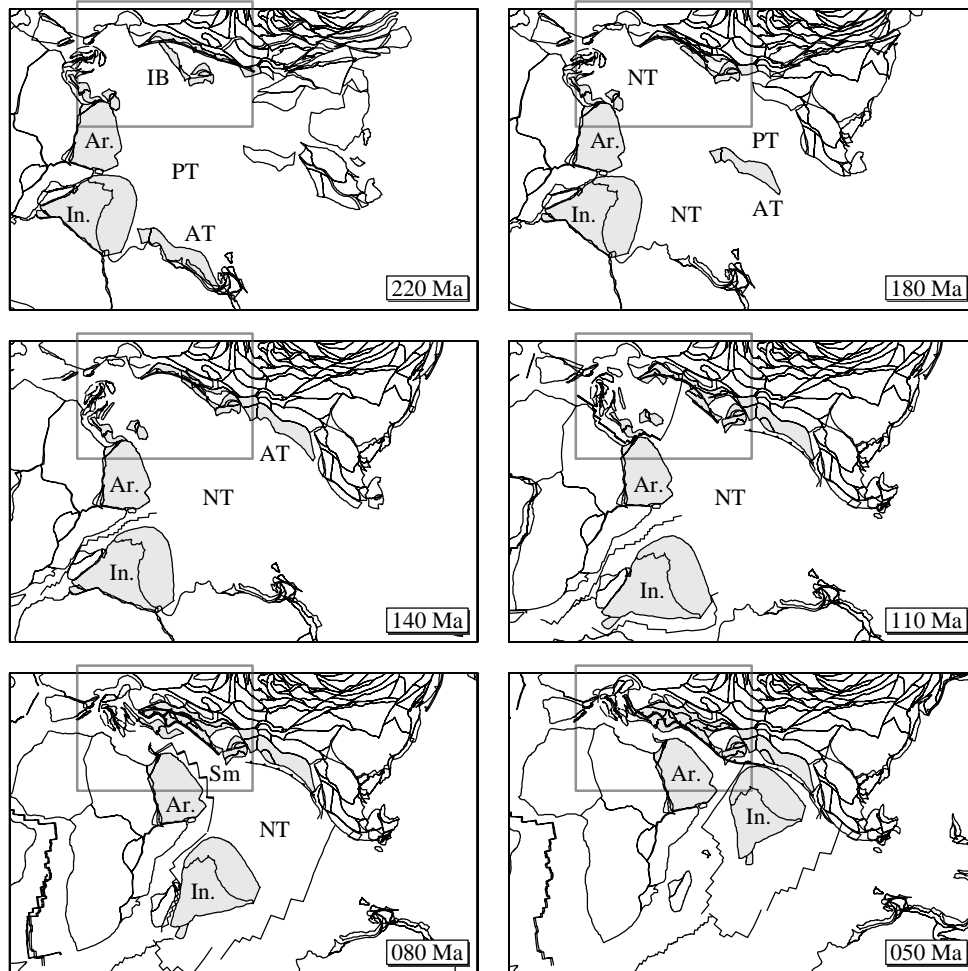
Figure 2.7: Six stages in the evolution of the Tethyan region according to the plate tectonic recon-struction of ExxonMobil (*Norton*, 1999) with the Eurasian plate held fixed to its present-day position. Some of the fragments discussed in this section are marked for reference: IB = Iranian blocks, AT = Afghanistan/South Tibet, Ar. = Arabian continent, and In. = Indian continent (see Figs. 2.2 and 2.8 for more details on the smaller blocks). The Southeast Asian blocks are not separately shown here because their accretion times predate the timespan of our interest. Also indicated are the Paleo-Tethys (PT), Neo-Tethys (NT), and Semail (Sm) oceanic basins. From upperleft to lowerright we can see at 220 Ma: Closure northern Paleo-Tethys (= Accretion Iranian blocks), 180 Ma: Northward drift Afghanistan and South Tibet, 140 Ma: Closure southern Paleo-Tethys (= Accretion Afghanistan/South Tibet), 110 Ma: Northward drift Kirşehir and Taurides-Menderes, 80 Ma: Spreading and obduction Semail Ocean, and 50 Ma: Closure Neo-Tethys (= Accretion Kirşehir and Taurides-Menderes). Each map is plotted in a Mercator projection with the great circle starting at (0°N,65°E) with azimuth 90° as an equator. The shown box is the approximate area plotted in Figure 2.8.
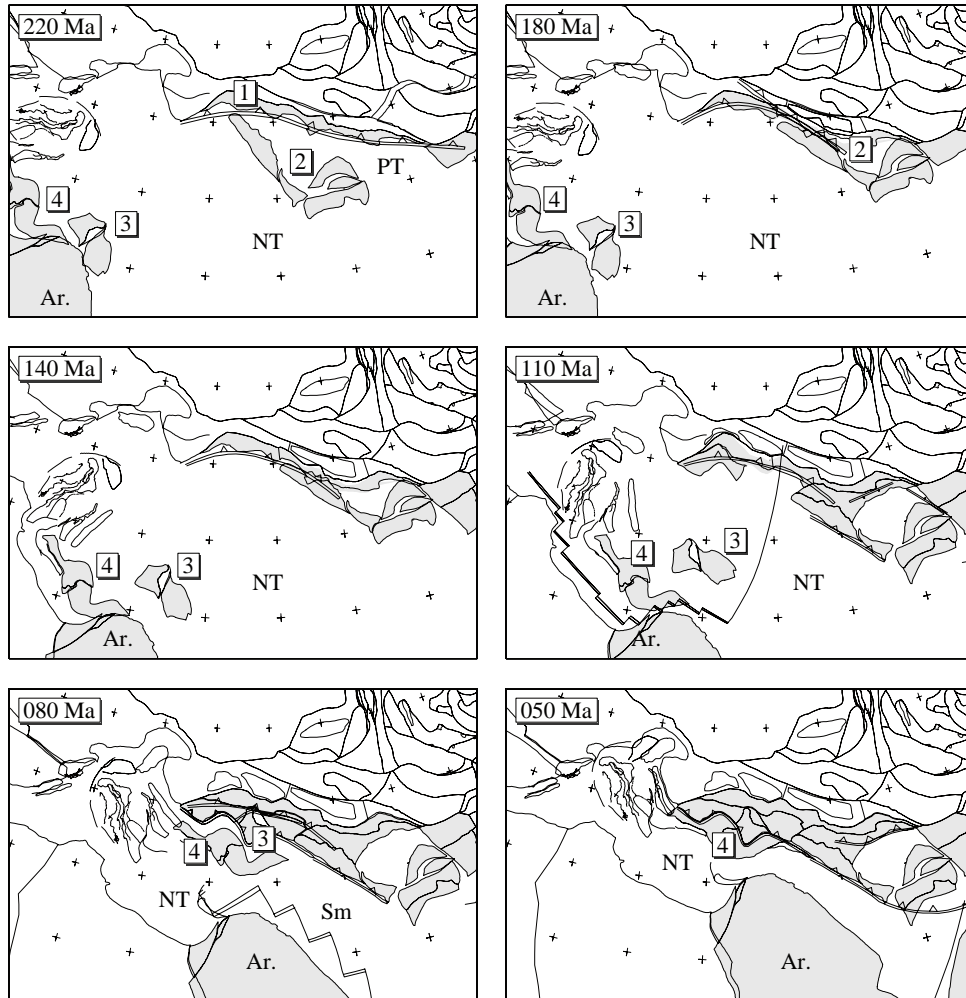
Figure 2.8: Six stages in the evolution of the Eastern Mediterranean and Middle East according to ExxonMobil (*Norton*, 1999). In this figure: [1] = Pontides/Farah, [2] = Iranian blocks, [3] = Kirşehir/east-Taurides, and [4] = Menderes/west-Taurides (see Fig. 2.2 for further details). Also indicated are the Paleo-Tethys (PT), Neo-Tethys (NT), and Semail (Sm) oceanic basins. From upperleft to lowerright we can see at 220 + 180 Ma: Accretion Iranian blocks (= Closure northern Paleo-Tethys), 140 Ma: Rifting Kirşehir and east-Taurides, 110 Ma: Rifting Menderes and west-Taurides, 80 Ma: Accretion Kirşehir and east-Taurides, and 50 Ma: Accretion Menderes and west-Taurides (= Closure Neo-Tethys). The Pontides and Farah blocks already accreted onto the Eurasian margin prior to 200 Ma. Each map is plotted in a Mercator projection with the great circle starting at (35°N,35°E) with azimuth 90° as an equator.

2.3   Evolutionary aspects of main importance for this thesis

The Mesozoic-Cenozoic closure of the Tethys Ocean has been dominated by the movements of the African-Arabian and Indo-Australian plates relative to Eurasia. The characteristics of the various regions within the Tethyan area show some remarkable differences: In the *Eastern Mediterranean*, several microcontinents amalgamated with Eurasia during Cenozoic times, thereby closing the intermediate oceanic basins. If active spreading within these basins has occurred while they were already subducting, this will have increased the amount of subduction in the region. The Cimmerian blocks in the *Middle East* accreted to Eurasia largely by Early Jurassic times already. During the Cenozoic, the western part of the area might have been affected by the accretion of the Eastern Mediterranean microcontinents, but the larger part of the region is only influenced by the Arabian continental collision with Eurasia. The *Himalayan area* is, of course, highly influenced by the Cenozoic indentation of India into Eurasia. Furthermore, accretion of the fragments north of India (Afghanistan, South Tibet) already occurred in Early Cretaceous, and no intermediate oceanic basins are proposed for this area since that time. If additional spreading occurred in the Neo-Tethys or its back-arc basins, this will have affected the amount of subduction.

In this thesis, we will investigate whether the different characters of the regions are reflected in the volume, location and geometry of the subducted material. Below, we will give an overview of those aspects of the tectonic evolution that will be of importance for our analysis of the Tethyan region, and the comparison between the different reconstructions. As they will be discussed in more detail in Chapter 4 and 5, we also indicate the sections in which each particular aspect is primarily addressed. Because the reconstructions of Van der Voo and Yang comprise more general descriptions of the Tethyan evolution (see p. 15), only the reconstructions of Dercourt, Şengör, ExxonMobil, and Stampfli will be discussed in the following.

The motion along the Owen Fracture Zone (4.4)   The Owen Fracture Zone in the Middle East is associated with the strike-slip motion of the Indo-Australian plate relative to the Africa-Arabian plate during the Cenozoic. Only in the plate model of Dercourt, Neo-Tethyan lithosphere north of India is proposed to have been subducted westward along the plate boundary as well. The large-scale motion of India can be expected to have influenced the process of subduction and thus the resulting geometry of the subducted material.

The subduction of the Paleo-Tethys (5.5)   The northern Paleo-Tethys closed around Late Triassic according to all reconstructions, and we therefore expect *no* active spreading within the Paleo-Tethys since that time. Most reconstructions propose the Paleo-Tethyan oceanic lithosphere has been subducted northward underneath Eurasia. However, a more eastward subduction of the Paleo-Tethys has been proposed by Stampfli, and southward subduction underneath the Cimmerian blocks by Şengör. For a large oceanic basin like the Paleo-Tethys, the ancient direction of subduction will have had a large effect on the present-day location of the subducted oceanic lithosphere.

The effect of continental collision (5.5/5.7)   We expect that we can see the effect of the Cenozoic collisions of the Arabian and Indian continents with Eurasia in the geometry and position of the subducted material. Although the Afghanistan and South Tibet blocks are much smaller than the Arabian and Indian continents, their collisions - associated with the closure of the Paleo-Tethys - may have affected the slab morphology and its present position in the mantle as well.

Neo-Tethyan ridge spreading and subduction (5.6)   Spreading within the Neo-Tethys has been active after the rifting of the Iranian blocks from Gondwana. The eventual subduction of the Neo-Tethyan spreading ridge is proposed by ExxonMobil, Şengör, and Dercourt in the Late Cretaceous (∼90-80 Ma), but already in Early Cretaceous (∼140-120 Ma) by Stampfli. Evidently, we expect *no* active spreading within the Neo-Tethys after ridge subduction. Moreover, it is likely that the morphology of the subducted material will have been affected by ridge subduction, although later processes may have overprinted these effects.

The role of the back-arc oceanic basins (5.6)   In the reconstruction of Stampfli, the Semail Ocean in the Middle East, and the Spongtang Ocean in the Indian region, came into existence right after the Neo-Tethyan ridge subducted in Early Cretaceous. Spreading within these back-arc oceans occured at the direct expense of the Neo-Tethys, and the Semail/Spongtang oceanic ridges obducted onto the Gondwana margin by the end of the Cretaceous. Although the existence of these back-arc basins will have led to additional subduction in the region, the absence of Neo-Tethyan lithospheric spreading will probably have neutralised this amount. Because the Neo-Tethys is proposed to have been subducted *northeastwardly* underneath the Semail Ocean, the locations and geometries of subducted material may give an indication of the Semail vs. Neo-Tethyan spreading and subduction history.

Additional convergence by drifting Mediterranean fragments (5.8)   In the western part of the region, separate rifting of continental fragments has been proposed in addition to the large-scale Africa vs. Eurasia motion (ExxonMobil, Şengör, Dercourt). On the contrary, Stampfli assumes that rifting and spreading of the oceanic basins between these fragments already took place before the Jurassic, and instead proposes the Cretaceous opening of a Vardar back-arc ocean. Because Stampfli assumes *no* Neo-Tethyan oceanic spreading where the Vardar Ocean is active, we expect the differences between Vardar vs. Neo-Tethyan spreading to be relatively small. Apart from the additional amount of convergence, we expect that subduction of intermediate basins along different trench systems will have led to a different distribution of subducted material than subduction of one single (Neo-Tethyan) oceanic basin. Also the Cretaceous subduction of a single oceanic basin with the size of the Vardar Ocean may be visible as a separate identity today.

Chapter 3

Methods

In this study, we want to relate subducted lithospheric material, as predicted from tectonic reconstructions, to the seismic wave speed anomalies in the mantle as imaged by tomography. How to interpret the velocity anomalies of a seismic tomographic model will be discussed in Section 3.1. Each seismic anomalous volume associated with subducted lithosphere is assumed to represent a predominantly thermally perturbed region. In Section 3.2, it will be shown how to determine the past plate velocities and amount of convergence from a tectonic reconstruction, leading to a prediction of the lithospheric surface that must have been subducted in the past. A method to estimate the initial and present-day thermal structure of the subducted lithospheric surface will be addressed in Section 3.3.

3.1   Positive velocity anomalies from seismic tomography

Seismic tomography is a technique to image the three-dimensional velocity structure of the Earth's interior. Based on previous work concerning the relationship between tomographic mantle structure and thermal heterogeneities associated with subduction (e.g. *Richards and Engebretson*, 1992; *Wen and Anderson*, 1995; *Bunge et al.*, 1998), we expect that subducted lithosphere will be detected as positive velocity anomalies in tomographic models, primarily as a result of the effect of temperature on seismic wave speeds. Interpretation of the relevant seismic anomalies in terms of volumes of subducted material requires understanding of the information content of a tomographic image. Therefore, the tomographic method is explained briefly in Section 3.1.1, and a discussion on the uncertainties in the imaged velocity anomalies follows in Section 3.1.2. As we will work with the tomographic model of *Bijwaard et al.* (1998) in this study, specific attention will be paid to their BSE-model. Care should be taken when interpreting seismic velocity anomalies in terms of quantities like temperature, composition, and anelasticity. The relative importance of these is summarised in Section 3.1.3. As will be argued in that section, the tomographic anomalies that are associated with subducted lithosphere are largely due to temperature anomalies. We can therefore use the temperature derivatives of seismic velocities to convert subduction-related seismic anomalies to thermal

perturbations. We will propose adequate values for the derivatives and discuss the method of conversion in Section 3.1.4.

3.1.1 The tomographic method

Seismic tomography methods image the 3-D variations of seismic velocity within the Earth. A tomographic model is constructed from the differences between observed seismological data and data predicted by a particular reference structure of the Earth. The wave-speed heterogeneities imaged by seismic tomography are typically represented in terms of deviations from the reference model. The structure inverted by tomography depends on, among others, the reference velocity model, the data set, the model parameterisation, and the inversion strategy.

Reference models in which wave speeds vary only with depth are mostly worked with in seismic tomography. Some reference models, like the widely-used PREM of *Dziewonski and Anderson* (1981), are constructed from a large amount of normal mode, surface and body-wave data, and travel times. Other reference models, like the models of *Kennett and Engdahl* (1991), *Morelli and Dziewonski* (1993) and *Kennett et al.* (1995), have been determined from travel times only, incorporating a wide range of seismic phases.

Travel-time tomography is based on the arrival times of P- or S-wave phases, or a combination of both. When more phases are included than just the first arrival times, the hypocenters can be determined more accurately. *Bijwaard et al.* (1998) have used the data set of *Engdahl et al.* (1998) to perform their tomographic inversion. *Engdahl et al.* (1998) recalculated the travel times and hypocenters from the ISC database using the ak135 model of *Kennett et al.* (1995), and a more accurate earthquake location procedure.

Tomographic models have to be parameterised, e.g. by dividing them into non-overlapping cells or a grid with interpolated values between the nodes. Such parametrisations usually allow for detailed imaging, but the large number of model parameters makes it necessary to use iterative solvers (see Section 3.1.2). Cell sizes can also be adopted to sampling density, leading to an irregular network of cells (e.g. *Spakman and Bijwaard*, 2001).

In the model of *Bijwaard et al.* (1998), the cell sizes in densely sampled regions are as small as 0.6° in the upper mantle (∼66 km), 1.2° down to 1100 km depth (∼110 km), and 1.8° down to the CMB (∼165 km). The layer thicknesses vary from 35 km in the upper mantle to 200 km in the lowermost mantle.

Bijwaard et al. (1998) performed an inversion for the entire mantle, but were able to retain the degree of detail usually imaged by regional-scale tomography for some regions because of their irregular cell parameterisation. In general, continental and tectonically active regions, like the Tethyan area, are relatively well sampled, while low-ray density regions encompass the mantle below major oceans like the Pacific.

3.1.2 Uncertainties in the tomographic model

There are several important uncertainties in the tomographic method itself that will influence the imaged wave-speed anomalies. Due to data errors and lack of data, the tomographic matrix that has to be inverted is usually inconsistent and underdetermined. Therefore, it is necessary to apply some form of regularisation (i.e. damping) to constrain the solution. The

optimum damping needs to be assessed experimentally (e.g. see *Bijwaard*, 1999; *Deal et al.*, 1999).

A disadvantage of large-size tomographic inversions is that the resolution and covariance matrices cannot be calculated. Formal resolution analyses require the inversion of matrices to compute spatial resolution and model covariance. For large-size tomographic problems, like that of *Bijwaard et al.* (1998), such matrix inversions are computationally not feasible at present. These tomographic inverse problems have to be solved with approximate, iterative procedures, and separate synthetic tests need to be done to assess the model resolution (*Spakman and Nolet*, 1988). Sensitivity analyses like these (e.g. with permuted data tests, impulse response tests, or layer-cake tests) have potential shortcomings (*Lévêque et al.*, 1993), yet it is the most practical way of estimating the resolution.

For the model of *Bijwaard et al.* (1998), sensitivity analyses showed that the resolution in well-resolved regions is often at the scale of the cell size used locally. Because spatial resolution generally varies strongly with position in the model, sensitivity test results must be analysed for each particular region of interest separately. Using permuted data tests (*Spakman*, 1991), *Bijwaard et al.* (1998) found an average error of 0.21% of the background velocity, with a standard deviation of 0.16%, which should be treated as an upper limit for the model uncertainty.

Modelled amplitudes of seismic velocity anomalies are in the order of 2-3% in the upper mantle, but typically decrease to 0.5% in the lower mantle. Although this observed decrease in amplitude with depth seems to be a real feature (e.g. *Spakman et al.*, 1993; *Van der Hilst*, 1995; *Bijwaard et al.*, 1998), the values are also influenced by the tomographic inversion. According to *Bijwaard and Spakman* (2000), the inverted anomalies are approximately 20-30% smaller than the true values in well-resolved regions.

Many global models are obtained from linearised tomographic inversions, and do not account for nonlinear processes like ray bending through the inferred velocity heterogeneities. *Bijwaard and Spakman* (2000) performed a non-linear inversion of the same data set from which the BSE-model was constructed and found that amplitudes changed, and images were more focussed, in the uppermost mantle of several regions. However, both models were found to be quite similar below 200-300 km depth, although the inferred structure was slightly sharpened.

3.1.3   Interpreting the seismic velocity anomalies

P- and S-wave velocities (V_p/V_s) are dependent on density ρ as well as the elastic parameters κ and μ via

$$V_p = \sqrt{(\kappa + 4\mu/3)/\rho} \quad \text{and} \quad V_s = \sqrt{\mu/\rho} \tag{3.1}$$

in an isotropic elastic medium. Both density and elastic parameters are related to temperature, pressure, and composition. The relations are complex and generally poorly known for the deeper Earth. It is therefore difficult to determine the origin of the seismic velocity anomalies imaged in tomographic models. Mineral physics studies have led to estimates of the density and elastic parameters, as well as their pressure and temperature derivatives, of relevant materials at various pressure and temperature conditions. The parameters are typically determined for an average mineral assemblage in the mantle. Beside the assumptions

on mantle composition, there are many uncertainties in the extrapolation of the experimental results. For example, the parameters determined in laboratory experiments have to be extrapolated (using an equation of state) to Earth-like pressures and temperatures (e.g. *Jackson and Rigden*, 1998). Variations in sound velocity under adequately high pressures have been determined at ultrasonic frequencies, but these values must be extrapolated to velocities with seismic frequencies (see *Karato*, 1993; *Jackson and Rigden*, 1998). Whereas many estimates from experimental data are restricted to the upper mantle (*Ranalli*, 1996; *Goes et al.*, 2000), recent studies have also proposed values for temperature and compositional derivatives lower in the mantle (e.g. *Trampert et al.*, 2001; *Cammarano et al.*, 2003; *Deschamps and Trampert*, 2003).

In the following, the importance of thermal perturbations and variations in composition in the interpretation of seismic velocity anomalies will be discussed first. Next, the influence of anelasticity and anisotropy, and the presence of partial melt or water, will be addressed. Pressure is important for the absolute values of all seismic parameters. However, pressure derivatives are too small to affect the observed velocity variations (e.g. *Trampert et al.*, 2001) and will therefore not be discussed here. We will focus on the seismic velocity anomalies that are associated with slab remnants.

Temperature

To convert velocity anomalies to thermal perturbations, the temperature dependence of seismic velocities needs to be resolved. The linear extrapolation of density and elastic parameters to realistic temperature and pressure conditions in the lower mantle often includes the assumption of a constant thermal expansion coefficient. However, thermal expansivity has been found to decrease with increasing depth, and mainly in the lower mantle, by a factor 2-4 (*Ranalli*, 1996) or even 3-5 (*Čadek et al.*, 1994). Consequently, seismic velocities will be less sensitive to temperature variations with increasing depth, and the amplitudes of the velocity anomalies for a particular temperature variation will be smaller for large depths than for shallow depths. Since the values of thermal expansivity are uncertain, the true amplitudes of the anomalies are difficult to assess.

Tomographic models have been inverted for absolute temperature, and the results compared to heat flow calculations and surface tectonics. *Goes et al.* (2000) and *Goes and van der Lee* (2002) have suggested that temperature variations in the uppermost mantle of Europe and North America are the most important cause of seismic velocities. For the lower mantle down to 1200 km depth, *Saltzer et al.* (2001) compared the structure underneath regions were there has been subduction in the last 120 Myr to the structure beneath regions without subduction. Both regions showed well correlated V_s and V_p anomalies, and a similar ratio between to two, indicating that the perturbations had a thermal origin. For the lower mantle between 1000 and 2600 km depth, *Trampert et al.* (2001) found that velocities are sensitive to even small temperature variations. This would mean that rather precise temperature variations could be inferred from the tomographic velocity anomalies, assuming of course that the tomographically induced errors are reasonably small. For P-waves, the amplitudes of temperature derivatives range from 4-6 $\cdot 10^{-5}$ K^{-1} in the upper mantle (*De Jonge et al.*, 1994; *Ranalli*, 1996; *Deal et al.*, 1999; *Goes et al.*, 2000) to 1-3 $\cdot 10^{-5}$ K^{-1} in the lower mantle

(*Karato*, 1993; *Trampert et al.*, 2001; *Cammarano et al.*, 2003).

Most seismological studies thus suggest that seismic velocity anomalies in the mantle are primarily caused by temperature variations, although they cannot totally explain them (e.g. *Forte et al.*, 1994; *Ranalli*, 1996; *Röhm et al.*, 2000; *Trampert et al.*, 2001; *Goes and van der Lee*, 2002). This is an important conclusion, since temperature variations within the Earth can be coupled to geodynamical processes like subduction of cold lithosphere and upwelling of hot mantle material.

Composition

Parameters describing the composition dependence of seismic velocities are usually determined for an average mineral assemblage for the mantle. An indirect way of assessing the possible compositional origin of velocity anomalies is to compare perturbations in P-, S- and bulk-wave speed ($V_\phi = \sqrt{\kappa/\rho}$). Temperature variations will lead to a similar behaviour of all elastic parameters, so the differences between the velocity anomalies based on thermal variations alone can be predicted. As a result, systematic differences between V_p, V_s and V_ϕ will suggest variations in composition.

The contribution of compositional variations to the seismic velocity anomalies in the upper mantle seems to be small compared to thermal variations, and a significant contribution has been found only for the uppermost mantle beneath old cratons (*Saltzer et al.*, 2001). Also calculations of *Goes et al.* (2000) showed that, for the upper 50-200 km beneath Europe, effects of compositional variations are below the level that can currently be resolved with tomography. The seismic velocities in the lower mantle seem to be sensitive to modest changes in composition, although temperatures are still found to be most important (e.g. *Trampert et al.*, 2001). Compositionally anomalous, low-velocity, domains probably exist in the lowermost mantle (e.g. *Čadek et al.*, 1994; *Van der Hilst and Kárason*, 1999; *Saltzer et al.*, 2001; *Trampert et al.*, 2001).

Anelasticity

During the passage of a seismic wave through an anelastic structure, energy is lost due to internal friction. This viscoelastic relaxation leads to attenuation, decreasing the amplitude of the wave. Furthermore, the different frequency components in a seismic wavelet will travel through an anelastic structure with different velocities, leading to dispersion of the wave. Since anelastic effects make seismic velocities more sensitive to temperature than due to anharmonic effects alone (*Karato*, 1993; *Ranalli*, 1996; *Goes et al.*, 2000), they can be important for interpreting seismic velocity anomalies.

The energy loss per cycle of oscillation is usually expressed in terms of the quality factor Q, with a low quality factor indicating strong anelastic behaviour. The Earth behaves almost elastic at seismic frequencies, in which case a so-called anharmonic approach would be adequate. However, observations of dispersion and attenuation of seismic waves do show that anelastic effects are not totally negligible. The quality factor Q is not constant throughout the Earth, but is systematically larger for P-waves than for S-waves (*Karato*, 1993) and is dependent on frequency itself (*Karato*, 1993; *Jackson and Rigden*, 1998). More importantly, Q is very sensitive to temperature because viscoelastic relaxation is thermally activated, which

means that higher relaxation will occur as temperatures are closer to the melting temperature. Anelastic effects depend on pressure as well, and generally decrease with increasing depths. However, available experimental parameters that describe anelasticity are poorly constrained, especially for the lower mantle.

Highest attenuation (thus lowest Q) is found in the uppermost mantle ($\sim$80-220 km) and underneath oceanic regions, where the geotherm is near the melting temperature (*Jackson and Rigden*, 1998). In low-Q regions within the upper mantle, anelastic effects can double the value of the temperature dependence of seismic velocities ($\partial V/\partial T$) due to anharmonic effects alone (*Karato*, 1993; *Jackson and Rigden*, 1998). On the contrary, the anelastic effects on $\partial V/\partial T$ seem to be negligible in relatively cool regions (e.g. *Goes and van der Lee*, 2002). Furthermore, the attenuating effect will be much smaller below the uppermost mantle (*Karato*, 1993). Because the anharmonic contribution to $\partial V/\partial T$ decreases significantly with increasing depth, the anelastic effect becomes relatively important again in the deeper parts of the mantle. Nevertheless, it can probably be neglected in the lower mantle (*Trampert et al.*, 2001). An increased sensitivity to temperature will generally lead to even lower velocities in relatively warm regions, and even higher velocities in cold regions. In other words, the temperature perturbations calculated from seismic velocity anomalies while accepting anelasticity will be lower than those estimated assuming anharmonic effects alone, so we will overestimate the thermal perturbations when neglecting anelasticity.

Anisotropy

Elastic anisotropy causes seismic wave velocities to be dependent on the direction of propagation. This feature seems to play an important role in the Earth, but is still not well understood. Flow in the mantle may force crystals to align in a specific orientation, resulting in seismic waves propagating faster in the direction (or inclined to the direction) of the flow (e.g. *Ribe*, 1989).

Seismic anisotropy is mainly observed in the uppermost mantle (e.g. *Montagner*, 1994), but has also been detected in the transition zone (*Trampert and van Heijst*, 2002). In the PREM model of *Dziewonski and Anderson* (1981), a radial anisotropy $\sim$2-4% for both P- and S-waves in the upper 220 km of the mantle is used. *Ekström and Dziewonski* (1998) suggested the model provides a good average for most of the world, and only the anisotropic variations in the velocities beneath the Pacific plate were found to be $\sim$5% larger.

Global travel-time tomographic models usually ignore the effect of anisotropy on seismic velocities. However, the azimuthal velocity variations associated with strong anisotropy are probably larger in magnitude than most compositional variations (*Jackson and Rigden*, 1998). This would imply that, as opposed to the compositional effect, the incorporation of anisotropy may be important. This will especially hold for the uppermost mantle where the strongest anisotropy has been detected.

Partial melt

Partial melt is found in the mantle when maximum temperatures are close to the melting temperatures, for example beneath tectonically active and young oceanic regions (e.g. *Saltzer et al.*, 2001). Volatiles significantly reduce the solidus temperature, and thus influence the

38

amount of partial melt. The effect of the presence of partial melt on seismic velocities is not well constrained yet, but it will probably yield a decrease in seismic velocities. Moreover, partial melting causes an increase in attenuation, leading to a further decrease in velocity amplitudes (as discussed above). If the mantle in hot regions is partially molten, then the calculated temperatures will be overestimated if we do not take into account the effect of this melt (e.g. *Röhm et al.*, 2000). In any case, the presence of partial melt is not important for the interpretation of relatively cold regions. Moreover, especially P-waves seem to be rather insensitive to the composition variations associated with basalt extraction (*Jackson and Rigden*, 1998).

Conclusions

Compared to the transition zone and most of the lower mantle, the uppermost mantle ($\sim$top 220 km) is characterised by large wave-speed variations, marked elastic anisotropy, and strong attenuation. For the interpretation of the positive velocity anomalies associated with cold, subducted material below that depth, however, we can conclude the following: Partial melt is not important since temperatures within the slabs will be well below the solidus temperatures. Anelasticity does not significantly contribute to the temperature-sensitivity of seismic velocities at the relatively low slab temperatures, in particular for P-wave velocities. Anisotropy may be of importance in the crust and uppermost mantle, but much less below that depth. Temperature seems to play a dominant role in the lower mantle, and the effect of variations in composition is relatively small. Hence, the seismic velocity heterogeneities associated with slab remnants can largely be explained by a thermal origin.

3.1.4 Converting velocity anomalies to temperature variations

To interpret the seismic velocity anomalies in tomographic images of the mantle in terms of temperature anomalies, we need to determine which thermal perturbation will be the source of a particular velocity anomaly. Restricted to temperature effects only, we can express the velocity anomaly ΔV in a first order approximation as

$$\Delta V \; = \; \Delta T \, \frac{\partial V}{\partial T} \; \text{or, in percentages,} \quad \frac{\Delta V}{V} \; = \; \frac{1}{V} \frac{\partial V}{\partial T} \, \Delta T \; = \; \frac{\partial \ln V}{\partial T} \, \Delta T \qquad (3.2)$$

where ΔT is the thermal perturbation, and $\partial \ln V / \partial T$ the relative, depth-dependent temperature derivative of the seismic velocity. To interpret the P-wave velocity model of *Bijwaard et al.* (1998), only values for $\partial \ln V_p / \partial T$ will be discussed below.

Values for $\partial \ln V_p / \partial T$ in the mantle

To choose adequate values for $\partial \ln V_p / \partial T$, we compare currently available estimates of the anharmonic temperature derivatives of seismic P-wave velocities within the mantle. Discussed here are the values from *Karato* (1993), *De Jonge et al.* (1994), *Trampert et al.* (2001) and *Cammarano et al.* (2003). In Figure 3.1, the proposed distributions of $\partial \ln V_p / \partial T$, as well as the uncertainties therein, are shown. The temperature derivatives of V_p are always negative,

but their absolute values decrease with increasing depth. Thus, the effect of a particular thermal perturbation on the velocity anomalies in the deeper mantle will be smaller than the effect of the same perturbation in the upper mantle.
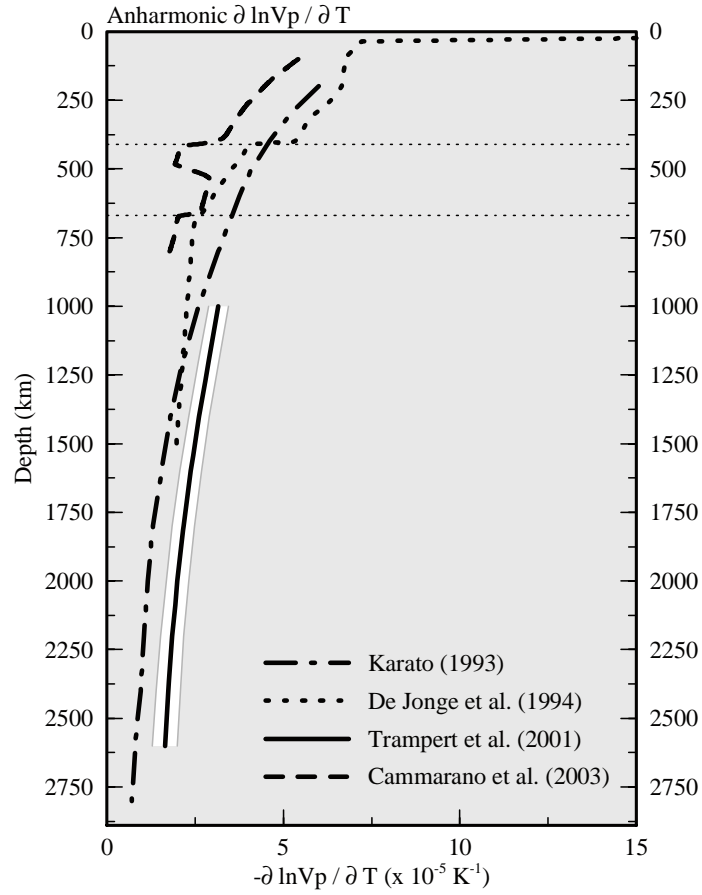
Figure 3.1: The distribution of the anharmonic temperature derivative of the seismic P-wave velocity, based on estimates from *De Jonge et al.* (1994), *Karato* (1993), *Trampert et al.* (2001) and *Cammarano et al.* (2003). For *Trampert et al.* (2001), error bounds are also given.

The anharmonic contribution to $\partial \ln V_p / \partial T$ of *Karato* (1993) is compiled from laboratory measurements of *Isaak* (1992), *Duffy and Anderson* (1989), and *Chopelas and Boehler* (1992). Their amplitudes decrease from $6.0 \cdot 10^{-5}$ K^{-1} at 200 km to $0.7 \cdot 10^{-5}$ K^{-1} at 2800 km. *De Jonge et al.* (1994) compiled $\partial V_p / \partial T$ down to 1500 km depth for various possible values of the elastic parameters for olivine, based on different extrapolated laboratory results (see *De Jonge et al.* (1994) for references). In Figure 3.1, the values of *De Jonge et al.* (1994) have been divided by the seismic P-wave velocity $V_p(z)$ from the ak135 model to obtain

$\partial \ln V_p/\partial T$. The amplitudes of $\partial \ln V_p/\partial T$ range from $7.2 \cdot 10^{-5}$ K^{-1} just below the crust down to $1.9 \cdot 10^{-5}$ K^{-1} at 1500 km.

Trampert et al. (2001) estimated the anharmonic components of $\partial \ln V_p/\partial T$ for the depth range of 1000 to 2600 km. The sensitivity of seismic velocities to temperature, pressure and composition was calculated for a whole range of input parameters, like pressure, average composition, and thermo-elastic parameters. The sensitivities were averaged to obtain the final values for $\partial \ln V_p/\partial T$, ranging from $3.2 \cdot 10^{-5}$ K^{-1} at 1000 km depth, to only $1.6 \cdot 10^{-5}$ K^{-1} at 2600 km. The authors calculated a standard deviation around the average of approximately 0.28 to $0.35 \cdot 10^{-5}$ K^{-1}, which is $\sim$10-20% of $\partial \ln V_p/\partial T$.

Also *Cammarano et al.* (2003) recently extrapolated the elastic parameters and density to high pressure and temperature conditions. The temperature derivatives of V_p were calculated for the mantle down to 800 km depth. The values for $\partial \ln V_p/\partial T$ shown in Figure 3.1 decrease from $5.5 \cdot 10^{-5}$ K^{-1} at 100 km depth, to $3.0 \cdot 10^{-5}$ K^{-1} just above the transition zone, and down to $\sim 2.0 \cdot 10^{-5}$ K^{-1} from 660 km downwards.

Minimum and maximum profiles for $\partial \ln V_p/\partial T$

From the discussed values for $\partial \ln V_p/\partial T$, we have constructed the minimum and maximum profile shown in Figure 3.2. The minimum profile follows the distribution of *Cammarano et al.* (2003) in the upper mantle down to 800 km depth, and the values of *Karato* (1993) from 1400 km downwards. We have kept $\partial \ln V_p/\partial T$ at a constant value in the missing depth interval. The values for the maximum profile are a combination of the distribution of *De Jonge et al.* (1994) in the upper mantle, and the upper limits for $\partial \ln V_p/\partial T$ calculated by *Trampert et al.* (2001). In Figure 3.2 (see label at upper X-axis), also the associated seismic velocity anomalies $\Delta V_p(\%)$ expected for a thermal perturbation ΔT of -100 K, as calculated from Equation 3.2, are shown. The anomalies range from approximately 0.4-0.6% in the uppermost mantle, to 0.2-0.5% in the transition zone, and 0.1-0.3% in the lower mantle.

In addition, we have determined the depth intervals in which particular values for the seismic velocity anomalies are expected for the minimum and maximum profiles. In Table 3.1, the shown depths correspond to values used in the depth discretisation of the tomography model of *Bijwaard* (1999) (see Section 3.1). Displayed here are the values of $\Delta V_p(\%)$ expected for a thermal perturbation of -100 K and more negative in each depth interval.

Conclusions

In this study, we will use both profiles of Figure 3.2. The profiles give a minimum and maximum value for $\Delta V_p(\%)$ to define the boundary of each seismic velocity anomaly of our interest. However, as the upper bound of the amplitude uncertainty in the anomalies in the model of *Bijwaard et al.* (1998) is estimated at 0.21% (Section 3.1.2), we choose to take into account values of ΔV_p larger than 0.2% only. When calculating the size of the relevant anomalies, the use of the minimum profile will provide us with an upper limit, and the maximum profile with a lower limit, of the volume. Since the maximum profile is given down to a depth of 2600 km only, we will not interpret any anomalies below that depth. Also anomalies in the top $\sim$220 km of the model will not be analysed, because the

ΔV_p (%)	Depth interval (km) *minimum* profile	Depth interval (km) *maximum* profile
$> 0.5\%$	$0-170$	$0-530$
$> 0.4\%$	$170-290$	$530-860$
$> 0.3\%$	$290-410$	$860-1400$
$> 0.2\%$	$410-660$	$1400-2560$
$> 0.1\%$	$660-2200$	$2560-2889$
$< 0.1\%$	$2200-2889$	$-$

Table 3.1: Depth intervals (km) in which the indicated values for the seismic velocity anomalies $\Delta V_p(\%)$ are expected for a thermal perturbation of -100 K and more negative. The depths are chosen to coincide with certain depths used for the parameterisation of the tomographic BSE-model of *Bijwaard* (1999). The values are determined from the minimum and maximum profiles for the anharmonic $\partial \ln V_p / \partial T$ distribution shown in Figure 3.2.

seismic velocities in this depth interval are likely to be highly influenced by compositional heterogeneities, attenuation and anisotropy (Section 3.1.3).

Because of the spatial variations in the resolution of the tomography model (see Section 3.1.2), the actual resolution for each tomographic image needs to be investigated separately. In the upper mantle of the model of *Bijwaard et al.* (1998), the resolution is at best about 65-100 km laterally and 35-65 km vertically. In the lower mantle, the lateral resolution is approximately 150-300 km and the vertical resolution 100-200 km at best. Furthermore, the amplitudes of the inverted seismic velocity anomalies are probably underestimated by 20-30% (Section 3.1.2), and temperature perturbations derived from these anomalies are underestimated by the same percentage as a result.
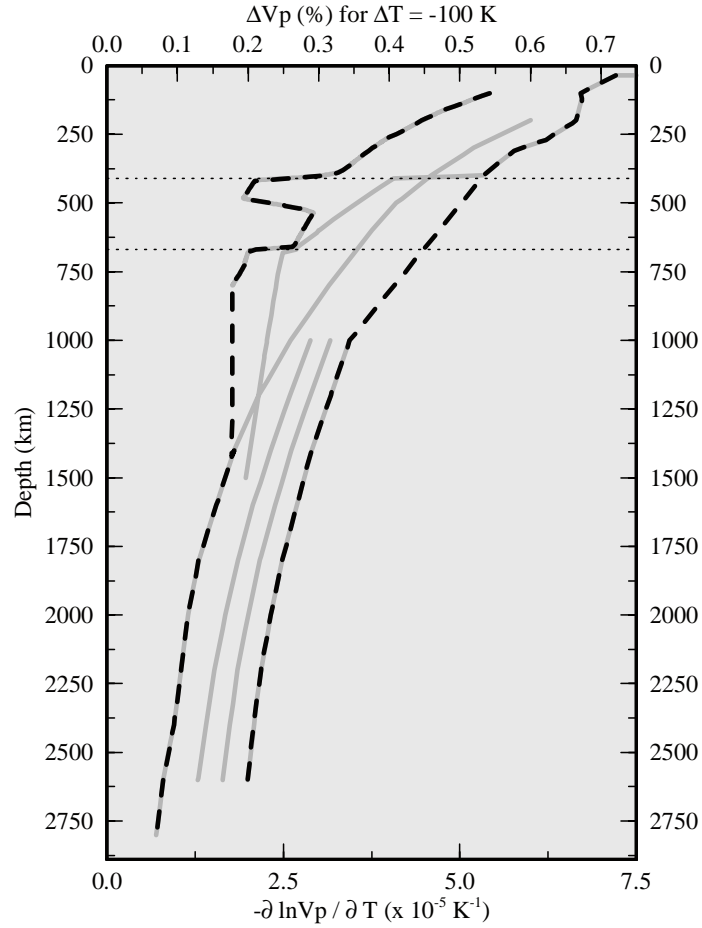
Figure 3.2: Minimum and maximum profiles (black dashed lines) for the anharmonic temperature derivatives of the seismic P-wave velocity. Also indicated (upper X-axis) are the associated seismic velocity anomalies $\Delta V_p(\%)$ expected for a thermal perturbation ΔT of -100 K. The values from Figure 3.1 are shown in grey colours for reference. The minimum profile follows the distribution of *Cammarano et al.* (2003) down to 800 km depth, and of *Karato* (1993) from 1400 km downwards, with a constant value in the intermediate depth interval. The maximum profile is a combination of the distribution of *De Jonge et al.* (1994) in the upper mantle, and of the upper limit for the values of *Trampert et al.* (2001) in the lower mantle. Note that the maximum profile will lead to a minimum estimate of the size of the seismic anomalies, and the minimum profile to a maximum estimate.

3.2 The amount of convergence from tectonic reconstructions

Plate tectonic reconstructions describe the past motions of the tectonic fragments identified in a particular region. The modelling of these motions is based upon some key concepts of the rotation of rigid bodies over a spherical surface. The basic mathematical techniques for working with past plate motions will be summarised in Section 3.2.1. For a more extensive description of the mathematics of rotations, e.g. see *Goldstein* (1950) and *Cox and Hart* (1986). In Section 3.2.2 and 3.2.3, it will be shown how this theory can be used to calculate past plate velocities and the total amount of convergence.

3.2.1 The theory of plate rotations

The movement of a rigid plate over the surface of a spherical Earth can be described by a rotation about a pivot axis and an angle of rotation, as illustrated in Figure 3.3. The rotation axis points from the centre of the Earth to the surface, and each point on the plate will follow a specific small circle path around it.
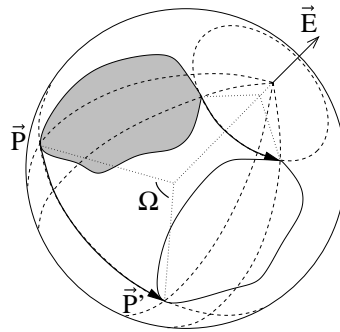
Figure 3.3: Schematic figure showing the movement of a plate over the surface of a sphere, i.e. a rotation of a rigid, spherical cap about a pivot axis. Each point on the plate will follow a small circle path around the pole, as illustrated for the motion of point $\vec{P}$ to $\vec{P}'$. The angle of rotation Ω determines the covered angular distance.

A point $\vec{P}$ on the Earth's surface is usually expressed in its longitude ϕ and latitude λ, but can also be defined by a Cartesian vector, with the Cartesian set of global coordinate axes for the Earth generally oriented in the equatorial plane (x and y) and along the Earth's spin axis (z). The relative displacement of a particular point $\vec{P}$ on plate B with respect to a chosen reference frame, e.g. another plate A, is mathematically equivalent to a rotation of $\vec{P}$. The components of position point vector $\vec{P}'$ after rotation of $\vec{P}$ are found by multiplying the original vector with a rotation matrix $\mathbf{R}$, i.e. $\vec{P}' = \mathbf{R}\,\vec{P}$ (see p. 227 of *Cox and Hart* (1986) for the definition of the rotation matrix $\mathbf{R}$). The pivot axis associated with this rotation matrix is called the Euler pole $\vec{E}$, a unit vector with components along the (x, y, z)-axis that crosses the Earth's surface

at (ϕ_E, λ_E). Also the finite angle of rotation Ω can be determined from $\mathbf{R}$, and is measured positive counterclockwise.

It is possible to add any arbitrary sequence of finite rotations, and describe the total operation with one equivalent rotation. This composite rotation is obtained by multiplication of the associated rotation matrices. Since matrix multiplications are not, in general, commutative, any composite rotation will depend on the order in which the sequence of finite rotations is performed. The operator that changes $\vec{P}'$ back into $\vec{P}$ is the inverse $\mathbf{R}^{-1}$ of the rotation matrix. For orthogonal matrices as $\mathbf{R}$, the inverse $\mathbf{R}^{-1} = \mathbf{R}^{\mathrm{T}}$.

Total reconstruction poles Total reconstruction poles are the Euler poles associated with finite rotations starting at the present and going backwards in time, and total forward poles describe the finite rotations from a certain time t in the past to the present. We will use the symbol $_A^0\mathrm{ROT}_B^t$ to mean the finite rotation of a plate B with respect to plate A from its present position to its position at time t in the past (*Cox and Hart*, 1986). Because of the orthogonality of the associated matrices (see above), total poles have the useful property that

$$_A^0\mathrm{ROT}_B^t \;=\; -{}_A^t\mathrm{ROT}_B^0 \quad \text{and} \quad {}_A^0\mathrm{ROT}_B^t \;=\; -{}_B^0\mathrm{ROT}_A^t \tag{3.3}$$

Thus, using a matrix formulation, if $\vec{P}'_B = \mathbf{R}\,\vec{P}$ and $\vec{P} = \mathbf{R}^{-1}\,\vec{P}'_B$ for a point $\vec{P}$ on plate B vs. plate A, then $\vec{P}'_A = \mathbf{R}^{-1}\,\vec{P}$ and $\vec{P} = \mathbf{R}\,\vec{P}'_A$ for a point $\vec{P}$ on A vs. B. This means that a total forward pole (the finite rotation between time t in the past $\rightarrow 0$) and a total reconstruction pole (that of $0 \rightarrow$ time t in the past) have an equal angle of rotation, but antipodal Euler poles. They can also be described by the same Euler pole but reversed angles. The same holds for the rotations of plate A relative to plate B and vice versa.

If the rotation of plate C relative to plate B ($_B^0\mathrm{ROT}_C^t$) is also known, the motion of plate C relative to plate A is found by simply adding the rotations $_A^0\mathrm{ROT}_C^t = {}_A^0\mathrm{ROT}_B^t + {}_B^0\mathrm{ROT}_C^t$. This is equivalent to multiplying the associated rotation matrices. Note that the order is important, i.e. $_A^0\mathrm{ROT}_C^t \neq {}_B^0\mathrm{ROT}_C^t + {}_A^0\mathrm{ROT}_B^t$. On Earth, we usually have to add several rotations to get the relative displacement between the plates we are interested in. When calculating plate motions in a particular region, this is usually done by holding one of the larger plates involved fixed. Absolute plate motions, generally defined as the movement of the lithospheric plates relative to the mean angular velocity of the underlying mantle, can be analysed in the same way as the motions of plates relative to each other.

Stage poles Stagepoles are finite rotations that occurred during a specific interval of time in the past. The stagepole giving the finite rotation of plate B vs. plate A between time t_1 and t_2, with increasing time t going backwards in time, is defined from two total poles using

$$_A^{t_1}\mathrm{ROT}_B^{t_2} \;=\; -{}_A^0\mathrm{ROT}_B^{t_1} + {}_A^0\mathrm{ROT}_B^{t_2} \tag{3.4}$$

Stagepoles require a more cautious usage than total poles (Eq. 3.3) since

$$_A^{t_1}\mathrm{ROT}_B^{t_2} \;=\; -{}_A^{t_2}\mathrm{ROT}_B^{t_1} \quad \text{but} \quad {}_A^{t_1}\mathrm{ROT}_B^{t_2} \;\neq\; -{}_B^{t_1}\mathrm{ROT}_A^{t_2} \tag{3.5}$$

That is to say, if for a point $\vec{P}$ on plate B relative to A the total rotations give $\vec{P}'_A = \mathbf{R_1}\,\vec{P}$ for $[t_0, t_1]$, and $\vec{P}''_A = \mathbf{R_2}\,\vec{P}$ for $[t_0, t_2]$, then $\vec{P}''_A = \mathbf{R_2}\,\mathbf{R_1}^{-1}\,\vec{P}'_A$ for $[t_1, t_2]$. The stagepole describing the motion of $\vec{P}$ on B vs. A between t_1 and t_2 is thus associated with the matrix $\mathbf{R_2}\mathbf{R_1}^{-1}$. Similarly, for a point $\vec{P}$ on A relative to B the inverse rotations give $\vec{P}'_B = \mathbf{R_1}^{-1}\,\vec{P}$ for $[t_0, t_1]$, and $\vec{P}''_B = \mathbf{R_2}^{-1}\,\vec{P}$ for $[t_0, t_2]$, which gives $\vec{P}''_B = \mathbf{R_2}^{-1}\,\mathbf{R_1}\,\vec{P}'_B$ for $[t_1, t_2]$. The stagepole for $\vec{P}$ on A vs. B between t_1 and t_2 is thus associated with the matrix $\mathbf{R_2}^{-1}\mathbf{R_1}$. Whereas for total rotations $(\mathbf{R}^{-1})^{-1} = \mathbf{R}$ (Eq. 3.3), for stagepoles $(\mathbf{R_2}^{-1}\mathbf{R_1})^{-1} = \mathbf{R_1}^{-1}\mathbf{R_2} \neq \mathbf{R_2}\mathbf{R_1}^{-1}$ (Eq. 3.5). In other words, although the initial, total rotation matrices are equal (with reversed angles), the final stage rotation for plate B relative to plate A is generally different from that for plate A relative to plate B. Since the motions still yield an equal (though reversed) angle of rotation, the Euler poles associated with the stage rotations are not exactly antipodal (see also *Cox and Hart* (1986), p. 240). The small differences in Euler pole positions will affect the direction of plate motions during a specific time interval, as will be discussed in Section 3.2.2.

3.2.2 Calculating velocities

To describe past plate velocities, it would be useful to represent the finite rotations by single vectors. To be qualified as vectors, they must be commutative in addition. However, the addition of two finite rotations corresponds to the product of the two associated matrices, and this operation is usually *not* commutative. A direction can be assigned (namely the Euler pole $\vec{E}$) and a magnitude (Ω), but it is impossible to construct a vector representing a finite rotation.

For an infinitesimal rotation, however, the rotation matrix $\mathbf{R}$ differs from the identity transformation matrix $\mathbf{I}$ only by a very small amount, i.e. $\vec{P}' = (\mathbf{I} + \epsilon)\,\vec{P}$. The product of two infinitesimal transformations becomes $(\mathbf{I} + \epsilon_1)(\mathbf{I} + \epsilon_2) = \mathbf{I} + \epsilon_1 + \epsilon_2 = (\mathbf{I} + \epsilon_2)(\mathbf{I} + \epsilon_1)$ if higher order infinitesimals $\epsilon_1\epsilon_2$ and $\epsilon_2\epsilon_1$ are neglected (e.g. *Goldstein*, 1950). As infinitesimal rotations commute in addition, they can be represented by a vector $\mathrm{d}\vec{\Omega}$ that is parallel to the axis of rotation $\vec{E}$ and has a length equal to the small angle of rotation $\mathrm{d}\Omega$. The matrix ϵ of an infinitesimal rotation is antisymmetric, and therefore the change in position $\mathrm{d}\vec{P} = \epsilon\,\vec{P}$ can be written as

$$\mathrm{d}\vec{P} = \vec{P} \times \mathrm{d}\vec{\Omega} \tag{3.6}$$

as illustrated in Figure 3.4. The vector $\mathrm{d}\vec{P}$ is perpendicular to both $\mathrm{d}\vec{\Omega}$ and $\vec{P}$, and its magnitude $\mathrm{d}P$ equals $R \sin\theta\,\mathrm{d}\Omega$ to first order, with θ the angle between $\vec{P}$ and $\mathrm{d}\vec{\Omega}$.

The rate of change of $\mathrm{d}\vec{P}$ is obtained by dividing the equation by the differential time $\mathrm{d}t$, i.e.

$$\frac{\mathrm{d}\vec{P}}{\mathrm{d}t} = \vec{P} \times \vec{\omega} \tag{3.7}$$

The vector $\vec{\omega}$ has the orientation of the axis $\mathrm{d}\vec{\Omega}$ at time t and is called the instantaneous axis of rotation. Its magnitude $\omega = \mathrm{d}\Omega/\mathrm{d}t$ is defined as the instantaneous angular rate of rotation. The instantaneous rate of motion at $\vec{P}$ therefore equals, to first order,

$$\frac{\mathrm{d}P}{\mathrm{d}t} = R \sin\theta\,\frac{\mathrm{d}\Omega}{\mathrm{d}t} = \omega\,R \sin\theta \tag{3.8}$$
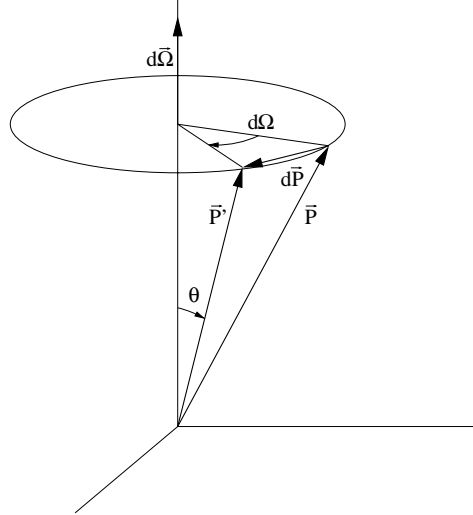
Figure 3.4: The change in a vector $\vec{P}$ (of length R) as produced by an infinitesimal rotation of an angle $d\Omega$ about the axis of rotation $d\vec{\Omega}$. The vector $d\vec{P}$ is perpendicular to both $\vec{P}$ and $d\vec{\Omega}$, and its magnitude equals R $\sin\theta$ $d\Omega$, with θ the angle between $\vec{P}$ (or $\vec{P}'$) and $d\vec{\Omega}$.

Infinitesimal rotations thus can be used to calculate the rate and direction of motion of a particular point $\vec{P}$ at a given time t. For example, current plate motions are described by such instantaneous rotations. It is important to realise that for the past, however, real instantaneous motions are not known: The finite (not infinitesimal) rotations that determine ancient plate positions cannot be represented by vectors. Having said this, consider an Euler pole $\vec{E}$ describing the finite rotation of a point $\vec{P}$ on a lower plate with respect to an upper plate during a specific timespan $[t_0, t_1]$. The rotation will make $\vec{P}$ move a finite angle Ω along a particular small circle path about $\vec{E}$. The direction of motion at point $\vec{P}$ will be parallel to this small circle constantly, and thus perpendicular to the great circle through $\vec{E}$ and $\vec{P}$. Defining $\bar{\omega}$ as the average angular rotation rate $\Omega/(t_1 - t_0)$, a global velocity vector can be defined from these vectors as

$$\vec{V} = (\bar{\omega}\,\vec{E}) \times (R\,\vec{P}) = \bar{\omega}\,R\,(\vec{E} \times \vec{P}) \tag{3.9}$$

with R the radius of the Earth. The rate of motion will equal the length of the velocity vector, i.e.

$$V = |\vec{V}| = \bar{\omega}\,R\,|\vec{E} \times \vec{P}| = \bar{\omega}\,R\,\sin\theta \tag{3.10}$$

with θ the angular distance between point $\vec{P}$ and pole $\vec{E}$.

To describe the actual plate velocity at the Earth's surface, it can be useful to use the local northward and eastward components of the global velocity vector $\vec{V}$ (Eq. 3.9). The downward component of $(\vec{E} \times \vec{P})$ is zero by definition. To convert the global velocity vector to a vector expressed in its local northward, eastward and downward components, we need to

perform another matrix multiplication $\vec{V}_L = \mathbf{T} \vec{V}$ (see p. 155 of *Cox and Hart* (1986) for the definition of $\mathbf{T}$). Although the (x, y, z)-axes of the global system are always the same, the local (n, e, d)-axes differ for each point on the Earth's surface. Therefore, the Cartesian components of the local velocity vector, as well as the transformation matrix $\mathbf{T}$, depend on the coordinates (ϕ, λ) of $\vec{P}$. The length of the velocity vector is not changed by the operations, so $V_L = V$.

Equation 3.10, defining the average rate of motion during a finite rotation, is equal to the one shown for the instantaneous rate of motion, Equation 3.8. However, we have seen before that the Euler pole representing a finite rotation can *not* be treated as a vector because rotations are order-dependent. The velocity vector determined from a finite rotation will give an indication of the velocity of a particular point on a particular time only. We will refer to these velocity vectors as being *quasi-instantaneous*. To give an estimate of the past plate velocities, we will use the stagepoles constructed from the given total reconstruction poles, and calculate the convergence velocity at a particular moment in time, e.g. at the start of each stage interval. Because the direction of motion is determined by the Euler pole position (Eq. 3.9), which for a stagepole depends on which plate was held fixed (Eq. 3.5), the velocity components are dependent on the chosen reference plate.

3.2.3   Estimating the amount of convergence

In this section, a method to estimate the amount of convergence at a particular trench point will be addressed. Taking the product of the quasi-instantaneous velocity vector, determined for a particular finite rotation, and the associated timespan seems to be the most straightforward way. Consider a specific time interval $[t_0, t_1]$ during which lower plate point $\vec{P}$ moves from position $\vec{P}_0$ at the trench to a particular point $\vec{P}_1$ behind it (Figure 3.5). Note that we here describe the process of convergence at the trench going forward in time from t_0 to t_1, as we will do in the following. As explained earlier, the total motion is that of a finite angle Ω along a small circle path about Euler pole $\vec{E}$. The covered distance will equal $\Omega\,R\sin\theta$, leading to an average angular rotation rate $\bar{\omega} = \Omega/(t_1 - t_0)$ (see definition of Eq. 3.10). At trench point $\vec{P}_0$ itself, the lower plate moves with rate $\bar{\omega}$ in a direction $(\vec{E} \times \vec{P}_0)$ constantly (Eq. 3.9). The total arc length of the plate crossing $\vec{P}_0$ during $[t_0, t_1]$ in this direction satisfies the product of the velocity $|\vec{V}|$ and the timespan of the subduction, thus

$$d_{\text{tot}} \;=\; |\vec{V}|\,(t_1 - t_0) \;=\; \bar{\omega}\,(t_1 - t_0)\,R\sin\theta \;(= \Omega\,R\sin\theta) \tag{3.11}$$

For the total amount of material transport perpendicular to the trench at $\vec{P}_0$, we take the inner product of $\vec{V}$ and the trench normal $\vec{n}$ at $\vec{P}_0$. With α the angle between the trench normal and the direction of motion,

$$d_{\perp} \;=\; |\,\vec{V}\cdot\vec{n}\,|\,(t_1 - t_0) \;=\; \bar{\omega}\cos\alpha\,(t_1 - t_0)\,R\sin\theta \;=\; d_{\text{tot}}\cos\alpha \tag{3.12}$$

This is the projection of the displacement below $\vec{P}_0$ in the direction of $\vec{V}$ on the great circle represented by the trench normal $\vec{n}$.
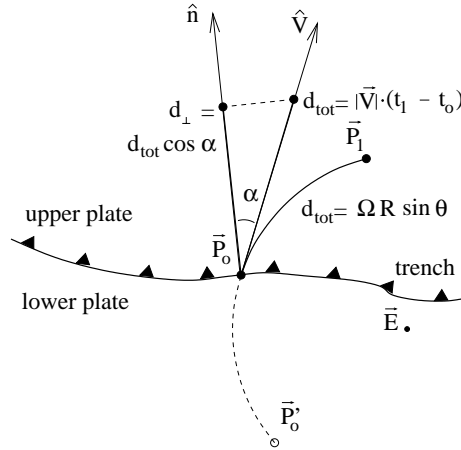
Figure 3.5: Calculation of convergence from the quasi-instantaneous velocity vector as given in Equations 3.11 and 3.12. This schematic figure shows the lower plate movement from position $\vec{P}_0$ at the trench to $\vec{P}_1$ behind it during time interval $[t_0, t_1]$, and lower plate point $\vec{P}'_0$ moving to trench point $\vec{P}_0$ in the same time. The quasi-instantaneous velocity vector $\vec{V}$ at $\vec{P}_0$ makes an angle α with the trench normal $\vec{n}$ at $\vec{P}_0$. With the total small circle displacement d_{tot}, the length of $\vec{V}$ equals $d_{tot} / (t_1 - t_0)$. The total flux d_{tot} at $\vec{P}_0$ has a value of $\Omega R \sin \theta$ (Eq. 3.11). The total amount of subduction perpendicular to the trench determined from $\vec{V} \cdot \vec{n}$ is equal to $d_{tot} \cos \alpha$ (Eq. 3.12).

The accumulated distance $d_\perp$, estimated from the quasi-instantaneous displacement at the trench, seems an appropriate measure of the total amount of convergence, but has two major drawbacks:

First, the division into a trench-normal and tangential component is generally misleading when particle trajectories are considered. Analogous to Figure 3.5, the convergence calculated from the quasi-instantaneous velocity vector at the trench is also illustrated in Figure 3.6 (1). Evaluated at $\vec{P}_0$, this displacement equals the arc length of the small circle d_{tot} covered by the finite rotation (Eq. 3.11). The direction of the displacement at the trench is perpendicular to the direction of the great circle through $\vec{P}_0$ and $\vec{E}$, and thus parallel to the small circle path of displacement at that point. The projection of this displacement on the trench normal (see Fig. 3.5 and Eq. 3.12) is illustrated with (2). Furthermore, the convergence shown with (3) in Figure 3.6 is the angular distance to the tip of the plate now present perpendicular to the trench behind $\vec{P}_0$. The trench-normal displacement $d_\perp$ of a point originally at a particular position at the trench, will be different from the actual length of the slab finally present in a section perpendicular to the trench at that original position. It can therefore be more practical to have a measure of the *total* displacement instead, for example by taking the small circle path, or particle trajectory, around $\vec{E}$ itself (4). Especially in Chapter 4 and 5, the total values will be useful and adequate because the complete Tethys Ocean has disappeared by subduction today.

Second, the material flux at a fixed trench point on the Earth, and thus the relative rotation of two plates, should be unique and independent of the frame of reference. In the above
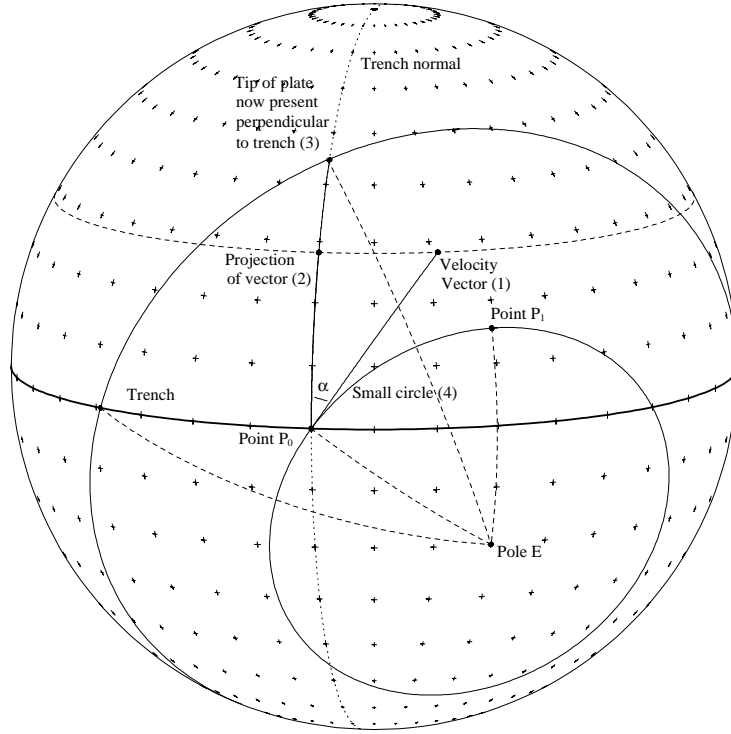
Figure 3.6: Schematic illustration of a few possible methods for calculating the convergence, in this example for the displacement of point $\vec{P}_0$ at (0,0) to point $\vec{P}_1$ at (30,15), caused by a finite rotation of 60° about Euler pole $\vec{E}$ at (30,-20). The equator and the meridian through $\vec{P}_0$ are assumed to represent the trench and the trench normal, respectively. For computing the convergence, we can use the **(1)** Linear, quasi-instantaneous displacement evaluated at $\vec{P}_0$ (shown here is a line of constant azimuth, namely the azimuth α of the small circle path of motion at $\vec{P}_0$, and with a length equal to the small circle distance d_{tot} covered by the rotation); **(2)** Projection of the quasi-instantaneous displacement on the trench normal; **(3)** Angular distance to the tip of the slab now present perpendicular to trench behind $\vec{P}_0$.; **(4)** Small circle path around the pole.

described approach, the total flux $d_\perp$ calculated at a fixed $\vec{P}_0$ from a rotating lower plate $\vec{P}$ is equal to the one estimated from a fixed lower plate with rotating upper plate indeed. Now, however, consider a second stage of rotation: Let lower plate point $\vec{P}$ move from $\vec{P}_1$ to $\vec{P}_2$ during time interval $[t_1, t_2]$, again going forward in time. If we assume that the lower plate extends until below $\vec{P}_0$, we can calculate again the displacement $d_\perp$ at the original upper plate trench point $\vec{P}_0$ using Equation 3.12. However, if we do the opposite, i.e. we keep the lower plate fixed and rotate the upper plate during both intervals of time, we get different values for $d_\perp$ at the trench. The reason for this is that, as stated in the previous sections, the stage pole for a particular plate A relative to another plate B is different from the stagepole for B relative to A: They have the same angle of rotation, but the rotation axes are not exactly antipodal. In Equation 3.12, both the angles θ (between $\vec{P}$ and $\vec{E}$) and α (between $\vec{n}$ and the direction

of motion $\vec{E} \times \vec{P}$) are thus slightly different. So although we would expect the total flux $d_{\perp}$ to remain independent of the reference frame, as in the first stage, this is not the case for a sequence of stages.

Also if we estimate the total amount of convergence from i successive stages, the sum of the stage values is different from the amount of convergence estimated from the total reconstruction pole comprehending the subsequent stages. This can be easily seen from Figure 3.7, where the displacements $d_1 + d_2 \neq d_{tot}$ in general. Furthermore, the position of a rotating point at the end of a certain stage (say $\vec{P}_i$) is the starting position of the point for the rotation in the next stage. When a stagepole is used to calculate the displacement at the original trench position $\vec{P}_0$ instead of $\vec{P}_i$, the total convergence d'_2 will be different once more because the distance from $\vec{P}_0$ to the stage Euler pole $\vec{E}$, as well as the direction $(\vec{E} \times \vec{P}_0)$, is different. In this example, the displacements $d_1 + d'_2 \neq d_1 + d_2 \neq d_{tot}$. The small circle displacement from a *total* reconstruction pole is the only measure of convergence that is independent of the chosen frame of reference.
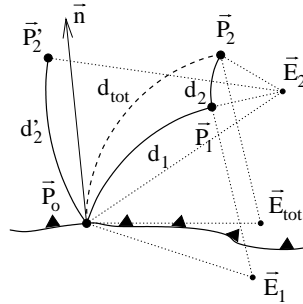

Figure 3.7: Schematic figure showing that the small circle displacement estimated from successive stages will be different from the displacement estimated from the total reconstruction pole comprehending the subsequent stages, thus $d_1 + d_2 \neq d_{tot}$. Also when the motion in the second stage is evaluated at the original trench point $\vec{P}_0$, the value of $d_1 + d'_2 \neq d_{tot}$. Both d_2 and d'_2, and all values for the following stages, depend on the chosen frame of reference.

To get an idea of the errors that can be made in calculating the amount of convergence, an example for the Tethyan region will be useful. Consider the Indian vs. Eurasia convergence during the past 180 Myr, evaluated at point (18°N,78°E) on the current boundary between these continents. When using the summation of the quasi-instantaneous displacements determined from subsequent stages, the rotation of the Indian plate with respect to Eurasia will give us a trench-normal displacement of almost 9900 km and a trench-parallel motion of 3100 km. However, when we keep the Indian plate fixed and move Eurasia relative to it, the trench-normal displacement is about 10,000 km and the trench-parallel motion 4500 km. The values thus significantly depend on the chosen frame of reference, and the differences are 2% of the trench-normal and 30% of the trench-parallel motion. The total accumulated displacements, found by adding the stage trench-normal and trench-parallel components, are ~10,300 vs. 11,000 km. When using the small circle displacements from the successive stagepoles instead, the total accumulated displacements are 11,000 vs. 12,000 km - again dependent on the chosen reference plate - and about 9% more. Finally, for the small circle displacement

from the total reconstruction pole directly, the total displacement in the past 180 Ma is about 10,400 km, independent of the chosen frame of reference. The differences with the values determined from the local components of the quasi-instantaneous velocity vectors are 1 and 6%, and the differences with the small circle displacements from the successive stagepoles are 6 and 13%. Possible errors in the total displacements are generally less significant when smaller rotations are concerned.

We conclude that summation of the quasi-instantaneous displacements at a trench point during successive stages is *not* a good measure of the amount of convergence, in particular when large-scale motions are concerned. In the Tethyan region investigated in Chapter 4 and 5, we will therefore work with the total displacement along the small circle path, thus the particle trajectory, from a total reconstruction pole to determine the amount of convergence between every given time and present. We will approximate the convergence during the subsequent stages by subtracting the total values. By using total poles, the small circle displacements, as well as the trench-normal and tangential components thereof, are independent of the frame of reference.

For the more recent and ongoing subduction in the Indonesian region, investigated in Chapter 6, we prefer to work with the quasi-instantaneous velocity vectors because they enable us to use the trench-normal components as input for the thermo-kinematic modelling of the subduction zones. As we will consider the convergence in the past 40-60 Myr in that chapter only, the trench-normal displacements in this area will be considerably smaller than in the above example, and the possible errors relatively small as well.

3.3 The thermal structure of subducted lithosphere

Comparison of thermal modelling results with, among others, seismic tomography have led to a better understanding of the geodynamic evolution of subduction zones (back to ∼80 Ma) all over the world (e.g. *De Jonge et al.*, 1994; *Ponko and Peacock*, 1995; *Deal et al.*, 1999; *Bunge and Grand*, 2000; *Daniel et al.*, 2001; *Schmid et al.*, 2002; *Van Hunen et al.*, 2002; *Pysklywec et al.*, 2003). For actively subducting slabs like those in the Indonesian region (Chapter 6), information on parameters like the convergence velocity, age of the oceanic lithosphere, and trench migration - used to constrain the kinematic boundary conditions in numerical models - can usely be reasonably well estimated. In Chapter 4 and 5, however, we are concerned with the long-time subduction history (∼200 Ma) of an oceanic plate that has almost completely disappeared today. Because the lithosphere is entirely lost at the surface, we have no direct information on the lithospheric ages upon subduction. Also our knowledge on the ancient spreading systems of the subducted plate is limited. Thus, although the continent-continent motions are relatively well known, the actual subduction velocities at the trenches are not. Moreover, the subduction of oceanic lithosphere was followed by collision of the converging continents along the major part of the trench system considered. Due to the large-scale deformation caused by the continental collisions, the precise configuration and the possible migration of the trench system are unknown. Furthermore, the long timespan and large amount of subduction will have led to a complex present-day geometry of the subducted material.

In view of the many complications, we will here develop a simplified method to approximate the present thermal signature of the subducted Tethyan oceanic lithosphere investigated Chapter 4 and 5. The thermo-kinematic modelling procedure applied to the Indonesian region will be discussed separately in Chapter 6. In Section 3.3.1, we address the initial thermal structure of the subducting oceanic lithosphere. The evolution of the temperature distribution during subduction, and the thermal signature that can be expected for particular slab volumes within the mantle, is analysed in Sections 3.3.2 and 3.3.3.

As discussed earlier, we will bound the seismic anomalous volumes imaged with tomography using values of the velocity anomalies $\Delta V_p(z)$ that can be associated with a constant temperature perturbation ΔT of -100°C (Section 3.1.4). To account for the $\sim$30% amplitude damping in the tomographic model (see Section 3.1.2), we will determine the thermal volumes associated with the subducting lithosphere that are bounded by an anomaly ΔT of -143°C relative to the unperturbed mantle temperature.

3.3.1 The initial thermal structure and thickness of the lithosphere

The initial thermal structure of a subducting plate can be estimated with cooling models of the oceanic lithosphere. These models give the temperature distribution as a function of the age of the lithosphere, i.e. the time since formation at its oceanic spreading ridge.

One way of describing the thermal structure of oceanic lithosphere, is to consider the cooling of a semi-infinite half-space (e.g. *Carslaw and Jaeger*, 1959; *Turcotte and Oxburgh*, 1967). In such a boundary layer model, the temperature at depth z in the lithosphere is given by

$$T(z, t) = T_m \cdot \text{erf} \left(\frac{z}{2\sqrt{\kappa t}} \right) \tag{3.13}$$

where κ is the thermal diffusivity, t the age of the lithosphere, and the surface temperature is fixed to 0°C. As the temperature $T(z, t)$ approaches the mantle temperature T_m asymptotically, the definition of the lithospheric thickness in a half-space model is arbitrary.

To approximate the initial thickness of the subducting plate, i.e. its thermal thickness upon subduction, a particular isotherm - for example the one that is 90% of the mantle temperature - needs to be defined. For a differential $\Delta T = -143$°C between this isotherm and a mantle temperature of 1330°C, the depth of the isotherm, thus the thickness of the oceanic lithosphere, can be approximated by

$$z_L = 2.28 \sqrt{\kappa t} \tag{3.14}$$

As opposed to the half-space model, the plate cooling model (e.g. *McKenzie*, 1967; *Parsons and Sclater*, 1977) implicitly takes into account basal heating of the oceanic lithosphere by mantle convection. Whereas cooling in the half-space model continues for all ages, the basal heating in the plate model balances the heat lost at the seafloor for older ages, and the geotherm of the lithosphere approaches a steady state at larger times. The temperature at depth z in the plate model is given by

$$T(z, t) = T_m \cdot \left[\frac{z}{z_m} + \frac{2}{\pi} \sum_{n=1}^{\infty} \frac{1}{n} \exp \left(\frac{-\kappa n^2 \pi^2 t}{z_m^2} \right) \sin \left(\frac{n\pi z}{z_m} \right) \right] \tag{3.15}$$

with a fixed plate thickness z_m and mantle temperature $T_m = T(z_m, t)$. The oceanic seafloor subsidence calculated from the thermal structure defined by the plate model is in much better agreement with the observations than those predicted by the half-space model (*Parsons and Sclater*, 1977; *Stein and Stein*, 1992). *Parsons and Sclater* (1977) found the best-fitting parameters to include a plate thickness z_m of 125 km and mantle temperature T_m of 1333°C. For the GDH1-model of *Stein and Stein* (1992), a much thinner and warmer plate is proposed, with $z_m = 95$ km and $T_m = 1450$°C.

Although the plate thickness in the plate model is fixed to z_m, the depth z_L of the isotherm that has a temperature of $(T_m - |\Delta T|)$ gradually increases towards the base of the lithosphere with increasing age. For oceanic lithosphere aged less than ~50 Ma, the half-space and plate models predict similar thermal structures, and give comparable results when deducing heat flow and subsidence data from it. For older lithosphere, the differences between the models become increasingly clear. For example, the thickness z_L of 50-Ma old lithosphere is about 80-90 km (for $\kappa = 1 \cdot 10^{-6}$ m^2 s^{-1}, $T_m = 1330$°C, and $\Delta T = $ -145°C). For oceanic lithosphere of 100 Ma, the half-space cooling model predicts a thickness of about 125 km, while the plate models lead to thicknesses of 85 km (*Stein and Stein*, 1992) and 105 km (*Parsons and Sclater*, 1977) instead.

We define the initial thermal volume of a slab that has subducted a timespan t at a rate v as $V_i (= v \cdot t \cdot z_L)$ for a 2D section, and expect that the subduction process will affect the slab and mantle temperatures in such a way that the evolving thermal volume associated with the slab V_p differs a particular factor from the initial volume V_i, that is to say

$$V_p = c(t) \cdot V_i \tag{3.16}$$

with t the time since initiation of subduction. The effect of the initial thermal structure of the subducting plate, as defined by one of the lithospheric cooling models, on the final temperature distribution will be discussed in Section 3.3.3.

3.3.2 Modelling the evolution of slab temperatures during subduction

The evolution of the temperatures in a subduction zone is governed by thermal conduction, convection in the mantle wedge, phase transitions, and frictional heating at the plate contact. Re-heating of the slab therefore depends on several parameters, including the initial thermal structure (discussed above), the convergence rate, and the total residence time in the mantle.

Thermo-kinematic modelling procedure

We use the thermo-kinematic modelling procedure of *De Jonge et al.* (1994); *De Jonge* (1995) to predict the thermal volume V_p associated with a subducting slab of initial volume V_i. The calculations are similar to the subduction zone modelling method developed by *Minear and Toksöz* (1970) and *Toksöz et al.* (1971, 1973): The subduction process is modelled by shifting the initial temperatures step-wise into the mantle along a prescribed path, in combination with entrained mantle flow. Thermal diffusion is calculated after each timestep by solving for the

2D heat equation

$$\frac{\partial T}{\partial t} = \kappa \nabla^2 T \tag{3.17}$$

where the thermal diffusivity $\kappa = k/(\rho c_p)$, with k the thermal conductivity, ρ the density, and c_p the specific heat (see also Table 3.2). Radiogenic heat production in the oceanic crust and mantle is ignored in this equation. The Alternating Direction Implicit method, having the same stability and convergence properties as a 2D Cranck-Nicholson operator but with reduced computational effort, is used to solve the differential equation (see *De Jonge*, 1995). After the calculation of heat diffusion, the temperatures are shifted again for the next timestep until the advection-diffusion problem has been solved for the entire timespan of interest.

parameter		*value*	*unit*
thermal diffusivity	(κ)	10^{-6}	$\text{m}^2\,\text{s}^{-1}$
thermal conductivity	(k)	3.34	$\text{W m}^{-1}\,{}^\circ\text{C}^{-1}$
heat capacity	(c_p)	1050	$\text{J kg}^{-1}\,{}^\circ\text{C}^{-1}$
density	(ρ)	3400	kg m^{-3}
thermal expansion	(α)	$2.0 \cdot 10^{-5}$	${}^\circ\text{C}^{-1}$
gravity	(g)	9.9	m s^{-2}

Table 3.2: Material properties for the mantle as used in the thermal modelling procedure.

Boundary conditions for the model include a fixed 0°C at the top, a small constant heat flux into the base of the model, and no heat flow through the left and right sides of the model. The initial thermal structure of the subducting plate is set up with one of the lithospheric cooling models discussed in Section 3.3.1.

To account for the increase in temperature associated with adiabatic compression in the convecting mantle, the temperatures are converted to their real values after the diffusion problem has been solved (*McKenzie*, 1970). The real temperatures below the conductive lithosphere are approximated by

$$T(z) = T(z_m) \cdot \exp\left(\frac{\alpha g z}{c_p}\right) \tag{3.18}$$

with g the gravitational acceleration, and α the thermal expansion coefficient. The phase transitions around the 410-km and 660-km discontinuities are modelled as abrupt temperature jumps of 90°C and -70°C, respectively (*Turcotte and Schubert*, 2002).

Uncertainties in subduction zone modelling

The thermal conductivity k, defining the relation between heat flow and the temperature gradient, is taken to be constant in our modelling procedure but is really dependent on both pressure and temperature. In general, the conductivity decreases with temperature but increases with pressure, and phase changes probably greatly influence the value (*Hofmeister*, 1999). For subduction of older oceanic lithosphere, the slab temperatures with variable conductivity were found to be significantly higher only for high ($\sim$12 cm/yr) subduction rates

(*Hauck et al.*, 1999). With the present uncertainties in the variation of the thermal conductivity with depth, it is often taken as a constant in subduction models (e.g. *McKenzie*, 1969; *Minear and Toksöz*, 1970; *Davies and Stevenson*, 1992; *Peacock*, 1996; *Schmid et al.*, 2002). For very fast subducting slabs the inferred thermal volumes may be overestimated.

The volume expansion coefficient α is about 3-5 $\cdot 10^{-5}$°C^{-1} near the surface, but decreases strongly with increasing depth: Values as low as 1-2 $\cdot 10^{-5}$°C^{-1}, corresponding to adiabatic gradients of about 0.15-0.3°C km^{-1}, have been proposed for the lowermost mantle (*Chopelas and Boehler*, 1992; *Tackley*, 1996; *Goes et al.*, 2004). We here use an average value for the thermal expansion of 2.0 $\cdot 10^{-5}$°C^{-1} throughout the entire model. This will underestimate the values in the uppermost mantle and somewhat overestimate those in the lower half of the mantle, but only with a few percent at most.

Frictional heat generated at the plate contact is of importance for the temperatures in the overriding plate and at the slab surface, but the temperatures at deeper levels within the slab and below the bottom of the overriding plate remain unaffected (e.g. *Van den Beukel and Wortel*, 1988; *Peacock*, 1996).

3.3.3 Estimating the thermal signature of subducted material

From the modelled 2-D thermal structures of subduction zones, we estimate the area in which the temperatures differ from the unperturbed mantle temperature $T(z)$ with at least a perturbation of ΔT = -143°C. The integrated anomalies are considered as the predicted thermal volume V_p of the initial volume V_i of the material subducted. Note that here with V_i we mean the thermal volume of the same slab when *not* affected by thermal diffusion. During ongoing subduction, thus when the amount of subducted material is actually increasing, both V_p and V_i change with time. After subduction has ceased, and the slab continues to heat up in the mantle passively, V_i is constant.

In this section, we will analyse the thermal volume V_p as a function of V_i as well as the time t since initiation of subduction. To approximate the present thermal signature of the subducted Tethyan oceanic lithosphere, we can use these values to estimate the present (0 Ma) thermal volume associated with a slab that started to subducted at a particular time t in the past (thus at t Ma). Although we are ultimately interested in the total present thermal volume of the subducted Tethyan lithosphere, the variation of the ratio V_p/V_i with time - thus the thermal factor $c(t)$ of Equation 3.16 - will be useful.

Parameter sensitivity of thermal volumes

To assess the parameter sensitivity of the thermal factor $c(t)$, the evolution of the subducting slab has been modelled for different lithospheric ages, rates of subduction, and timespans of subduction. The effect of the choice in lithospheric cooling model on the final thermal signature of the subducted material is investigated here as well. The sensitivity of the total area of perturbed temperatures to the slab dip was also tested, but found to be negligible. The reference parameters considered here are given in Table 3.3. When testing a particular parameter of the subduction process, the other parameters are kept at their reference values.

Reference initial lithosphere	
Age upon subduction	100 Ma
Based on plate cooling model:	
Plate thickness (z_m)	125 km
Temperature at z_m (T_m)	1330°C

Reference subduction process	
Timespan of subduction	100 Myr
Convergence velocity	3 cm/yr
Dip angle	45°
Thermal perturbation (ΔT)	-143°C

Table 3.3: Reference subduction case considered in this section. The volumes V_i and V_p are bounded by the temperatures that differ ΔT from the unperturbed mantle temperatures $T(z)$.

In the following figures, we show the modelled thermal volumes V_p as a function of the time t since initiation of subduction. In addition, the volumes $V_p(t)$ divided by the initial volume of the slab part subducted at that time $V_i(t)$, thus the thermal factors $c(t)$, are displayed. In Figure 3.8 and Figure 3.9, the values for $V_p(t)$ and $c(t)$ are those for subducting lithosphere with the initial volumes based on three different cooling models: 1) a plate model with z_m = 125 km and T_m = 1330°C (the reference case), 2) a plate model with z_m = 95 km and T_m = 1450°C, and 3) a half-space model with T_m = 1330°C. Figure 3.10 and 3.11 illustrate the evolution of $V_p(t)$ and $c(t)$ resulting from three different subduction processes: 1) a slab subducting during 100 Myr with a subduction rate of 3 cm/yr and residing in the mantle thereafter (the reference case), 2) a slab subducting for 300 Myr with a rate of 1 cm/yr, and 3) an end-member scenario in which oceanic lithosphere of 3000-km length is placed into the mantle instantaneously after which it continues to heat up for 300 Myr. Whereas V_i is time-dependent during subduction process (1) and (2), the total oceanic plate that is eventually subducted has the same (reference) V_i in all three cases. Figure 3.12 shows $c(t)$ for a) different timespans of subduction in the reference subduction case, and b) different slab lengths - corresponding to these timespans - in the end-member scenario of instantaneous subduction. The values of $c(t)$ in Figure 3.13 are deduced from the thermal volumes that are bounded by different perturbations ΔT from the reference mantle temperature $T(z)$.

Lithospheric age upon subduction Evidently, subduction of young oceanic lithosphere will result in a smaller thermal volume V_p than old lithosphere will (Figs. 3.8 and 3.10). The dependence on age, however, is relatively large for the initial volumes (see values at $t = 0$ for the instantaneous case in Fig. 3.10), with V_i for an age of 25 Ma about 30% smaller than that for an age of 150 Ma. For the reference subduction scenario, the differences in $V_p(t)$ remain clear but the relative variations decrease to 20% with increasing time (Fig. 3.8). As a result, the ratio V_p/V_i for 25-Ma aged lithosphere will be larger than that of older lithosphere instead (Fig. 3.9). The thermal factors $c(t)$ are similar for oceanic lithosphere >50 Ma.
A particular slab volume V_i will initially have largest heat flux for old (cold) oceanic lithosphere that has subducted fast to large (warm) depths, which is associated with a quick increase in V_p. This means that especially for the instantaneous subduction scenario, the thermal volumes for different ages will strongly diverge right from the beginning, as can be seen in Figure 3.10. Note that in the instantaneous case, the values of $c(t)$ for the youngest lithosphere are smallest. In any subduction scenario, the mantle surrounding the slab volume will eventually be cooled so much, and the slab re-heated accordingly, that the thermal gradients change sign: V_p has reached a maximum value and starts to decrease thereafter. Because of

the initially high gradients, the instantaneously subducted volumes will reach their maximum values before those of the reference subduction scenario do. The effect of subduction rates on the evolution of $V_p(t)$ and $c(t)$ will be discussed further below.

Plate vs. half-space cooling models Because the half-space and plate models predict comparable temperatures for oceanic lithosphere of ages up to ∼50 Ma (Section 3.3.1), the anomalous volumes V_p only differ significantly for older ages (Fig. 3.8): In the half-space model the lithosphere continues cooling, and the predicted thermal volume V_p of the slab material keeps increasing accordingly. In both plate models, the values of V_p are similar for ages of 100 Ma and older. Because the initial V_i varies with lithospheric age most strongly for the half-space model, the ratios V_p/V_i for the three models differ more than the values of V_p (Fig. 3.9). When predicting the present thermal volume V_p from the half-space model, or plate model 2, instead of the reference plate model 1, this will result in significant differences (10% at most) for lithospheric ages of 150 Ma only. Up to 100 Ma, the differences are less than 5%.

Rates of subduction Whether we have largest V_p for a slowly or rapidly subducting slab at a particular point in time will depend on the exact rate and timespan of subduction, and the age of the lithosphere (Fig. 3.10). During ongoing subduction (e.g. until $t = 100$ Myr in the reference subduction case), the instantaneous end-member scenario will result in largest values for $V_p(t)$. Soon after cessation of subduction, however, the values for the reference case will be largest instead. About 200 Myr after initiation of subduction, the maximum timespan of our interest, the differences in $V_p(200)$ are at most 10% for lithospheric ages of about 100 Ma and older, and at most 30% for slabs of 50 Ma. As young oceanic lithosphere is associated with small values of $c(t)$ for the instantaneous case of subduction, but relatively large values for smaller subduction rates (as discussed above), the differences for lithospheric ages of 25 Ma can be as large as 75% for the shown subduction scenarios.
Figure 3.11 suggests that the subduction rate does not control the values of $c(t)$ for plates older than 50 Ma. That is to say, the differences are at most 10 and 30% for ages of 100 and 50 Ma, respectively, at $t = 200$ Myr. Considering slabs younger than 50 Ma probably needs more detailed investigation of the subduction rates and associated values for $c(t)$.

Timespan of subduction The calculations for different timespans of subduction in the reference scenario, shown in Figure 3.12, result in comparable values for $c(t)$ as long as subduction is ongoing. However, the values diverge as soon as subduction ceases. For the end-member subduction scenario, in which the different amounts of lithosphere are instantaneously subducted, the associated values for $c(t)$ start to diverge right from the beginning. During active subduction in the reference subduction scenario, the instantaneous values of $c(t)$ are therefore always higher (at most 10%), but this is the other way around very soon after subduction has ceased: The values of $c(200)$ for the instantaneous subduction scenario are about 10% lower than those for the reference case for any particular slab length.
At $t = 100$ Myr, the thermal factors $c(100)$ for the reference subduction case are similar for all timespans, except for the shortest timespan which requires 5% smaller values. In the instantaneous scenario, $c(100)$ for the 25-Myr timespan (c.q. a slab length of 750 km) is 15%
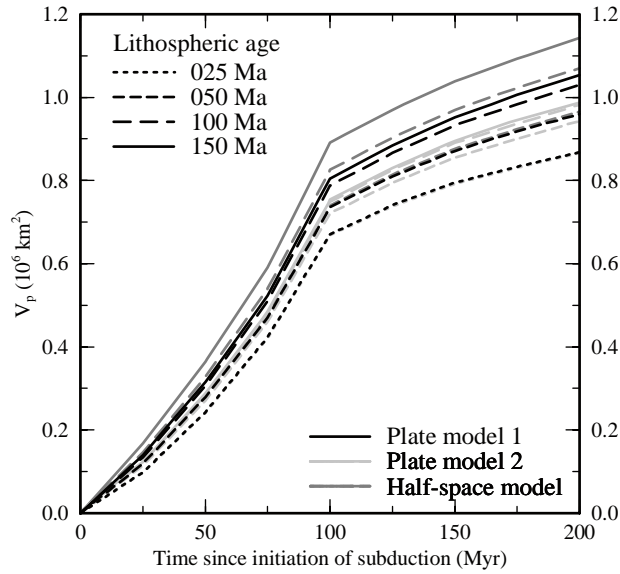
Figure 3.8: Evolution of the predicted thermal volumes V_p associated with the reference subduction process (Table 3.3). The initial volumes V_i are based on three different cooling models: The two plate cooling models include 1) a model with $z_m = 125$ km and $T_m = 1330°C$ (the reference case), and 2) a model with $z_m = 95$ km and $T_m = 1450°C$. The half-space model is defined for T_m of 1330°C.
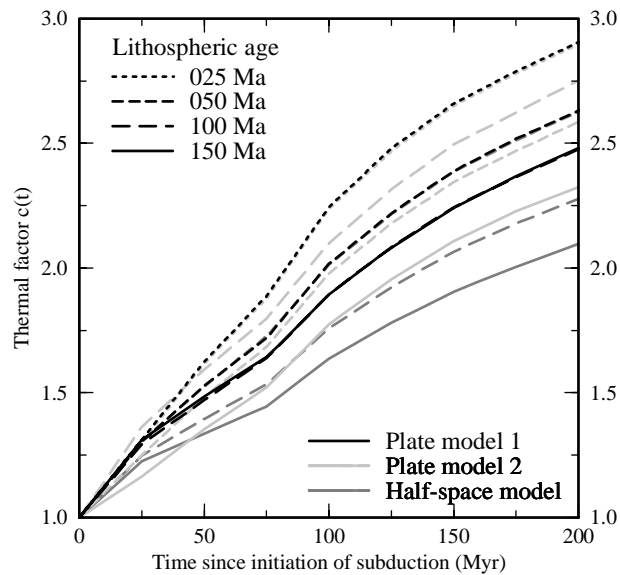

Figure 3.9: $V_p/V_i = c(t)$ for the predicted volumes V_p of Figure 3.8 and the initial volumes V_i of the slab subducted at that time (constant after $t = 100$ Myr). See text for further discussion.
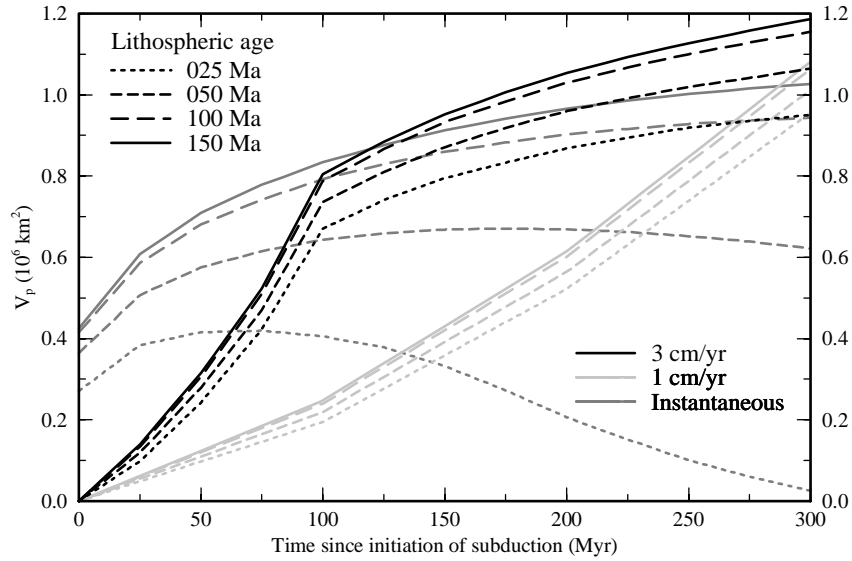
Figure 3.10: Evolution of the predicted thermal volumes V_p associated with three different subduction processes: 1) a slab subducting during 100 Myr with a subduction rate of 3 cm/yr and residing in the mantle thereafter (the reference case), 2) a slab subducting for 300 Myr with 1 cm/yr, and 3) an end-member scenario in which oceanic lithosphere of 3000-km length is placed into the mantle instantaneously after which it continues to heat up for 300 Myr. After cessation of subduction, the oceanic plates in the shown cases all have the same (reference) initial thermal volume V_i^r.
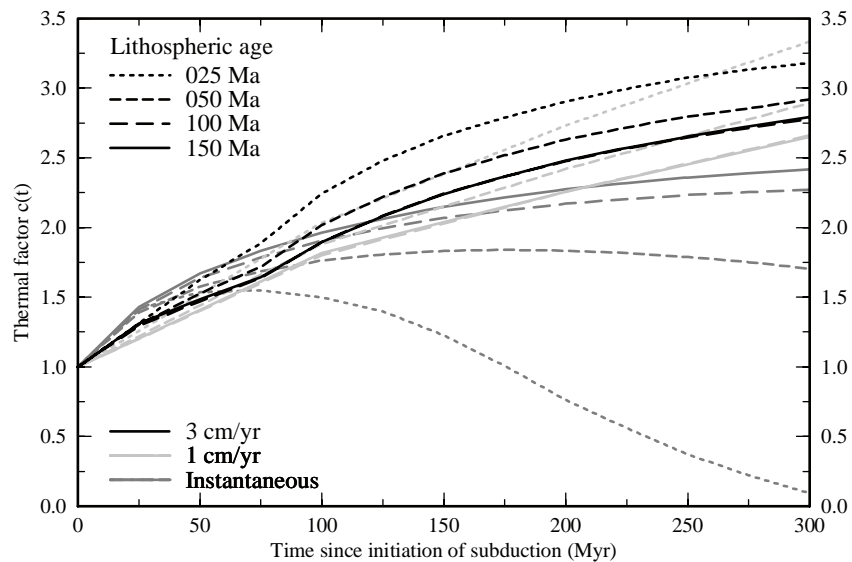
Figure 3.11: $V_p/V_i = c(t)$ for the predicted volumes V_p of Figure 3.10 and the initial volumes V_i of the slab subducted at that time. See text for further discussion.
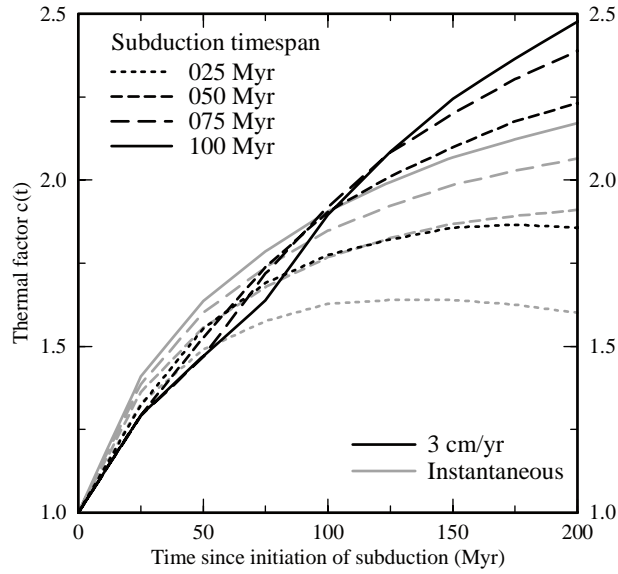
Figure 3.12: $V_p/V_i = c(t)$ for different slab lengths. For the reference subduction process (black lines), the 25-Myr timespan of subduction results in a total slab length of 750 km, while the 100-Myr timespan of subduction results in a slab length of 3000 km (reference case). The grey lines show $c(t)$ for the end-member scenario (like in Fig. 3.11) in which slabs with the appropriate lengths are placed into the mantle instantaneously.
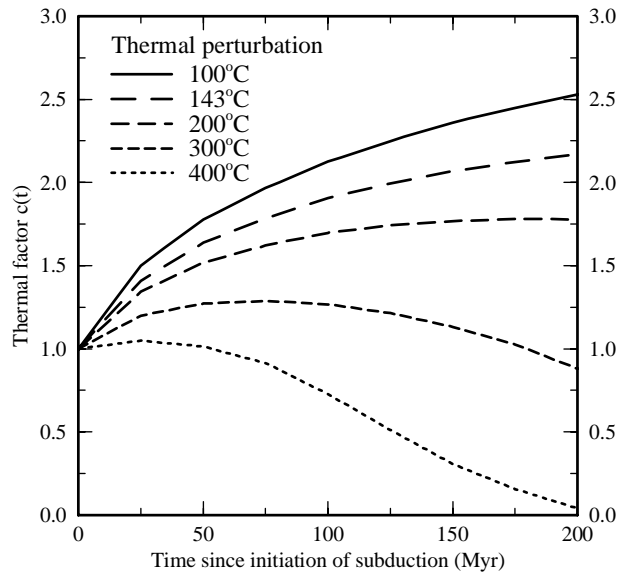
Figure 3.13: $V_p/V_i = c(t)$ for an instantaneous subduction process (like in Fig. 3.11). The temperatures bounding V_p are different values of ΔT lower than the reference mantle temperature at that depth.

lower than that for the 100-Myr timespan (c.q. 3000-km slab) at that moment. For the 50-Myr timespan, thus for a slab length of about 1500 km, the thermal factor is 5% lower only. At $t = 200$ Myr, the values of $c(200)$ for the different timespans are in the same proportion to each other in both subduction scenarios. That is to say, $c(200)$ for the 25 and 50-Myr timespans are about 20% and 10%, respectively, lower than those for the 100-Myr timespan.

Choice of differential temperature By definition, the size of the volumes V_i and V_p depend on the temperature chosen to bound the thermal anomalies. In Figure 3.13, V_p/V_i is shown for temperatures that differ a series of ΔT from the reference mantle temperature $T(z)$ for the instantaneous subduction case of Figure 3.11. Initially, the thermal gradients are high, but with increasing time they will slowly decrease while the volume broadens. The maximum values for $V_p(t)$ will be reached most quickly for the largest thermal perturbations ΔT. Figure 3.13 shows that after 100 Myr, the thermal factors $c(100)$ are relatively large for the smallest perturbations. For $\Delta T = 400°C$, $c(100)$ has already decreased to less than 1, i.e. $V_p < V_i$. After 200 Myr, $c(200)$ has further increased for perturbations up to 200°C, but the values for $\Delta T = 300°C$ have decreased to less than 1 now. For $\Delta T = 400°C$, the thermal volume $V_p(t)$ has practically disappeared.

Summary of sensitivity analysis

We summarise the main outcomes of the sensitivity analysis for the 200-Myr timespan that is of our interest when investigating the Tethyan region. For realistic (<150 Ma) ages of oceanic lithosphere, the predicted thermal volumes V_p were found not to be controlled by the lithospheric cooling model defining the initial volumes V_i. The modelling results indicate that the differences will be at most 5% for lithosphere of 100 Ma, and negligible for younger ages.

Whereas the age-dependence of oceanic lithosphere is straightforward when determining the initial volumes of subducted material V_i (see Section 3.3.1), its importance for the final thermal volume V_p was found to be more complicated and to depend on both the rate and timespan of subduction as well. To describe the effect of convergence rates, we will consider lithosphere older and younger than about 50 Ma separately:

1. Lithosphere older than 50 Ma: The age-dependence of $V_p(t)$ and $c(t)$ was found to be larger for high subduction rates - as illustrated with an end-member scenario of instantaneous subduction - than for small (1-3 cm/yr) subduction rates. As long as subduction is ongoing in the reference scenario, thus until $t = 100$ Myr, the values of $c(t)$ for the end-member scenario of instantaneous subduction were found to be at most 10% larger. However, about 200-Myr after initiation of subduction, the end-member values will *under*estimate the values of $c(200)$ for a 3 cm/yr subduction scenario with about 30% for oceanic lithosphere of 50 Ma instead. For lithospheric ages of 100 Ma, the differences in $c(200)$ are less than 10%, and for older ages they are negligible. In other words, if using the instantaneous $c(t)$ for slabs that have subducted at low (1-3 cm/yr) rates, the present thermal volumes V_p will be underestimated with about 10-30% at most. For still actively subducting slabs, however, the use of the instantaneous $c(t)$ will result in *over*estimates of V_p with at most 10% for old oceanic lithosphere only.

2. Lithosphere younger than 50 Ma: For lithosphere of 25 Ma, the volume $V_p(t)$ was found to be strongly dependent on the rate of subduction. For the end-member scenario of instantaneous subduction, the modelled values for $c(t)$ are relatively small and decrease to less than 1 within 200 Myr after initiation of subduction. On the contrary, for the low subduction rates (1-3 cm/yr) investigated here, $c(t)$ is relatively large, i.e. larger than those for older lithosphere ($\geq$50 Ma). With a rate of 3 cm/yr, $c(200)$ can be as much as 75% larger than the values for the instantaneous case of subduction. In other words, if using the instantaneous $c(t)$ for very young lithosphere, we will strongly underestimate the present thermal volumes if this lithosphere has been subducted at very slow rates. When considering lithosphere that is much younger than 50 Ma, this would therefore require more detailed investigation of the subduction rates and associated values of $c(t)$.

Finally, if using values of $c(t)$ for 100-Myr timespans of subduction or, more precisely, slabs of 3000-km length to predict the present thermal structure of the subducted material, the volumes V_p for smaller slab lengths will be systematically overestimated. The differences after a total 200 Myr can be as large as 10 to 20% for slab lengths of $\sim$1500 and 750 km, respectively, in any particular subduction scenario.

Slab thickening

In thermo-kinematic models as the one used here, slabs are assumed to descend into the mantle along a fixed dip angle. However, many laboratory and numerical studies have shown that the dip of a slab is a function of the time since initiation of subduction, and that slabs can significantly deform during their descent into the mantle (e.g. *Kincaid and Olson*, 1987; *Gurnis and Hager*, 1988; *Gaherty and Hager*, 1994; *Guillou-Frottier et al.*, 1995; *Christensen*, 1996; *Han and Gurnis*, 1999; *Becker et al.*, 1999). In the Tethyan region, the large amount of material that has been subducted in the past must have resulted in slabs that simply cannot have kept their original, plate-like geometry.

Slabs subducting slowly at small angles do not typically penetrate into the lower mantle, but flatten and loose their plate-like geometry above the 660-km discontinuity. These slabs may already have thickened to twice their original width by the time they reach the base of the transition zone (*Gaherty and Hager*, 1994; *Becker et al.*, 1999). Fast and steeply subducting slabs can fold and thicken strongly when they enter into the more viscous lower mantle. The actual style of deformation, however, is highly dependent on the strength of the slab and the viscosity contrast between the upper and lower mantle. Thickening by at most a factor of 2-2.5 has been modelled for cases with moderate $\sim$30-fold viscosity contrasts at the 660-km discontinuity (e.g. *Gaherty and Hager*, 1994; *Christensen*, 1996), and with a factor as high as 4-5 for large ($\sim$100-fold) and sharp viscosity contrasts (*Gaherty and Hager*, 1994; *Guillou-Frottier et al.*, 1995). The rheological properties of slabs seem complex and are only partly understood. In general, only low viscosity slabs show the most intense folding and thickening discussed above (*Houseman and Gubbins*, 1997).

If slabs flatten or buckle within the mantle, this will not necessarily change the process of re-heating. However, if the folds are subparallel, or if pure shear thickening occurs, the time for this slab to reach thermal equilibrium with the mantle by diffusion will increase. Since many slab thermal models do not account for such thickening - including the one used in this study - they will generally underestimate this equilibrium time, and thus overestimate the

thermal volume associated with the subducted material. To account for the expected Tethyan slab deformation, we will consider pure shear thickening of the slab material by a factor of 2 and 3. If more deformation is required, this is thus implicitly assumed to have been produced by simple buckling or flattening of the slabs. Evidently, the present seismic velocity signature of buckled slabs can still appear as simple broadened structures, similar to that of (pure shear) thickened slabs, in tomographic models.

We investigate here the evolution of the ratio V_p/V_i with time for the subduction of 'doubled' and 'tripled' lithosphere. Assuming that lithosphere experiences instantaneous and pure shear thickening, the initial thermal structure of the doubled and tripled lithosphere is modelled by using plate thicknesses of $2z_m$ and $3z_m$ instead of z_m (see Eq. 3.15), and total slab lengths of 1500 km and 1000 km instead of 3000 km, respectively. In Figure 3.14 and 3.15, the resulting values for V_p/V_i - both for instantaneous subduction and for 3 cm/yr subduction rates - are shown together with the values for the instantaneous subduction of normal, 'single' lithosphere (e.g. as in Fig. 3.11). We will refer to the ratio V_p/V_i for doubled lithosphere as $c_2(t)$, and that for tripled lithosphere as $c_3(t)$, hereafter. The thermal factor $c(t)$ for single, unthickened lithosphere will be denoted $c_1(t)$.

From Figure 3.14 it can be seen that $c_2(t)$ for doubled lithosphere is much less dependent on the exact age of the oceanic lithosphere than $c_1(t)$ for single lithosphere. The modelled value of $c_3(t)$ for tripled lithosphere (Fig. 3.15) does not significantly depend on the age of the subducting lithosphere at all. For $c_2(t)$, the instantaneous values are found to be somewhat lower that those for slabs subducted with 3 cm/yr, but not as much as for the single $c_1(t)$ discussed above. For ages ∼25 Ma, the difference turns out to be at most 30% at a maximum $t = 200$ Myr, but for older ages this is 10% at most. For the tripled values of $c_3(t)$, the differences between the instantaneous and slower subducting slabs are negligable. Only for the 25-Ma slabs, the difference is ∼15% at most, at $t = 200$ Myr.

Our modelling results indicate that $c_2(t)$ and $c_3(t)$ especially depend on the reduced slab surface area, and are determined to a lesser extent by the exact temperature distribution inside the slab. For a plate that is much longer than thick, pure shear doubling of a volume will approximately halve the slab surface. Analogous, pure shear tripling will lower the surface to about 1/3 the original surface. In other words, if the change in volume dV by diffusion during a small timespan is primarily dependent on the surface indeed, dV for a doubled volume will be only half of that for the original volume, and dV for a tripled volume one third of that. With V_p/V_i equal to $(V_i+dV)/V_i = 1+dV/V_i$, an original ratio of 2.2 (e.g. for our reference subduction case at $t = 200$ Myr) will thus become 1.6 for a doubled slab, and 1.4 for a tripled slab. Indeed, the values of $c_2(t)$ are similar to those approximated from the single value of $c_1(t)$ directly (Fig. 3.14), and $c_3(t)$ is about 10% smaller only (Fig. 3.15).

To account for slab thickening in the lower mantle, the values of $c_1(t)$ for the subduction of lithosphere with a normal thickness should be used in the upper mantle, providing that no thickening occurs in the upper mantle already. In most cases, however, the total residence time in the upper mantle will be unknown, and slab thickening may also occur above the 660-km discontinuity already. We therefore prefer a simple, end-member approach in which the lower-bound values of $c_2(t)$ and $c_3(t)$ are tested against the upper-bound values of $c_1(t)$ directly, thus without making additional assumptions on the exact subduction history.

Conclusions

In Chapter 4 and 5, we will use the reference plate model (based on *Parsons and Sclater*, 1977) to approximate the initial thermal volumes of subducted Tethyan oceanic lithosphere. To determine the present volumes V_p from the initial volumes of lithosphere V_i, we will use the age-dependent values of $c_1(t) = V_p/V_i$ that we derived for the end-member scenario of instantaneous subduction discussed above.

Using values of $c_1(t)$ for the instantaneous subduction scenario to predict the final volumes V_p for slowly and still actively subducting slabs will generally result in overestimates of the volumes of 10% at most. After subduction has ceased, which is actually the case for the larger part of the Tethyan region, the end-member values of $c_1(t)$ will *under*estimate the present thermal volumes instead. About 100 Myr after cessation of subduction this is at most 10-30%, depending on the lithospheric age. For very young lithosphere ($\sim$25 Ma), the volumes of V_p will be underestimated more. However, the average age of subducting lithosphere will generally be larger than that. The thermal volumes of relatively small slabs, say of <1000-km length, will be *over*estimated with at most 10-20% around a total 200 Myr after initiation of subduction.

As slabs can thicken by a factor of 2 or 3 during subduction, the thermal volumes predicted with the modelled $c_1(t)$ for unthickened lithosphere may represent an upper-bound. In view of the abundant subduction in the Tethyan region, a certain factor of slab thickening seems likely indeed. As lower-bound values for the present thermal volumes of the subducted Tethyan slabs. we will therefore use the values of $c_2(t)$ and $c_3(t)$ for slab doubling and tripling due to instantaneous pure shear thickening. Using $c_2(t)$ of instantaneous subduction for slowly subducted slabs will generally lead to overestimates of the volumes of 10% at most (i.e. at 200 Myr after initiation of subduction), whereas this effect is negligable for $c_3(t)$. For young ($\sim$25 Ma) lithosphere, the volumes for instantaneous and slow subduction will differ 15-30% at most.

In Section 3.3.2 it was discussed that the way we handle several uncertainties in our modelling procedure results in an overestimate of the thermal volumes. However, to approximate the Tethyan slab volumes we have used these modelling results to derive a method with which the thermal volumes will generally be *under*estimated instead. Only for active, unthickened, and small slabs, the thermal volumes will probably be even more overestimated. The exact differences will depend on the time of initiation of subduction, as well as that of the cessation thereof, and will significantly decrease with an increasing factor of thickening.
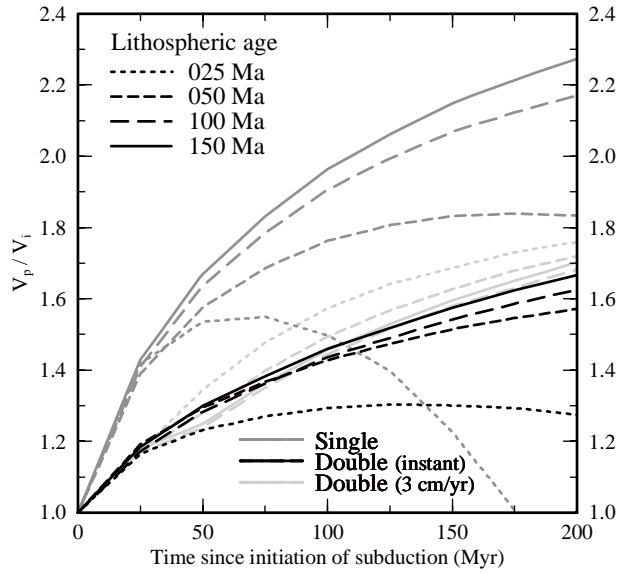
Figure 3.14: $V_p/V_i = c_1(t)$ for the instantaneous subduction process shown in Figure 3.11 (dark grey lines), as well as the factor $c_2(t)$ resulting from an instantaneous subduction of this lithosphere 'doubled' (black lines). This lithosphere is assumed to have experienced pure shear thickening from length l to $l/2$ and thickness z_m to $2z_m$ instantaneously. Also displayed (light grey lines) is $c_2(t)$ for subduction of the same thickened lithosphere at a rate of 3 cm/yr.

Figure 3.15: As in Figure 3.14, but now for the subduction of 'tripled' lithosphere, c.q. the lithosphere is assumed to have experienced pure shear thickening from length l to $l/3$ and thickness z_m to $3z_m$.

Chapter 4

A volume analysis of subducted Tethyan oceanic lithosphere

4.1 Introduction

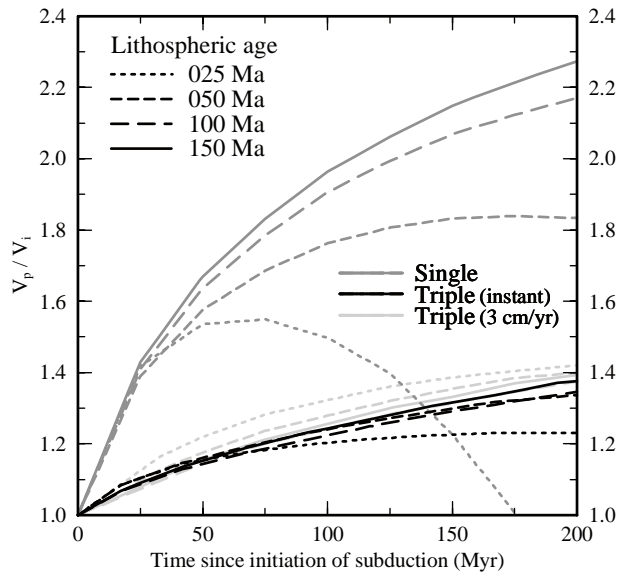In this chapter, we investigate the large-scale history of subduction within the Tethyan region. Although studies of the geodynamic evolution of this area have resulted in many different plate tectonic reconstructions (e.g. *Dercourt et al.*, 1993; *Şeng ör and Natal'in*, 1996; *Stampfli and Borel*, 2002), the motions of the African-Arabian and Indian plates relative to Eurasia dominate in all scenarios. Since tectonic reconstructions are primarily based on surface data, we examine here whether we can contribute to a better understanding of the Tethyan evolution by making a quantitative comparison between tomographic mantle structure and the volumes of subducted lithosphere predicted from these reconstructions.

The tomographic model of *Bijwaard et al.* (1998) is used here to analyse the large positive velocity anomalies that can be found in tomographic images of the mantle underneath the area. To estimate the size of the anomalous volumes of our interest, we use the depth-dependent temperature derivative of the seismic velocity. The large volumes, and the large depths at which they are found, indicate that they must have resulted from long periods of subduction in Cenozoic and Mesozoic times.

We follow the tectonic reconstruction of ExxonMobil (*Norton*, 1999) to study the large-scale surface motions within the region from 200 Ma to present. In this timespan, all Mesozoic-Cenozoic motion of the African-Arabian and Indian plates relative to Eurasia took place and dominated the closure of the Neo-Tethyan oceanic basins. We estimate the subducted surface, and approximate the present thermal signature associated with this material, for the amount of convergence calculated from the tectonic reconstruction.

The resolution of the tomographic model as well as the uncertainties in the tectonic models, and thus the actual errors in the anomalous volumes and subducted surface derived from these, are unknown and difficult to assess. We therefore necessarily take both the tomographic and tectonic models as they are. Other uncertainties in our calculations are accounted for as much as possible, e.g. by using upper and lower limits of the temperature-sensitivity of the seismic

velocities, and by assuming two end-member scenarios for the lithosphere subducted. Because the Tethyan evolution comprises the long-time subduction history of oceanic lithosphere that is almost entirely lost today, we have to use a simplified method to approximate the present thermal signature of the subducted lithosphere. Although the approach is limited by several uncertainties and assumptions made, e.g. on the age of the lithosphere and the residence time in the mantle, the predicted thermal volumes will be shown to be useful for investigating the Tethyan region as a whole. Analyses of more detailed aspects of the Tethyan evolution require more specified predictions of the thermal volumes, and will be addressed in Chapter 5.

4.2   Mantle structure imaged by tomography

4.2.1   The tomographic model

The volumes of the positive seismic velocity anomalies in the Tethyan region are determined from the tomographic BSE-model of *Bijwaard et al.* (1998). This model has a global and whole-mantle coverage yielding sufficient detail because of its irregular cell parameterisation (Section 3.1.1). The seismic velocities in the uppermost mantle (down to ∼220 km) are likely to be highly influenced by compositional heterogeneities, attenuation and anisotropy (Section 3.1.3). Furthermore, we can use values for the temperature sensitivity of the seismic anomalies down to a depth of 2600 km depth only (Section 3.1.4). Therefore, from the 26 layers in the BSE-model, the upper 5 layers (top 230 km of the model) and lower 2 layers (lower 2560-2889 km of the mantle) are not taken into account when analysing the tomographic model. The effect of neglecting the anomalies related to subducted material in the upper 230 km will be discussed further in Section 4.3 and 4.4. The seismic anomalies underneath the Tethyan region that are of our interest can all be found above 2600 km depth, as can be seen in Figures 4.2 and 4.3.

Calculating the seismic anomalous volumes

The volumes of the relevant anomalies are determined from a series of cross-sections through the tomographic model (Fig. 4.1). The cross-sections are great circle arcs, have a length of 50°, and are separated by 0.5° each. All sections are crossed half-way by the same great circle. This great circle has been chosen because it follows the general orientation of those positive velocity anomalies in the tomographic model that are thought to represent the Mesozoic slab remnants of the Tethyan oceans (Fig. 4.3).

Within each section, those areas are determined that have an anomaly higher than a particular cut-off value for ΔV_p. The values of ΔV_p assumed to bound the anomalous volumes of our interest are the minimum and maximum profiles displayed in Figure 3.2 (Section 3.1.4, p. 43), and correspond to thermal perturbations of -100°C. To account for the uncertainty in the seismic anomalies, values of ΔV_p smaller than 0.2% will be ignored. For each relevant anomaly, both a minimum and maximum value of its volume is calculated. The anomalous areas in each section (km^2) are assumed to be representative for the small 0.5° segment surrounding it. The 0.5° distance between the sections is ∼55 km at the Earth's surface in the
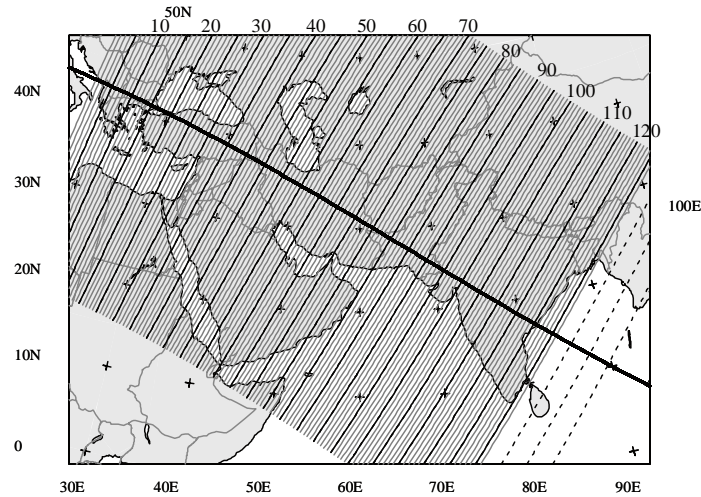
Figure 4.1: Overview of the cross-sections used to analyse the anomalies in the tomographic model underneath the Tethyan region, with every 5th section highlighted here. The easternmost sections are dotted because they have been used to determine the anomalies, but will not be used in the comparison with the volumes calculated from the tectonic reconstruction later. The sections are perpendicular to a great circle that is roughly aligned with the deep positive velocity anomalies within the tomographic model, and crosses the sections half-way. All cross-sections have a length of 50°, and are separated by 0.5° each. The shown Mercator projection is centered along a great circle starting at (22°N,21°E) with azimuth 73° and length 70°.

middle of the sections, but will decrease with both depth and the distance from the lateral centre of the section. Therefore, we directly calculate the volumes for each section segment (km^3) by multiplying each area with the appropriate dimensions.

Resolution of the anomalies

In analysing the results, the trench segment volumes that are thought to belong to the same anomalous volumes within the model are grouped together. To be recognised as a separate anomalous body, or a possible discontinuity instead, the resolution of the tomographic model, approximately 65-100 km laterally and 35-65 km vertically in the upper mantle (Section 3.1), has been taken into account. In the lower mantle, the lateral resolution is about 150-300 km and the vertical resolution 100-200 km. Apart from the volume of each anomalous body, both the geographical location and the depth within the mantle is therefore of importance in the analysis. Especially for anomalies in the lower mantle, a relatively small gap between two adjacent anomalies can thus easily be overlooked. This means that an apparently continuous anomaly is not necessarily related to one single slab volume. In this chapter, some of the discussed anomalies seem to be continuous and therefore could have been identified as a single body just as well. However, because they are clearly separated at other depths, or because they have different strikes or geometries, we prefer to mention them separately here. Whether or not to take them together can be decided later in this thesis.

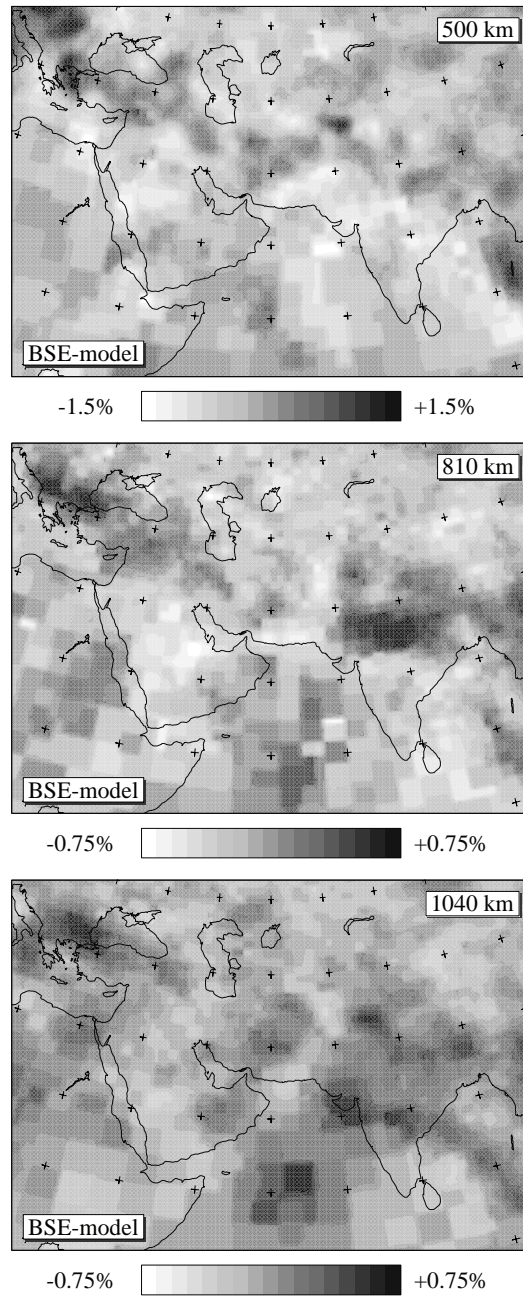**Figure 4.2:** Horizontal sections through the tomographic BSE-model of *Bijwaard et al.* (1998) at 500, 810 and 1040 km depth. For a colour version of this figure, see Figure A.6 in the Appendix.
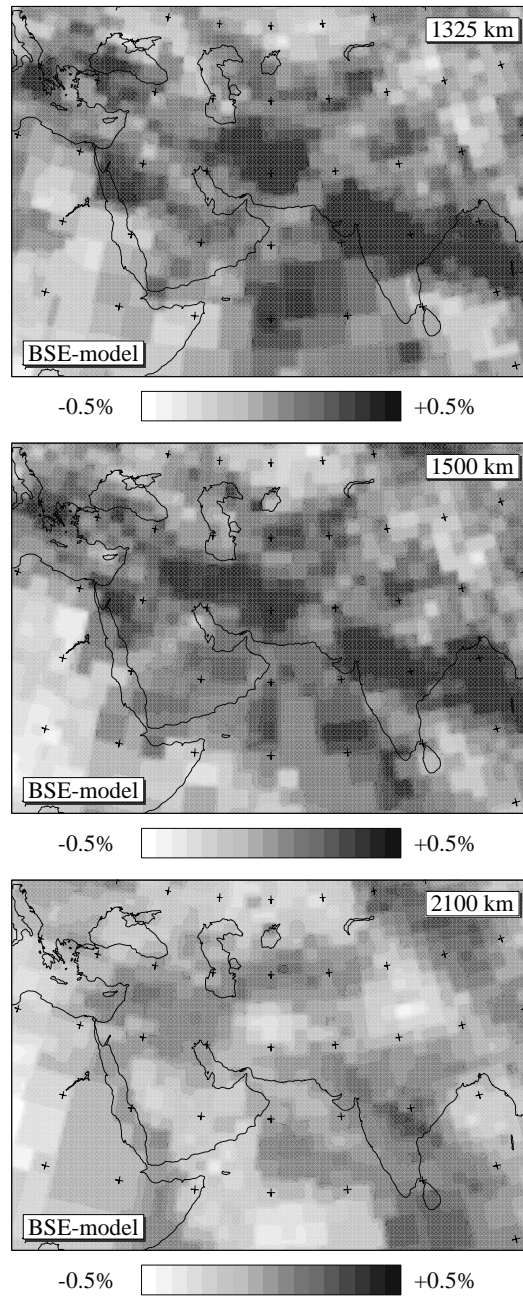
Figure 4.3: Horizontal sections through the tomographic BSE-model of *Bijwaard et al.* (1998) at 1325, 1500 and 2100 km depth. For a colour version of this figure, see Figure A.7 in the Appendix.

4.2.2 Overview of the anomalies

We determine the minimum and maximum boundary of the seismic anomalous volumes that can potentially be associated with subducted material in each section of Figure 4.1. The separate anomalous bodies that are recognised throughout the region are shown in Figures 4.4-4.6, in which the contour line of each body is a projection of its maximum horizontal cross-section in the given depth interval. A selection of six of the vertical sections across the tomographic model, also indicated in Figures 4.4-4.6, is shown in Figure 4.7. Moreover, vertical sections approximately perpendicular to the cross-sections of Figure 4.7 are shown in Figure 4.8. The contour lines in each section show the maximum volumes calculated. The positions and characteristics of all anomalies are summarised in Table 4.1, and will be discussed below.

Depth range of 230 to ∼660 km

Between 230 and 660 km depth, we find the anomalies shown in Figure 4.4. In the transition zone, the anomalies underneath Greece (Gr), Turkey (wT/eT), and the Caucasus (Ca) seem to be continuous with each other. However, anomaly wT and Ca extend until the bottom of the upper mantle only, while the two other anomalies have their main volume in the lower mantle. Although anomalies Gr, wT, eT and Ca might belong to one single body, we identify them separately here. Anomaly Zs underneath the northern Zagros Suture and anomaly HK beneath the Hindu Kush and Pamirs are found primarily in the upper mantle, although they continue in the lower mantle as well. Both anomalies are clearly separated from the surrounding volumes. The several upper mantle anomalies below Iran and Afghanistan are somewhat separated from each other, but we prefer to put them together as one single volume IA[1]. More to the east, the anomalies underneath the Himalayan chain (Hi[1]) and the Indian Ocean (Io) have their main volume in the lower mantle. The upper mantle parts of anomalies Hi[1] and Io might be separate upper mantle volumes, but because of their relatively minor sizes we include them within the larger lower mantle anomalies instead. Anomalies My[2] and My[1] are found east of the sections that are used to calculate the convergence from the tectonic reconstruction. Although anomaly My[2] underneath Myanmar and southwest China is found primarily in the lower mantle, this volume clearly starts in the transition zone already. Anomaly My[1] underneath Myanmar and the Andaman Sea is mainly found in the upper mantle. Although it partly overlaps anomaly My[2] in the north, the difference between the two volumes is clear. Both anomalies can be associated with the still active subduction along the Sunda-Java trench, or recent subduction along the sutures in Myanmar, but will not be discussed further in this chapter. In the westernmost part of the Tethyan area, anomaly Yu beneath Yugoslavia is clearly separated from anomaly Gr underneath Greece. However, Yu does not seem to belong to the Tethyan history of subduction and will be left out of the discussion as well.

Depth range of ∼660 to 1100 km

Figure 4.5 shows the anomalies that are found between approximately 660 and 1100 km depth. The exact depth below which the anomalies fade away is different for each anomaly. Compared to its upper mantle part, anomaly Gr underneath Greece is associated with a much larger area in the lower mantle, extending until below Yugoslavia and eastern Turkey now.
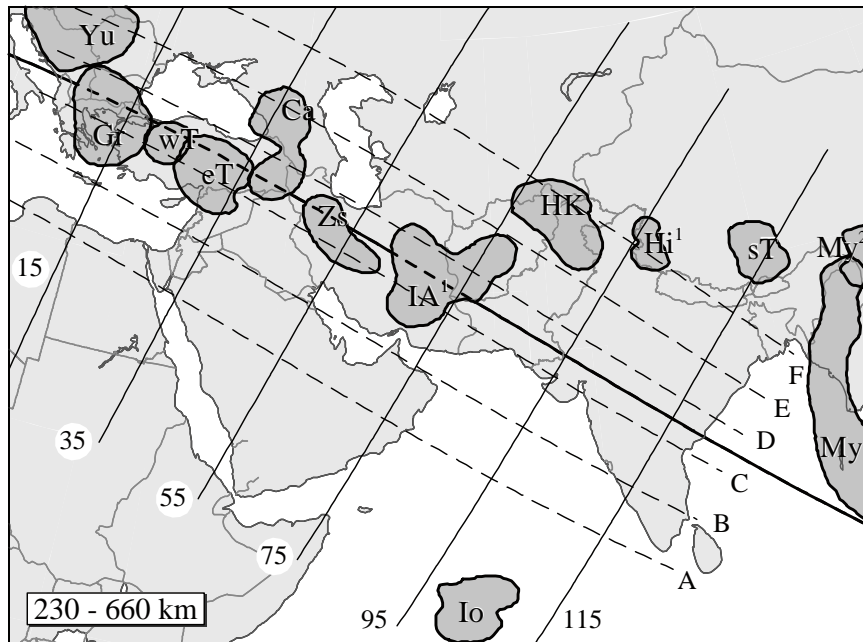
Figure 4.4: 230 - 660 km depth interval: Overview of the separate anomalous bodies within the tomographic BSE-model that are considered to represent volumes of subducted Tethyan lithosphere between 230-660 km depth (cf. Fig. 4.2). The contour line of every body is a projection of its maximum horizontal extension in the given depth interval. The names of the anomalous bodies refer to their approximate geographical locations. From west to east these are: Yu = Yugoslavia, Gr = Greece, wT = west Turkey, eT = east Turkey, Ca = Caucasus, Zs = Zagros suture, IA^1 = Iran/Afghanistan (upper volume), HK = Hindu Kush, Io = Indian ocean, Hi^1 = Himalayas (upper volume), sT = south Tibet, My^1 = Myanmar/Andaman (upper volume), and My^2 = Myanmar/China (lower volume). The lines and numbers indicate the vertical cross-sections that are shown in Figs. 4.7 and 4.8.

Also anomaly eT is broader than in the upper mantle, extending until beneath the Caucasus. Although the anomalies of eT underneath the Caucasus might have been part of upper mantle anomaly Ca originally, there is now a clear gap between these two across the 660-discontinuity. The main part of the anomalies underneath the Himalayas Hi^1 is clearly found in the upper part of the lower mantle as well. Although the eastern part of Hi^1 is close to the western part of anomaly My^2, we can identify My^2 because it has a very different geometry. Furthermore, anomalies Zs and HK simply fade away below ∼1100 km depth. Both anomaly Io underneath the Indian Ocean and anomaly Ic below the Indian continent are parallel to Hi^1, but the volumes can be easily separated from each other at this depth interval. Below eastern Iran, Afghanistan and southern Saudi Arabia, we recognise anomalies IA^2 and SA that are mainly situated below ∼1100 km depth. Anomaly IA^2 is found right underneath IA^1 but is clearly separated from it. Beneath northeast Egypt and the Sinaï, anomaly Eg is also found isolated from the surrounding anomalies.

Figure 4.5: Overview of the separate anomalous bodies within the tomographic BSE-model that are considered to represent volumes of subducted Tethyan lithosphere between 660-1100 km depth (cf. Fig. 4.2). The contour line of every body is a projection of its maximum horizontal extension in the given depth interval. The names of the anomalous bodies refer to their approximate geographical locations: Gr = Greece, eT = east Turkey, Eg = Egypt, Zs = Zagros suture, SA = Saudi Arabia, IA^2 = Iran/Afghanistan (lower volume), HK = Hindu Kush, Io = Indian ocean, Ic = Indian continent, Hi^1 = Himalayas (upper volume), and My^2 = Myanmar/China (lower volume). The lines and numbers indicate the vertical cross-sections that are shown in Figs. 4.7 and 4.8.

Depth range of ∼1100 to 2560 km

The anomalies in Figure 4.6 can be found in the lower mantle below ∼1100 km depth. In the western part of the area, volume Gr almost reaches the region underneath the eastern borders of Turkey and the southern Ionian Sea. Below 1800 km, the anomaly even seems to be continuous with anomaly Eg underneath Egypt as well as an anomaly underneath Syria, Iraq and Iran (SI). Anomaly SI is clearly detached from eT and Zs above it. Both anomaly Eg and anomaly SA now extend until central Saudi Arabia. The volumes appear to be continuous above ∼1500 km, but because they split again below that depth we prefer to keep the anomalies separated. Because anomaly IA^2 is much larger now as well, the boundary between SI and IA^2 below Iran is not always very distinct. However, below 1600 km depth, their volumes are more clearly separated: Anomaly SI seems to be continuous with Eg and Gr instead, while anomaly IA^2 merely appears to be in connection with SA. From the tomographic model alone, both the combinations of Eg-SA and SI-IA^2, as well as the combinations of Eg-SI and SA-IA^2, seem to be plausible. East of the Owen Fracture Zone, anomalies Io, Ic and Hi^2 are
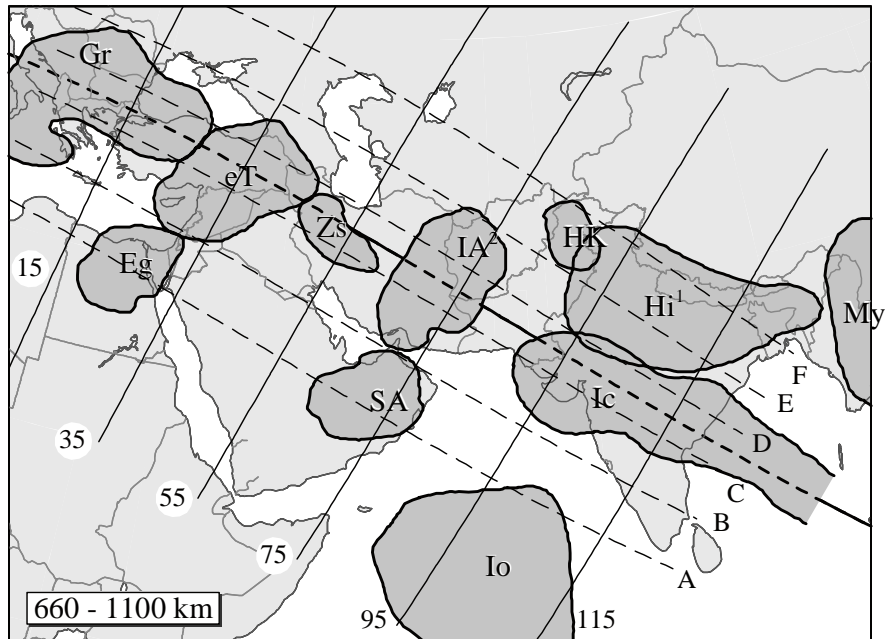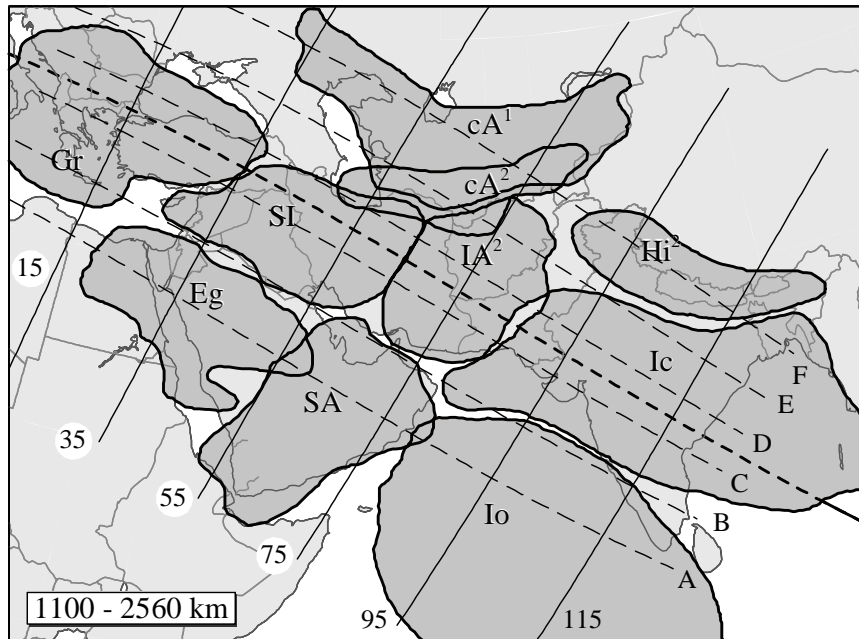
74

Figure 4.6: Overview of the separate anomalous bodies within the tomographic BSE-model that are considered to represent volumes of subducted Tethyan lithosphere between 1100-2560 km depth (cf. Fig. 4.3). The contour line of every body is a projection of its maximum horizontal extension in the given depth interval. The names of the anomalous bodies refer to their approximate geographical locations: Gr = Greece, Eg = Egypt, SI = Syria/Iraq/Iran, cA^1 = central Asia (upper volume), cA^2 = central Asia (lower volume), SA = Saudi Arabia, IA^2 = Iran/Afghanistan (lower volume), Io = Indian ocean, Ic = Indian continent, and Hi^2 = Himalayas (lower volume). The lines and numbers indicate the vertical cross-sections that are shown in Figs. 4.7 and 4.8.

parallel to each other over their whole longitudal distance. Although the boundaries between the anomalies are not at all depths very clear, their different geometries allow us to recognise the volumes as separate indentities. The anomalies of SA and Io, as well as those of IA^2 and Ic, partly overlap across the mantle underneath the Owen Fracture Zone and the eastern limit of the Makran ranges in Pakistan, respectively. However, their volumes are clearly separated in most layers. Underneath the Himalayan chain, anomaly Hi^2 is on the same position but somewhat lower in the mantle than Hi^1. Because the lower anomaly seems to be detached from the upper one, we keep Hi^2 and Hi^1 as separate volumes here.

Anomalies cA^1 and cA^2 are found underneath Central Asia. Although the lowermost anomaly cA^2 is on the same geographical position in the mantle as anomaly cA^1 above it, the volumes seem to be separated from each other. The current position of cA^1 and cA^2, i.e. far north of the Cenozoic Zagros Suture, suggest that the anomalies are related to an Early Mesozoic or even Paleozoic phase of subduction. They will not be discussed further in this chapter.
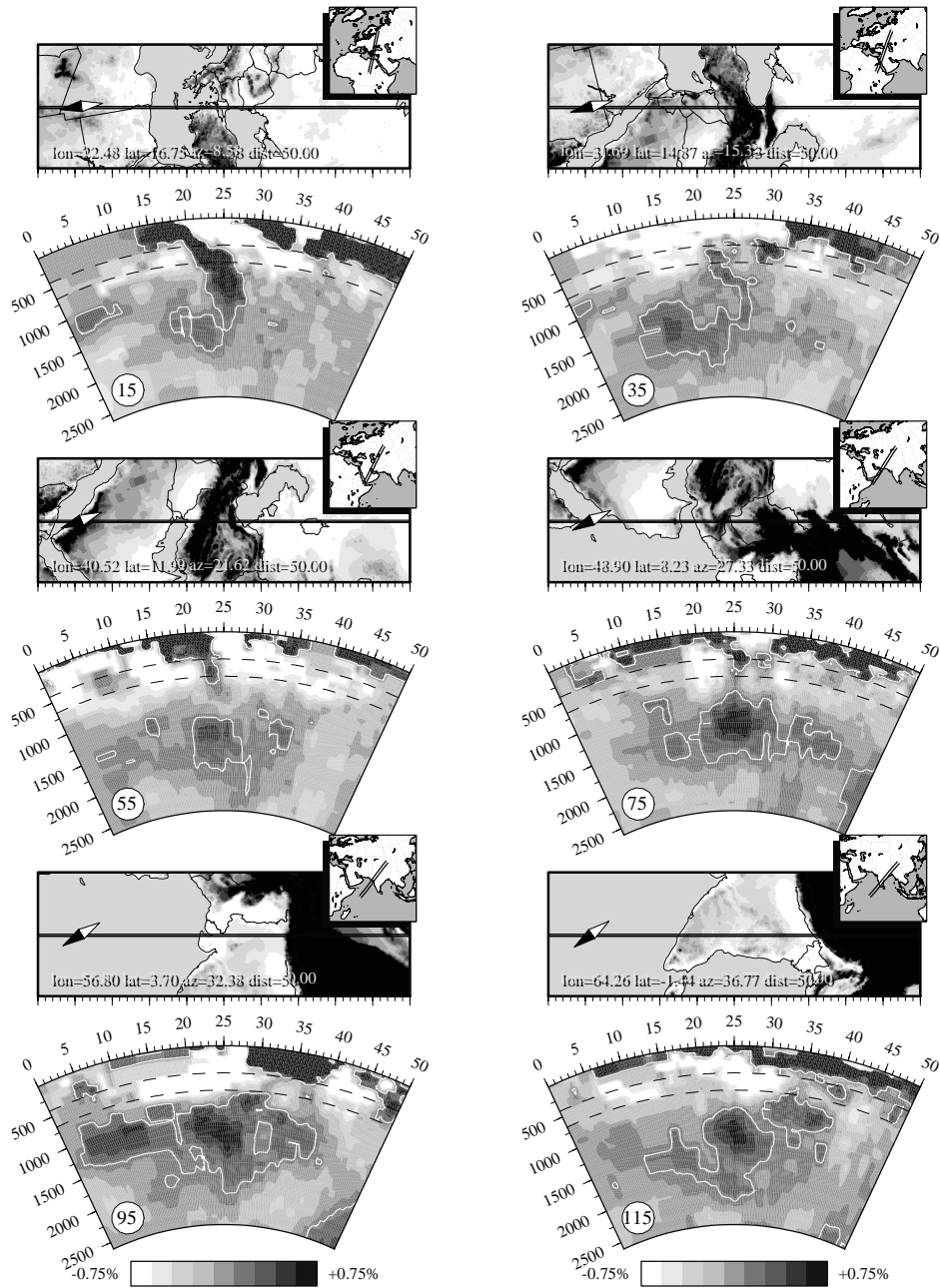
Figure 4.7: Vertical sections through the tomographic model of *Bijwaard et al.* (1998). From top to bottom: Sections 15 and 35, sections 55 and 75, and sections 95 and 115 of Figures 4.4-4.6 down to 2600 km depth. In each section the 0.2% contour lines, indicating the approximate maximum volumes calculated, are shown as well. For a colour version of this figure, see Figure A.8 in the Appendix.

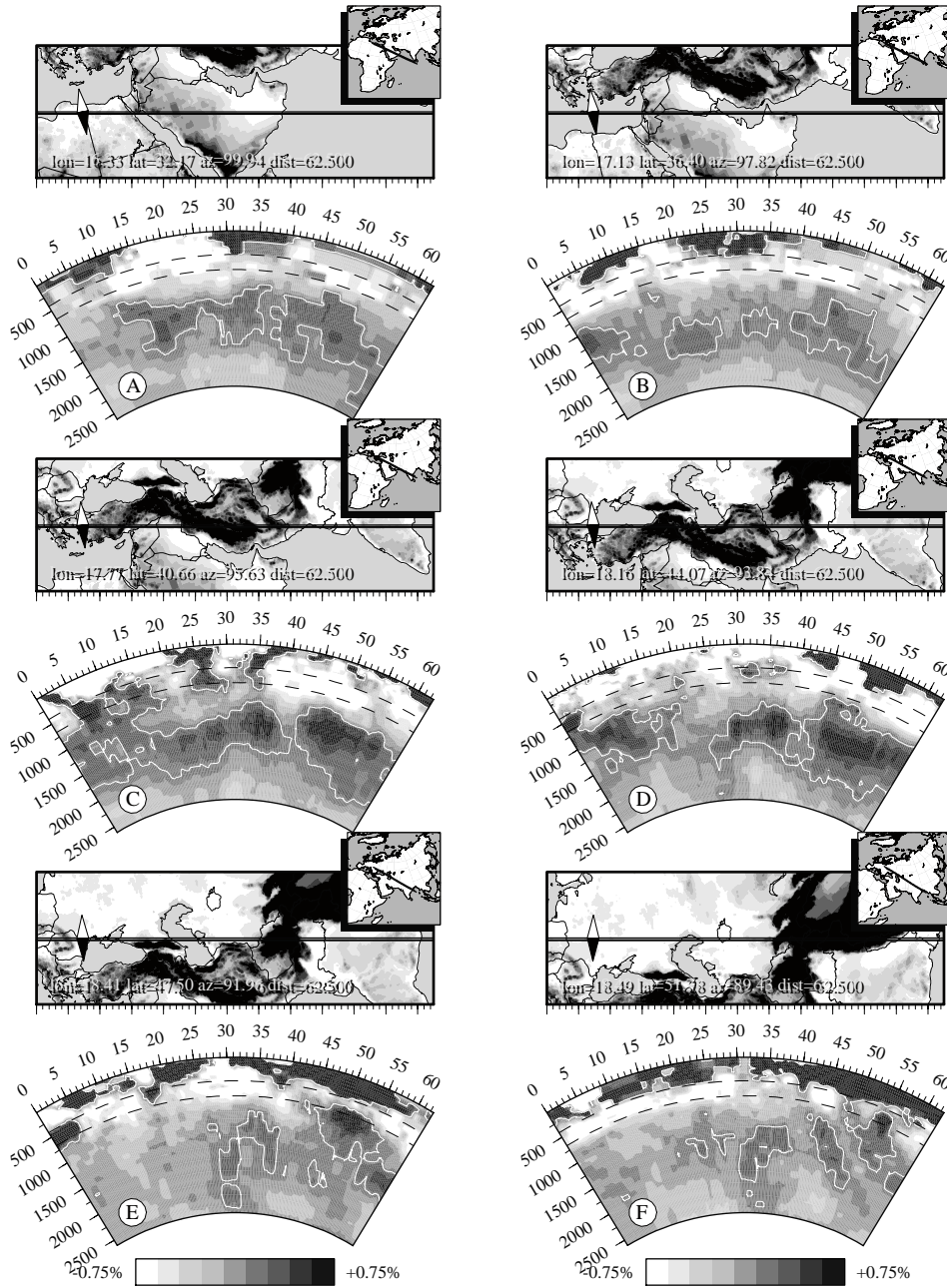**Figure 4.8:** Vertical sections through the tomographic model of *Bijwaard et al.* (1998), approximately perpendicular to the cross-sections of Figure 4.7, down to 2600 km depth. The sections are indicated in Figures 4.4-4.6. In each section the 0.2% contour lines, indicating the approximate maximum volumes calculated, are shown as well. For a colour version of this figure, see Figure A.9 in the Appendix.

77

Name Anom.	Section segments	Geographical location	Depth interval (km)	Main position				Volume ($\cdot 10^6$ km^3)
				up	tz	lo	dp	
Yu	1−10	Yugoslavia	300−760		x			60−80
Gr	1−36	Greece	230−2000	x	x	x	x	680−830
wT	20−25	west Turkey	230−660	x				10−20
eT	26−46	east Turkey	230−1250	x	x	x		60−150
Ca	33−43	Caucasus	230−660	x				20−40
Eg	20−60	Egypt	860−1800			x	x	320−430
SI	24−64	Syria/Iraq/Iran	1000−2200				x	470−500
Zs	47−61	Zagros suture	230−1000	x	x	x		50−90
cA^1	32−84	central Asia	860−2400				x	360−430
cA^2	50−80	central Asia	2000−2560				x	70−70
SA	52−82	Saudi Arabia	760−2000			x	x	340−410
IA^1	62−78	Iran/Afghanistan	230−760	x				50−90
IA^2	65−87	Iran/Afghanistan	660−2000			x	x	430−510
HK	75−90	Hindu Kush	230−1000	x	x	x		70−90
Io	81−141	Indian ocean	300−2400		x	x	x	1170−1470
Ic	81−141	Indian continent	600−2400			x	x	1530−1760
Hi^1	85−126	Himalayas	410−1400		x	x		400−650
Hi^2	86−126	Himalayas	1000−2200				x	250−300
sT	108−118	south Tibet	300−660		x			10−30
My^1	124−141	Myanmar	230−860	x				120−150
My^2	125−141	Myanmar/China	410−1250		x	x		160−280

Table 4.1: Overview of the bodies of positive velocity anomalies within the mantle underneath the Tethyan region, roughly from west to east, as determined from the tomographic BSE-model. For each anomaly is listed here: the great circle trench sections in which it can be seen, its approximate geographical location, the depth interval in which the anomaly is found (between 230-2560 km only), the main position within the mantle, and the approximate volume of the body. The main position within the mantle is roughly divided into *up* = uppermost mantle ($\sim$230-400 km), *tz* = transition zone ($\sim$400-660 km), *lo* = lower mantle ($\sim$660-1100 km), and *dp* = deepest mantle ($\sim$1100-2560 km). The volumes are determined for *all* 141 sections, so the volumes of Io, Ic, My^1 and My^2 will be smaller when considering the first 126 sections only.

4.2.3 Volumes of the anomalies

As discussed above, anomalies Yu, cA^1, cA^2, My^1 and My^2 of Figures 4.4-4.6 are considered not to belong to the 200-Ma Tethyan history of subduction. Therefore, all volumes discussed hereafter will be without the volumes of these anomalies. The volumes of the seismic velocity anomalies in the Tethyan region are plotted vs. the section segments in which they can be seen in Figure 4.9. In Figure 4.10, the total volumes in the section segments 1-126 are plotted vs. the depth intervals in which they are found in the BSE-model. The minimum and maximum volumes for each separate anomaly are given in Table 4.1.
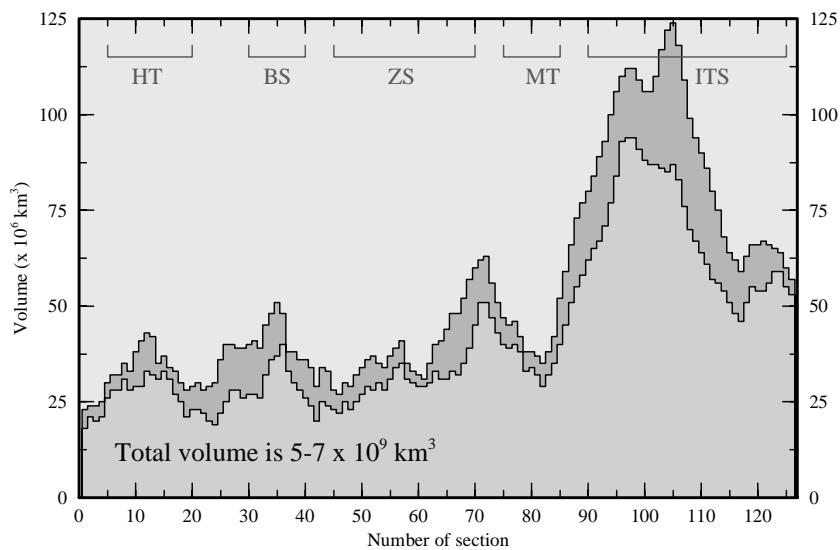

Figure 4.9: Distribution of the total minimum and maximum anomalous volumes in the tomographic BSE-model (230-2560 km depth interval only) per section segment of Figure 4.1. The volumes of anomalies Yu, cA^1, cA^2, My^1 and My^2 are not included. Tectonic features as in Figure 4.11 are given for reference, with HT = Hellenic Trench, BS = Bitlis Suture, ZS = Zagros Suture, MT = Makran Trench, and ITS = Indus-Tsangpo Suture.

In the western part of the Tethyan region, say throughout sections 1-80, many different anomalous volumes can be recognised. The smallest anomalies are found in the upper mantle, of which anomaly wT has a volume of 10-20·10^6 km^3, anomaly Ca of 20-40 ·10^6 km^3, and anomaly IA^1 of 50-90 ·10^6 km^3 only. Anomalies eT, Zs and HK are not only found in the upper mantle, but also in the uppermost part of the lower mantle. These bodies have volumes of 60-150 ·10^6 km^3, 50-90 ·10^6 km^3, and 70-90 ·10^6 km^3, respectively. Anomaly Gr is much larger and extends from the surface down to deep in the lower mantle. It has a volume of ∼680-830 ·10^6 km^3 in total, of which most material is found below 1100 km depth. Even larger are the volumes that are found throughout the whole lower mantle, mainly between ∼1100 and 2000 km depth. From west to east, we have anomalies Eg of 320-430 ·10^6 km^3, SI of 470-500 ·10^6 km^3, SA of 340-410 ·10^6 km^3, and IA^2 of 430-510 ·10^6 km^3.
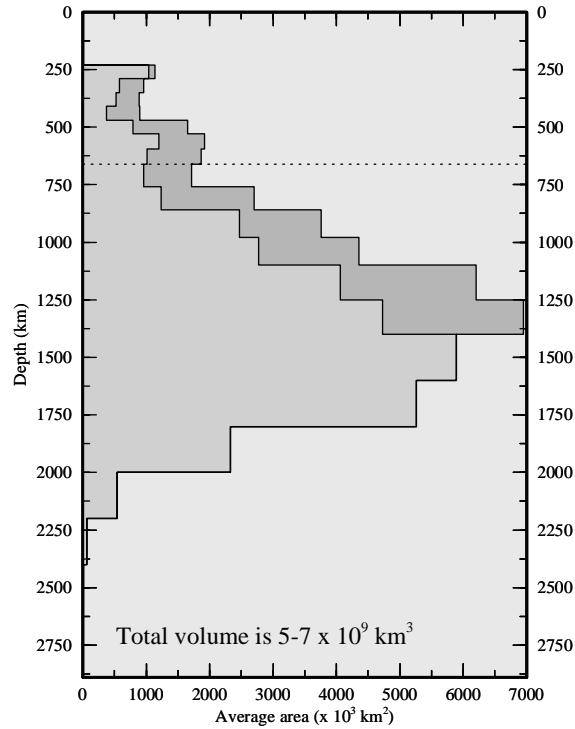
79

Figure 4.10: Distribution throughout the tomographic BSE-model of the total minimum and maximum anomalous volumes from section segments 1-126 of Figure 4.1.

In the eastern part of the Tethyan region, approximately from section 80 onwards, the anomalies are large and mainly found in the lower mantle (Figs. 4.5 and 4.6). Only anomaly sT is restricted to the upper mantle, with a volume of just $10\text{-}30 \cdot 10^6$ km^3. Parts of anomalies Io and Hi^1 are found in the transition zone as well, but their main bodies lie within the lower mantle. Anomaly Hi^1, with a volume of $400\text{-}650 \cdot 10^6$ km^3, extends down to modest depths only. Anomaly Io can be traced down to much larger depths, and its volume is much larger, namely $1170\text{-}1470 \cdot 10^6$ km^3. An even larger volume of $1530\text{-}1760 \cdot 10^6$ km^3 has been determined for anomaly Ic which is found throughout the whole lower mantle as well. In the lower mantle below anomaly Hi^1, we have anomaly Hi^2 with a volume of $250\text{-}300 \cdot 10^6$ km^3.

Summary

Throughout the Tethyan region, a total volume of $5.3\text{-}6.8 \cdot 10^9$ km^3 is found for the positive seismic velocity anomalies that can potentially be associated with subducted Tethyan lithosphere. As a specific regional division of the anomalous volumes requires further knowledge of the tectonic evolution of the area, this will be addressed in Section 4.4.2 instead (e.g. Fig. 4.9, p. 79). The tomographic bulk volumes, for the total Tethyan region as well as for the Aegean/Arabian and Indian regions separately, are given in Table 4.3 (p. 94).

4.3 Subducted oceanic lithosphere

4.3.1 The tectonic reconstruction

To assess the total amount of convergence in the Tethyan region, we use the tectonic reconstruction of ExxonMobil (*Norton*, 1999), a global plate motion model in which the positions through time of all tectonic fragments are given digitally. Because the Mesozoic-Cenozoic closure of the Tethys Ocean has been dominated by the movements of the African, Arabian and Indian plates relative to Eurasia (see also Chapter 2), we calculate the displacements of the continents on the first three plates with respect to the Eurasian plate. In the reconstruction of ExxonMobil, the African plate is proposed not to have experienced internal deformation in the past 200 Myrs. Only from 124 and 112 Ma some very small movements occurred between the western and northeastern part of the African plate. The Arabian plate that we use for the Middle Eastern area has moved together with the African plate until 30 Ma. The motion of Arabia relative to Africa since that time is calculated from the stagepoles of *LePichon and Gaulier* (1988). Further east, the movements of India with respect to Africa are primarily based on the Indian Ocean magnetic anomalies. Finally, the western European and Siberian cratons are assumed to have been a single Eurasian plate during the past 200 Myrs. Both the African plate and the Eurasian plate are coupled to the global plate circuit via the Atlantic magnetic anomalies. Our reconstruction uses the motions of the Eurasian plate with respect to North America from *Lawver et al.* (1990) and *Srivastava and Roest* (1989), while the rotations of Africa vs. North America are based on work from *Gahagan et al.* (1988) and *Klitgord and Schouten* (1986). Motions of intermediate fragments, plate boundary deformation (e.g. the recent trench migration within the Aegean area), and the subduction of back-arc oceanic basins are not taken into account in this first-order analysis. The larger marginal basins will be addressed in Chapter 5. The smaller basins, however, will only have led to shallow subduction of lithosphere which is likely not to be visible below the top 230 km of the tomographic model that is analysed here (see Section 4.2).

Calculating the plate convergence

With the poles of rotation known, we need to specify the trench points at which we want to perform our calculations. The present-day trenches and suture zones in the Tethyan region are intensely deformed by the latest stages of continent-continent collision. Further back in time, the precise configuration of the zone at which the convergence has been accommodated becomes increasingly uncertain. It is plausible that before collision, the subduction zones in the region were situated more to the south, and had less complex configurations. Furthermore, the convergence directions of the major Tethyan oceans have been primarily northward (Section 2.2.2). For a large-scale analysis of the past 200 Myrs, it therefore seems appropriate to take a roughly NW-SE trending line as the zone to evaluate the rates and amounts of convergence at. The exact location of the trench system will not be of major importance for the outcome of the calculations. To represent this trench line, we take the same great circle that was used to define the cross-sections through the tomographic model (Fig. 4.11). Section 31, presently the approximate boundary between the African and Arabian plates, will be used to split up the Aegean and Arabian region. Section 87, roughly aligned with the boundary
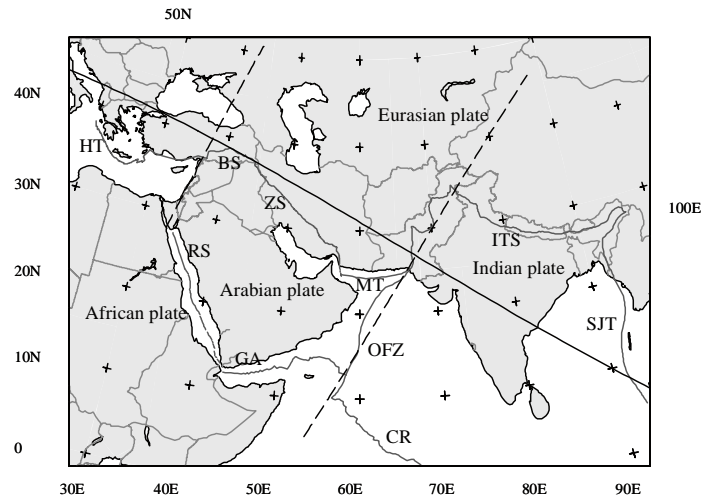
Figure 4.11: Overview of the studied area showing the present-day trenches and highly deformed suture zones. From west to east: HT = Hellenic Trench, BS = Bitlis Suture, ZS = Zagros Suture, MT = Makran Trench, ITS = Indus-Tsangpo Suture, and SJT = Sunda-Java Trench. Also shown are the main active features, i.e. the rifts in the RS = Red Sea and GA = Gulf of Aden, as well as the OFZ = Owen Fracture Zone and CR = Carlsberg Ridge. To assess the total amount of convergence in the Tethyan region, we take the shown great circle (from Fig. 4.1, roughly aligned with the deep positive velocity anomalies within the tomographic model) as trench line. Along the trench, every fifth point at which the calculations are performed is plotted here. The area is divided into an Aegean region (points 1-31), Arabian region (points 31-87), and Indian region (points 87-126).

between the Arabian and Indian plates, is chosen to split up the Arabian and Indian regions. The calculations will be made until section 126 only. East of this section, the history of sub-duction has been significantly affected by the more recent movements of the Australian plate as well, as will be discussed separately in Chapter 6. Keeping the trench system fixed to the Eurasian plate through time, the calculations on convergence are performed at the same points along the great circle that were crossed by the tomographic sections. We take the small circle distance that a particular point has rotated about the total reconstruction pole as the amount of total convergence for that section (Section 3.2.3). The convergence at each point will give an estimate of the average convergence along the trench segment that separates this point from its adjoined points. Subsequently, the surface subducted per region is approximated by multiplying the estimated convergence at each trench section by the width of the segment.

Summary tectonic evolution

In analysing the results, some particular times in the past will be of our major interest. Of fundamental importance is, of course, the opening of the Atlantic and Indian Oceans. Al-though the first rifting events must have taken place around 200 Ma, active spreading along the Atlantic ridges started after 180 Ma. As a result of the opening of the Atlantic Ocean, both Africa (including the Arabian continent still attached to it) and Eurasia separated from

America. India started to move a little with respect to Africa after 180 Ma, somewhat more after 150 Ma, and the first parts of the Indian ridge became active after 120 Ma. Between 124 and 112 Ma, there were some movements between the west and northeast components of the African plate, but these motions will not have had much impact on the amount of convergence. Around 90 Ma, the Central Indian Ridge became active. At 48 Ma, the continental part of Greater India collided into the Eurasian continent. As a result, the Lhasa subduction zone along which the Tethys Ocean had been consumed was closed and became the present Indus-Tsangpo suture zone. In the Aegean area, the Izmir-Ankara arc system (south of Menderes, north of Kirşehir) also closed around this time, and the convergence is assumed to be accommodated along the present Hellenic trench system (south of Turkey) thereafter. At 30 Ma, Arabia started to move slightly with respect to Africa. The Arabian continent collided into Eurasia at 22 Ma.

4.3.2   Subducted plate surface

The total backward convergence calculated along the trench is shown in the upper panel of Figure 4.12. Furthermore, we define the total forward convergence as the convergence between the start of our period of interest (i.e. 200 Ma) and a more recent time in the past. Values for this forward convergence, calculated directly from the backward values, are shown in the lower panel of Figure 4.12. The total surface subducted along the trench system, i.e. the summation of all section values, with time can be seen in Figure 4.13.

The Jurassic has been a relatively quiet period, and most of the Tethyan Oceans must have disappeared since 120 Ma. We find total convergence values varying from 1500 to 3000 km along the trench in the Aegean region, 3000 to 5500 km north of Arabia, and 8500 to 11,000 km between India and Eurasia. The values increase from west to east, as the total poles of rotation are positioned just west of the Tethyan area. The trend between the Aegean and Arabia is almost continuous since the Northeast African and Arabian plates have experienced different motions in the past 30 Myrs only.

Because the top 230 km of the tomographic model has not been taken into account (Section 4.2), it may be important to estimate the convergence accommodated in this depth interval. From a simple geometric point of view, this amount will be 200-400 km - depending on the dip angle - for a 100-km thick plate. In the Aegean region, where the last remnants of Tethyan oceanic lithosphere are being subducted, 400 km of convergence is 20-25% of the 1500-2500 km of convergence along the Hellenic trench system (Points 1-20 in Figure 4.11 and 4.12). For the rest of the Tethyan region, the lithospheric thickness in the present continental collisional setting is likely to be larger than 100 km. For a 200-km thick plate, the amount of convergence that needs to be subtracted from the total value will be 50-100 km only. Throughout the Tethyan region, 100 km is at most 4% of the convergence in the eastern Aegean region and becomes less than 1% of the convergence in the Indian region.

Aegean region   Between 200 and 120 Ma, the flux of material has been very low and only $0.5 \cdot 10^6$ km^2 has been subducted. The rate of subduction has been higher during Late Mesozoic times (1.5-3.5 cm/yr) with a surface of $1.25 \cdot 10^6$ km^2 subducted between 120 and 90 Ma,

the time during which the Pontides arc is assumed to have been active. A similar amount was found for the 90- to 50-Ma period, when active subduction must have been accommodated along the Izmir-Ankara arc. From 50 Ma onwards, the rate of subduction along the present Hellenic arc has decreased further, and only 450 to 600 km has been subducted per section. If subduction has been accommodated along three separate trench systems, we would expect a total subducted surface of about $0.87 \cdot 10^6$ km^2 beneath the Hellenic arc, $1.13 \cdot 10^6$ km^2 beneath the Izmir-Ankara arc, and $1.25 \cdot 10^6$ km^2 beneath the Pontides arc.

Arabian region In the Arabian region, about $2.99 \cdot 10^6$ km^2 of material must have been subducted during the first 200-120 Ma. The most active timespan in this area was that between 120 and 90 Ma. A total of $4.37 \cdot 10^6$ km^2 has been calculated for the lithospheric surface to be subducted in this period, which yields a flux of almost $1.5 \cdot 10^6$ km^2 per 10 Myr. After 90 Ma, the rate of subduction decreased to less than $1 \cdot 10^6$ km^2 per 10 Myr (2-3 cm/yr). From 50 to 20 Ma, the flux was slightly lower than from 20 Ma to present, even though the Arabian continent started its collision into the Eurasian margin around 22 Ma. Between 90 and 20 Ma, a total surface of $\sim 5 \cdot 10^6$ km^2 (1300 to 1900 km per section) has been subducted.

Indian region Until approximately 90 Ma, the amount of convergence along the trench in the Indian region was comparable to that in the Aegean and Arabian region. As the India vs. Africa motion yielded a negative contribution to the convergence at the Eurasian southern margin, the average flux during the first 200- to 120-Ma period has been lower for the Indian region than for the Arabian region. However, the rate of consumption increased after 120 Ma in a similar way as in the Arabian region. By far the most active period for the Indian region was that between 90 and 50 Ma. Within this 40-Myrs timespan, almost 4300 to 4900 km of convergence between India and Eurasia must have been accommodated along each trench section (a total of over $10 \cdot 10^6$ km^2). This yields an approximate rate of convergence of about 10-12 cm/yr. Although the $\sim$50-Ma continental collision must have had a large effect on the subduction process, the flux of material decreased only little after that moment.

Summary

The total lithospheric surface subducted along the Tethyan trench system in the past 200 Myrs is found to be $40 \cdot 10^6$ km^2, of which $4 \cdot 10^6$ km^2 within the Aegean, $14 \cdot 10^6$ km^2 in the Arabian, and $22 \cdot 10^6$ km^2 in the Indian regions. The values for the subducted plate surface are shown in the second column of Table 4.3 (p. 94). The calculated amounts of subducted material can be considered as minimum values, as active oceanic spreading might have added to the amount of convergence. The surface likely to be accommodated down to 230 km depth is about 2-4% from the total surface subducted in the Aegean/Arabian region, and at most 1% in the Indian region. Although these values have not been accounted for in the present section, we will further discuss the implications of incorporating these in Section 4.4.
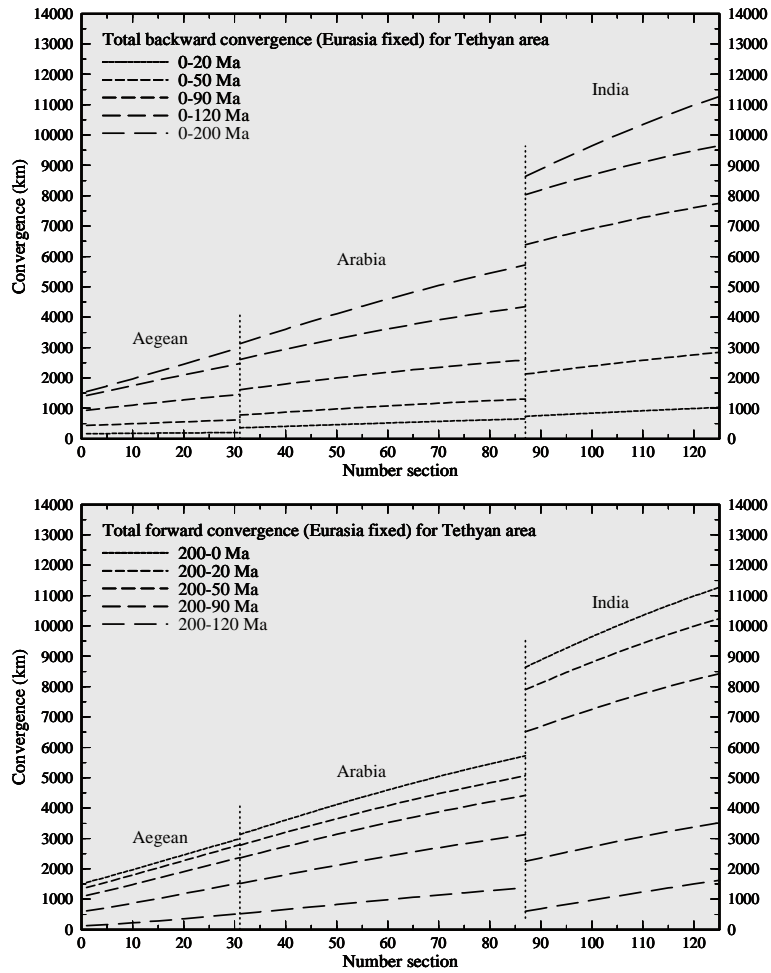
Figure 4.12: Total convergence per section for the Aegean, Arabian and Indian trench systems, calculated along the great circle of Figure 4.11 and with the Eurasian plate held fixed. Backward values, defined as the amount of convergence between present-day and the indicated time in the past, are shown in the upper panel; Forward values, defined as the amount of convergence between 200 Ma and the indicated time, in the lower panel.
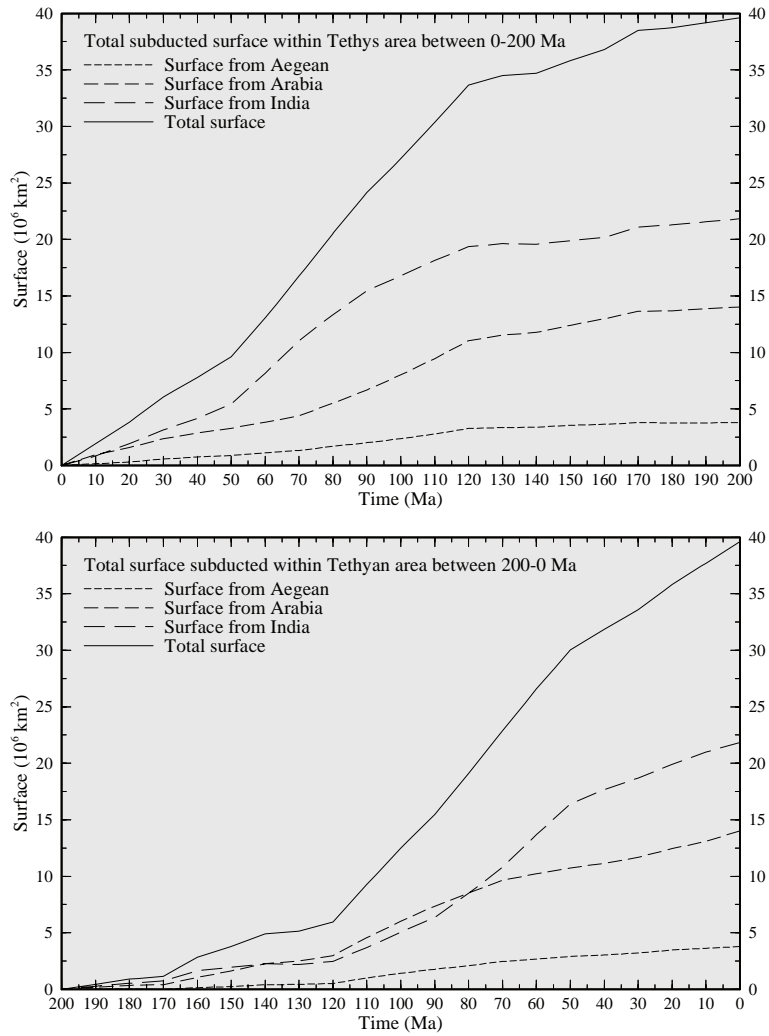
Figure 4.13: Total subducted surface within the Tethyan area. In the upper panel, the total backward values are shown, i.e. the amount of subduction between present-day and the indicated time in the past. The total forward values are shown in the lower panel, giving the surface subducted since 200 Ma until the indicated time. Values for the Aegean, Arabian and Indian regions are given separately as well. For each section, the total convergence from Figure 4.12 is multiplied with the width of the trench segment. The total subducted surface is determined by summation of all section values.

4.3.3   Initial volume of subducting plate

We first determine the initial thermal volumes that can be associated with the surface of subducted material calculated in the previous section. The initial thermal thickness of a subducting plate is a function of its lithospheric age (Section 3.3.1). Because the subducted Tethyan lithosphere is lost at the surface today, we have no direct information on the lithospheric ages upon its subduction. We will therefore reconstruct here simplified scenarios for the variation of the age of the subducted Tethyan lithosphere (Fig. 4.15). Although the ages upon subduction can vary significantly with time, we will use the 200-Ma average to approximate the age of the subducted lithosphere as a whole. The various oceanic basins, and the associated averages, will be considered separately in Chapter 5.

Lithospheric spreading scenarios

Two possible end-member scenarios for the spreading history of the Tethyan Oceans will be considered. Whereas both scenarios are not very realistic, and simplify the complicated evolution of the area to a 2D situation, they do provide upper and lower bounds on the thermal volumes associated with the lithospheric plate surface calculated from the continent-continent motions only.
Lower bound: In one scenario, all oceanic spreading systems remain active until the ridges are eventually subducted (left side of Fig. 4.14). This scenario will lead to relatively young ages of the subducting lithosphere, and thus results in minimum thermal volumes for the plate surface calculated from the continent motions. In the following, the scenario with ongoing lithospheric spreading until ridge subduction, as well as the associated thermal volumes, will be denoted by *A*.
Upper bound: In the other scenario, spreading within the oceanic basins stops at the very moment the plate starts subducting (right in Fig. 4.14). The relatively old lithospheric ages upon subduction will result in large thermal perturbations, and therefore give maximum volumes for the plate surface. The scenario in which spreading ceases immediately after initiation of subduction of the plate will be referred to as *B*.

As illustrated in Figure 4.14, the plate surface calculated from the continent-continent motions alone *is* the total Tethyan lithosphere subducted for spreading scenario *B* (right panel). On the contrary, the relatively small thermal volumes determined for scenario *A* are implicitly assumed to be lower limits of the total values (left panel): If active spreading ridges *have* existed between the already converging continents, as assumed with scenario *A*, this spreading will have added to the amount of subduction. In scenario *A*, the actual thermal volumes are unknown, but will be larger than those for the calculated plate surface only. As the total volumes for scenario *A* may be similar to the relatively large volumes for spreading scenario *B*, it can be difficult to distinguish between the two scenarios in some cases.

Average age of Tethyan lithosphere upon subduction

In the Aegean/Arabian region, spreading within the Neo-Tethys commenced with the rifting of the Iranian blocks from Gondwana around 270 Ma according to our reconstruction. The
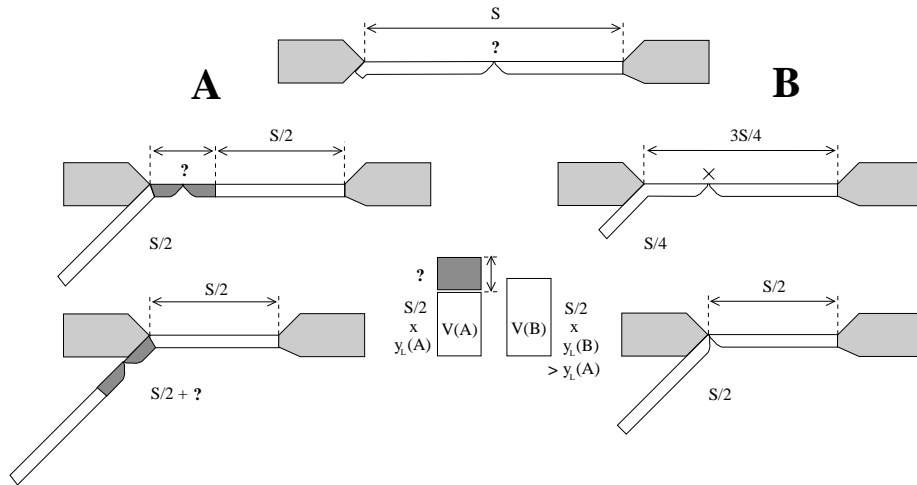
Figure 4.14: Two possible end-member scenarios for the spreading history of the Tethyan Oceans: *Scenario A* in which the spreading system remains active until the ridge is subducted, and *scenario B* in which spreading stops at the very moment the plate starts subducting. As the average lithospheric thickness y_L of A is less than $y_L(B)$, the thermal volume predicted from the continent-continent motions alone will be smaller for A than for B as well. If an active spreading ridge *has* existed between the already converging continents, this spreading will have added to the total amount of subduction in scenario A, and the actual thermal volume of A may be similar or larger to that of B.

Neo-Tethys started to subduct after collision of these blocks with Eurasia around 200 Ma, and active spreading in the Neo-Tethys must have stopped with the subduction of its ridge around 80 Ma at the latest. The Neo-Tethys disappeared with the Arabia-Eurasia collision at ~20 Ma.

In *spreading scenario A*, the age of the subducting oceanic lithosphere is assumed to be 70 Ma at initiation of subduction at 200 Ma, to linearly decrease to 0 Ma when the ridge subducted at 80 Ma, and to increase again until the oldest parts of the oceanic lithosphere were aged 250 Ma at 20 Ma. The average age of the subducting oceanic lithosphere in this scenario was 65 Ma. In *spreading scenario B*, the age of the fossil Neo-Tethyan ridge was already 120 Ma at the moment of subduction, and the average age of the subducting lithosphere during the whole timespan was 125 Ma.

In the Indian region, the Neo-Tethys opened around 220 Ma. It was subducted from 140 Ma onwards, i.e. after collision of Afghanistan and south Tibet with Eurasia, and disappeared completely with the India-Eurasia collision around 50 Ma. The Neo-Tethys must have stopped spreading with the subduction of its ridge around 80 Ma at the latest. For the period prior to 140 Ma, we need to include the lithospheric age of the southern Paleo-Tethys that was totally subducted after collision of Afghanistan and south Tibet with Eurasia only. The Paleo-Tethys was a Paleozoic ocean that started spreading around 270 Ma, with the separation of North Tibet from Gondwana. For simplicity, we here assume that the Paleo-Tethyan
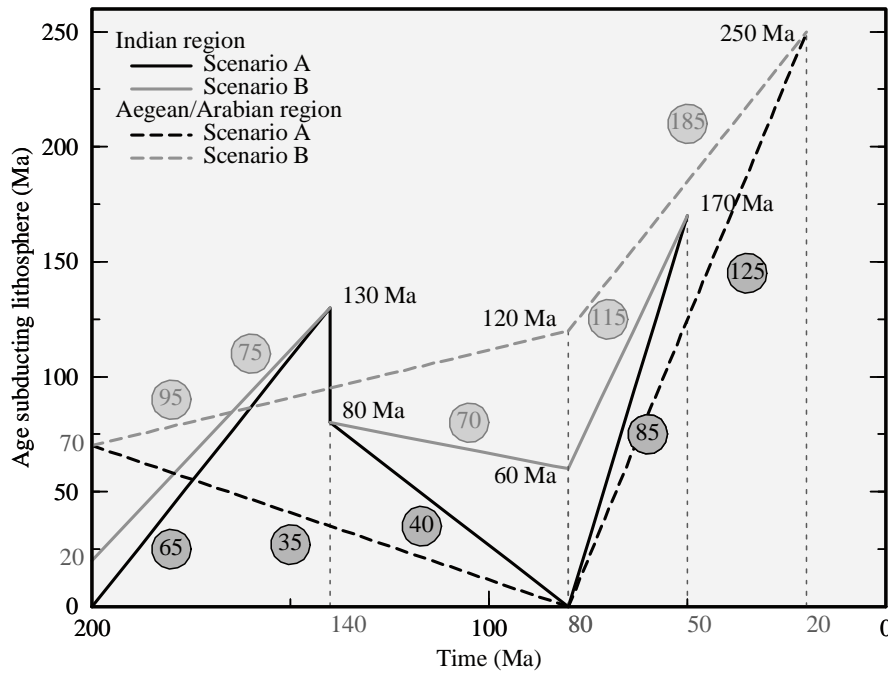
Figure 4.15: The variation of the age of the Tethyan lithosphere upon subduction for two end-member spreading scenarios (see p. 87). The encircled numbers approximate the average ages of the separate oceanic domains. Aegean/Arabian region: Subduction of the Neo-Tethys (average age in the past 200 Ma is 65-125 Ma). Indian region: Subduction of the Paleo-Tethys before 140 Ma and the Neo-Tethys thereafter (average age in the past 200 Ma is 60-80 Ma).

ridge subducted at 200 Ma. Being more specific about the exact timing of ridge subduction is difficult and will not change the results significantly.

In *spreading scenario A*, the age of the subducting oceanic lithosphere would be 80 Ma at initiation of subduction at 140 Ma, linearly decreases to 0 Ma when the ridge subducts at 80 Ma, and increases again until the oldest part of the oceanic lithosphere is aged 170 Ma at 50 Ma. Assuming that the ridge kept spreading until its subduction, the age of the subducting Paleo-Tethyan lithosphere varied from 0 Ma at 200 Ma to a final 130 Ma at 140 Ma. The 200-Ma average for the age of the subducted oceanic lithosphere was 60 Ma.

In *spreading scenario B*, both the Paleo-Tethys and the Neo-Tethys are assumed to have stopped spreading at the moment they started subducting underneath Eurasia. If spreading within the Paleo-Tethys ceased when the Neo-Tethys opened at 220 Ma, the ages upon subduction between 200 and 140 Ma varied from 20 to 130 Ma instead. As for the Neo-Tethys, the age of the fossil ridge was already 60 Ma when it subducted at 140 Ma. For this scenario, the 200-Ma average age of the subducting oceanic lithosphere during the whole timespan was 80 Ma.

Average thickness of subducting plates

As discussed above, the seismic anomalous volumes were bounded by wave-speed perturbations that can be associated with a temperature perturbation of -100°C. To account for ∼30% amplitude damping in the tomographic inversion (Section 3.1), we will determine the initial lithospheric thickness of the subducting oceanic plates as the depth of the isotherm that differs -143°C with the ambient mantle temperature in the plate cooling model of *Parsons and Sclater* (1977) (see Section 3.3.1).

The average age of the subducting oceanic lithosphere is assumed to have been 60-80 Ma in the Indian region, depending on the spreading scenario. This 60-80 Ma is associated with a lithospheric thickness of 94-102 km. In the Aegean/Arabian region, an average age of 65-125 Ma was calculated for the subducting oceanic lithosphere, which corresponds to a lithospheric thickness of 96-108 km. As a lower limit (*spreading scenario A*) for the total thermal thickness of the subducting lithosphere during the past 200 Myr, we will therefore use a value of 95 km for both regions. As an upper limit (*spreading scenario B*), a thickness of 105 km will be used for the Indian region, and 110 km for the Aegean/Arabian region. See Table 4.2 for an overview.

Initial thermal volumes of subducting plates

The volumes subducted per region are approximated by multiplying the estimated surface per region with the appropriate initial thicknesses of the oceanic lithosphere, i.e. 95-110 km for the Aegean/Arabian and 95-105 km for the Indian region. We find an initial lithospheric volume to be subducted in the Aegean/Arabian region of $1.7\text{-}2.0 \cdot 10^9$ km^3, and $2.1\text{-}2.3 \cdot 10^9$ km^3 for the Indian region, which is a total volume of $3.8\text{-}4.3 \cdot 10^9$ km^3 for the whole Tethyan region. The initial thermal volumes of the subducted lithospheric surface, shown in the third column of Table 4.3 (p. 94), will be referred to as V_i hereafter.

	Surface ($\cdot 10^6$ km^2)	Age (Ma)	Thickness (km)	$c_1(200)$ *Undefo.*	$c_2(200)$ *Doubled*	$c_3(200)$ *Tripled*
Aeg/Arab	17.81	65 / 125	95 / 110	2.0 / 2.2	1.6 / 1.6	1.3 / 1.3
Indian	21.83	60 / 80	95 / 105	2.0 / 2.1	1.6 / 1.6	1.3 / 1.3

Table 4.2: Overview of the values used to quantify the initial and predicted present thermal volumes of the surface subducted in the Aegean/Arabian and Indian regions: In the left three columns: The subducted surface of oceanic lithosphere, the average lithospheric age upon subduction, and the initial thermal thickness of oceanic lithosphere of this age. The last three columns give the thermal factor with which the initial thermal volumes will be multiplied to approximate the present thermal volumes of the subducted lithosphere: $c_1(200)$ for slabs that did not thicken during subduction, $c_2(200)$ for slabs that thickened by a factor of 2, and $c_3(200)$ for slabs that thickened by a factor of 3. See text for details on the assumptions made.

4.3.4   Present volume of subducted slabs

During the subduction of the oceanic lithosphere, the slab and mantle temperatures will have been affected in such a way that the present thermal volume V_p associated with the slab differs a particular factor from the initial volume V_i, that is to say

$$V_p = c(t) \cdot V_i$$

with t the time since initiation of subduction. The thermal factor $c(t)$ is determined on the basis of numerical modelling results for the thermal evolution of a subduction zone. By multiplying the total initial volume of the subducted Tethyan lithosphere derived from the tectonic reconstruction with $c(t)$, we can approximate the present thermal volume associated with these slabs.

Time-dependence of the thermal signature

A thermo-kinematic modelling procedure (*De Jonge et al.*, 1994) is used to estimate the thermal signature that can be associated with a specific volume of subducted material (Section 3.3.2). From the 2D subduction zone models, we determine the area in which the temperatures differ from the unperturbed mantle temperature at that depth with at least -143°C. The ratio of these integrated thermal anomalies and the initial volume of the subducted slab (V_p/V_i) will be used to approximate the thermal factor $c(t)$.

Figure 4.16 shows the variation of $c(t)$, during a 200-Myr timespan, for a subduction scenario in which oceanic lithosphere of 3000-km length is placed into the mantle instantaneously at $t = 0$. These values will be denoted $c_1(t)$ for 'single' lithosphere in the following, as these slabs kept their plate-like geometry during subduction. As discussed extensively in Section 3.3.3, using values of $c_1(t)$ for such an instantaneous subduction scenario will generally *over*estimate the final volumes V_p for slowly, still actively subducting slabs with 10% at most. After subduction has ceased, which is actually the case for the larger part of the Tethyan region, the values of $c_1(t)$ will *under*estimate the volumes V_p instead: Within the shown timespan, this will be at most 10-30%, depending on the lithospheric age, at $t = 200$ Myr. The effects of the exact values of parameters like thermal conductivity, thermal expansion, and the dip angle on the results for V_p were found to be relatively small.

As slabs can fold and thicken by a factor of 2-3 when they penetrate into the lower mantle (e.g. *Gaherty and Hager*, 1994; *Christensen*, 1996, see Section 3.3.3), the volumes V_p predicted with the model-derived $c_1(t)$ for undeformed, i.e. unthickened, lithosphere are likely to represent *upper-bound* values. We therefore consider pure shear thickening of the slab material with a factor of 2 and 3, and quantify the values of $c(t)$ for the instantaneous subduction of a 'doubled' and 'tripled' lithosphere analogous to those for undeformed lithosphere. The thermal factors will be referred to as $c_2(t)$ and $c_3(t)$ for slabs thickened by a factor of 2 and 3, respectively.

The instantaneous thermal factors for thickened slabs will only little underestimate the volumes for slowly subducted slabs: At most 10% at $t = 200$ Myr for thickening by a factor of 2, and a few percent at most for a factor of 3 thickening. Because the residence time and amount of thickening in the upper mantle are unknown, we will use the values for $c_2(t)$ and

$c_3(t)$ for the *total* slab volumes, which will give us a *lower-bound* for the present thermal volumes. If more deformation is required, this is thus implicitly assumed to have been caused by simple buckling or flattening of the slabs. See Section 3.3.3 for a more detailed discussion.
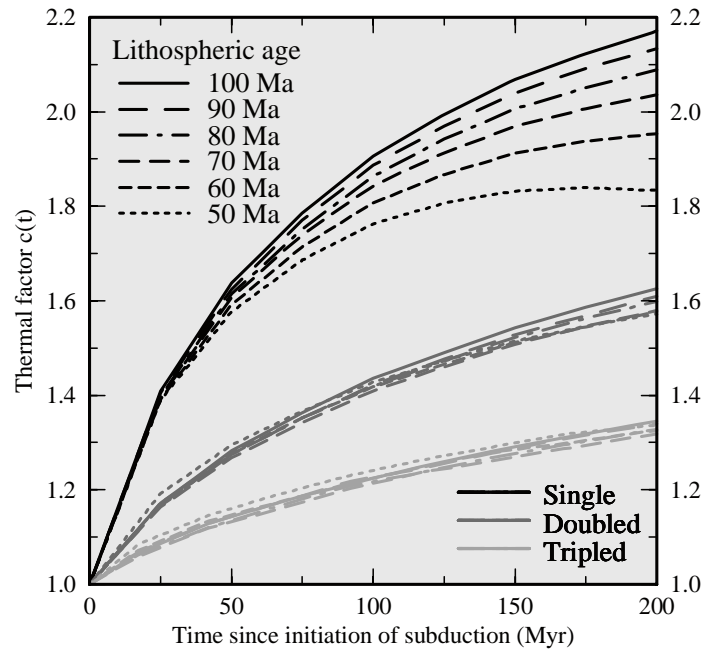

Figure 4.16: The thermal factor $c(t)$ with which the initial thermal volumes will be multiplied to approximate the present thermal volumes of the subducted lithosphere: $c_1(t)$ for 'single' cases (black lines) in which the slabs kept their plate-like geometry, and $c_2(t)$ and $c_3(t)$ for 'doubled' and 'tripled' cases (grey lines), respectively, for lithosphere that is assumed to have experienced instantaneous pure shear thickening by a factor of 2 and 3. See text for further details and assumptions made.

Present thermal volumes of subducted slabs

In this first-order analysis, we will use the values of $c(t)$ at $t = 200$ Myr after initiation of subduction, c.q. 200 Myr before present. The assumption of an instantaneous subduction of all material at 200 Ma implies that all slabs within the Tethyan region are assumed to have been subducted as a single plate within the same region. Its is more likely, however, that the material has been subducted as separate slabs and in different parts of the mantle: Continental collisions and ridge subduction have affected the geometry of slabs and may have caused the material to subduct in new, unperturbed mantle regions. Within the Indian region, subduction of the Neo-Tethys only started at 140 Ma, after the south Tibet vs. Eurasia collision, which would lead to a factor $c(140)$ of 1.9-2.0 for the undeformed material instead. Material subducted after ridge subduction around 80 Ma may be associated with a factor

$c(80)$ of 1.7-1.8, assuming no slab deformation, only. Finally, the most recent collisions of the Arabian and Indian continents with Eurasia may have caused the subducted slab to break off. The material subducted after slab detachment will require even lower values for $c(t)$.

The values of $c(200)$ thus provide an upper limit for the thermal factor $c(t)$, and for the predicted thermal volumes accordingly. The rate of change, however, is largest immediately after subduction and decreases with increasing time. For the trends shown in Figure 4.16, the values of $c(100)$ are approximately 10% smaller than $c(200)$. The effects of tectonic processes like continental collision and ridge subduction on the present thermal volumes of the subducted material will be addressed in Chapter 5.

For the Aegean/Arabian region investigated here, with an average age of the subducted lithosphere of 65-125 Ma, the thermal factor $c_1(200)$ is 2.0-2.2 (see fourth column of Table 4.2). For the Indian region, the average 60-80 Ma is associated with values for $c_1(200)$ of 2.0-2.1. A thermal factor $c_2(200)$ of 1.6 for both the Aegean/Arabian and Indian region is needed if all slabs have doubled in the lower mantle, and a factor $c_3(200)$ of 1.3 if the material has thickened by a factor of 3 (values given in Table 4.2 as well). For spreading scenario A, yielding the youngest ages, we may somewhat underestimate the values of $c_1(200)$ and $c_2(200)$, especially for the Aegean/Arabian region where the convergence rates have been relatively low (see Section 3.3.3).

If we multiply the initial thermal volumes with the appropriate thermal factors, we arrive at present thermal volumes of $3.4\text{-}4.3{\cdot}10^9$ km^3 for the Aegean/Arabian region, and $4.0\text{-}4.8{\cdot}10^9$ km^3 for the Indian region, for slabs that did not thicken during subduction. For the whole Tethyan region, we thus find a total $7.4\text{-}9.0{\cdot}10^9$ km^3 for the present thermal volumes of the subducted material. For slabs that have thickened by a factor of 2, we arrive at a total present volume of $6.0\text{-}6.9{\cdot}10^9$ km^3, which is about 75-80% of the volume predicted for unthickened lithosphere only. A present thermal volume of $5.0\text{-}5.7{\cdot}10^9$ km^3 is found for slabs that have thickened by a factor of 3, which is about 60-70% of that for unthickened lithosphere. The thermal volumes, for the Aegean/Arabian and Indian regions separately as well as for the Tethyan region in total, are displayed in the fourth column of Table 4.3 (p. 94).

4.4   Comparison and discussion

Now we have determined the volumes associated with the Mesozoic-Cenozoic history of subduction within the Tethyan region, we can make a first comparison between the amount of subducted material predicted from the reconstruction (V_p) and that inferred from seismic tomography (V_t). In the following, the ratio of the tomographic volumes and the predicted thermal volumes will be referred to as the *T/P-ratio*, thus

$$\textit{T/P-ratio} = V_t/V_p$$

and will provide us with a useful measure in analysing the results.

4.4.1 Volumes for total Tethyan region

For the Tethyan region as a whole, the T/P-ratios are given in Table 4.3 (upper panel, right-most column) and Figure 4.17. For undeformed slabs, the ratios are found to be about 0.7-0.9 in spreading scenario *A*, and 0.6-0.8 in scenario *B*. This means that the predicted thermal volumes are significantly larger than the tomographic volumes, and will be even larger when accounting for the uncertainties in our thermal modelling. Assuming slab thickening by a factor of 2, the T/P-ratios are as large as 0.9-1.1 for spreading scenario *A* and 0.8-1.0 for scenario *B*. For slabs thickened by a factor of 3, the T/P-ratios would be 1.1-1.4 and 0.9-1.2, respectively. These ratios indicate that the predicted volumes are comparable to the tomographic volumes, or somewhat smaller. These results suggest that most Tethyan slabs have thickened in the mantle by a factor of 2 at least. This is indeed quite likely in view of the large amount of subducted lithosphere, which simply cannot have kept a plate-like geometry in the mantle, and the bulk volumes of the seismic anomalies.

Total region	$V_{t(omo)}$ ($\cdot 10^9$ km^3)	$S_{s(ubducted)}$ ($\cdot 10^6$ km^2)	$V_{i(nitial)}$ ($\cdot 10^9$ km^3)		$V_{p(redicted)}$ ($\cdot 10^9$ km^3)		$V_{t(omo)}/V_{p(redicted)}$ (T/P-ratio)	
			A	*B*	*A*	*B*	*A*	*B*
Undefo.	5.32-6.78	39.64	3.76	/ 4.25	7.41	/ 9.04	$0.72 - 0.92$	/ $0.59 - 0.75$
Doubled					5.95	/ 6.86	$0.90 - 1.14$	/ $0.78 - 0.99$
Tripled					4.97	/ 5.65	$1.07 - 1.37$	/ $0.94 - 1.20$
Aegean/Arabian region								
Undefo.	2.44-3.08	17.81	1.69	/ 1.96	3.37	/ 4.25	$0.73 - 0.92$	/ $0.58 - 0.73$
Doubled					2.67	/ 3.19	$0.91 - 1.15$	/ $0.77 - 0.97$
Tripled					2.23	/ 2.63	$1.09 - 1.38$	/ $0.93 - 1.17$
Indian region								
Undefo.	2.88-3.70	21.83	2.07	/ 2.29	4.04	/ 4.79	$0.71 - 0.92$	/ $0.60 - 0.77$
Doubled					3.28	/ 3.67	$0.88 - 1.13$	/ $0.79 - 1.01$
Tripled					2.74	/ 3.03	$1.05 - 1.35$	/ $0.95 - 1.22$

Table 4.3: Comparison of the seismic anomalous volumes inferred from the tomographic model and the thermal volumes predicted from the tectonic reconstruction for the total Tethyan region (upper panel), and the Aegean/Arabian and Indian regions separately (middle and lower panels). *First row* (Undefo.): Results for a subduction process where the slabs kept their plate-like geometry. *Second row* (Doubled) and *third row* (Tripled): Values based on the assumption that the slabs have thickened by a factor of 2 and 3, respectively. *Column 1*: Minimum and maximum volumes (V_t) determined from the tomographic model (Section 4.2). *Column 2*: Subducted plate surface (S_s) calculated from the tectonic reconstruction (Section 4.3.2). *Column 3*: Estimated initial thermal volumes (V_i) of the plate surface (Section 4.3.3), calculated for spreading scenarios *A* and *B* (see p. 87). *Column 4*: Predicted present thermal volumes (V_p) of the initial volumes (Section 4.3.4). *Column 5*: T/P-ratio $\equiv V_t/V_p$. The values for the initial lithospheric thickness and factor $c_1(t)$ used to obtain V_i and V_p from S_s are given in Table 4.2. The predicted volumes for slabs that have thickened in the mantle, calculated with the appropriate factors from Table 4.2, are shown in Figure 4.17.
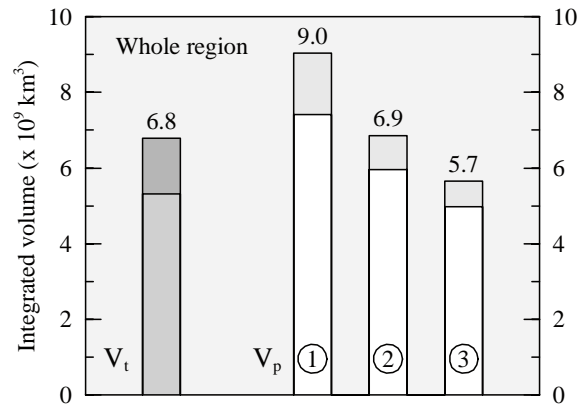
Figure 4.17: Comparison of the seismic anomalous volumes inferred from the tomographic model and the thermal volumes predicted from the tectonic reconstruction for the total Tethyan region. *Left*: Tomographic minimum and maximum volumes V_t (1st column Table 4.3). *Right*: Predicted present thermal volumes V_p (4th column Table 4.3), for spreading scenario *A* (lowerbound) and scenario *B* (upperbound). The values for V_p are predicted for slabs that (1) kept their plate-like geometry, (2) thickened by a factor of 2, and (3) thickened by a factor of 3. The calculations for undeformed slabs can be found in Table 4.3, the factors necessary to perform the calculations for thickened slabs in Table 4.2.

4.4.2   Volumes for Aegean/Arabian and Indian region

In Figure 4.18 it can be seen that both the tomographic volumes and predicted thermal volumes gradually increase along the Tethyan trench system. Moreover, the trend shows a clear, abrupt jump towards the Indian volumes. To see whether the different convergence histories of the Aegean/Arabian and Indian regions, discussed in Section 4.3, are reflected in the volume, location and geometry of the subducted material, we will divide the volumes in regional subvolumes. Whereas the subducted surfaces calculated from the tectonic reconstruction have been separated already (Section 4.3), the tomographic volumes will need to be investigated in more detail here.

Regional division tomographic volumes

Indian region: When computing the subducted surface from the reconstruction, section 87 was chosen to split up the Arabian and Indian regions. The Owen Fracture Zone, the marked boundary between the Arabian and Indian plates, roughly follows this section (Fig. 4.11, p. 82). As the fracture is associated with the strike-slip motion of the Indian plate relative to the African-Arabian plate during the Cenozoic, we expect that the large-scale motion has influenced the process of subduction and thus the resulting geometry of the subducted material. Indeed, the boundary between anomalies Io/Ic and SA/IA [2] is almost parallel to section 87 (Fig. 4.6, p. 75), although parts of their volumes are found west of it (see also Fig. 4.18). The transition between the Arabian and Indian regions is thus relatively easy to make, and

anomalies Io, Ic, Hi^2, Hi^1 and sT will be considered as volumes belonging to the Indian region. Although HK is largely situated west of section 87, it is considered as Indian anomaly as well because it is located underneath the Indus-Tsangpo Suture. The seismic anomalies in the Indian region have a total volume of 2.9-3.7·10^9 km^3 (first column Table 4.3).

Aegean/Arabian region: In the reconstruction, we have split up the Aegean and Arabian regions at section 31, presently the approximate boundary between the African and Arabian plates (Fig. 4.11). For the seismic anomalous volumes, such a strict division does not seem to be very useful. Since the Arabian and African plates have moved together until 30 Ma, and have not experienced the same large relative motions as the Arabian and Indian plates have, the tomographic volumes associated with subduction prior to that time may be more or less continuous along the trench system. Indeed, the boundary between the anomalies in this area is not as clear as the boundary between the Arabian and Indian regions (Fig. 4.18). For example, anomaly eT and Eg (Figs. 4.4-4.6, pp. 73-4.6) can be found in the lower mantle beneath the Arabian region, but a significant part of their upper mantle volumes can be found underneath the Aegean region. We therefore prefer to keep the volumes belonging to the Aegean and Arabian region, i.e. anomalies Gr, wT, eT, Ca, Eg, SI, Zs, SA, IA^1 and IA^2, together. In the Aegean/Arabian region, the seismic anomalies have a total volume of 2.4-3.1·10^9 km^3 (Table 4.3).

Comparison of tomographic and predicted volumes

In the middle and lower panels of Table 4.3 (rightmost column), as well as in Figure 4.19, the T/P-ratios for separate Aegean/Arabian and Indian regions are shown. For undeformed slabs, we find a ratio of 0.7-0.9 for spreading scenario *A*, in both regions. For scenario *B*, the T/P-ratios are 0.6-0.7 and 0.6-0.8 in the Aegean/Arabian and Indian region, respectively. Especially for the Aegean/Arabian region, the thermal volumes may be somewhat underestimated, and thus the T/P-ratios overestimated accordingly. Assuming doubling of the subducted lithosphere, the values of T/P-ratio increase to 0.9-1.2 and 0.9-1.1 for spreading scenario *A*, and to 0.8-1.0 in both regions for scenario *B*. For slabs thickened by a factor of 3, the ratios are 1.1-1.4 for scenario *A*, and 0.9-1.2 for scenario *B*.

In all three cases, and in both spreading scenarios, the T/P-ratios of the total volumes for the Tethyan region are found to be practically similar to those for the two separate subregions. Once more, this is evidence for at least a factor of 2 thickening of the subducted Tethyan slabs.
The predicted thermal volumes will be somewhat smaller when subtracting the convergence accommodated down to 230 km depth (Section 4.3): The values for the Indian region will be less than 1% smaller and thus not significantly affect the T/P-ratios. In the Aegean/Arabian region, the volumes are at most 4% smaller, and the T/P-ratio 4% larger. This somewhat reduces the similarity between both regions for spreading scenario *A*, but slightly increases the similarity for scenario *B*. We will further elaborate on this in Chapter 5.
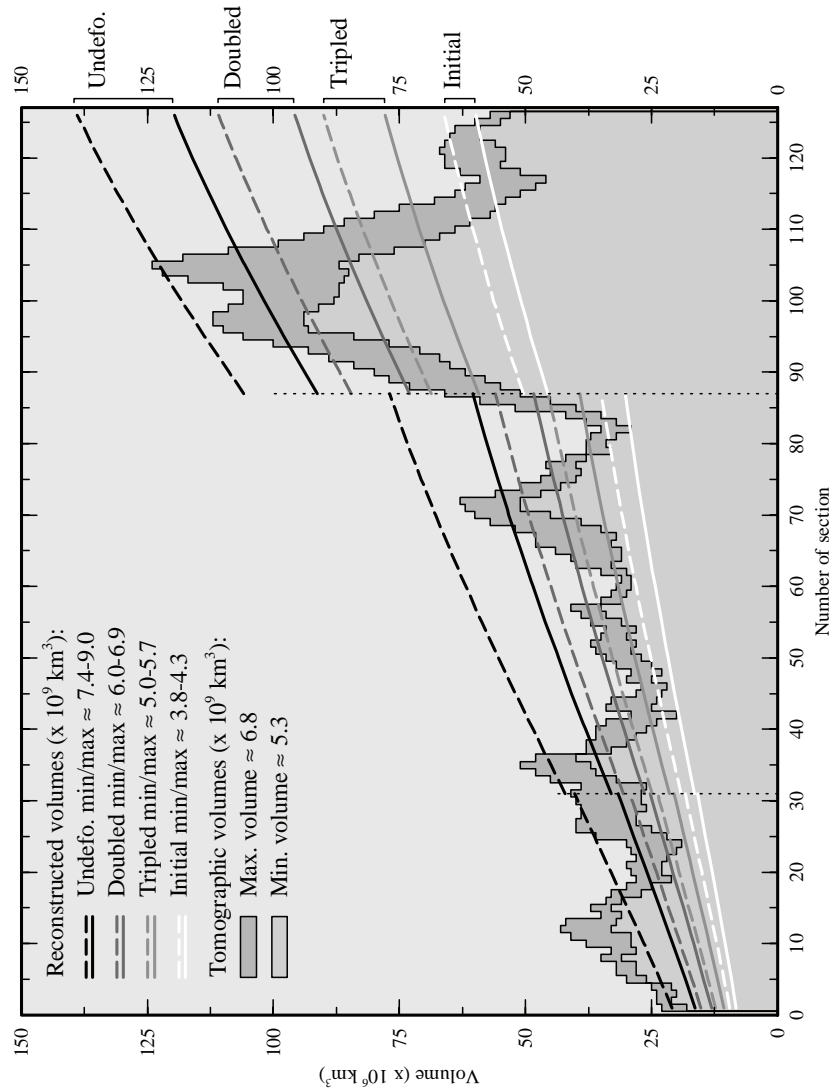
Figure 4.18: Comparison of the seismic anomalous volumes inferred from the tomographic model and the thermal volumes predicted from the tectonic reconstruction throughout the Tethyan region. The distribution of the total minimum and maximum tomographic volumes is similar to that in Figure 4.9. The predictions of the initial and present thermal volumes of subducted lithosphere are derived from the calculated amount of convergence displayed in Figure 4.12. From the present thermal volumes: *Undefo.* = Results for a subduction process where the slabs kept their plate-like geometry. *Doubled* = Values based on the assumption that the slabs have thickened by a factor of 2. *Tripled* = Values based on the assumption that the slabs have thickened by a factor of 3.

Figure 4.19: As in Figure 4.17, but now separately for the Aegean/Arabian and Indian regions.

4.4.3   Location and depth of the subducted material

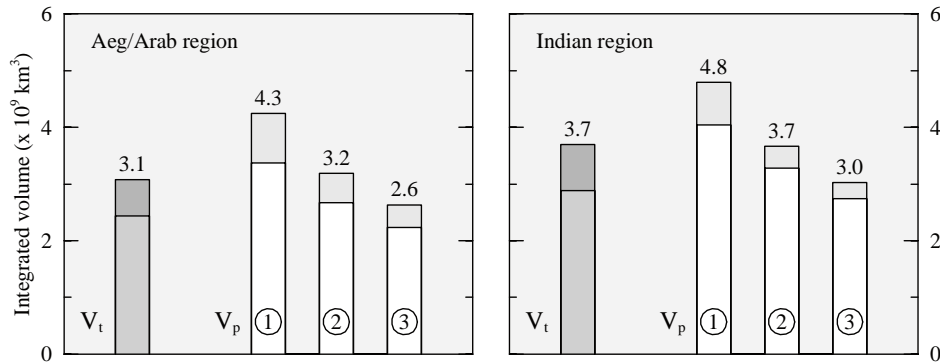To better couple the volumes of subducted material predicted from the tectonic reconstruction to the seismic anomalous volumes, we need to give an estimate of the expected geographical location and present-day depth of the subducted material.

Geographical distribution

We expect the most recently subducted lithosphere underneath the present subduction zones and youngest sutures. Because reconstructions generally assume northward subduction of these slabs, the material can also be found somewhat north of these regions. For the material subducted further back in time, we already discussed that the trench system has been situated more towards the south before the continent-continent collisions (Section 4.3). Moreover, the absolute motions of all continents involved are primarily directed north to northeast since at least 60 Ma (*Müller et al.*, 1993; *Duncan and Richards*, 1991). We therefore expect that the material subducted prior to that time can be found south to southwest of the present trenches and most recent sutures in the region. The upper mantle anomalies wT, Ca, Zs, IA[1], HK and sT, as well as the larger part of the lower mantle anomalies Gr, eT, SI, IA[2], Hi[1] and Hi[2], are all situated underneath the present-day positions of these sutures and trenches, or just north of it (Figs. 4.4-4.6). On the contrary, anomalies Eg, SA, Io and Ic, as well as parts of the lower mantle anomalies of Gr and SI, are situated more to the southwest.

In the distribution of tomographic volumes along the trench system in Figure 4.18 some remarkable peaks can be noticed. The most western maximum is anomaly Gr beneath the Hellenic trench (Fig. 4.11, section 1-20). Because active subduction is ongoing and the slab will have experienced relatively little internal deformation yet, the thermal volumes for undeformed lithosphere seem to adequately predict the tomographic volumes in this segment and may actually be even smaller (Section 3.3.3). The two middle peaks result from the anomalous bodies of Eg and SI (section 20-40) and SA and IA[2] (section 60-80) in the 600-1100 km depth interval (Fig. 4.5). Especially in the Indian region, the peak around section 100 is

striking. Anomaly Ic, and the deep mantle part of Io, extend along the whole Indian trench system, and even further east towards the Indonesian archipelago (Fig. 4.6). Anomalies Hi[1] and Hi[2], however, fade away east of section 115, and also anomaly Io has its major body in the western part of the Indian region (Fig. 4.5-4.6). The drop in total volumes per section is almost as clear as the one on the western side of the Indian region that is associated with the large strike-slip motion of the Indian plate in the Cenozoic. This suggests that a comparable geodynamic process has occurred in the eastern part, and separated the Indian region from Southeast Asia. The distribution of the separate volumes will be discussed in more detail in Chapter 5.
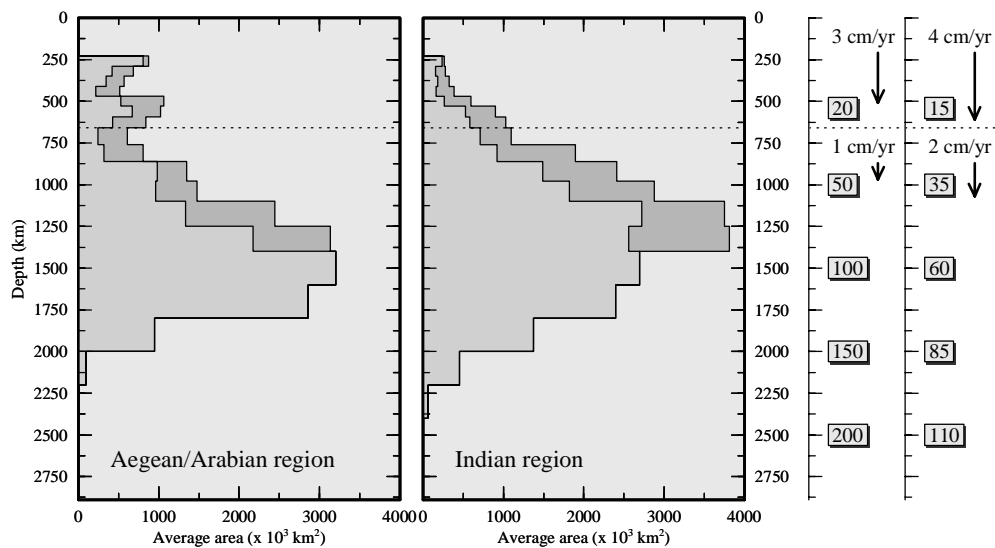

Figure 4.20: As Figure 4.10, but now for the anomalies in the Aegean/Arabian and Indian region separately. Rightmost panel: The approximate time (Myrs) needed for subducted material to reach the shown depths when sinking with a rate of 3-4 cm/yr in the upper mantle and 1-2 cm/yr in the lower mantle. The integrated volumes below 1400 km depth are similar for both regions. Between 800-1400 km depth, the Aegean/Arabian volumes are only 2/3 of the Indian volumes.

Depth distribution

As for the depth in the mantle reached, the bulk of the lower mantle anomalies in the Tethyan region can be found between ∼800 and 1800 km depth. However, more material can be seen down to about 2200 km depth. The bulk volumes below 1400 km depth are similar for both the Aegean/Arabian and Indian region (Fig. 4.20), namely $1.4 \cdot 10^9$ km^3. Between ∼800 and 1400 km depth, however, the volume of $0.8\text{-}1.3 \cdot 10^9$ km^3 found in the Aegean/Arabian region is only two-third of the $1.3\text{-}2.0 \cdot 10^9$ km^3 in the Indian region.

In the upper mantle, estimates of the vertical sinking velocities of slabs are comparable to plate convergence rates (e.g. *Bunge et al.*, 1998; *Becker et al.*, 1999; *Bercovici et al.*, 2000).

When slabs enter the lower mantle, the large viscosity contrast with the upper mantle causes the sinking velocities to be reduced significantly. Estimates of sinking rates for the slabs through the lower mantle typically range from 1 to 3 cm/yr (*Bunge et al.*, 1998; *Lithgow-Bertelloni and Richards*, 1998; *Han and Gurnis*, 1999; *Steinberger*, 2000), although slabs were found to sink faster (rates up to 4 cm/yr) in regions with abundant subduction in the same area (*Steinberger*, 2000).

Prior to 150 Ma, the relative velocities between the converging continents have been very small only (Fig. 4.13). For the material that has subducted since 150 Ma, a modest sinking rate of 3 cm/yr in the upper mantle and 1 cm/yr in the lower mantle will be enough to reach the ~2000-km depths of the anomalies found in the tomographic model (rightmost panel of Fig. 4.20). In that case, the difference in Aegean/Arabian and Indian volumes between 800 and 1400 km depth could be associated with an increased amount of subduction in the Indian region between about 95 and 35 Myrs ago. Indeed, the amount of subduction between 90 and 20 Ma, and especially between 90 and 50 Ma, has been significantly higher for the Indian region than for the Aegean/Arabian region (Fig. 4.13).

In periods of fast subduction, sinking rates may be higher, and the above-mentioned depths can be reached in a shorter timespan. With sinking rates of 4 cm/yr in the upper mantle and 2 cm/yr in the lower mantle, however, a 2000-km depth is reached after 85 Myrs already (Fig. 4.20). In our case, this would require the material subducted prior to 85 Ma to have flattened above this depth. This would be in accordance with suggested stratification in the deep mantle, in which the bottom 1000 km of the mantle is proposed to be compositionally distinct from the upper two-thirds of the mantle, and fossil subducted slabs would collect at the interface between the two domains (*Kellogg et al.*, 1999; *Van der Hilst and Kárason*, 1999). However, the 800 to 1400 km depth interval would be associated with a sinking timespan of only 25-55 Myrs, which cannot be as readily explained from the tectonic reconstruction as the larger 35-95 Myrs timespan for sinking rates in the mantle of 3 cm/yr and 1 cm/yr (see Fig. 4.13).

4.4.4 Additional spreading and convergence in the Tethyan region

In this study, we have predicted the thermal volumes of the subducted material associated with the motion of the African, Arabian and Indian continents with respect to Eurasia, for two spreading scenarios for the Tethyan oceanic lithosphere (p. 87).

If lithospheric thickening is taken into account, the thermal volumes predicted for spreading scenario *B* are approximately similar to, or slightly more than, the tomographic volumes. Whereas the spreading ridges are assumed to be inactive during subduction in scenario *B*, rifting of intermediate continental fragments as well as back-arc spreading could affect the volumes in this scenario. Because the predicted thermal volumes are similar to the tomographic volumes, however, rifting and back-arc spreading cannot have led to a significant amount of additional subducted material here.

If active spreading ridges did exist between the already converging continents, as assumed with scenario *A*, this spreading will have added to the total amount of subduction. Indeed, the volumes for scenario *A* leave room for an additional subducted volume of ~0.2-0.3 times the tomographic volume, i.e. about $1\text{-}2{\cdot}10^9$ km^3, depending on the amount of thickening. In the case of lithospheric doubling, the additional thermal volume of $1{\cdot}10^9$ km^3 must origi-

nate from an initial volume that is a factor 1.6 smaller (Table 4.2). Subsequently, this initial $0.6 \cdot 10^9$ km^3 can be divided by a minimum 95-km thickness and related to a plate surface of $7 \cdot 10^6$ km^2. For lithospheric tripling, the initial volume is a factor 1.3 smaller than the additional $2 \cdot 10^9$ km^3. This initial $1.5 \cdot 10^9$ km^3 can be related to a plate surface of $16 \cdot 10^6$ km^2. To give an estimate of the expected spreading velocities, we assume that the creation of this surface was evenly distributed along a ridge system with the same width of the Tethyan trench system of Figure 4.11. For this $\sim$7000 km length, the 7-$16 \cdot 10^6$ km^2 will need $\sim$1000-2000 km of spreading per unit width. In a 100-Myr timespan, this requires an average total spreading rate of 1-2 cm/yr, which is in agreement with presently observed values.

4.5   Summary and conclusions

To analyse the history of subduction in the Tethyan region, we have predicted the present thermal signature of the subducted material associated with the movements of the African, Arabian and Indian plates relative to Eurasia since 200 Ma. These volumes have been compared to the seismic anomalies that can be determined from tomographic images of the mantle underneath the area. In this study, we found that the volumes, locations and depths of the tomographic anomalies can be well explained by the thermal volumes predicted from these first-order motions.

We expect the most recently subducted material to be situated underneath the present subduction zones and known sutures, or just north of it. The material subducted further back in time is expected to be found south to southwest of that area. Indeed, the geographical locations of the several tomographic anomalies are in accordance with this expectation. With sinking rates of 3 cm/yr in the upper mantle and 1 cm/yr in the lower mantle, a 150-Myr timespan will be enough for the subducted material to have reached the $\sim$2000-km depths of the anomalies found in the tomographic model. The difference in Aegean/Arabian and Indian volumes between 800 and 1400 km depth might be related to the relatively large amount of subduction in the Indian region between 90 and 20 Ma.

Assuming subduction of the Tethyan slabs at 200 Ma, we have predicted an upper limit of the present thermal volume of the subducted material for both a scenario allowing ongoing spreading within the lithosphere during its subduction, and for a scenario in which oceanic spreading stops at the onset of subduction. Without allowing for any slab thickening, the thermal volumes are found to be at least 10% larger than the maximum tomographic volumes. When slab thickening by a factor of 2 or 3 is taken into account, however, the predicted volumes are comparable to the tomographic volumes or somewhat smaller. For the Tethyan region as a whole, as well as for the Aegean/Arabian and Indian region separately, our results indicate that most Tethyan slabs must have thickened in the mantle by at least a factor of 2.

For a scenario without additional spreading, the predicted volumes are approximately similar to the tomographic volumes if the slabs have thickened in the mantle. This suggests that the rifting of intermediate continental fragments and back-arc spreading cannot have led to a significant amount of additional subducted material. For a scenario including active spreading during subduction, the volumes leave room for an additional subducted volume of $\sim$0.2-0.3 times the tomographic volume, depending on the amount of thickening. For a wide ridge

system and a 100-Myr timespan, this would require an average total spreading rate of 1-2 cm/yr.

The simplified method used to approximate the present thermal signature of the subducted Tethyan lithosphere necessitates a cautious interpretation of the results. More specified predictions of the thermal volumes are clearly required to investigate the Tethyan evolution in more detail. Nevertheless, the present results show that our approach does enable us to evaluate the bulk volumes associated with the large-scale history of subduction in the Tethyan region as a whole.

Chapter 5

Evolution-related aspects of subduction in the Tethyan region

5.1   Introduction

In the previous chapter, we have analysed the history of subduction within the Tethyan region as deduced from the motions of the African-Arabian and Indian plates relative to Eurasia in the past 200 Ma. From the amount of convergence between the continents we predicted the present thermal volumes associated with the subducted material, and compared these to the seismic anomalous volumes in the tomographic images of the mantle underneath the area. We found that, to first-order, the volumes and distribution of the tomographic anomalies were in agreement with the predicted volumes.

Here we will investigate the Mesozoic-Cenozoic subduction within the Tethyan region in more detail. Whereas we have only used the digitised reconstruction of *Norton* (1999) to study the Tethyan region as a whole, other plate tectonic reconstructions of the area, e.g. those of *Dercourt et al.* (1993), *Şengör and Natal'in* (1996) and *Stampfli and Borel* (2002, 2004), generally agree on the first-order motions explored so far. However, no overall consensus has been achieved on, for example, the movements of various continental fragments, nor on the spreading and subduction history of the intermediate oceanic basins. Possible back-arc spreading and the subsequent subduction of the lithosphere created may have increased the amount of subducted material, and also lithospheric spreading within the Neo-Tethys during its subduction may have added to the total convergence significantly. Therefore, the total volume of subducted material in the Tethyan region is likely to be larger than calculated from the African-Eurasian convergence alone, and probably different for the various tectonic reconstructions.

Moreover, so far we have only considered the volume of subducted material as a whole, and second-order effects on the subduction processes have not been taken into account. For example, continental collisions may have led to slab break-off, and the subduction of a mid-oceanic ridge system may have created a completely slabless or apparent window in the thermal volumes of the subducted material. To analyse such processes, we will isolate the appropriate

subvolumes, for which the average ages and residence times in the mantle will generally be different from that of the total volume comprehending these subvolumes. Furthermore, the possible distribution of the slab volumes in the mantle will be affected by the absolute motion of the plates since subduction. We expect that incorporation of these various aspects in our comparison with tomography will enable use to better understand the geodynamic evolution of the Tethyan region.

5.2 Tectonic evolution

We briefly summarise here the aspects of the tectonic evolution that are expected to have had major implications for the specific subdivision, location and geometry of the lithosphere subducted within the Tethyan region. We address other reconstructions than that of *Norton* (1999), hereafter referred to as the ExxonMobil reconstruction, where relevant.

Separate Paleo-Tethyan volume

In the Indian region, the Paleo-Tethys closed when the Afghanistan and south Tibet blocks collided with Eurasia. This happened around Late Triassic (thus before 200 Ma) according to *Stampfli and Borel* (2002, 2004), but in other reconstructions, this closure has been proposed for Late Jurassic - Early Cretaceous times (∼140 Ma) instead (ExxonMobil, *Dercourt et al.*, 1993; *Şengör and Natal'in*, 1996). The subducted Paleo-Tethyan lithosphere may be visible as a separate volume in the tomographic images today.

The approximate direction of subduction is likely to be reflected in the present-day location of the subducted oceanic lithosphere. Some reconstructions propose the Paleo-Tethyan oceanic lithosphere to have been subducted northward underneath Eurasia (ExxonMobil, *Dercourt et al.*, 1993), whereas others have suggested a southward subduction of the Paleo-Tethys underneath south Tibet and Afghanistan (*Şengör and Natal'in*, 1996). In the reconstruction of *Stampfli and Borel* (2002, 2004), subduction occurs in a more or less northeast to eastward direction instead.

Slab volumes after ridge subduction

Because the morphology of the subducted material may have been affected by ridge subduction, we will investigate three broadly accepted subduction scenarios for the Tethyan lithosphere and its spreading ridges.

The two end-member *spreading* scenarios for the oceanic lithosphere discussed in the previous chapter (p. 87) are considered for all three subduction scenarios: *Spreading scenario A* in which all oceanic spreading systems are assumed to remain active until the ridges are subducted, and *spreading scenario B* in which spreading within the oceanic basins stops at the very moment the plates start subducting. We aim at testing the tectonic reconstructions underlying the various scenarios as they are, i.e. without an a-priori judgement of their quality.

Subduction scenario I   Subduction scenario I (Fig. 5.1, upper panel) is the most simple, straightforward scenario, e.g. proposed by ExxonMobil and by *Şengör and Natal'in* (1996)

for the subduction of the Neo-Tethys in the Indian region. This is basically the scenario we have discussed in Chapter 4. In this scenario, all displacement between the converging African/Arabian/Indian and Eurasian continents, as well as the possible additional spreading in between them, is accommodated along the same trench system at the Eurasian margin. For such a scenario we would expect all Neo-Tethyan slab material to be subducted relatively close to the present Zagros/Indus-Tsangpo Sutures, even when ridge subduction has affected the morphology of the material.

Subduction scenario II   Subduction scenario II (Fig. 5.1, middle panel) is often proposed for the Arabian region (e.g. *Dercourt et al.*, 1993; *Şeng ör and Natal'in*, 1996) to explain the ∼80 Ma emplacement time of the Oman ophiolites on the Arabian continental margin. In this scenario, the ridge of the Neo-Tethys resided very close to the Arabian continent. Subsequently, during a short period of intra-oceanic subduction, the spreading ridge was obducted onto Arabia. Because the distance between the ridge and the Arabian continent is proposed to have been small, the amount of lithosphere subducted at this location will be small as well. Basically the entire Neo-Tethyan lithosphere is assumed to be subducted underneath the Eurasian margin, as in scenario I.

Subduction scenario III   Subduction scenario III (Fig. 5.1, lower panel) is proposed by *Stampfli and Borel* (2002, 2004) for both the Arabian and Indian region. This scenario assumes an early (∼140-120 Ma) subduction of the Neo-Tethyan ridge to have triggered the opening of two distinct back-arc basins within the Eurasian margin: The Semail Ocean in the Middle East and the Spongtang Ocean in the Indian region. In the Arabian region, the Neo-Tethys had disappeared completely with the obduction of the Semail spreading ridge onto the Arabian peninsula at ∼80 Ma, after which the Semail Ocean subducted northward underneath Eurasia again. The exact closure times of the Neo-Tethys and Spongtang Oceans in the Indian region are not so clear, but are probably around 65 and 50 Ma, respectively.
Because spreading within the back-arc oceans occured at the direct expense of the Neo-Tethys, this will have added certainly to the amount of subduction as calculated from the converging continents alone. Furthermore, we expect two or three separate slab volumes for this scenario, namely 1) a Neo-Tethyan slab part subducted beneath the Eurasian margin, 2) the remaining Neo-Tethyan slab subducted near the Arabian and Indian continental margins, and 3) the slab of the back-arc ocean subducted underneath Eurasia again.

Slab break-off after Cenozoic continental collisions

There is general agreement that the continental part of Greater India collided with the Eurasian continent in Early Eocene times, and the collision of Arabia with Eurasia took place in the Early Miocene. We will here use the accretion times of ExxonMobil, namely ∼48 Ma and ∼22 Ma, respectively. We will investigate whether these continental collisions have caused the subducting slabs to break-off and, if so, at what time. If slab detachment occurred, the present-day depth and location of the slab material in the lower mantle must be in accordance with the time of break-off. Also the volumes, both of the slab broken off and the lithosphere still attached to the surface, may help us at this point.
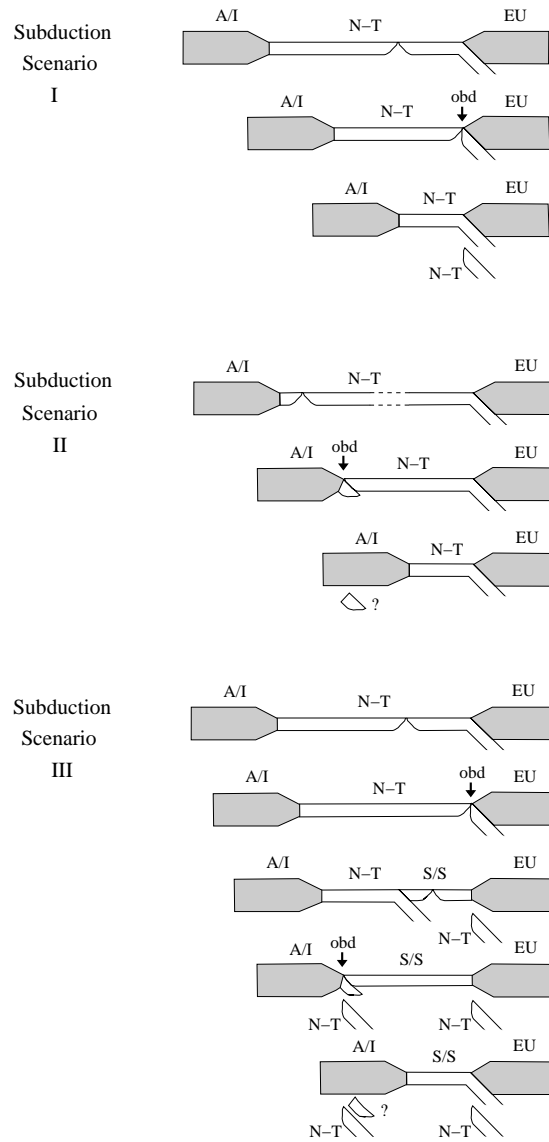
Figure 5.1: Three subduction scenarios for the Neo-Tethys: **Subduction scenario I**: All Neo-Tethyan subduction is accommodated along one single trench system at the Eurasian margin. **Subduction scenario II**: The Neo-Tethyan ridge is emplaced onto the Arabian/Indian margin, whereas basically all Neo-Tethyan lithosphere is subducted along the same Eurasian trench system. **Subduction scenario III**: Neo-Tethyan ridge subduction underneath Eurasia is followed by the opening of a Semail/Spongtang back-arc basin. After this oceanic basin has completely overridden the Neo-Tethys, and its ridge is obducted onto the Arabian/Indian margin, its lithosphere is subducted below Eurasia. *Key*: A/I = Arabian/Indian continent, EU = Eurasian continent, N-T = Neo-Tethys Ocean, S/S = Semail/Spongtang Ocean, and obd = ridge obduction.

5.3   Absolute motion

Whereas the predicted division of the volumes associated with the subducted lithosphere will depend on the assumed subduction scenario, the actual distribution of the slab material is a function of the absolute motion of the plates since the time of subduction. By plate motion in an absolute reference frame we generally mean the motion relative to the underlying mantle.

In a hotspot reference frame, it is assumed that the distance between a group of individual hotspots remains nearly constant over long periods of time such that the hotspot tracks give us the direction of absolute plate motion (e.g. *Morgan*, 1971; *Gordon and Jurdy*, 1986; *O'Connor and le Roex*, 1992; *Müller et al.*, 1993). There is increasing evidence, however, that hotspots are not very stable with respect to one another, and therefore to the lower mantle (e.g. *Tarduno and Gee*, 1995; *Norton*, 2000; *Torsvik et al.*, 2002; *O'Neill et al.*, 2003).

To account for the present uncertainties in defining absolute plate motion, we will here consider the geographical locations of the Arabian/Indian and Eurasian continental margins in three different reference frames: One in which the Eurasian craton is held fixed (EU), a fixed hotspot reference frame based on *Duncan and Richards* (1991) for the past 30 Ma and *Müller et al.* (1993) prior to that time (HS), and the hotspot reference frame of *O'Neill et al.* (2003) based on the motion of hotspots in the Indian Ocean (MHS). In Figures 5.2-5.4, the positions of the continental blocks that formed the margins considered are shown at a few relevant times since 120 Ma (EU, HS) and 65 Ma (MHS) until 20 Ma.

As can be seen in Figures 5.2 and 5.3, the locations of the Arabian/Indian and Eurasian continental margins plotted in the EU frame significantly differ from those given in the HS frame: Around 80 Ma, the positions in the HS frame are ~4-5° south of those plotted with Eurasia fixed. As the HS frame is uncertain prior to 84 Ma, the remarkably northern location of the Eurasian margin at 120 Ma (lowerright panel Fig. 5.3) may not be correct. The actual position of Eurasia around 120 Ma was suggested to have been much further south than in the HS frame, and to have remained stationary until 90 Ma, by *Torsvik et al.* (2002).

In the MHS frame, India is placed much further north and west than in fixed hotspot models as HS. During the past 65 Myr, the locations of the Arabian/Indian and Eurasian continental margins in this MHS frame have similar or even higher latitudes than those in a EU frame (Fig. 5.4 vs. 5.2). Moreover, the continents are positioned much further west in the MHS frame than in both the HS and EU frame. The large westward shift was needed to fit the moving hotspots, but could not be independently constrained and was suggested by the authors not to be as robust as the northward shift.

In the following, we want to compare the positions of the various tomographic anomalies with the past locations of the trench systems. We have therefore also plotted in Figures 5.2-5.4 the tomographic anomalous bodies associated with subducted Tethyan lithosphere from Figures 4.5 and 4.6 (pp. 74 and 75). The lowermost mantle anomalies underneath the Tethyan region (~1100-2560 km) are likely to be associated with Mesozoic subduction, whereas the Cenozoic evolution will probably be reflected in the more shallow anomalies (~660-1100 km). The upper mantle anomalies of Figure 4.4 (p. 73) can be primarily associated with the most recent phases of subduction only.
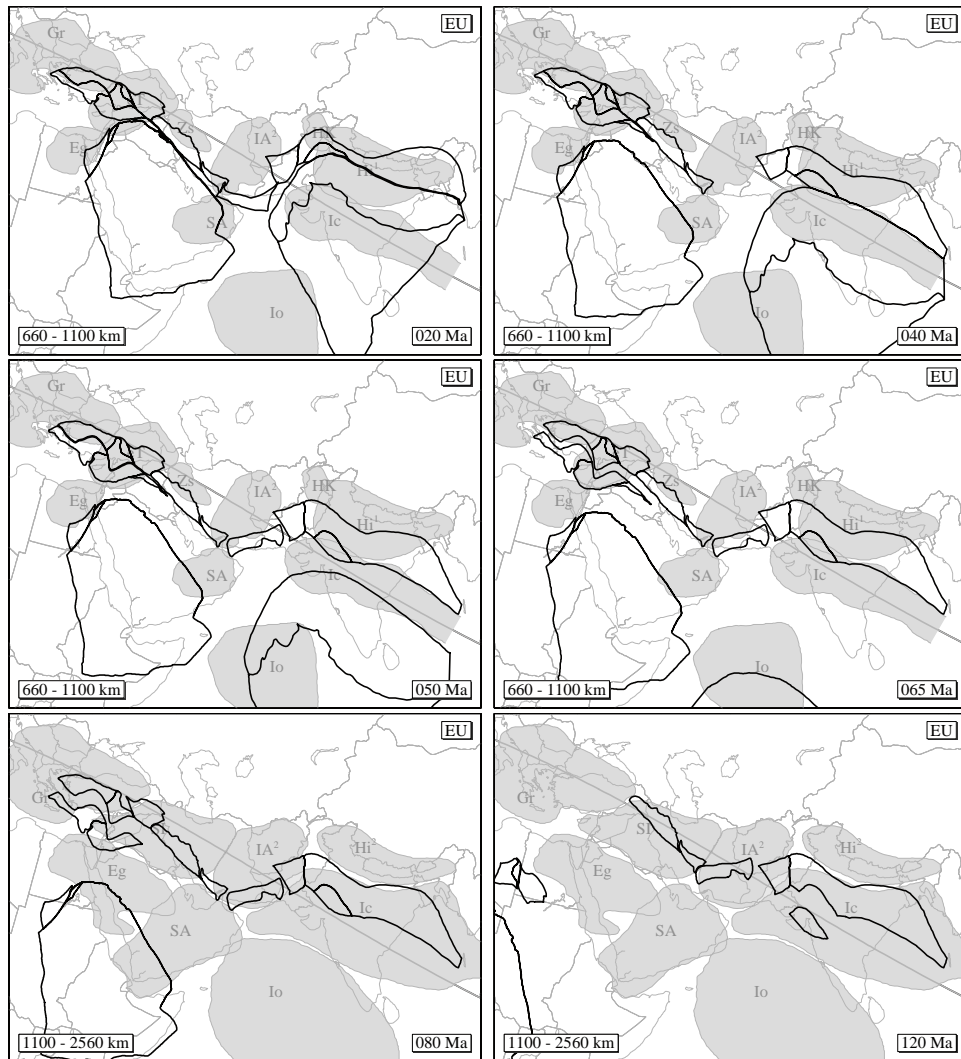
Figure 5.2: Geographical locations of the continental blocks that form the Eurasian and Arabian/Indian margins from ExxonMobil with Eurasia fixed, shown together with the tomographic anomalous bodies associated with Tethyan subducted lithosphere in this study. Present coastlines and political borders are given for reference only. *Top panel*: Positions at 20 and 40 Ma with tomographic anomalies between 660-1100 km depth; *Middle panel*: Positions at 50 and 65 Ma with anomalies between 660-1100 km depth; *Lower panel*: Positions at 80 and 120 Ma with anomalies between 1100-2600 km depth. For clarity, only the southernmost fragments on the Eurasian margin are shown (cf. Figs. 2.2 and 2.7-2.8, pp. 17-29).

Figure 5.3: Geographical locations of the Eurasian and Arabian/Indian continental margins as in Figure 5.2, but now plotted in the hotspot reference frame of *Duncan and Richards* (1991) at 20 Ma and of *Müller et al.* (1993) prior to that time. Note that the positions at 120 Ma are uncertain.
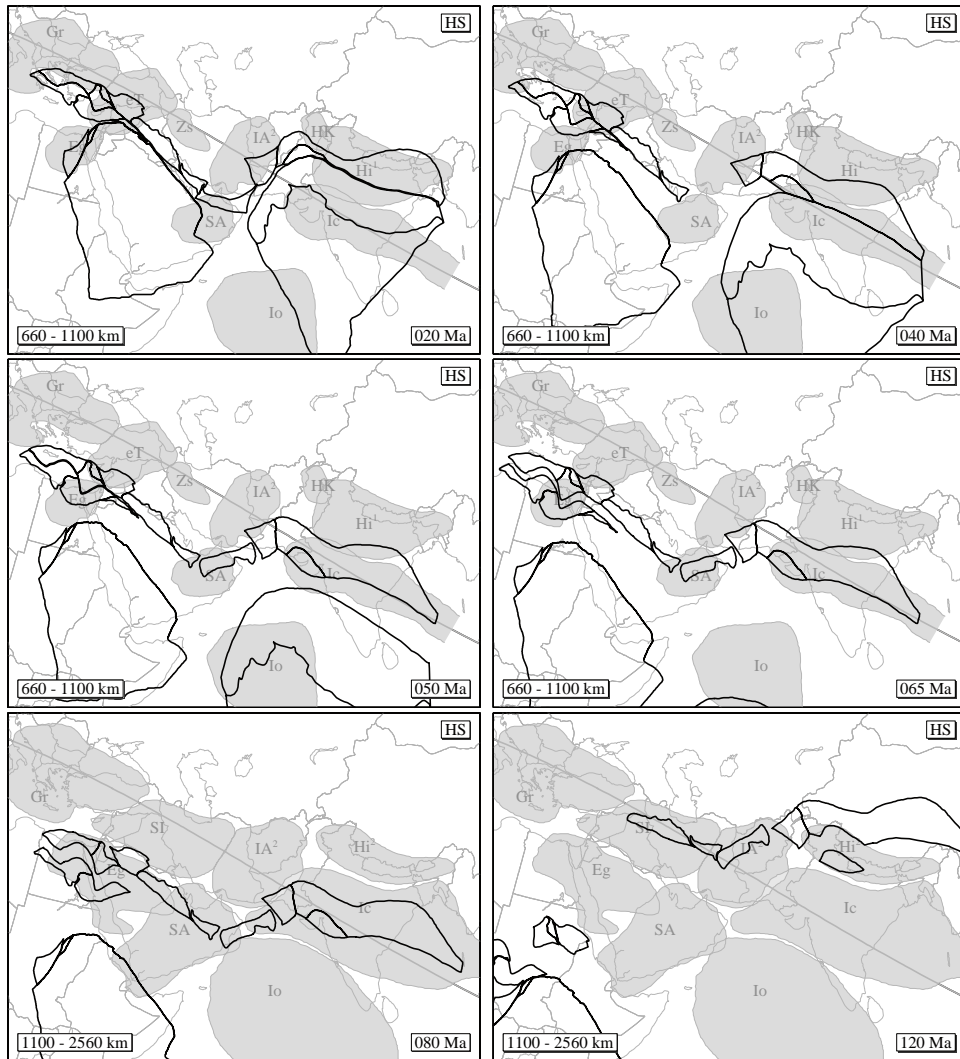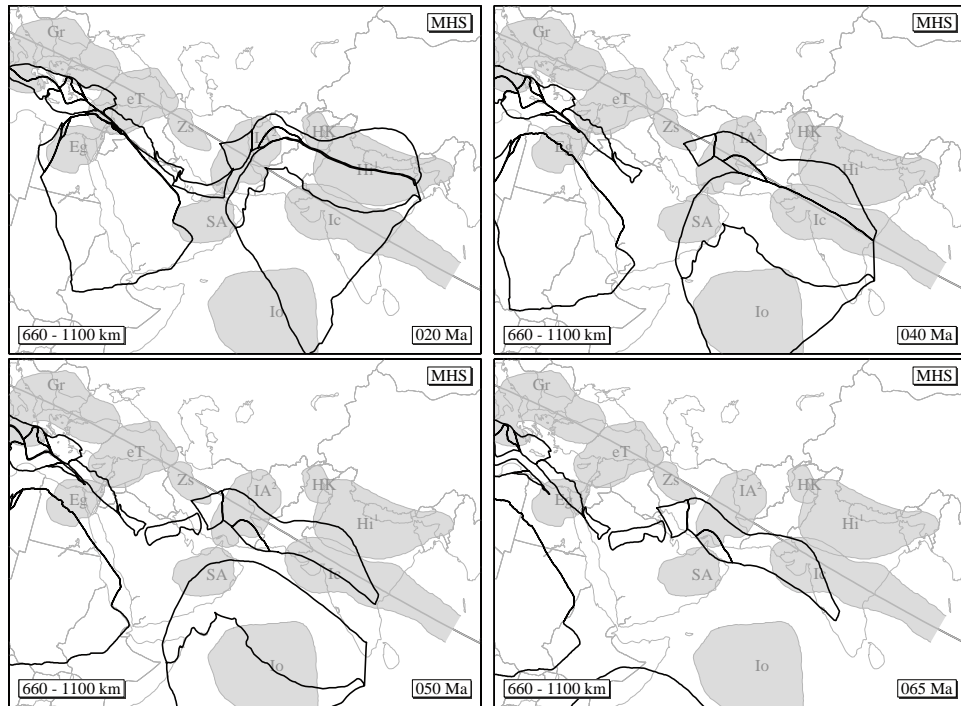
Figure 5.4: Geographical locations of the Eurasian and Arabian/Indian continental margins as in Figure 5.2, but now plotted in the moving hotspot reference frame of *O'Neill et al.* (2003) for the past 65 Ma.

5.4 Bulk volumes for various subduction scenarios

Subduction scenario I

In the previous chapter, the thermal volume of the subducted material - approximately following subduction scenario I - has been predicted for an average lithospheric age upon subduction based on the plate reconstruction of ExxonMobil. The resulting ratios of tomographic and predicted volumes are summarised in the left columns of Table 5.1, p. 114. For the Tethyan region as a whole, as well as for the Aegean/Arabian and Indian region separately, the predicted volumes are found to be significantly larger than the tomographic volumes when no slab deformation is assumed (T/P-ratios <1). If lithospheric thickening by a factor of 2 or 3 is taken into account, considered to be necessary for the large Tethyan slabs, the resulting thermal volumes associated with the subducted material decrease: The thermal volumes predicted for *spreading scenario B* are approximately similar to the tomographic volumes (T/P-ratios ≈1). For *spreading scenario A* the volumes (T/P-ratios >1) leave room for an additional subducted volume of ∼0.2-0.3 times the tomographic volume, i.e. about $1\text{-}2\cdot10^9$ km^3, depending on the amount of thickening.

Subduction scenario II

The variation of the age of the lithosphere in subduction scenario II is relatively simple (see Fig. 5.5). As in subduction scenario I, the age of the Tethyan lithosphere was 70 Ma at initiation of subduction underneath Eurasia. In *spreading scenario A*, its ridge stopped spreading upon obduction onto the Arabian continental margin at 80 Ma. Therefore, the last remnants of lithosphere to be subducted around 20 Ma along the Eurasian trench system were aged 60 Ma, and the 200-Ma average was 65 Ma. In *spreading scenario B*, the ridge stopped spreading when subduction of the Neo-Tethys commenced at 200 Ma. Subsequently, the fossil ridge was aged 120 Ma when obducting onto the Arabian margin, and the last remnants of Neo-Tethyan lithosphere had an age of 180 Ma upon subduction underneath Eurasia at 20 Ma. In this scenario, the average age of the subducting lithosphere was 125 Ma.
Analogously, it can be derived that the 200-Ma average age of the small lithospheric surface to be subducted underneath the obducting Neo-Tethyan ridge was 95-155 Ma. However, because the distance between the ridge and the Arabian continent must have been small (*Dercourt et al.*, 1993; *Şengör and Natal'in*, 1996), we will not consider this slablet separately. All Mesozoic-Cenozoic convergence, as well as the possible additional convergence in spreading scenario *A*, is assumed to be accommodated underneath Eurasia. As in subduction scenario I, the 200-Ma average age of the Tethyan lithosphere upon subduction is 65-125 Ma. The thermal volumes predicted for subduction scenarios I and II will therefore be equal, as well.

Subduction scenario III

For subduction scenario III, we consider here an alternative scenario for the variation of the lithospheric age upon subduction based on the reconstruction of *Stampfli and Borel* (2002, 2004) (see Figs. 2.3-2.6, pp. 22-25) as shown in Figure 5.5. Although the reconstructed isochrons of *Stampfli and Borel* (2002, 2004) would allow for a more detailed assessment of this variation in the future, we here use similar approaches for all three subduction scenarios.
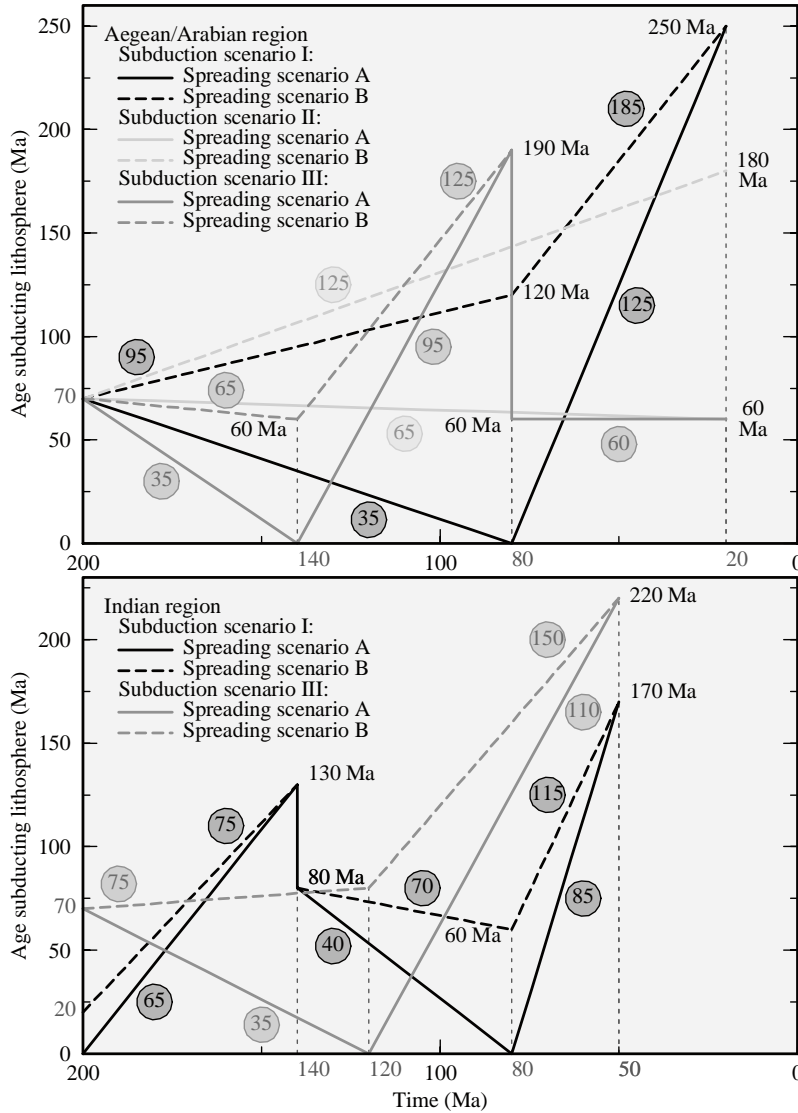
Figure 5.5: The variation of the age of the Tethyan lithosphere upon subduction for two end-member spreading scenarios (p. 87) and three different subduction scenarios (p. 106). The encircled numbers approximate the average ages of the separate oceanic domains. *Aegean/Arabian region* (top panel): Subduction scenario I (black lines) and II (light grey) that consider subduction of the Neo-Tethys only (200-Ma average age, based on ExxonMobil, is 65-125 Ma). Subduction scenario III (dark grey) includes the existence of a separate Semail Ocean as well (average age, based on *Stampfli and Borel* (2002, 2004), is 65-85 Ma). *Indian region* (bottom panel): Subduction scenario I (black lines) considers subduction of the Paleo-Tethys before 140 Ma and the Neo-Tethys thereafter (average age is 60-80 Ma). Subduction scenario III (grey lines), based on *Stampfli and Borel* (2002, 2004), assumes subduction of the Neo-Tethys since 200 Ma (average age is 70-110 Ma). See text for more detailed explanation.

In the Aegean/Arabian region, the age of the oceanic lithosphere was 70 Ma at initiation of subduction at 200 Ma, and active spreading within the Neo-Tethys must have stopped with the subduction of its ridge around 140 Ma at the latest. Triggered by the ridge subduction, the Semail back-arc ocean started spreading at direct expense of the Neo-Tethys. At 80 Ma, the Neo-Tethys closed completely with the obduction of the Semail spreading ridge onto the Arabian peninsula. Thereafter, the Semail Ocean subducted northward underneath Eurasia until it had disappeared around 20 Ma. For *spreading scenario A*, the Neo-Tethys lithospheric age upon subduction linearly decreased to 0 Ma when the ridge subducted at 140 Ma, and linearly increased again until the oldest parts of the Neo-Tethys were 190 Ma when subducted at 80 Ma. At that time, the Semail Ocean started to subduct with its oldest lithosphere aged 60 Ma. With cessation of spreading at 80 Ma, the youngest parts of the Semail oceanic lithosphere were still only 60 Ma when subducting at 20 Ma. In this spreading scenario, the 200-Ma average age of the subducting lithosphere was 65 Ma. For *spreading scenario B*, the age of the fossil ridge was already 60 Ma when it subducted, and the average age of the oceanic lithosphere was 85 Ma.

In the Indian region, the Neo-Tethys started spreading around 270 Ma as in the Aegean/Arabian region. Furthermore, the Paleo-Tethys already disappeared around 200 Ma, and the Neo-Tethyan ridge subducted around 120 Ma. In *spreading scenario A*, the age of the subducting oceanic lithosphere varied from 70 Ma at initiation of subduction at 200 Ma, to 0 Ma when the ridge subducted at 120 Ma, and to a final 220 Ma at 50 Ma. The average age of the subducted oceanic lithosphere was 70 Ma in this scenario. In *spreading scenario B*, the age of the fossil ridge was 80 Ma when it subducted, and the 200-Ma average was 110 Ma. In the reconstruction of *Stampfli and Borel* (2002, 2004), the Spongtang back-arc Ocean is proposed to have started spreading after subduction of the Neo-Tethyan ridge at 120 Ma (e.g. Fig. 2.6, p. 25). Because the eventual closure time of this basin is not very clear and its size relatively small, we will not use it for predicting the 200-Ma average age of the Tethyan oceanic lithosphere here, and have not incorporated it in Figure 5.5 either. However, the Spongtang back-arc Ocean will be discussed in Section 5.6, where - assuming subduction of the basin between 65 and 50 Ma (*Stampfli and Borel*, 2004) - the average age of the oceanic lithosphere upon subduction will be taken as 65 Ma.

Based on the plate reconstruction of *Stampfli and Borel* (2002, 2004), we propose a 200-Ma average for the age of the subducting Tethyan lithosphere of 65-85 Ma for the Aegean/Arabian region, and 70-110 Ma for the Indian region. The alternative averages lead to values for the initial lithospheric thickness and thermal factor $c(200)$ that are slightly different from those used for the reconstruction of ExxonMobil in the previous chapter (see Table 5.7, p. 141).

The total thermal volume of the subducted material is found to be 7.8-$9.2 \cdot 10^9$ km^3 for undeformed lithosphere, 6.1-$6.9 \cdot 10^9$ km^3 for slab thickened by a factor of 2, and 5.1-$5.7 \cdot 10^9$ km^3 for 3-fold thickened slabs (see Fig. 5.6). The resulting values of the T/P-ratios are similar to those for a separate Aegean/Arabian and Indian region (Table 5.1), with the values for the Indian region being a few percent smaller than those for the Aegean/Arabian region. However, the thermal volumes of the Aegean/Arabian region may be somewhat underestimated, and thus the T/P-ratios overestimated accordingly, due to the relatively small convergence rates in the area (Section 3.3.3). As can be seen from Figure 5.6 and Table 5.1, the values based on
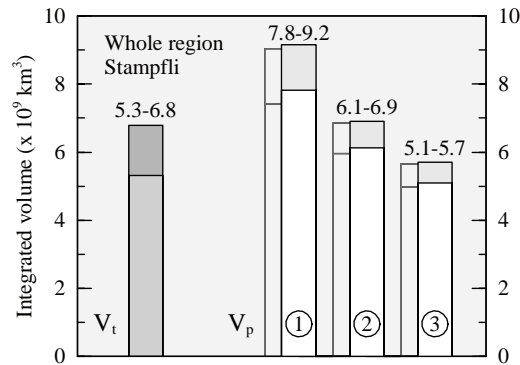
Figure 5.6: Tomographic volumes (V_t) vs. predicted thermal volumes (V_p) for slabs that either (1) kept their plate-like geometry, (2) thickened by a factor of 2, or (3) thickened by a factor of 3. The values for V_p are calculated for averages of the age of the subducted oceanic lithosphere based on the reconstruction of *Stampfli and Borel* (2002, 2004) for two end-member spreading scenarios (see p. 87). The calculations based on ExxonMobil (from Fig. 4.17, p. 95) are given for reference in the background. The predicted bulk volumes for ExxonMobil are representative for subduction scenarios I and II, and those of *Stampfli and Borel* (2002, 2004) for subduction scenario III.

Total	T/P-ratio: *ExxonMobil*		T/P-ratio: *Stampfli*	
region	*A*	*B*	*A*	*B*
Undefo.	$0.72 - 0.92$ /	$0.59 - 0.75$	$0.68 - 0.87$ /	$0.58 - 0.74$
Doubled	$0.90 - 1.14$ /	$0.78 - 0.99$	$0.87 - 1.11$ /	$0.77 - 0.98$
Tripled	$1.07 - 1.37$ /	$0.94 - 1.20$	$1.05 - 1.33$ /	$0.93 - 1.19$
Aegean/Arabian region				
Undefo.	$0.73 - 0.92$ /	$0.58 - 0.73$	$0.73 - 0.92$ /	$0.62 - 0.78$
Doubled	$0.91 - 1.15$ /	$0.77 - 0.97$	$0.91 - 1.15$ /	$0.82 - 1.03$
Tripled	$1.09 - 1.38$ /	$0.93 - 1.17$	$1.09 - 1.38$ /	$0.98 - 1.24$
Indian region				
Undefo.	$0.71 - 0.92$ /	$0.60 - 0.77$	$0.65 - 0.83$ /	$0.55 - 0.71$
Doubled	$0.88 - 1.13$ /	$0.79 - 1.01$	$0.84 - 1.07$ /	$0.74 - 0.95$
Tripled	$1.05 - 1.35$ /	$0.95 - 1.22$	$1.01 - 1.30$ /	$0.90 - 1.15$

Table 5.1: T/P-ratios (V_t/V_p) for two end-member spreading scenarios *A* and *B* (see p. 87). *Left column*: Ratios for averages of the lithospheric age based on ExxonMobil (as in Table 4.3 on p. 94). *Right column*: Ratios for averages based on the reconstruction of *Stampfli and Borel* (2002, 2004). The predicted bulk volumes for ExxonMobil are representative for subduction scenarios I and II, and those of *Stampfli and Borel* (2002, 2004) for subduction scenario III. Values for the lithospheric thickness and thermal factor $c(t)$ used to obtain V_p are given in Table 5.7 (p. 141).

Stampfli and Borel (2002, 2004) do not significantly differ from the values calculated for the averages based on ExxonMobil.

Conclusions

Although the variations in the age of the lithosphere upon subduction based on ExxonMobil are significantly different from those based on *Stampfli and Borel* (2002, 2004), the 200-Ma averages are quite similar and the predicted thermal volumes accordingly. The thermal volumes in the Arabian region for subduction scenario II are the same as those for subduction scenario I based on ExxonMobil, and thus similar to subduction scenario III (*Stampfli and Borel*, 2002, 2004) as well. These results indicate that, based on the bulk volumes alone, we cannot distinguish between the different reconstructions. All three subduction scenarios predict volumes of subducted lithosphere that are in agreement with the tomographic bulk volumes when Tethyan slab thickening by at least a factor of 2 is taken into account.

5.5 Separate Paleo-Tethyan volume

5.5.1 Predicted and tomographic slab volumes

In the Indian region, the Paleo-Tethys closed prior to 200 Ma according to *Stampfli and Borel* (2002, 2004), but only around 140 Ma according to ExxonMobil, Şeng ör and Natal'in (1996), and *Dercourt et al.* (1993). Following the reconstruction of ExxonMobil and others, we will separate the volume associated with subduction in the Indian region prior to 140 Ma from that of subduction thereafter to isolate the subducted Paleo-Tethys. We will refer to the Paleo-Tethyan subvolume as *P-T*, and the remaining Neo-Tethyan volume as *N-T*. The Aegean/Arabian region, in which all the volumes are assumed to be *N-T* in our 200-Myr timespan, will not be discussed here.

Present thermal signature of subducted material

The total subducted surface between 200 and 140 Ma is isolated as *P-T* in the Indian region (lower panel Fig. 5.16, p. 140). The average age of this Paleo-Tethyan oceanic lithosphere upon subduction is assumed to be 65-75 Ma (Fig. 5.5). Furthermore, we take values of the thermal factors $c_1(t)$, $c_2(t)$ and $c_3(t)$ at $t = 200$ Myr. For the remaining Neo-Tethys oceanic lithosphere, subducted between 140 Ma and present, the average age is assumed to be 55-85 Ma. For this *N-T* volume, we select the thermal factors at $t = 140$ Myr. The values for the initial lithospheric thicknesses and thermal factors used can be found in Table 5.7 (p. 141). The predicted thermal volumes are shown in Figure 5.7. The subducted surface and initial volumes for undeformed slabs are given in Table 5.2.

Volumes of seismic anomalies

A first option that will be considered here, is that all tomographic volumes represent remnants of subducted Neo-Tethyan lithosphere only. In that case, we exclude volume *P-T* from the total predicted thermal volume, and compare this purely *N-T* volume with the total 2.9-3.7$\cdot 10^9$

km^{3}of Indian tomographic volumes. The results for the option with the Paleo-Tethyan volume *excluded*, referred to as *Excl. P-T* hereafter, are given in the upper panel of Table 5.2 and left panel of Figure 5.7.

A second option that will be discussed is that the tomographic volumes represent both the *P-T* volume and the *N-T* volume. In an attempt to relate the Paleo-Tethys to a particular volume, we select anomaly Hi^2 in the tomographic model as a good candidate, following the suggestion made by *Van der Voo et al.* (1999) (lower panel Fig. 5.17, p. 142). In that case, we compare the predicted *P-T* volume to the volume of anomaly Hi ^{2}, and the predicted *N-T* volume to the remaining tomographic anomalies. The results for the option with the Paleo-Tethys *included*, denoted *Incl. P-T*, are shown in the lower panels of Table 5.2 and right panels of Figure 5.7.

5.5.2 Comparison and conclusions

Option Excl. P-T

When comparing only the predicted *N-T* volume to the Indian tomographic anomalies, a T/P-ratio of 0.9-1.1 (spreading scenario *A*) to 0.7-0.9 (spreading scenario *B*) is found for undeformed lithosphere (upper panel Table 5.2). This is significantly larger than previously found for the Indian region (e.g. Table 5.1). The same holds for the thermal volumes predicted for slabs thickened by factor of 2 and 3, which are not given separately in Table 5.2, but can be seen in Figure 5.7 (left panel). For both spreading scenarios, the thermal volumes for
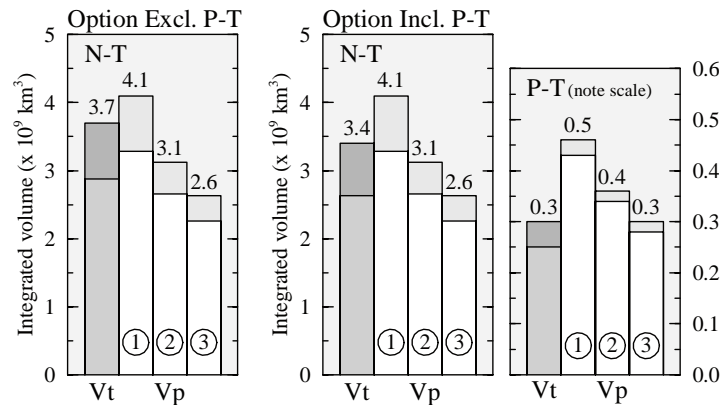

Figure 5.7: Tomographic volumes (V_t) vs. predicted thermal volumes (V_p) in the Indian region, divided into a separate Paleo-Tethys (*P-T*) and Neo-Tethys (*N-T*) part for two end-member spreading scenarios (see p. 87). *Left panel* (*Excl. P-T*): All tomographic volumes discussed in this chapter are assumed to represent Neo-Tethyan slab remnants, so the predicted *P-T* volume is excluded from the total Indian value. *Right panels* (*Incl. P-T*): The Paleo-Tethys is compared to anomaly Hi^2 of the tomographic volumes (right), and the Neo-Tethyan volumes are compared to the remaining tomographic volumes (left). The calculations for slabs that kept their plate-like geometry (1) can be found in Table 5.2, the factors necessary to perform the calculations for thickened slabs (2/3) are given in Table 5.7 (p. 141).

Volumes Excl. P-T	$V_{t(omo)}$ ($\cdot 10^9$ km^3)	$S_{s(ubducted)}$ ($\cdot 10^6$ km^2)	$V_{i(nitial)}$ ($\cdot 10^9$ km^3)		$V_{p(redicted)}$ ($\cdot 10^9$ km^3)		$V_{t(omo)}/V_{p(redicted)}$ (T/P-ratio)	
			A	*B*	*A*	*B*	*A*	*B*
Aeg/Arab	2.44−3.08	17.81	1.69 /	1.96	3.37 /	4.25	0.73 − 0.92 /	0.58 − 0.73
Indian *N-T*	2.88−3.70	19.58	1.76 /	2.06	3.28 /	4.10	0.88 − 1.13 /	0.70 − 0.90

Volumes Incl. P-T	$V_{t(omo)}$ ($\cdot 10^9$ km^3)	$S_{s(ubducted)}$ ($\cdot 10^6$ km^2)	$V_{i(nitial)}$ ($\cdot 10^9$ km^3)		$V_{p(redicted)}$ ($\cdot 10^9$ km^3)		$V_{t(omo)}/V_{p(redicted)}$ (V_t/V_p)	
			A	*B*	*A*	*B*	*A*	*B*
Aeg/Arab	2.44−3.08	17.81	1.69 /	1.96	3.37 /	4.25	0.73 − 0.92 /	0.58 − 0.73
Indian *N-T*	2.63−3.40	19.58	1.76 /	2.06	3.28 /	4.10	0.80 − 1.04 /	0.64 − 0.83
Indian *P-T*	0.25−0.30	2.25	0.21 /	0.23	0.43 /	0.46	0.58 − 0.70 /	0.55 − 0.65

Table 5.2: Subduction scenario I and II: Comparison of volumes when isolating the subducted surface associated with Paleo-Tethyan lithosphere (*P-T*) for slabs that kept their plate-like geometry. *Column 1*: Minimum and maximum tomographic volumes (V_t). *Column 2*: Subducted plate surface (S_s). *Column 3*: Estimated initial thermal volumes (V_i) for two spreading scenarios (see p. 87). *Column 4*: Predicted present thermal volumes (V_p). *Column 5*: T/P-ratio $\equiv V_t/V_p$. *Upper panel* (Option *Excl. P-T*): All tomographic volumes discussed in this chapter are assumed to represent Neo-Tethyan slab remnants, so the *P-T* thermal volume is excluded from the total Indian value. *Lower panel* (Option *Incl. P-T*): The Paleo-Tethys is compared to anomaly Hi[2] of the tomographic volumes, and the Neo-Tethyan volumes are compared to the remaining tomographic volumes. The volumes of the Aegean/Arabian region remain unchanged with respect to the previously found values (e.g. Table 5.1). The predicted volumes for slabs that have thickened in the mantle, calculated with the appropriate factors from Table 5.7 (p. 141), are shown in Figure 5.7.

undeformed and doubled lithosphere are more similar to the tomographic volumes than found before (compare to right panel of Fig. 4.19, p. 98), and those predicted for tripled lithosphere even smaller.

Option Incl. P-T

When comparing volume *N-T* to the tomographic anomalies without anomaly Hi[2], the T/P-ratios become 0.8-1.0 to 0.6-0.8 for slabs that have remained undeformed (Table 5.2 and middle panel of Fig. 5.7). Including slab thickening, these ratios are somewhat smaller than for option *Excl. P-T*, and more similar to those calculated earlier for the total Indian region (e.g. as in Table 5.1 and Fig. 4.19, p. 98).

The *P-T* volume predicted here is approximately twice the volume of anomaly Hi[2] without slab deformation (Table 5.2 and rightmost panel of Fig. 5.7). When slab thickening by a factor of 3 is taken into account, probably necessary for this old lithospheric volume, the thermal volume is similar to the tomographic volume. However, subduction of the Paleo-Tethys must have started much earlier than our reconstructed 200 Ma: In the reconstruction of ExxonMobil, used to predict the *P-T* volume, the northern part of the Paleo-Tethys is likely to have been subducted around this time already (see Table 2.2, p. 20). This suggests that the older (>200 Ma) part of the Paleo-Tethyan lithosphere cannot be identified as a separate tomographic volume today, or has been accommodated elsewhere. In the previous chapter

(Section 4.2), we identified two anomalies underneath Central Asia that were assumed to be related to subduction prior to 200 Ma. These anomalies, cA^1 and cA^2 in Figure 4.6 (p. 75), may well represent remnants of the remaining Paleo-Tethyan lithosphere indeed.

If the *P-T* lithosphere has broken off after continental collision of Afghanistan and south Tibet with Eurasia around 140 Ma, the depth and geometry of anomaly Hi^2 may help us to further assess its subduction history. From Figure 5.19 (p. 144) it can be seen that Hi^2 is positioned between 1200 and 2200 km depth, which corresponds to a sinking time of ∼80-180 Myr for sinking rates of 3 cm/yr in the upper mantle and 1 cm/yr in the lower mantle. Even when considering a certain delay-time for slab break-off, which could be as large as 25 Myr in view of the slow (∼1 cm/yr) convergence rates at that time (*Van de Zedde and Wortel*, 2001), something must have slowed down the upper part of the sinking slab considerably. Moreover, as visible in Figure 4.7 (p. 76, section 95) and Figure 4.8 (p. 77, section F), the most shallow parts of the anomaly can be found in the northwest, i.e. below northwest India. If the slab has subducted northwards, as often proposed (e.g. *Dercourt et al.*, 1993), slab break-off probably occurred on the eastern side of the plate but not, or much later, on the western side. The extreme dip of the anomaly, however, cannot be readily explained by diachronous slab break-off only. This suggests that the direction of subduction was eastward, as proposed to some degree by *Stampfli and Borel* (2004), or southward (*Şeng ör and Natal'in*, 1996), rather than northward. As can be seen in the Triassic reconstruction of *Stampfli and Borel* (2004) in Figure 2.3 (p. 22), subduction of the eastern Paleo-Tethys partly occurred in a direction parallel to the north Tibetan (nT) block. If the slab has subducted eastward indeed, although in this reconstruction already before 200 Ma, the depth distribution of Hi^2 suggests that the slab did not really break off but more or less remained attached to the surface. It seems plausible that the continental fragments of south Tibet and Afghanistan collided with Eurasia, but that complete slab break-off did not occur, for example, because the zone of subduction - accommodating the further convergence between India and Eurasia - moved towards the southern margin of these blocks instead, and the continental lithosphere did not subduct deep enough to trigger slab detachment.

Conclusions

Our results indicate that anomaly Hi^2 could represent part of the subducted Paleo-Tethyan lithosphere if (1) the subducted slab has thickened by a factor of 3, (2) the remaining part of the Paleo-Tethyan lithosphere has been accommodated elsewhere (e.g. at the locations of anomalies cA^1 and cA^2) or is not detectable by tomographic means at present, and (3) the slab did not completely detach from the surface until 80 Ma at least. As all three points seem plausible, we will assume that Hi^2 is the Paleo-Tethyan slab remnant indeed in the following. The ancient direction of the subducting slab cannot be well constrained anymore, although the geometry of the anomaly suggests a southeastward rather than a northward direction of subduction.

5.6   Slab volumes after ridge subduction

5.6.1   Consequences of spreading center subduction

The oceanic spreading centers between converging and colliding continents, either active or not, eventually subduct underneath the overriding continental margins. In tectonic reconstructions, the timing of ridge subduction is typically associated with the emplacement time of ophiolites. Based on thermo-mechanical modelling results, it has been suggested that very young (<30 Ma) oceanic lithosphere can break up during the early phase of its subduction and lead to the incorporation of a thin sheet of oceanic lithosphere into the forearc region (*Van den Beukel*, 1990). Upon closure of the oceanic basin, this sheet can be incorporated into the orogenic belt as ophiolites indeed.

If an oceanic ridge continues to spread when it subducts, asthenospheric material can fill the space between the diverging plates and a slab window is formed. Such continuous spreading, however, requires the young plates to remain coherent during subduction which has been suggested to be unlikely by *Van den Beukel* (1990). If the subducted ridge stops spreading, the major thermal differences between the two subducting plates rapidly disappear because of thermal diffusion (*DeLong et al.*, 1979; *Daniel et al.*, 2001). *Daniel et al.* (2001) argued that continuing separation but at a greatly diminished rate is the most plausible hypothesis for spreading center subduction in southern Chili. However, *Van Wijk et al.* (2001) showed that a complete slabless window is not needed to explain observed heat flow, magmatism and tomography for the subducted Farallon ridge in North America: Model results for a normal ridge thermal structure of a stalled slab were found to fit the data equally well.

Either with or without continuous separation between the leading and trailing plates after ridge subduction, the thermal anomaly associated with the young and warm ridge segment is likely to be small relative to the older parts of the subducted oceanic lithosphere. The ridge segment will be thermally re-equilibrated with the surrounding mantle, and thus not detectable by seismic tomographic means, relatively fast. As a result, the anomalous volume associated with the subducted oceanic lithosphere may be imaged as two separate subvolumes. In this section, we will assume that the thermal volumes associated with the subducted oceanic lithosphere will split into two subvolumes at the time of ridge subduction. Because the leading plate is composed of progressively younger and warmer lithosphere, and the trailing plate of progressively older and cooler lithosphere instead, the material subducted prior to ridge subduction is likely to be somewhat more equilibrated with its surroundings than the material subducted thereafter.

5.6.2   Predicted and tomographic slab volumes

Subduction scenario I   For this subduction scenario, we assume that the Neo-Tethyan spreading ridge subducted around 80 Ma (ExxonMobil, *Şeng ör and Natal'in*, 1996; *Dercourt et al.*, 1993) and caused the subducted material to split into two subvolumes in both the Aegean/Arabian and Indian region. In the following, we will refer to the volumes associated with subduction prior to ridge subduction and thereafter as *BRS* and *ARS* (Before and After Ridge Subduction), respectively.

Subduction scenario II   For subduction scenario II in the Arabian region (*Dercourt et al.*, 1993; *Şengör and Natal'in*, 1996), the proposed asymmetric age distribution within the Neo-Tethyan lithosphere will have resulted in two different volumes as well: One basically consisting of all Neo-Tethyan lithosphere, and one very small volume subducted underneath the obducted ridge. As this subduction scenario will not result in separate *BRS* and *ARS* subvolumes, we do not have to predict new thermal volumes here.

Subduction scenario III   For this third subduction scenario, *Stampfli and Borel* (2002, 2004) propose Neo-Tethyan ridge subduction to have occurred around 140 Ma, and obduction of the Semail Ocean spreading ridge onto the Arabian continent at 80 Ma, in the western part of the area. This may have caused the subducted material to split into three separate volumes instead of the two considered in subduction scenario I. In the Indian region, the Neo-Tethyan ridge is proposed to have been subducted around 120 Ma, and the Spongtang oceanic back-arc basin between ∼65-50 Ma, which would result into yet another division of subvolumes.

Present thermal signature of subducted material

Subduction scenario I   For the *BRS* group, we take the total surface subducted prior to 80 Ma in the Aegean/Arabian region (Fig. 5.16, p. 140), and that between 140 and 80 Ma - thus without the Paleo-Tethyan volume addressed in the previous chapter - in the Indian region. For the *ARS* group, we put the surface subducted since that time. As a result of the subdivision, the average ages of the lithospheric basins in groups *BRS* and *ARS* change significantly (Fig. 5.5). Especially the young age of *BRS* in the Aegean/Arabian region for spreading scenario *A*, namely 35 Ma, is remarkable. As discussed in Section 3.3.3, values of the thermal factor $c_1(t)$ are very uncertain for such young ages, and $c_2(t)$ and $c_3(t)$ may underestimate the actual values with 10-20%. The age-dependent values of the thermal factors for the *BRS* volumes are taken at $t = 200$ Myr in the Aegean/Arabian region, and 140 Myr in the Indian region. For the *ARS* volumes, we use the appropriate values at $t = 80$ Myr instead. The values for the average ages, initial thicknesses, and thermal factors used for each group can be found in Table 5.7 (p. 141).

Subduction scenario III   In the Arabian region, additional subducted material is expected from the Semail Ocean in this subduction scenario. As the Semail oceanic basin is proposed to have overridden the complete Neo-Tethys between 140-80 Ma, we assume that the maximum size of the basin equals the surface subducted between Arabia and Eurasia from 80 Ma until the onset of continental collision at 22 Ma. The surface of the Semail Ocean is therefore an *additional* $4 \cdot 10^6$ km² (i.e. 80-22 Ma surface in the Arabian region of Fig. 5.16, p. 140). In the Indian region, additional subducted material may result from the Spongtang back-arc basin, but this amount is not very clear. We approximate the maximum size of this basin, analogous to that for the Semail Ocean, by the surface subducted between India and Eurasia between 65 Ma - the start of its subduction - and 48 Ma - the time of first continental collision. For subduction scenario III, we select for *BRS* the total surface subducted prior to 140 Ma and 120 Ma in the Aegean/Arabian and Indian region, respectively. In the *ARS* group, we put the

surface of the Neo-Tethys that has been subducted underneath the back-arc basins, c.q. the 140-22 Ma surface in the Arabian region, and the 120-43 Ma surface in the Indian region. The convergence calculated for the final period of continental collision, i.e. 22-0 Ma and 43-0 Ma, is added to the Semail and Spongtang surfaces, as these are the last oceanic basins to be subducted. See Table 5.7 (p. 141) for an overview of the averages ages, lithospheric thicknesses and thermal factors used. Again, the predicted *BRS* volumes for spreading scenario *A* have relatively young ages, which may result in underestimates of the actual thermal volumes.

Volumes of seismic anomalies

The relative distribution of the volumes associated with *BRS* and *ARS* is predicted from the assumed subduction scenario, but their actual position within the mantle has to be inferred from the plate motions in an absolute frame of reference. Here we consider the reference frames discussed in Section 5.3, namely those of *Müller et al.* (1993), *O'Neill et al.* (2003) and Eurasia fixed (see Figs. 5.2-5.4, pp. 108-110), to establish the approximate locations of the subduction zones in each subduction scenario.

Similarly to the overview of the horizontal extent of the seismic anomalous bodies in three different depth intervals (Figs. 4.4-4.6, pp. 73-75), we have plotted the vertical distribution of these anomalies in two bands of cross-sections in Figures 5.8 and 5.9. For the Arabian anomalies, the contour lines represent a projection of the maximum size of the anomalies between the vertical cross-sections 40 and 80 as in Figure 4.1, p. 69 (cf. section 55 and 75 in Fig. 4.7, p. 76). Note that the Arabian continental margin was not exactly perpendicular to these cross-sections further back in time (e.g. 80 Ma reconstruction in Fig. 5.2, p. 108). The tomographic anomalies in the Indian region are a projection of their maximum extent between sections 90 and 120 as in Figure 4.1, p. 69 (cf. section 95 and 115 in Fig. 4.7, p. 76). In the Indian region, the approximate direction of subduction was in the plane of this projection.
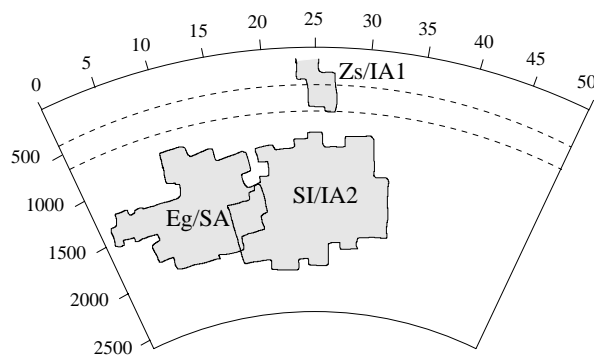

Figure 5.8: Vertical distribution of tomographic anomalies in the Arabian region. The contour line of each anomalous body is a projection of its maximum extent approximately between cross-sections 40 and 80 as in Figure 4.1 (p. 69) and Figure 5.17 (p. 142).
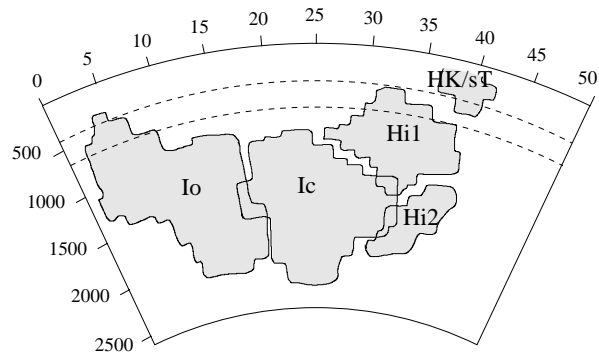
Figure 5.9: Vertical distribution of tomographic anomalies in the Indian region. The contour line of each anomalous body is a projection of its maximum extent approximately between cross-sections 90 and 120 as in Figure 4.1 (p. 69) and Figure 5.17 (p. 142).

Subduction scenario I   In the Aegean/Arabian region, the Eurasian southern margin is positioned approximately above anomalies SI and IA [2] around the 80 Ma of ridge subduction in the EU frame (lowerleft panel Fig. 5.2, p. 108). However, in the HS frame (Fig. 5.3, p. 109) the trench system is situated just above the southernmost anomalies Eg and SA instead. Although Eg and SA are positioned relatively far south, it seems plausible that the *BRS* material - subducted prior to 80 Ma underneath Eurasia - can be found in the tomographic volumes Eg and SA (Fig. 5.17, p. 142). Because the Eurasian continental margin has moved only northwards since that time in all three reference frames considered here, we associate the remaining tomographic anomalies with the *ARS* volumes.

In the Indian region, the Eurasian continental margin is situated right above anomaly Ic at 80 Ma in both the EU and HS frame. Because Eurasia has moved further northwards since that time, both the *BRS* and *ARS* volumes in the subduction scenario are likely to be represented by Ic and the more northerly positioned anomalies. However, from our earlier analyses (e.g. Fig. 5.7 for the *P-T*/*N-T* volumes in the Indian region) we found that all tomographic volumes are needed to explain the predicted thermal volumes, also the southernmost anomaly Io. Although Io seems to be too far south to be explained by subduction scenario I, we will consider it as *BRS* volume for the moment (see Fig. 5.17, p. 142) and will discuss the implications below. This will leave the remaining anomalies as to be associated with the *ARS* volumes, except for anomaly Hi [2] that is assumed to represent the Paleo-Tethyan lithosphere (Section 5.5).

Subduction scenario II   In this subduction scenario for the Arabian region, almost the complete Neo-Tethys has been subducted as one single volume underneath the Eurasian margin, and a small amount of subduction is accommodated at the Arabian margin around 80 Ma. As the Arabian continental margin is positioned above Eg and SA at this time in both the EU and HS frame (Figs. 5.2-5.3), this small slablet could be associated with anomalies Eg and SA. In that case, the Neo-Tethyan (*N-T*) volumes accommodated along the Eurasian margin may be represented by the remaining anomalous volumes.

Because the Eurasian continental margin is positioned above Eg and SA during the Cenozoic in the HS frame (Fig. 5.3), as discussed above, part of *N-T* may be incorporated in these anomalies. Again, however, the continental margins are just north of Eg and SA in the EU frame (Fig. 5.2). In the MHS frame (Fig. 5.4), the positions seem to be too far west for adequately predicting the tomographic volumes in the eastern Arabian region. As the westward shift of MHS relative to HS is not well constrained (*O'Neill et al.*, 2003), the location of the continental margins could have been more to the east, and more similar to those of the EU frame. Thus, in reference frames other than HS, it is not likely that remnants of *N-T* are accommodated in Eg and SA in this subduction scenario.

Subduction scenario III   Although the hotspot reference frame is uncertain prior to 84 Ma, the *BRS* volumes in the Arabian region seem to have been subducted not far south of the present Zagros suture zones - and probably above anomalies SI and IA[2] in any case - around 120 Ma (lowerright panels Figs. 5.2 and 5.3). Semail back-arc spreading will have resulted in *ARS* subduction much further south, with its southernmost extent around the position of the northern Arabian continental margin at 80 Ma. Both the EU and HS frame suggest that this location was above anomalies Eg and SA, although in the HS frame Arabia seems to be positioned too far south to be associated with Eg. Subduction of the Semail Ocean must have been accommodated along the northward moving Eurasian margin since that time. We will test here whether the *ARS* volumes can be associated with anomaly Eg and SA, and both the *BRS* and Semail volumes with the remaining anomalies. Note that this is the *opposite* of the division assumed for subduction scenario I and displayed in Figure 5.17 (p. 142).

In the Indian region, anomaly Hi[2] is again assumed to represent the Paleo-Tethyan lithosphere, although in the shown HS frame this anomaly seems to be a good candidate for the *BRS* volume as well (lowerright Fig. 5.3). In the EU frame, however, the southern Eurasian margin is positioned right above anomaly Ic instead. As the hotspot reference frame is very uncertain this far back in time, we consider here the possibility that the *BRS* volumes are part of Ic, e.g. represented by its lowermost anomalies. With the Neo-Tethys subducting underneath the southward migrating Spongtang Ocean until 65 Ma, the *ARS* volumes are coupled to both anomaly Io and Ic, even though they seem to be separated in the tomographic images. Again, this is the *opposite* of the division for subduction scenario I and displayed in Figure 5.17. Around 65 Ma, the Indian continental margin is positioned right above the southern, shallow anomalies of Io in all three reference frames. Note that the EU and HS frame seem to predict India somewhat too far east, and the MHS frame too far west instead. Anomaly Hi[1] is assumed to represent part of the *ARS* volumes as well. However, as will be discussed later, this anomaly may also be associated with the separate Spongtang oceanic lithosphere instead.

5.6.3   Comparison and conclusions

Aegean/Arabian region

Subduction scenario I   For spreading scenario *A* and undeformed slabs, the predicted *BRS* volume is somewhat larger than the tomographic volumes (left panel Fig. 5.10), and the T/P-

ratios of 0.6-0.8 (Table 5.3) are similar to those found before (e.g. Table 5.1). However, for spreading scenario *B* the predicted volumes are much larger than the tomographic volumes, with a T/P-ratio of 0.3-0.4 only. When taking into account slab thickening, the volumes for spreading scenario *A* remain similar because of the young age of the *BRS* lithospheric basin in this scenario (see Fig. 5.10). The predicted volumes in spreading scenario *B* will decrease significantly with increasing factors of thickening, but not enough to level with the tomographic volumes. For the *ARS* volumes, the T/P-ratio for undeformed slabs is 1.2-1.6 for both spreading scenarios (Table 5.3), which is quite high. The predicted thermal volumes cannot account for the large volume of the tomographic anomalies, and to do this the volumes need to be 25-50% larger (Fig. 5.10). Taking into account slab thickening will further lower the thermal volumes, and increase the difference with the tomographic volumes even more.
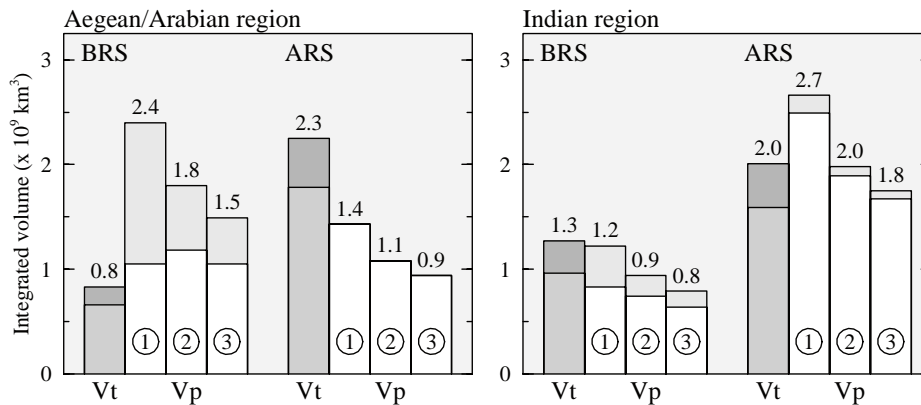

Figure 5.10: Subduction scenario I: Tomographic volumes (V_t) vs. predicted thermal volumes (V_p), divided into a part before ridge subduction (*BRS*) and a part after ridge subduction (*ARS*), for two end-member spreading scenarios (see p. 87). Note that the *ARS* volumes are similar for both spreading scenarios due to the relatively old age of this part of the oceanic lithosphere. The calculations for undeformed slabs (1) can be found in Table 5.3, the factors necessary to perform the calculations for thickened slabs (2/3) in Table 5.7 (p. 141).

The results displayed in Figure 5.10 suggest that, if both subduction scenario I and the associated *ARS*/*BRS* subdivision are correct, spreading scenario *B* is very unlikely. For spreading scenario *A*, however, the calculated volumes for *BRS* are probably underestimated due to the young lithospheric age of this basin. An even larger volume of *BRS* would certainly leave no room for the implicitly assumed spreading and additional amount of subduction. One possible solution would be to let the ridge subduct earlier in time so that the thermal volume will become smaller for *BRS* and larger for *ARS*. However, to change the volumes significantly, a larger timeshift is necessary than is justified by the reconstructions followed here (ExxonMobil, *Şengör and Natal'in*, 1996; *Dercourt et al.*, 1993). Another solution would be to conclude that all subducted material, *ARS* as well as *BRS*, have basically subducted right underneath the Zagros Suture indeed - as one would infer from the absolute plate motions discussed above (Figs. 5.2-5.4). For a factor of 3 thickening, the *BRS* and *ARS* predicted vol-

umes are only little more than the *ARS* tomographic volume shown in Figure 5.10. However, this would leave the volumes of anomalies Eg and SA unexplained and exclude the possibility of additional subduction by intermediated spreading.

Considering the depth ranges of the tomographic anomalies, Eg and SA of the older *BRS* group can be found mainly between ∼1000-1800 km and 800-2000 km depth, respectively (Fig. 5.19, p. 144). However, lower mantle anomalies SI and IA [2] of the younger *ARS* group are positioned between 1000-2200 km and 800-2000 km depth. Especially in the western part of the region, anomaly SI (∼younger group *ARS*) can be found *lower* than anomaly Eg (∼older *BRS*), with a relatively large volume between 1400-2200 km depth.
The deep position of SI can only be explained by subduction *after* 80 Ma when we assume average sinking rates of about 4 cm/yr in the upper mantle and 2 cm/yr in the lower mantle. However, this would imply that the ∼800-1000 km of the top of the older anomalies Eg and SA would correspond to sinking times of ∼25-35 Myr only, which is not in agreement with subduction *prior* to 80 Ma. Assuming slower sinking rates of 3 and 1 cm/yr, the 800-1000 km can be reached within ∼40-60 Myr, which is still somewhat fast but seems reasonable. In that case, however, the ≥2000 km deep bottom of anomalies SI and IA [2] would correspond to a total sinking time of ∼160 Myr, which is far too much for this subduction scenario. Although the implications of the depth intervals of the several anomalies are somewhat speculative, their agreement with the proposed subduction scenario I is not very satisfactory.

Volumes ARS/BRS	$V_{t(omo)}$ ($\cdot 10^9$ km^3)	$S_{s(ubducted)}$ ($\cdot 10^6$ km^2)	$V_{i(nitial)}$ ($\cdot 10^9$ km^3)		$V_{p(redicted)}$ ($\cdot 10^9$ km^3)		$V_{t(omo)}/V_{p(redicted)}$ (T/P-ratio)	
			A	*B*	*A*	*B*	*A*	*B*
Aeg/Arab								
ARS	$1.78-2.25$	7.20	0.79 /	0.79	1.43 /	1.43	$1.24-1.57$ /	$1.24-1.57$
BRS	$0.66-0.83$	10.61	0.80 /	1.11	1.05 /	2.40	$0.63-0.79$ /	$0.28-0.35$
Indian								
ARS	$1.67-2.14$	13.34	1.40 /	1.47	2.49 /	2.66	$0.67-0.86$ /	$0.63-0.81$
BRS	$0.96-1.27$	6.24	0.45 /	0.62	0.83 /	1.22	$1.16-1.53$ /	$0.79-1.04$
P-T	$0.25-0.30$	2.25	0.21 /	0.23	0.43 /	0.46	$0.58-0.70$ /	$0.55-0.65$

Table 5.3: Subduction scenario I: Comparison of volumes as in Table 5.2, but now with the predicted *N-T* volumes divided into a part before (*BRS*) and after (*ARS*) ridge subduction at 80 Ma, for two end-member spreading scenarios (see p. 87). Associated with *BRS* are the tomographic volumes Eg and SA in the Aegean/Arabian, and anomaly Io in the Indian region. The other tomographic anomalies, except for anomaly Hi[2] that is considered as Paleo-Tethys (*P-T*), are associated with the *ARS* groups. The subdivision of the subducted surface is illustrated in Figure 5.16. The predicted volumes for slabs that have thickened in the mantle, calculated with the appropriate factors from Table 5.7 (p. 141), are shown in Figure 5.10.

Subduction scenario II The original subducted surface and present thermal volumes of the slablet subducted at the Arabian continental margin is small, but not known. To explain the 0.66-0.83·10^9 km^3 of anomalies Eg and SA by the thermal volume of the slablet alone, the

initial volume must have been a factor 1.8, 1.4 or 1.2 smaller, depending on the amount of slab thickening assumed (similar to the *ARS* values as for subduction scenario I in Table 5.7, p. 141). The original subducted surface of the slablet would equal this initial volume divided by the 105-110 km lithospheric thickness appropriate for the 95-155 Ma average of the age of the lithosphere (see Section 5.4). Depending on the spreading scenario and the amount of thickening, a $0.66\text{-}0.83 \cdot 10^9$ km^3 thermal volume can thus be associated with a subducted surface of about 3.3 to $6.6 \cdot 10^6$ km^2. As can be seen in Figure 5.16 (p. 140), such a surface is actually quite large for the Arabian region and is similar to the surface subducted in the area during the past 90-50 Ma. This is clearly in contradiction with the proposed position of the spreading centre close to the Arabian continental margin: For the elongated Arabian continental margin, this surface would require an average $\sim$1000-2000 km of convergence, c.q. distance between the continent and the spreading center.
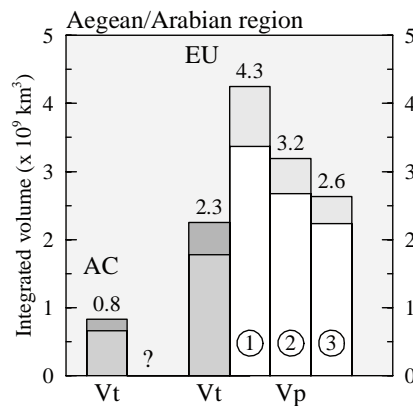

Figure 5.11: Subduction scenario II: Tomographic volumes (V_t) vs. predicted thermal volumes (V_p) for two end-member spreading scenarios (see p. 87). The tomographic volumes subducted near the Arabian continental margin (AC) and underneath Eurasia (EU) equal those of *BRS* and *ARS*, respectively, for subduction scenario I (Fig. 5.10). The predicted thermal volumes correspond to the bulk Aegean/Arabian volumes for which the calculations can be found in Table 4.3 (p. 94).

As discussed in Section 5.4, the predicted *N-T* volume in this subduction scenario corresponds to the bulk Aegean/Arabian volume (e.g. Table 4.3 and Fig. 4.19, pp. 94 and 98). Only if the slabs have thickened by a factor of 3, and for spreading scenario *A*, the *N-T* volumes fit the tomographic $1.78\text{-}2.25 \cdot 10^9$ km^3. As subduction is implicitly assumed in spreading scenario *A*, the northern parts of anomalies Eg and SA may contain *N-T* material. If this is indeed the case, only the southern parts of these anomalies need to be explained by the slablet discussed above. The southern anomalies of Eg and SA can all be found below 1200 km depth, which can be reached in $\sim$80 Ma for sinking rates of 3 cm/yr in the upper mantle and 1 cm/yr in the lower mantle.

However, although the HS reference frame allows *N-T* subduction above anomalies Eg and SA, the positions of the trench systems in the EU and MHS frames are too far north to come to a similar conclusion (Figs. 5.2-5.4). Moreover, in the HS frame also the Arabian continental

margin is positioned relatively far south. At 80 Ma, the approximate emplacement time of the Oman ophiolites, only subduction along the northern half of Arabia could explain the southernmost volumes of Eg and SA.

Subduction scenario III   As can be seen in Figure 5.12 (top panel, p. 130), the predicted volumes for the *BRS* group and Semail Ocean together are much smaller than the tomographic anomalies associated with these volumes: Even if the slabs have *not* thickened in the lower mantle, although very unlikely for the *BRS* volumes, the predicted total volume of $1.2\text{-}1.4 \cdot 10^9$ km^3 results in T/P-ratios between 1.3-1.9 (Table 5.4). The predicted volumes are likely to be underestimated, as discussed above (p. 120 or Section 3.3.3), but even with a maximum 20% increase the results suggest that Neo-Tethyan and Semail lithospheric spreading during the subduction of these oceans has accounted for the missing volume. On the contrary, however, the predicted *ARS* volume is much too large to be explained by the appointed anomalies Eg and SA alone. Even when a factor 3 of slab thickening is taken into account, the T/P-ratio is still only 0.4-0.5 for both spreading scenarios.

Apparently, the subdivision of the tomographic anomalies for subduction scenario III is not correct. Our results suggest a somewhat different subduction scenario: As trench migration is an effective mechanism for generating shallow dipping slabs (e.g. *Griffiths et al.*, 1995; *Guillou-Frottier et al.*, 1995; *Christensen*, 1996; *Olbertz et al.*, 1997), and the Neo-Tethyan *ARS* volume progressively disappeared underneath the spreading Semail back-arc basin, the slabs may have flattened down over the full width of the basin. Flattened slab structures below trenchward migrating, still active subduction zones have been globally imaged by seismic tomography, e.g. underneath the Izu-Bonin, Sunda and Tonga island arcs (e.g. *K árason and van der Hilst*, 2000; *Hall and Spakman*, 2002). If this has been the case, the oldest part of the *ARS* volume might be incorporated in volumes SI and IA [2] together with the *BRS* and Semail volumes, and only the youngest part of the *ARS* volume in Eg and SA. This scenario implies that the apparent division between anomalies Eg/SA and SI/IA [2] is not related to ridge subduction, and has another origin.

By taking half of the predicted *ARS* volumes as to be represented by the tomographic *BRS* instead of *ARS* anomalous volumes, the balance between the volumes improves (Fig. 5.12): For slabs thickened by a factor of 2, the predicted volume of *BRS*, half of *ARS*, and Semail together will be $1.8\text{-}2.0 \cdot 10^9$ km^3, which is quite similar to the tomographic volume of $1.8\text{-}2.3 \cdot 10^9$ km^3 (T/P-ratio $\sim$1.0-1.2). If thickened by a factor of 3, certainly realistic for the old and large *ARS* volume, the total of these slab volumes will be $1.6\text{-}1.7 \cdot 10^9$ km^3, which is even smaller (T/P-ratio $\sim$1.1-1.4). The remaining volume of *ARS*, $0.9\text{-}1.0 \cdot 10^9$ km^3 in this case, is still larger than the $0.7\text{-}0.8 \cdot 10^9$ km^3 of the tomographic anomalies, but not as much as before. Evidently, the actual division of the volumes is unknown, and a somewhat larger part of the predicted *ARS* volume can have been subducted in the northern part of the region just as well.

As mentioned above, the $\geq$2000 km depth of the bottoms of anomalies SI and IA [2] (Fig. 5.19, p. 144) could be reached in a time >160 Myr for sinking rates of $\sim$3 cm/yr in the upper and 1 cm/yr in the lower mantle. This would be in agreement with the subduction of *ARS* material prior to 140 Ma. Also the depths of the other anomalies seem to be in general agreement with

Volumes ARS/BRS	$V_{t(omo)}$ ($\cdot 10^9$ km^3)	$S_{s(ubducted)}$ ($\cdot 10^6$ km^2)	$V_{i(nitial)}$ ($\cdot 10^9$ km^3)		$V_{p(redicted)}$ ($\cdot 10^9$ km^3)		$V_{t(omo)}/V_{p(redicted)}$ (T/P-ratio)	
			A	B	A	B	A	B
Aeg/Arab								
Sml.+	?	5.51	0.52		0.91		?	
ARS	0.66−0.83	13.56	1.42 /	1.49	2.89 /	3.04	0.23 − 0.29 /	0.22 − 0.27
BRS	1.78−2.25	2.66	0.20 /	0.25	0.26 /	0.50	6.85 − 8.65 /	3.56 − 4.50
Indian								
Spt.+	?	9.59	0.91		1.46		?	
ARS	2.28−3.05	13.92	1.53 /	1.53	3.02 /	3.02	0.75 − 1.01 /	0.75 − 1.01
BRS	0.35	2.47	0.19 /	0.25	0.25 /	0.51	1.00 − 1.20 /	0.49 − 0.59
P-T	0.25−0.30	—	—		—		—	

Table 5.4: Subduction scenario III: Comparison of volumes when dividing the predicted *N-T* volumes into a part before and after ridge subduction, as in Table 5.3, but now at 140 Ma in the Arabian region, and 120 Ma in the Indian region. The convergence during the Cenozoic continental collisions is added to the volumes of the Semail (Sml.) and Spongtang (Spt.) oceanic back-arc basins. The predicted volumes for slabs that have thickened in the mantle, calculated with the appropriate factors from Table 5.7 (p. 141), are shown in Figure 5.12.

scenario III for these sinking rates: The major part of anomaly SI ($\sim$1400-2000 km depth) and IA^2 (1100-1400 km depth) would correspond to sinking times of 100-160 Myr and 70-100 Myr, respectively, which would be in accordance with subduction between 140-80 Ma. The somewhat deeper position of the eastern anomaly SA with respect to the western anomaly Eg (e.g. Fig. 5.19) may reflect the diachronous subduction of the Neo-Tethys underneath the Semail Ocean (e.g. see Early Cretaceous reconstruction of Fig. 2.5, p. 24). The $\sim$800-1000 km of the top of anomalies Eg and SA would correspond to sinking times of $\sim$40-60 Myr, which is only little shorter than expected for subduction *prior* to 80 Ma. Anomalies eT, Ca, Zs and IA^1, as well as the upper ($<$1100 km) anomalies of IA^2, are likely to represent the remnants of the Semail oceanic lithosphere subducted in the past 80 Myr.

Indian region

Subduction scenario I The predicted *BRS* volumes in the Indian region are approximately similar to the tomographic *BRS* volumes (right panel Fig. 5.10, p. 124). If all slabs have thickened by a factor of 2 or 3, the thermal volumes of the *BRS* group are clearly smaller than the tomographic volumes. This would leave room for additional lithospheric spreading, although it has to be acknowledged again that the *BRS* volumes are somewhat underestimated for spreading scenario *A* (Section 3.3.3). The T/P-ratios of 1.2-1.5 and 0.8-1.0 for undeformed slabs are indeed much larger than the previously found values (Table 5.3 vs. Table 5.1). For the *ARS* group, a factor of 3 thickening would be needed for the predicted volumes to become smaller than the tomographic volumes (Fig. 5.10), which is similar as found before.

Anomaly Io that was appointed as *BRS* volume (Fig. 5.17, p. 142) can be found in a large depth interval, and mainly between 800-2000 km depth (Fig. 5.19, p. 144). Very slow sinking

rates are required to make the top of anomaly Io fit with subduction of the *BRS* slab prior to the proposed 80 Ma. Remarkably, the most shallow parts of this anomaly (i.e. in the 660-1100 km depth interval, e.g. see Fig. 4.2, p. 70) are found far south of the southernmost position of the Eurasian margin (Fig. 5.3, p. 109).

Anomaly Ic from the *ARS* group is positioned between 1000-2200 km depth, which is even deeper than the older *BRS* group (Fig. 5.19). Only with faster ($\sim$2 cm/yr) sinking rates in the lower mantle, this deep level can be reached within the required $\sim$80 Myr. As slabs have been found to sink faster in regions with abundant subduction in the same area (e.g. *Steinberger*, 2000), the relatively high convergence rates between $\sim$90-50 Ma in the Indian region (Fig. 5.16, p. 140) may have led to these faster sinking rates indeed. Anomaly Hi [1] was identified separately from anomaly Ic because their geometries and positions are clearly different (e.g. Fig. 4.2, p. 70), but they belong to the same oceanic basin according to this scenario.

As opposed to the Aegean/Arabian region, subduction scenario I seems to adequately predict the subdivision of the volumes in the Indian region. On the other hand, the lateral distribution of the volumes can - again - not be readily explained by its simple evolution.

Subduction scenario III   In this subduction scenario, the predicted volume of the *BRS* material subducted prior to 120 Ma is small. In the lower panel of Figure 5.12 this *N-T-BRS* volume is compared with the lower 1800-2200 km part of anomalies Ic and Io. The $0.35 \cdot 10^9$ km^3 volume of Ic and Io in this depth interval (Fig. 5.19) can be explained by the $0.3 \cdot 10^9$ km^3 of *N-T-BRS* if slab thickening by a factor of 3 is taken into account. The predicted *ARS* volume is similar to the remaining tomographic volumes in the region if the slabs have kept their plate-like geometry (see Table 5.4), but is smaller if the slabs have thickened in the mantle (Fig. 5.12), which is likely to be the case. Because of the relatively old age of the subducting oceanic lithosphere (Table 5.7, p. 141), the predicted thermal volumes for the different spreading scenarios are similar. If the subducted slabs have thickened by a factor of 3, the T/P-ratios of 1.2-1.6 actually leave room for the additional volume that was predicted for the Spongtang oceanic basin as well. Analogous to the Arabian region, the southward migrating Spongtang back-arc may have caused the *N-T* slab to flatten down over the whole width of anomalies Io and Ic between $\sim$120 and 65 Ma.

As discussed for subduction scenario I, the 1000-2200 km depth of anomaly Ic and 800-2000 km depth of anomaly Io could be reached in $\sim$35-95 Myr and 25-85 Myr, respectively, with sinking rates $\geq$2 cm/yr in the lower mantle. The *ARS* material subducted since 120 Ma can have reached these depths easily. Whereas in the previous subduction scenario the top of anomaly Io needed to be explained by subduction prior to 80 Ma, this needs to be prior to $\sim$65-50 Ma in scenario III only.

For sinking rates of 1 cm/yr in the lower mantle, the 90-50 Ma timespan of subduction would correspond to a depth interval of $\sim$1000-1400 km, which is actually where most of the material of anomalies Ic and Io can be found. In that case, the 1400-1800 km anomalies would correspond to sinking times of 90-130 Myr, and could be explained by the subduction of *ARS*
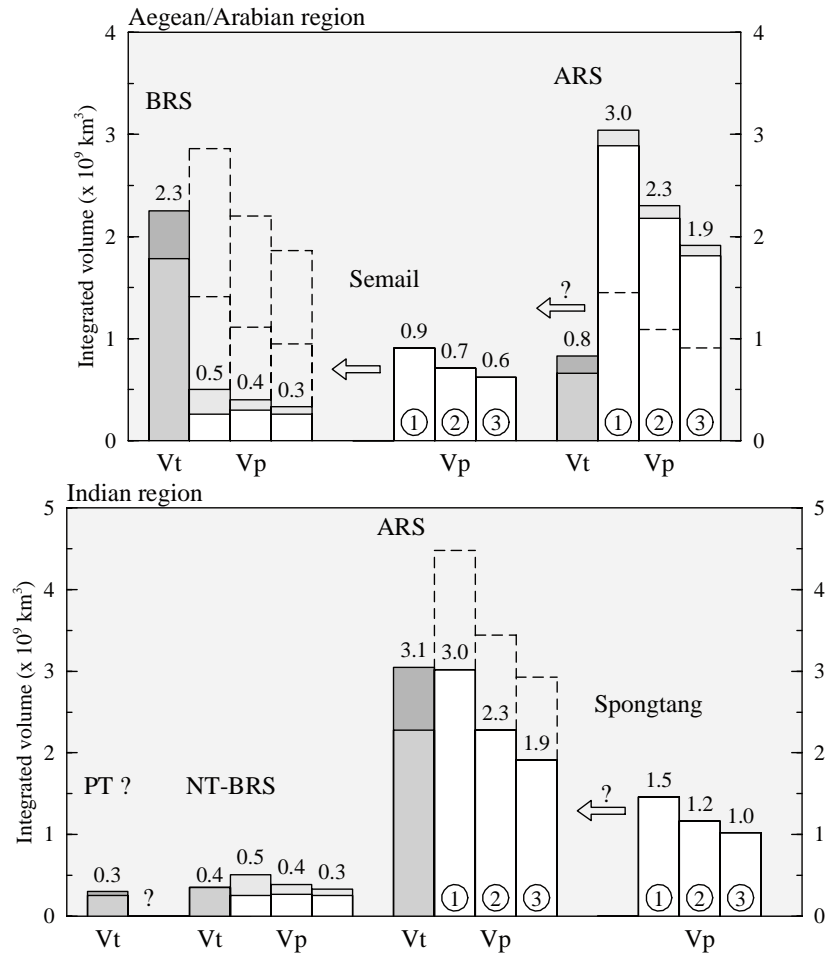
Figure 5.12: Subduction scenario III: Tomographic volumes (V_t) vs. predicted thermal volumes (V_p), divided into a part before ridge subduction (*BRS*) and a part after ridge subduction (*ARS*), for two end-member spreading scenarios (see p. 87). *Aegean/Arabian region* (upper panel): Ridge subduction at 140 Ma, and subduction of a separate Semail Ocean after 80 Ma. *Indian region* (lower panel): Ridge subduction at 120 Ma, and possible subduction of a separate Spongtang Ocean after 65 Ma. See text for further details and discussion. The calculations for undeformed slabs (1) can be found in Table 5.4, the factors necessary to perform the calculations for thickened slabs (2/3) in Table 5.7 (p. 141).

material since 120 Ma. Furthermore, the lower 1800-2000 km of these anomalies selected for the *BRS* volumes would correspond with sinking times $\geq$130 Myr.

With a sinking rate of 2 cm/yr in the lower mantle, the 1400 km depth of anomaly Hi[1] must have been reached in a total 50-60 Myr, which is in agreement with the subduction of the Spongtang basin since $\sim$65 Ma. However, for a 1 cm/yr sinking rate, the 1400 km depth of Hi[1] would require subduction since 90 Ma already. The 500-km deep top of anomaly Hi[1] could be reached in only 10-20 Myr with normal upper mantle sinking rates, which would require a large delay-time for slab break-off after continental collision around 48 Ma. This will be be discussed separately in Section 5.7 on the Cenozoic continental collisions.

The idea that the >1400 km deep volumes of anomalies Ic and Io are the result of subduction prior to 90 Ma may provide a solution for another interesting phenomenon in the Indian region: As can be seen in Figure 4.2 and 4.3 (pp. 70-71), anomaly Ic can be found over the full width of our trench system, and actually connects to the deep mantle anomalies beneath Indonesia below $\sim$1000 km depth. Only the small part of anomaly Ic close to Hi[1] is found above 1000 km (cf. Fig. 5.2), and within the restricted area (e.g. see Fig. 4.5). On the contrary, anomalies Hi[1] and Hi[2] fade away east of section 115, and also the larger part of anomaly Io underneath the Indian Ocean is restricted to the western part of the Indian region. In fact, anomaly Io can only be found east of $\sim$section 115 below 1400 km depth. An explanation for this feature could be that the fast northward motion of the Indian continent since 90 Ma resulted in a large-scale strike-slip motion on the eastern boundary of the plate, similar to the motion that has produced the gap between Arabian and Indian anomalies on the western side. Such a process has been suggested by *Stampfli and Borel* (2002, 2004) indeed (e.g. Fig. 2.6, p. 25), and may have affected the geometry of anomaly Io since 90 Ma. Ic has probably been affected only since $\sim$50 Ma, as this would correspond to the sinking time needed to reach the $\sim$1000-km depth of the anomalies extending east of section 115.

Conclusions

For the investigated subduction scenarios (p. 106), we found that:

Subduction scenario I can well explain the tomographic volumes in the Arabian and Indian region if the *N-T* slabs have thickened by a factor 2 at least. However, in all three reference frames the southern anomalies are positioned too far south to be explained by subduction at the Eurasian continental margin alone.

Subduction scenario II, for the Arabian region, does predict subduction at the right location, as opposed to scenario I. However, we found that subduction scenario II can only explain the tomographic volumes if (a) the Eurasian continental margin has been as far south in Late Mesozoic times as suggested by the fixed hotspot reference frame of *Müller et al.* (1993), (b) the total *N-T* slab has thickened by a factor of 2 at least, and (c) the distance between the Tethyan spreading ridge and the Arabian continental margin has been larger - in the order of 1000 km - than proposed by the tectonic reconstructions discussed here.

Subduction scenario III includes the opening of two large back-arc oceanic basins at the Eurasian margin, and is therefore least sensitive to the exact position of Eurasia. This subduction scenario was found to well explain the absolute locations of the tomographic anomalies in all three reference frames. Moreover, the scenario predicts thermal volumes - including

those of the separate Semail and Spongtang oceanic basins - that are in agreement with the tomographic volumes as well, if (a) the *N-T* and back-arcs slabs have thickened by at least a factor of 2 and 3, respectively, and (c) trench migration due to the Semail and Spongtang back-arc spreading has caused extensive flattening of the subducting *N-T* slabs.

We clearly prefer scenario III - based on the most recent reconstruction of *Stampfli and Borel* (2004) - for the Late Mesozoic-Cenozoic subduction of Tethyan lithosphere in the Indian region. The relative small, and westwardly decreasing, distances between the Arabian and Eurasian continental margins make it difficult to distinguish between the proposed scenarios for the Arabian region. However, as the absolute plate motions are quite uncertain, and subduction scenario II requires additional constraints that seem to be in contradiction with the tectonic reconstructions underlying the scenario (*Dercourt et al.*, 1993; *Şeng ör and Natal'in*, 1996), we prefer scenario III for the Arabian region as well. It thus appears that the tectonic model that explicitly incorporated the evolution of the plate boundaries through time (see Section 2.2, p. 15) can best explain the tomographic anomalous volumes associated with subducted Tethyan lithosphere.

5.7 Slab break-off after Cenozoic continental collisions

5.7.1 Timing of Tethyan slab break-off

Continent-continent collisions can cause slabs to break off and sink into the mantle (*Van den Beukel*, 1992; *Davies and von Blanckenburg*, 1995; *Wong A Ton and Wortel*, 1997; *Van de Zedde and Wortel*, 2001). The process of slab break-off depends on a wide range of parameters, including the thermal structure of the subducting plate and the convergence velocity. In general, subduction of colder continental lithosphere will lead to a deeper break-off depth after a longer timespan. Faster subduction rates also result in break-off at deeper levels, but after a much shorter timespan. *Van de Zedde and Wortel* (2001) showed that fast (about 6 cm/yr) subduction of continental lithosphere can lead to slab detachment at 140-330 km downdip distance from the trench, corresponding to ∼40-120 km depth, already 3-5 Myr after the onset of continental collision. Slower subduction rates (about 1 cm/yr) have been found to lead to slab detachment at 130-250 km downdip distance from the trench, corresponding to ∼35-80 km depth, after 17-25 Myr only.

Following the reconstruction of ExxonMobil, we assume that the Arabia vs. Eurasia and India vs. Eurasia continental collisions occurred around 22 Ma and 48 Ma, respectively (Fig. 2.2, p. 17). In the period of continental collision in the Arabian region, the rate of subduction, i.e. the trench-normal component of the relative velocity vector, ranged from 2.2 cm/yr in the west to 2.8 cm/yr in the east. During the collision event in the Indian region, the subduction velocities dropped from 12 to 5 cm/yr in the west, and from 13 to 6 cm/yr in the east.
We assume here that the Arabian and Indian continents had an average thermal structure (*Pollack et al.*, 1993), with a surface heat flow of 60 mW/m^2. Following *Van de Zedde and Wortel* (2001), the subduction rates of ∼3 cm/yr in the Arabian region are likely to have caused the subducting slab to break off ∼10 Myr after the onset of continental collision,

thus around 12 Ma. This could be somewhat later in the western part of the area, where the subduction rate of 2 cm/yr could have caused the slab to detach ~12 Myr after collision, i.e. around 10 Ma. For the Indian region, the high subduction rates (> 6 cm/yr) can be associated with slab break-off after ~5 Myrs only, thus around 43 Ma. Again, the somewhat lower subduction rates in the west could have led to a later break-off time. For both regions, slab break-off is assumed to have occurred at a 300-km downdip distance from the trench, corresponding to a depth of ~100 km. We assume that the detached volumes of lithospheric material have descended into the mantle vertically.

Recently, *Keskin* (2003) argued that slab steepening and break-off beneath Eastern Turkey has been the major controlling mechanism for the rapid block uplift and volcanism in the region around 10-11 Ma. *Kohn and Parkinson* (2002) suggested that slab break-off in the Himalaya around 40-45 Ma caused the production of K-rich lavas - associated with subcontinental lithosphere being exposed to asthenospheric upwelling (*Chung et al.*, 1998) - by 40 Ma. The break-off times for the Arabian and Indian slabs inferred from the *Van de Zedde and Wortel* (2001) models are in agreement with these studies.

5.7.2 Predicted and tomographic slab volumes

From the thermal volumes predicted for the subducted plate surfaces, as well as from the tomographic volumes, we separate the part that we expect to haven broken off after continental collision to isolate the smaller volumes that will be completely detached from the volumes lower in the mantle today (Fig. 5.13). In the following, we will refer to the volumes that have been detached after continental collision, and are continuous (C) with the deeper (D) volumes, as *CD*. The volumes that are still attached (A) to the surface after slab break-off (B), and thus *not* continuous with the volumes deeper in the mantle, are denoted by *AB*.

Figure 5.13: Isolation of the volumes that are still attached to the surface after slab break-off (*AB*) from the volumes that have been detached after continental collision and are still continuous with the deeper volumes (*CD*). If *no* slab break-off took place, as in the Aegean region, the whole slab is denoted *CD*.

Subducted plate surfaces

For the Arabian region (upper panel Fig. 5.16, p. 140), *group CD* is the slab that we expect to have been detached at 12 Ma after continental collision around 22 Ma. Here, *group AB* consists of the slab left attached after break-off, which corresponds to ~300 km of convergence, as well as the surface subducted since that time. In subduction scenarios I and II, the *ARS* volume of the Neo-Tethys discussed in the previous section will be used to create an *AB* and *CD* volume. Note that the oceanic lithosphere in the Aegean region is not assumed to

be detached from the surface: It is kept in group *CD* because the upper mantle volumes will be continuous with the volumes lower in the mantle still, as opposed to the volumes in group *AB*. In subduction scenario III, only the volume of the Semail oceanic basin will be split up. For the Indian region (lower panel Fig. 5.16, p. 140), *group CD* is the slab that we expect to have broken off at 43 Ma after continental collision around 48 Ma, corrected for the down-dip depth of detachment. Again, the Neo-Tethyan *ARS* slab will be used to create an *AB* and *CD* volume in subduction scenarios I and II. In subduction scenario III, the *CD* volume is the remaining part of the Spongtang Ocean only.

Because the top 230 km of the tomographic model has not been taken into account, we approximate the convergence likely to be accommodated in this depth interval (see also Section 4.3, p. 81): For the part of the Tethyan region that is at present in continental collision, the amount of convergence that needs to be subtracted from the total value will be about 100 km. For 100 km of convergence, the surface that is accommodated in the top 230 km will be $0.31 \cdot 10^6$ km^2 in the Arabian and $0.22 \cdot 10^6$ km^2 in the Indian region. When taking into account these estimates, the surface of group *AB* decreases with 15% in the Arabian region, and with 4% in the Indian region. The values shown in the second column of Table 5.5 are corrected for the part assumed to be accommodated in the top 230 km.

Present thermal signature of subducted material

Including the effect of continental collision will not change the average age of the subducted oceanic basins discussed in the previous sections. To calculate the initial lithospheric thicknesses and the thermal factors, we therefore use the ages of the *ARS* part of the Neo-Tethys (subduction scenarios I and II) and the Semail/Spongtang lithosphere (subduction scenario III) here (Table 5.7, p. 141). Calculations with the thermal structure of continental instead of oceanic lithosphere could increase the volumes a little more.

For the material of *group* CD we use the values for $c_1(t)$, $c_2(t)$, and $c_3(t)$ that where used for the *ARS* Neo-Tethys and Semail/Spongtang oceans in the previous section. After slab break-off, the detached material will sink further down into the mantle, and warm mantle material will fill the gap above it. The slabs of *group* AB will therefore penetrate into relatively unperturbed mantle again, leading to lower thermal factors. For the Indian region, we therefore use the values at $t = 43$ Myr, and for the Arabian region at $t = 12$ Myr. The predicted volumes for undeformed slabs are shown in Figure 5.14 and Table 5.5-5.6. For these slabs, the volumes estimated with $c_1(t)$ may *over*estimate the actual values with at most 10% (Section 3.3.3), but this will not significantly change the results. Because of the brief residence times t in the mantle, the differences of $c_2(t)$ and $c_3(t)$ with $c_1(t)$ are only small, and the associated thermal volumes accordingly. Moreover, the *AB* volumes are approximately similar for both spreading scenarios, and for all three subduction scenarios.

Volumes of seismic anomalies

Anomalies Ca, Zs and IA[1] in the upper mantle of the Arabian region (upper panel Fig. 5.17, p. 142) are assumed to represent the material still attached to the surface after slab break-off, and are considered as *group AB*. For subduction scenarios I and II, the complete Aegean

anomalies Gr, wT and eT are put together with the Arabian lower mantle anomalies Eg, SI, IA[2] and SA into *group CD* (Table 5.5). For subduction scenario III, a separate tomographic *CD* volume cannot be given because the subducted Semail back-arc basin is assumed to be incorporated in the same (SI and IA[2]) anomalies as the *N-T* volumes (see Section 5.6). Analogous, we isolate the volumes for the Indian *group AB* by taking only the upper mantle anomalies HK and sT (upper panel Fig. 5.17, p. 142). For subduction scenarios I and II, *group CD* consists of all the larger lower mantle anomalies, except for anomaly Hi[2]. For subduction scenarios III we have not yet assigned a particular volume to the Spongtang oceanic basin, but this volume may be represented by anomaly Hi[1] underneath the Indus-Tsangpo Suture (Fig. 5.17).

5.7.3 Comparison and conclusions

Arabian region

In the Arabian region, the T/P-ratios for the upper mantle *group AB* are found to be 0.6-1.0 to 0.7-1.2 (see Table 5.5 and 5.6). As can be seen in Figure 5.14 (left), the predicted thermal volumes are thus somewhat larger than the minimum tomographic volumes, and approximately similar to the maximum volumes, and do not depend on the possible amount of thickening.

Volumes AB/CD	$V_{t(omo)}$ ($\cdot10^9$ km^3)	$S_{s(ubducted)}$ ($\cdot10^6$ km^2)	$V_{i(nitial)}$ ($\cdot10^9$ km^3)		$V_{p(redicted)}$ ($\cdot10^9$ km^3)		$V_{t(omo)}/V_{p(redicted)}$ (T/P-ratio)	
			A	*B*	*A*	*B*	*A*	*B*
Aeg/Arab								
AB	$0.13-0.23$	1.70	0.19 /	0.19	0.23 /	0.23	$0.57-1.02$ /	$0.57-1.02$
ARS *CD*	$1.65-2.02$	5.18	0.57 /	0.57	1.03 /	1.03	$1.60-1.96$ /	$1.60-1.96$
Indian-43								
AB	$0.08-0.13$	4.97	0.52 /	0.55	0.81 /	0.85	$0.10-0.16$ /	$0.09-0.15$
ARS *CD*	$1.59-2.01$	8.15	0.86 /	0.90	1.52 /	1.62	$1.05-1.32$ /	$0.98-1.24$
Indian-20								
AB	$0.08-0.13$	1.71	1.89 /	1.89	0.25 /	0.25	$0.32-0.52$ /	$0.32-0.52$
ARS *CD*	$1.59-2.01$	11.41	1.19 /	1.25	2.13 /	2.27	$0.75-0.94$ /	$0.70-0.89$

Table 5.5: Subduction scenario I: Comparison of *ARS* part of *N-T* volumes as in Table 5.3, but now when incorporating slab break-off after continent-continent collisions in the Arabian at 22 Ma and Indian region at 43 Ma. From the tomographic volumes for the Arabian region we have separated Ca+Zs+IA[1], and for the Indian region HK+sT, for the *group AB* that represents the material assumed to be still attached to the surface after break-off (Fig. 5.17). The volumes that are detached, or still continuous with the deeper volumes, are denoted *CD*. The subdivision of the subducted surface is illustrated in Figure 5.16. *Lowermost panel*: Alternative calculations for the Indian region to illustrate the effect of slab detachment at 20 Ma instead of the 43 Ma assumed above (break-off depth not taken into account). The predicted *AB* volumes are corrected for the surface that is expected to be accommodated in the top 230 km of the Earth. Subduction scenario II, not shown here, results in approximately the same *AB* volumes as scenario I. For the discussed *AB* slabs, the predicted volumes including slab thickening, calculated with the appropriate factors from Table 5.7 (p. 141), are shown in Figure 5.14.

Volumes AB/CD	$V_{t(omo)}$ ($\cdot 10^9$ km^3)	$S_{s(ubducted)}$ ($\cdot 10^6$ km^2)	$V_{i(nitial)}$ ($\cdot 10^9$ km^3) A B	$V_{p(redicted)}$ ($\cdot 10^9$ km^3) A B	$V_{t(omo)}/V_{p(redicted)}$ (T/P-ratio) A B
Arabian					
AB	$0.13-0.23$	1.70	0.16 / 0.16	0.19 / 0.19	$0.68-1.21$ / $0.68-1.21$
Sml. *CD*	?	3.50	0.33 / 0.33	0.58 / 0.58	?
Indian-43					
AB	$0.08-0.13$	4.97	0.47 / 0.47	0.74 / 0.74	$0.11-0.18$ / $0.11-0.18$
Spt. *CD*	$0.40-0.65$	4.40	0.42 / 0.42	0.67 / 0.67	$0.60-0.97$ / $0.60-0.97$
Indian-20					
AB	$0.08-0.13$	1.71	1.16 / 1.16	0.22 / 0.22	$0.36-0.59$ / $0.36-0.59$
Spt. *CD*	$0.40-0.65$	7.66	0.73 / 0.73	1.16 / 1.16	$0.35-0.56$ / $0.35-0.56$

Table 5.6: Subduction scenario III: Comparison of volumes when incorporating slab break-off as in Table 5.5, but now for ages of the Semail (Sml.) and Spongtang (Spt.) oceanic lithosphere based on *Stampfli and Borel* (2002, 2004). For the discussed *AB* slabs (i.e. left attached after break-off), the predicted volumes including slab thickening, calculated with the appropriate factors from Table 5.7 (p. 141), are shown in Figure 5.14.

The top of the detached slab in the Arabian region will have reached a depth of about 600 km after 12 Myrs of sinking from 100 km downwards at a rate of 3 cm/yr. Although with a somewhat higher sinking rate (say 5 cm/yr) the material will have reached the lower mantle indeed, some of the material may still reside in the upper mantle of this region today. Anomalies SI and IA[2], positioned underneath the Bitlis and Zagros Sutures in the Arabian region (Fig. 5.17, p. 142), can be found in the lower mantle only (Fig. 5.19, p. 144): In the eastern part of the region, the depth of the top of IA[2] is in agreement with the previous suggestions, as is the $\sim$700-km depth of the bottom of *AB* volume IA[1] (e.g. section 75 in Fig. 4.7, p. 76). However, anomaly SI seems to be too deep to be explained by realistic sinking velocities, and *AB* volume Zs above SI (Fig. 5.17) extends down to a 1000-km depth instead (e.g. section 55 in Fig. 4.7). The 1000-km depth of the bottom of Zs and the top of SI would require an earlier slab detachment in this region.

As can be seen in Figure 5.17 (p. 142), the most shallow anomalies above SI can be found in anomaly eT. Whereas the westernmost part of eT is continuous to the surface, the easternmost part is positioned right underneath anomaly Ca in the Caucasus (compare upper and middle panel of Fig. 5.17). Together with the clear gap between anomalies eT and Ca across the 660-discontinuity (e.g. section 35 of Fig. 4.7), this may indicate that the lower mantle volume of eT represents the detached part of the upper mantle volume Ca, and that break-off did not occur in the westernmost part of the Arabian region. If this is case indeed, the upper mantle part of anomaly eT thus bounds the region where slab break-off has occurred (around section 36), and the predicted volume of group *AB* should consist only of the Arabian surface east of section 36. This would somewhat decrease the volumes of group *AB*, but will not change the results significantly.

The lack of slab break-off west of section 36, a deep $\sim$1000-km extent of the tomographic
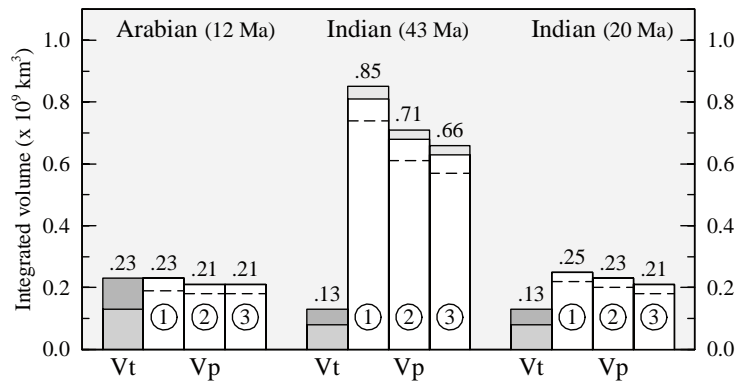
Figure 5.14: Subduction scenario I ($\sim$II): Tomographic volumes (V_t) vs. predicted thermal volumes (V_p) for the slabs in *group AB*, i.e. the volumes that were left attached to the surface after slab break-off (see Fig. 5.13). In the Arabian region, the break-off time is assumed to be 12 Ma. In the Indian region, both slab break-off at 43 Ma and 20 Ma is considered. The values of V_p are corrected for the part assumed to be accommodated in the top 230 km. The dotted lines for the predicted *AB* volumes indicate the values for subduction scenario III. The calculations for undeformed slabs (1) can be found in Table 5.5/5.6, the factors necessary to perform the calculations for thickened slabs (2/3) in Table 5.7 (p. 141).

AB volume in the central area (sections 45-60), and a $\sim$660-km boundary between the upper and lower mantle anomalies east of section 60, may illustrate the lateral variation in the response on the continental collision event (see also section C in Fig. 4.8, p. 77). As tectonic reconstructions generally suggest a first continental contact along the width of the Zagros suture zone, approximately between section 40 and 70 of our trench system, this may indicate that slab break-off occurred relatively quickly in the central Arabian region. There is no consensus on when precisely collision between the Arabian and Eurasian plates began. The age estimates of collision range from Early Miocene, as assumed here (e.g. *Gealey*, 1988; *Norton*, 1999; *Şengör and Natal'in*, 1996), to Oligocene times (e.g. *Dercourt et al.*, 1993; *Jolivet and Faccenna*, 2000). An earlier collision time could have led to slab detachment before 12 Ma in the central Arabian region. Subsequently, the tear in the slab may have propagated along the suture zone towards the east and west, leading to slab break-off around the expected 12 Ma underneath Turkey, as well as southern Iran. In the most western part of the Arabian region, convergence velocities may have been too low to lead to slab detachment.

An alternative explanation for III could be that *no* Cenozoic slab break-off occurred, and that the complete Semail oceanic lithosphere is represented by the tomographic volumes of group *AB*. However, as can be seen in Table 5.6, the total thermal volume predicted for the Semail remnants is much too large to be explained by these tomographic volumes alone. When assuming that the Semail oceanic basin had completely overridden the Neo-Tethys by a time later than the 80 Ma taken in Section 5.6, the predicted thermal volumes will decrease significantly (about 30% when using 65 Ma instead of 80 Ma) but not enough to level with the tomographic volumes.

Indian region

For the upper mantle *group AB* in the Indian region, a T/P-ratio of 0.1-0.2 is found for both spreading scenarios, and all three subduction scenarios (Table 5.5-5.6). As can be seen in Figure 5.14, the predicted volume is much larger than can be found in the tomographic model. One explanation for this discrepancy is that the missing tomographic anomalies all reside in the uppermost 230 km of the mantle, which seems not unlikely from Figure 4.7 (e.g. section 95) and Figure 4.8 (e.g. section E and F), and that the estimates made for the top 230 km are too simple for this region. The continuing convergence between India and Eurasia is not necessarily accompanied with the actual subduction of (continental) lithosphere into the mantle, and is probably accommodated partly by the further deformation of the older continental fragments and lithospheric thickening as illustrated schematically in Figure 5.15. Another explanation is that slab break-off took place much later than 43 Ma, in which case a larger slab volume *CD* will be found in the lower mantle today, and a smaller volume *AB* attached to the surface. This alternative scenario will be discussed below.
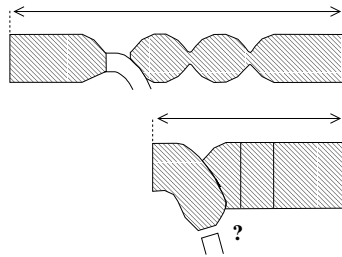
Figure 5.15: Continuing convergence between India and Eurasia after continental collision, possibly leading to slab break-off, is likely to be accommodated partly by the further deformation of the older continental fragments and lithospheric thickening.

Starting from a break-off depth of 100 km, the top of the detached Indian slab can have reached a depth of about 900 km in 43 Myrs, with a modest sinking rate of 3 cm/yr in the upper mantle and 1 cm/yr in the lower mantle. As completely detached material may sink even faster (e.g. *Bunge et al.*, 1998; *Han and Gurnis*, 1999; *Steinberger*, 2000), reaching the lower mantle cannot have been a problem for this material. Indeed, the bulk of the anomalies in the Indian region is positioned below 800 km depth (Fig. 5.19, p. 144). However, anomaly Hi[1] - found right beneath the Indus-Tsangpo Suture (Fig. 5.17) - covers a ~500-1500 km depth interval (Fig. 5.19), which allows for even lower sinking velocities or a later break-off time.

Note that in subduction scenarios I and II, the predicted *CD* volumes are much larger than the tomographic volumes (Table 5.5), even when slab thickening would be incorporated (not shown separately, but see thermal factors in Table 5.7). In subduction scenario III, the Spongtang *CD* volume fits the maximum tomographic volumes of Hi[1] well (Table 5.6). However, when slab thickening would be taken into account, the predicted volume becomes clearly smaller than the tomographic volumes (see thermal factors in Table 5.7).

Alternative scenario for Indian slab break-off

Within the Himalayan chain, two periods of magmatic activity are generally recognised: An early igneous phase ($\sim$55-45 Ma) associated with continental subduction, and a later episode ($\sim$35-20 Ma) caused by decompression of depleted mantle, c.q. partial melting (e.g. *Harrison et al.*, 1998; *Bertrand et al.*, 2001; *Danishwar et al.*, 2001; *Kohn and Parkinson*, 2002; *Mahéo et al.*, 2002). *Kohn and Parkinson* (2002) concluded that slab break-off in the Himalaya occurred no earlier than 45-55 Ma, as mentioned above, but they also argue that possibly a younger break-off age ($\sim$22 Ma) could be accommodated by placing greater emphasis on younger (ca. 25 Ma) K-rich lavas. Likewise, *Chung et al.* (1998) proposed that the occurrence of the two potassic magma suites suggests a diachronous break-off of the Indian slab, i.e. around 40 Ma in the east, and 20 Ma in the west. Also *Mahéo et al.* (2002) found that slab break-off in the Himalayas starting around 25-20 Ma could well explain the magmatic activities in west Tibet.

To examine the effect of slab detachment at 20 Ma instead of 43 Ma, we consider here the surface of $19.9 \cdot 10^6$ km^2 that must have been subducted prior to 20 Ma in the Indian region. Using adjusted values for the thermal factors (see Table 5.7, p. 141), we arrive at predictions for the thermal *AB* volumes of $0.2\text{-}0.3 \cdot 10^9$ km^3 still attached to the surface. As can be seen in Figure 5.16 and Table 5.5-5.6, these attached volumes differ a factor 0.3-0.5 with the tomographic volumes within the upper mantle, which is still an overestimate but is in better agreement than the previous calculations. Within 20 Myrs time, the slab volume can have sunk to about 600 km depth when sinking at 3 cm/yr, which is still deep enough to properly explain the top of anomaly Hi[1] (Fig. 5.19, p. 144).

Note that in subduction scenarios I and II, the predicted *CD* volumes are now much larger than the tomographic volumes (Table 5.5), but they would be in agreement when incorporating slab thickening (see thermal factors in Table 5.7). In subduction scenario III, the Spongtang *CD* volume is approximately twice the tomographic volume of Hi[1] (Table 5.6). If slab thickening by a factor of 3 would be taken into account, the predicted volume would be $\sim$25% smaller, but still larger than anomaly Hi[1].

Conclusions

For the Arabian region, our results indicate that slab break-off probably occurred first, and before 12 Ma, in the northern Zagros suture zone. Propagation of this tear led to slab detachment around 12 Ma in the east as well as in the western part of the region until $\sim$40° longitude.

In the Indian region, slab detachment at 20 Ma is found to best explain the size and depths of the volumes assumed to be left attached at the surface after break-off. If detachment occurred already at 43 Ma, a large amount of lithosphere must have been accommodated in the upper 230 km of the Earth. An intermediate scenario was found to best explain the detached volumes lower in the mantle: Such diachronous slab break-off, starting at 43 Ma in the eastern Himalayas but occurring only around 20 Ma in the central and western Himalayas, would be in accordance with geological studies (e.g. *Chung et al.*, 1998).
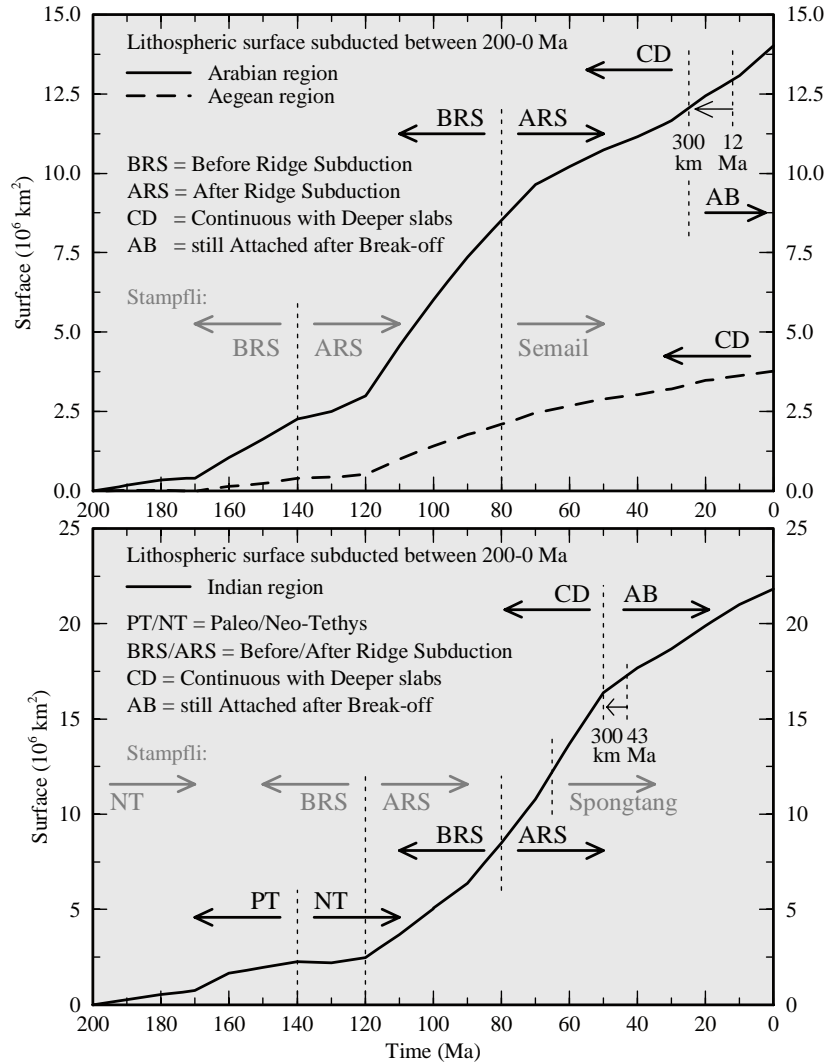
Figure 5.16: Division in separate oceanic basins for both the Aegean/Arabian (top) and the Indian (bottom) region as discussed for subduction scenario I. The alternative subdivision for subduction scenario III, based on the reconstruction of *Stampfli and Borel* (2002, 2004), is given in grey as well. In these figures: PT/NT = Paleo vs. Neo-Tethys (Indian region only, Section 5.5), BRS/ARS = Before vs. After Ridge Subduction (Section 5.6), and CD/AB = Continuous with Deeper slabs vs. still Attached after Break-off (Section 5.7).

	Age (Ma)	y_L (km)	t (Myr)	$c_1(t)$	$c_2(t)$	$c_3(t)$
5.4: Whole Tethys: ExxonMobil ($\sim$ Subduction scenarios I & II)						
Aeg/Arab	65/125	95/110	200	2.0/2.2	1.6	1.3
Indian	60/80	95/105	200	2.0/2.1	1.6	1.3
5.4: Whole Tethys: Stampfli ($\sim$ Subduction scenario III)						
Aeg/Arab	65/85	95/105	200	2.0/2.1	1.6	1.3
Indian	70/110	100/110	200	2.0/2.2	1.6	1.3
5.5: Separate Paleo-Tethys in Indian region ($\sim$ Subduction scenarios I & II only)						
Indian *N-T*	55/85	90/105	140	1.9/2.0	1.5	1.3
P-T	65/75	95/100	200	2.0/2.1	1.6	1.3
5.6: Neo-Tethyan Ridge subduction at 80 Ma ($\sim$ Subduction scenario I)						
Aeg/Arab						
ARS	125/185	110/110	80	1.8/1.8	1.4	1.2
BRS	35/95	75/105	200	1.3/2.2	1.5/1.6	1.3
Indian *N-T*						
ARS	85/115	105/110	80	1.8/1.8	1.4	1.2
BRS	40/70	80/100	140	1.7/2.0	1.5	1.3
5.6: Neo-Tethyan Ridge subduction at 140 and 120 Ma ($\sim$ Subduction scenario III)						
Aeg/Arab						
Semail	60	95	80	1.7	1.4	1.2
N-T ARS	95/125	105/110	140	2.0/2.0	1.5	1.3
BRS	35/65	75/95	200	1.3/2.0	1.5/1.6	1.3
Indian						
Spongtang	65	95	50	1.6	1.3	1.1
N-T ARS	110/150	110/110	120	2.0/2.0	1.5	1.3
BRS	35/75	75/100	200	1.3/2.1	1.5/1.6	1.3
5.7: ARS Slab break-off at 12 and 43/20 Ma: Subduction scenario I ($\sim$ II)						
Aeg/Arab *AB*	125/185	110/110	12	1.2/1.2	1.1	1.1
Indian *AB*-43	85/115	105/110	43	1.6/1.6	1.3	1.2
AB-20	85/115	105/110	20	1.3/1.3	1.2	1.1
5.7: Semail/Spongtang Slab break-off at 12 and 43/20 Ma: Subduction scenario III						
Aeg/Arab *AB*	60	95	12	1.2	1.1	1.1
Indian *AB*-43	65	95	43	1.6	1.3	1.2
AB-20	65	95	20	1.3	1.2	1.1

Table 5.7: Overview of the values used to predict the initial and present thermal volumes of the lithosphere subducted in the Tethyan region. For the various oceanic basins in this chapter are given here: The average lithospheric age upon subduction for spreading scenario *A* (left) and *B* (right) as on p. 87, the initial thermal thickness y_L of oceanic lithosphere of this age, and the residence time t of the slab within the mantle. The last three columns give the thermal factors with which the initial thermal volumes will be multiplied to approximate the present thermal volumes of the subducted lithosphere: $c_1(t)$ for a subduction process where the slabs kept their plate-like geometry and did not thicken, $c_2(t)$ for slabs that have thickened by a factor of 2, and $c_3(t)$ for slabs that have thickened by a factor of 3.
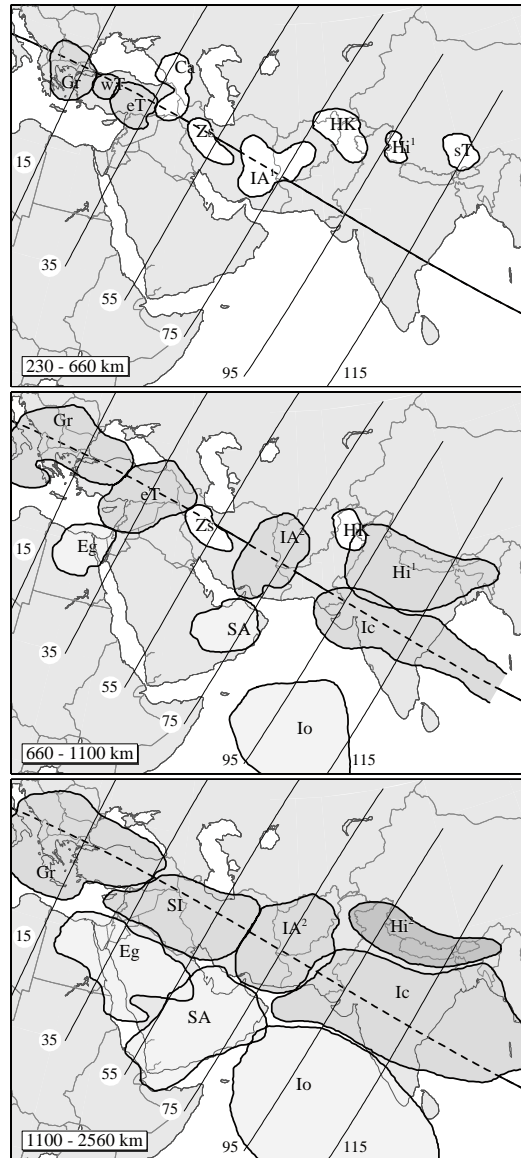
Figure 5.17: Overview of the tomographic anomalies that are considered to represent volumes of subducted Tethyan lithosphere between 230-660 km depth (upper panel), 660-1100 km depth (middle panel), and 1100-2560 km depth (lower panel). The contour line of every body is a projection of its maximum horizontal extension in the given depth interval. In these figures the colours indicate the subdivision of the volumes in this chapter: *White* (upper + middle panel only) = *AB* volumes discussed in Section 5.7; *Lightest grey* (middle + lower panel only) = *BRS* volumes of Section 5.6 for subduction scenario I; *Middle grey* (all panels) = *ARS* volumes of Section 5.6 for subduction scenario I; *Darkest grey* (lower panel only) = Possible *P-T* volume addressed in Section 5.5.
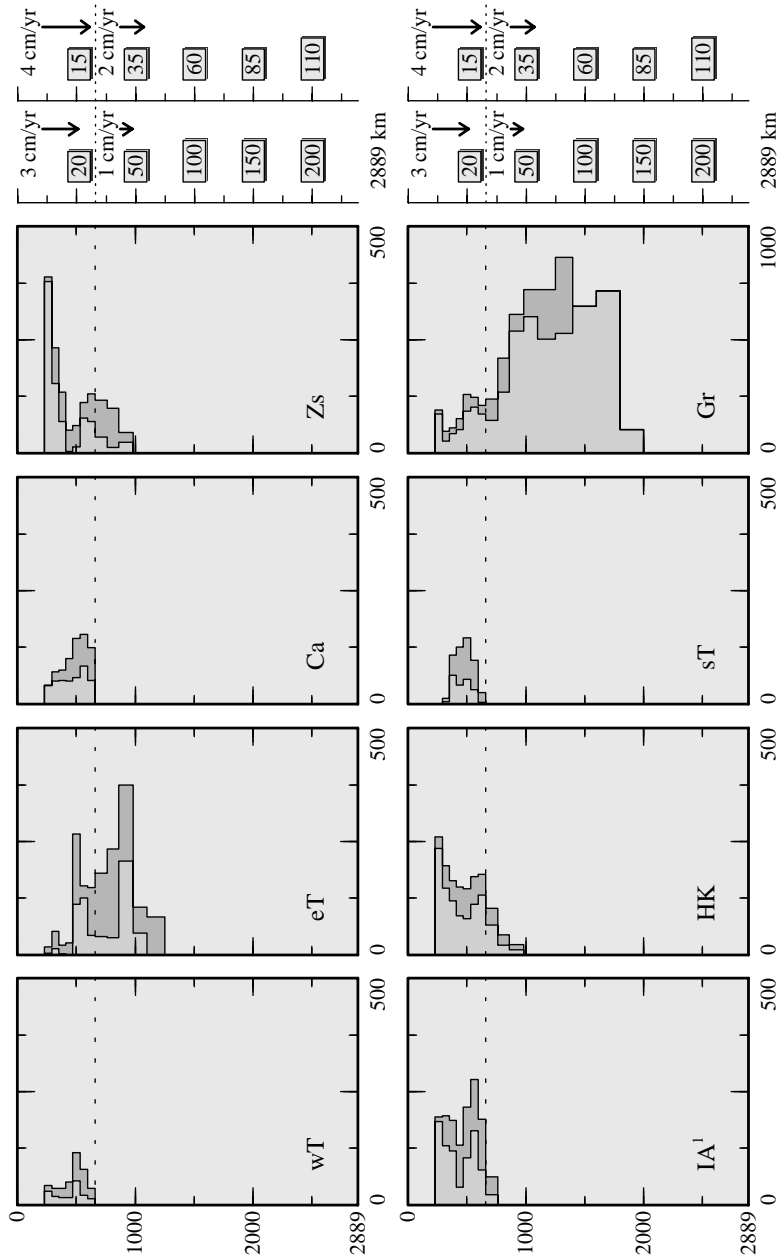
Figure 5.18: Distribution of the total minimum and maximum volumes of the separate tomographic anomalies: Shown depths range from 0-2889 km, with the anomalies integrated over a depth interval of 230-2560 km. The volumes of the anomalies range from 0-500·10^3 km^2, except for the volume of anomaly Gr (lowerright panel) that ranges from 0-1000·10^3 km^2. Rightmost panels: The approximate time (Myrs) needed for subducted material to reach the shown depths when sinking with a rate of 3–4 cm/yr in the upper mantle and 1-2 cm/yr in the lower mantle. Note that slab break-off after continental collision is assumed to occur at 100 km depth.

143
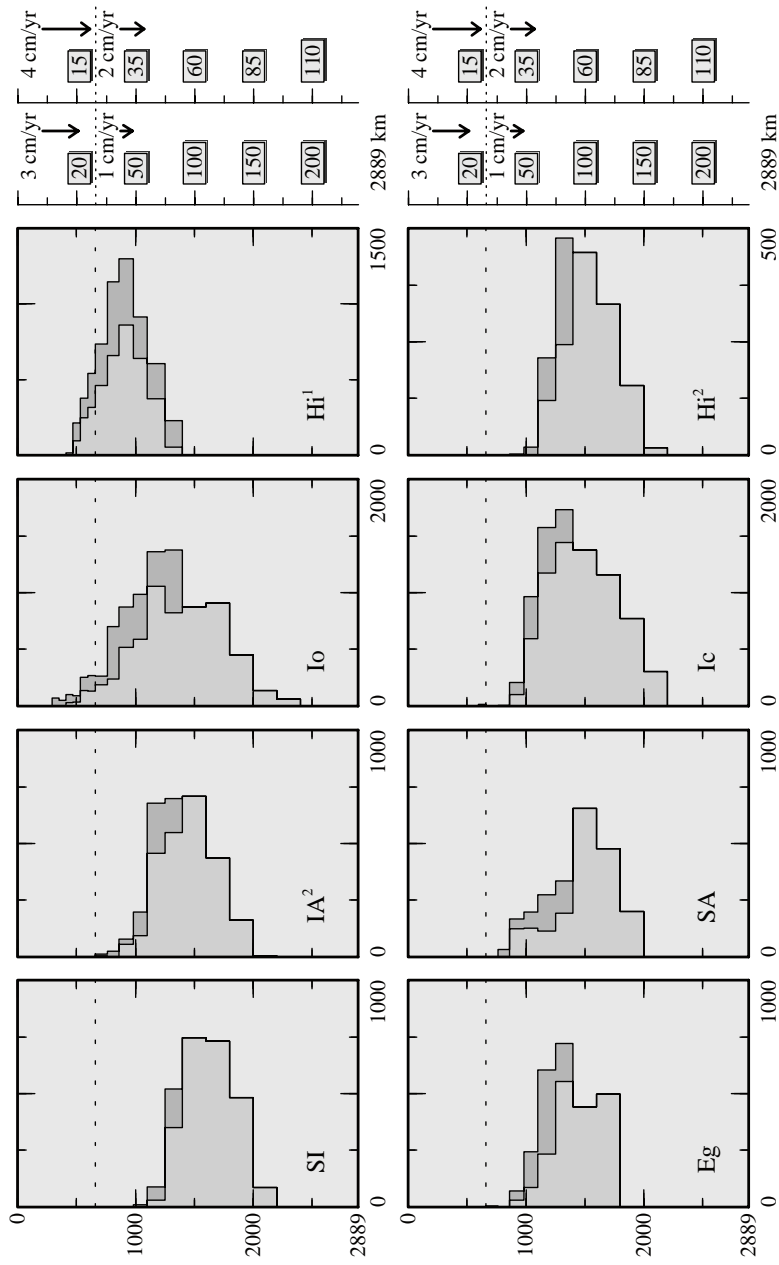
Figure 5.19: As in Figure 5.18. In this figure, the volumes of anomalies Eg, SA, SI and IA^2 (left four panels) range from 0-1000·10^3 km^2, and those of Io and Ic (third column panels) from 0-2000·10^3 km^2. The volume of anomaly Hi^1 (upperright panel) ranges from 0-1500·10^3 km^2, whereas the volume of anomaly Hi^2 (lowerright panel) ranges from 0-500·10^3 km^2 only.

5.8 Reconstructing the Tethyan history of subduction

5.8.1 Subduction scenarios for the Indian and Arabian regions

We here propose a scenario for the Late Mesozoic-Cenozoic subduction of the Neo-Tethyan oceanic lithosphere in the Indian and Arabian regions. This preferred model is based on the plate tectonic reconstruction of *Stampfli and Borel* (2004), to which we add our interpretation of the subduction process, and take into account also the absolute motion of the continental margins and the effects of the Cenozoic continental collisions as discussed above. Because the Paleo-Tethyan lithosphere has probably subducted prior to 200 Ma, it will not be discussed further here.

Illustrated in Figure 5.20 and 5.21 are the reconstructed scenarios for the Arabian region since 140 Ma and the Indian region since 120 Ma. The cross-sections for each region are representative for the bands of integrated tomographic anomalies shown in Figures 5.8 and 5.9 (p. 121). As the Arabian continental margin has not been exactly perpendicular to these sections (e.g. see Fig. 5.17), the southernmost anomalies in Figure 5.8 are the result of subduction further south - i.e. in a section further east - than illustrated in Figure 5.20.

Based on our analyses in the previous sections, we divide the subduction history into four phases:

1. Subduction of the Neo-Tethys underneath the Eurasian continental margin, followed by ridge subduction in Early Cretaceous times. The absolute positions of the continental margins are uncertain prior to 80 Ma, and are taken here with the Eurasian craton held fixed. The subducted part of the Neo-Tethyan lithosphere sinks down into the mantle slowly.

2. Subduction of the remaining part of the Neo-Tethys underneath the southward extending back-arcs of the Arabian Semail and Indian Spongtang Oceans, followed by the collision of the arcs onto the approaching Arabian/Indian continental margins. The relative fast trench migrations cause the slabs to flatten and spread over the full width of the back-arc basins.

3. After complete closure of the Neo-Tethys, around 80 Ma in the Arabian region and 65 Ma in the Indian region, the back-arc oceanic basins are being subducted underneath the Eurasian margin. As the Arabian/Indian continents move further northwards, the subducted Neo-Tethyan lithosphere is left behind within the underlying mantle.

4. Subduction of Arabian continental lithosphere underneath Eurasia causes the Semail slab to break off around 12 Ma, but probably somewhat earlier in the central Arabian region. Due to subduction of Indian continental lithosphere, detachment of the Spongtang slab starts at 43 Ma in the eastern Himalayas, but occurs only around 20 Ma in the central and western part of the Indian region.
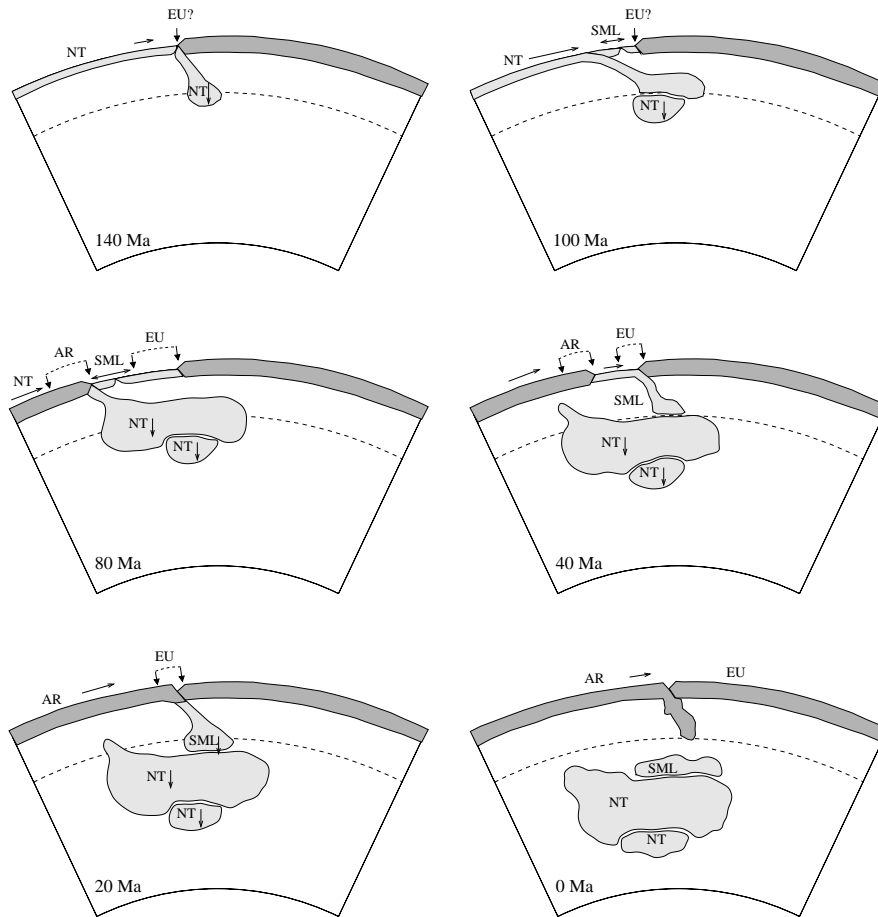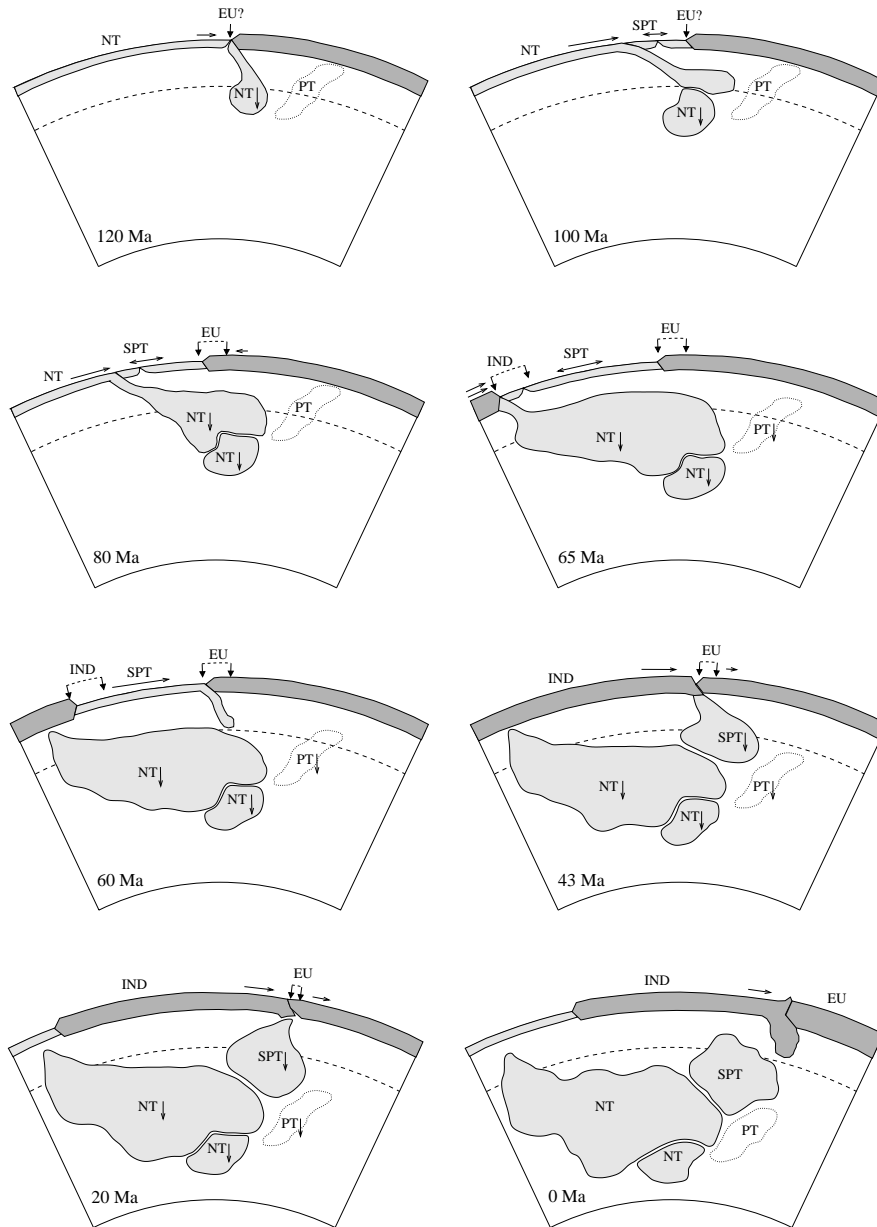
Figure 5.20: Reconstruction of the subduction history for the Arabian region from 140 Ma to present. The evolution is shown in an absolute reference frame, with the arrows indicating the uncertainties in the absolute position of the contintental margins (prior to 80 Ma unknown). *Key*: EU = Eurasia, AR = Arabia, NT = Neo-Tethys, SML = Semail. The cross-section for the present-day configuration is are largely representative for the band of integrated tomographic anomalies shown in Figure 5.8 (p. 121). Note that in that figure, the southernmost anomalies are the result of subduction further south - i.e. in a section further east, than illustrated in here.

Figure 5.21: Reconstruction of the subduction history for the Indian region from 120 Ma to present. The evolution is shown in an absolute reference frame, with the arrows indicating the uncertainties in the absolute position of the contintental margins (prior to 80 Ma unknown). *Key*: EU = Eurasia, IND = India, PT = Paleo-Tethys, NT = Neo-Tethys, SPT = Spongtang. The cross-section for the present-day configuration is representative for the band of integrated tomographic anomalies shown in Figure 5.9.

Implications for the Arabian region

Slab volumes   As illustrated in Figure 5.22, our preferred scenario implies that the part of the Neo-Tethyan lithosphere subducted before its ridge forms the present lowermost (depths $\geq$2000 km) volumes of anomalies SI and IA[2]. The remaining part of the lithosphere can be found both in these anomalies ($\sim$1100-2000 km depth) as well as in the southern anomalies Eg and SA ($\sim$800-2000 km depth). The Semail Ocean is incorporated in the top of anomalies SI and IA[2] again.

Our results for the preferred subduction scenario indicate that the Neo-Tethyan and Semail slab volumes in the Arabian region must have thickened by a factor of 3 to make their predicted thermal volumes fit to the tomographic volumes.

Moreover, the thermal volumes predicted for Arabian slab break-off around 12 Ma, and somewhat earlier underneath the central Zagros suture, are in agreement with the tomographic anomalies restricted to the upper mantle in this area.
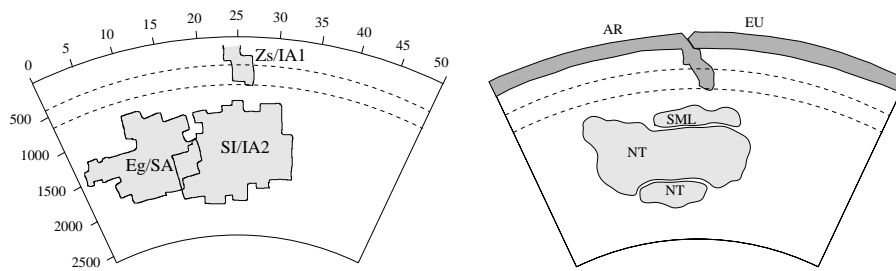
Figure 5.22: Interpretation of the vertical distribution of tomographic anomalies in the Arabian region (left panel, as in Fig. 5.8) in terms of subducted Tethyan oceanic lithosphere (right panel, as present-day reconstruction in Fig. 5.20). Note (see Fig. 5.17) that the southernmost part of the tomographic anomalies Eg and SA (left panel) are assumed to be the result of subduction in a section further east than illustrated in the right panel.

Lithospheric spreading during subduction   If thickened by a factor of 3, the predicted Neo-Tethyan and detached Semail volumes are larger than the minimum tomographic volumes associated with these slabs, but smaller than the maximum volumes. The ratios leave room for an additional 0.2-$0.4 \cdot 10^9$ km^3 volume, depending on the spreading scenario. The additionally subducted material is possibly the combined result of lithospheric spreading within the Neo-Tethys during its subduction, and the drifting and intermediate spreading of smaller continental fragments in the Mediterranean. As the latter will be addressed separately below (Section 5.8.2), we will here investigate the implications for the spreading rates for the case that the whole additional volumes is caused by Neo-Tethyan spreading.

We perform the same thermal calculations for predicting the present thermal volumes of subducted material, but in a reversed order, to establish the original subducted surface of the additional 0.2-$0.4 \cdot 10^9$ km^3 volume. Using the thermal factors and lithospheric thicknesses

as for the Neo-Tethyan oceanic basins (Table 5.7, p. 141), we arrive at an original surface of $\sim$1.5-3.2$\cdot$10^6 km^2 assuming that all these slabs have thickened by a factor of 3 in the mantle. If Neo-Tethyan spreading occurred over the full width of the Africa-Arabian continental margin, and during the entire 200-140 Ma time interval, this surface would require an average total spreading rate of 0.5-1 cm/yr. If the Neo-Tethyan ridge has been active in the Arabian region only, the average spreading rate must have been about 1-1.5 cm/yr.

Implications for the Indian region

Slab volumes   Our preferred scenario for the Indian region implies that the Neo-Tethyan lithosphere subducted before its oceanic ridge ($\sim$120 Ma) is incorporated in the lowermost, say $\geq$1800 km, volumes of anomaly Ic (Fig. 5.23). The second part of the Neo-Tethyan lithosphere can be found today in anomaly Ic ($\sim$1100-1800 km depth), as well as the southern anomaly Io ($\sim$800-2000 km depth). The Spongtang lithosphere is accommodated north of the Neo-Tethyan volumes and visible at present as anomaly Hi[1].

Our results for the preferred subduction scenario indicate that the Neo-Tethyan slab volumes must have thickened by a factor of 2 to make their predicted thermal volumes fit to the tomographic volumes. To leave room for additional subduction, however, the oceanic lithosphere must have thickened by a factor 3. The Spongtang lithosphere has probably thickened by a factor of 3 as well.

Spongtang slab detachment starting at 43 Ma but occurring primarily around 20 Ma can best explain both the depth and volumes of the tomographic anomalies underneath the Himalayas. This, however, implies that the continuing convergence between the Indian and Eurasian continents must have been partly accommodated by the deformation of earlier accreted continental blocks and lithospheric thickening above 230 km depth.
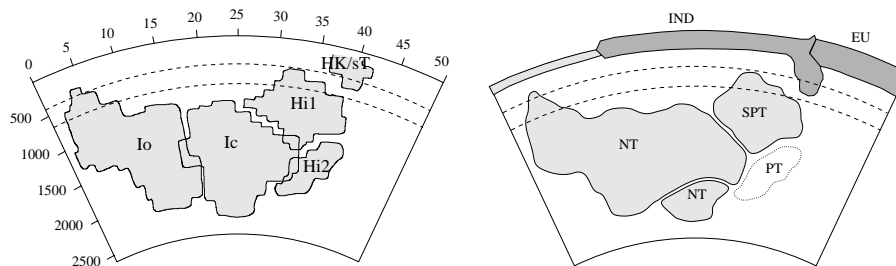

Figure 5.23: Interpretation of the vertical distribution of tomographic anomalies in the Indian region (left panel, as in Fig. 5.9) in terms of subducted Tethyan oceanic lithosphere (right panel, as present-day reconstruction in Fig. 5.21).

Lithospheric spreading during subduction   If thickened by a factor of 3, the predicted Neo-Tethyan slab volumes in the Indian region are only slightly more than the minimum tomographic anomalies of Io and Ic. The difference with the maximum volume of these anomalies is 0.4-0.5$\cdot$10^9 km^3, depending on the spreading scenario. Whereas this volume

149

could be partly explained by material of the Spongtang oceanic basin, it is more likely that the active spreading of the Neo-Tethyan lithosphere during its subduction added to the amount of subduction significantly.

Using similar thermal calculations for the Neo-Tethyan lithosphere as in the above sections (Table 5.7, p. 141), we find that the 0.4-$0.5 \cdot 10^9$ km^3 volume corresponds to an additional subducted plate surface of ~ 2.9-$4.0 \cdot 10^6$ km^2 if the slabs have thickened by a factor of 3. For continuous spreading within the Indian Neo-Tethys during the 200-120 Ma period before ridge subduction, this would correspond to an average full spreading rate of about 1.5-2.5 cm/yr.

5.8.2 Accretion but continuous subduction in the Aegean region

The westernmost part of the Tethyan region has not been given specific attention in the previous, as we have focussed primarily on the large-scale subduction in the combined Aegean-Arabian and Indian regions. In the Aegean area, however, the creation and subduction of several intermediate oceanic basins must have affected the amount of subduction significantly. Moreover, the present-day situation is completely different from that of the rest of the Tethyan region as subduction of the last remnants of Tethyan oceanic lithosphere along the Hellenic trench system (Points 1-20 in Fig. 4.11, p. 82) is ongoing. We therefore investigate here the volumes of subducted lithosphere for the first 20 sections of the Aegean region.

Phases of subduction   Based on the reconstruction of ExxonMobil, the subduction history of the Aegean region can be divided into four phases (see Fig. 2.8, p. 29), namely **(1) before 140 Ma**: Neo-Tethys subduction along the Pontides arc, prior to spreading of intermediate fragments; **(2) 140-80 Ma**: Additional subduction due to the spreading of the various fragments which is accommodated along the Pontides arc, and accretion of Kirşehir to Eurasia; **(3) 80-48 Ma**: Subduction accommodated along the Izmir-Ankara arc, and accretion of Menderes to Eurasia; and **(4) 48-0 Ma**: Subduction of the remaining Tethyan lithosphere underneath the present Hellenic arc. *Dercourt et al.* (1993) and *Şeng ör and Natal'in* (1996) propose similar subduction histories, although with other geometries of the intermediate fragments, and somewhat different rifting and accretion times (see Chapter 2).
In the reconstruction of *Stampfli and Borel* (2002, 2004) on which our preferred subduction scenario for the Arabian and Indian region is based (see Figs. 2.3-2.6, pp. 22-25), however, these phases are different. We here distinguish **(1)** Additional subduction of the Triassic Maliac oceanic basin due to the spreading of the overriding Vardar Ocean; **(2)** Subduction of the Vardar Ocean, and accretion of the Pelagonian zone to Eurasia; **(3)** Subduction of the Pindos basin, and accretion of the Ionian zone to Eurasia; and **(4)** Subduction of the Neo-Tethyan remnants as in the other reconstructions.

Additional surface   According to the reconstruction of ExxonMobil, Menderes is adjacent to northeast Africa until ~ 140 Ma and already close - although not yet accreted - to Eurasia around 80 Ma. As can been seen in Figure 2.8 (p. 29), the motion of Kirşehir relative to Eurasia has been only little more than that of Menderes vs. Eurasia, and has probably influenced the amount of subduction east of section 25 only. To approximate the additional amount of

convergence in the western Aegean region, we calculate the surface subducted due to the motion of Menderes relative to Eurasia between 140 and 80 Ma.

For our westernmost 20 sections ($\sim 10°$ width), we find in a total surface of $2.9 \cdot 10^6$ km^2 to be subducted in the past 200 Ma, instead of the $2.1 \cdot 10^6$ km^2 calculated from the African-Eurasian convergence alone, of which the larger part (almost 60%) belongs to phase (2). In the reconstruction of *Stampfli and Borel* (2004), the Maliac Ocean that was additionally subducted had a size of about $1 \cdot 10^6$ km^2 (i.e. $\sim 10° \times 10°$) (see Fig. 2.4, p. 23), whereas the maximum size of the Vardar Ocean seems to be *at most* $2 \cdot 10^6$ km^2 ($\sim 20° \times 10°$) around 120 Ma (Fig. 2.5, p. 24). Also in this reconstruction, the additional $0.8 \cdot 10^6$ km^2 thus seems to be a reasonable surface to be subducted in the western $10°$ of the Aegean region considered here. Again we take into account the fact that the top 230 km of the tomographic model has not been incorporated in our analysis. From a simple geometric point of view, the convergence accommodated in this depth interval will be ~ 200 km for a $45°$ slab dip below a 100-km thick plate. For the first 20 sections in the Aegean region, this yields a total surface of $0.2 \cdot 10^6$ km^2 to be subtracted from the surface of the latest phase of subduction (4). The most recent trench migration of the Hellenic trench system is not incorporated in the total surface. However, because this has probably caused flattening of the slab in the uppermost mantle only, the additional subduction may not be embodied in our tomographic anomalies either.

Including the additional surface, but corrected for the upper 230 km, the total subducted lithosphere yields an average convergence along our trench system of about 2400 km. During the 140-80 Ma timespan of phase (2), the subduction of 60% of this plate can be associated with an average convergence rate of 2.5 cm/yr. During the other phases, however, the convergence rates have been 1-1.5 cm/yr only.

Predicted thermal volumes Similar to the previous calculations, we predict the present thermal volume that can be associated with the subducted material. Because of the uncertainties in the exact spreading and subduction times of the intermediate basins, we make sure to end up with an upper limit of the predicted volumes by using an average 100-Ma age for all lithosphere. Much more important in this analysis are the shorter residence times in the mantle, namely $t = 200, 140, 80$ and 48 Myr for the four phases, respectively.

The slab material subducted in the oldest three phases is likely to have thickened by a factor of 2 or 3, but the slab of the most recent and still ongoing phase of subduction has probably not yet thickened significantly. Therefore, we take estimates of the thermal factors $c_2(t)$ and $c_3(t)$ for phase (1)-(3), and $c_1(t)$ for phase (4), to predict the total thermal volume for the western Aegean region. However, if we would use $c_2(t)$ and $c_3(t)$ for phase (4) as well, the results will be comparable due to the brief residence time in the mantle.

We find a total thermal volume of 0.42-$0.49 \cdot 10^9$ km^3, depending on the amount of slab thickening. From this volume, 17-18% belongs to phase (1), 55-57% to phase (2), 12-14% to phase (3), and 12-14% to phase (4). The volumes for the active phase (4) of subduction may be somewhat overestimated, with at most 10% (Section 3.3.3), but this will not change these values significantly.

Comparison to tomographic volumes We compare the predicted volumes to the most western anomaly Gr beneath the Hellenic trench (e.g. see Figs. 4.7 (p. 76, section 15) and

4.18 on p. 97). There is no evidence for other tomographic anomalies than Gr that may be related to one of the older phases of Aegean subduction. East of section 20, anomaly Gr is found only in the lower mantle, and east of section 25 below 1100 km depth only (Figs. 4.4-4.6, pp. 73-75). Throughout the westernmost 20 sections investigated here, the volume of anomaly Gr is $0.53\text{-}0.63 \cdot 10^9$ km^3. The $0.4\text{-}0.5 \cdot 10^9$ km^3 predicted for the thermal volume of the Aegean slab is in agreement with the size of anomaly Gr, and even allows for more subduction, e.g. from the Kırşehir block (ExxonMobil), or by a larger Vardar Ocean (*Stampfli and Borel*, 2002, 2004).

Location of subducted material   If subduction has been accommodated along the apparently separate trench locations displayed in the tectonic reconstruction of ExxonMobil, we may be able to see three separate slab volumes as well, and also a subducted oceanic basin like the Vardar Ocean (*Stampfli and Borel*, 2002, 2004) may be detectable as a separate identity today. The fact that we only see one tomographic anomaly in the Aegean region gives the impression that, although subduction along separate trench systems is proposed, the underlying lithospheric plates have continued their subduction without significant distortions. Whereas speculated on this scenario before (e.g. *Faccenna et al.*, 2003), we found that the approximate present thermal volume of the subducted slab material is in agreement with the volume of this tomographic anomaly indeed.

The depth distribution of anomaly Gr clearly shows that most of the material is positioned between ~750 and 1800 km depth (Fig. 5.18, p. 143). As can be seen in Figure 4.7 (p. 76), the bulk anomaly of Gr continues down to ~1600 km depth, and a somewhat separate volume is situated more south - and deeper - than the main anomaly. This lower ≥ 1600 km part of anomaly Gr has a volume of 19-22% of the total $0.53\text{-}0.63 \cdot 10^9$ km^3. The bulk volume between 750 and 1600 km depth is about 65-69% of these values, and the upper mantle subvolume 13-14%. As the rates of convergence have been relatively small, assuming an average sinking rate of 2 cm/yr in de upper mantle and 1 cm/yr in the lower mantle seems reasonable. In that case, the 750-1600 km depth interval of the bulk subvolume would require sinking times of ~50-130 Myr, which would correspond to our phase (2) and (3) of abundant subduction. Phase (1) could be associated with the lowermost ≥ 1600 km subvolume, and phase (4) with the upper mantle volume. Indeed, the relative amounts of the tomographic subvolumes correspond to those of the predicted thermal volumes for the same phases, namely ~20% for phase (1) and ~70% to phase (2) and (3) at most, and about 10-15% for phase (4).

The continuous subduction scenario sketched above for the reconstructions of ExxonMobil, *Dercourt et al.* (1993) and *Şengör and Natal'in* (1996) is schematically illustrated in Figure 5.24 for a section across the present Hellenic arc (cf. section 15 of Figure 4.7, p. 76). Herein, we took into account the predicted volumes of the subducted lithosphere, the possible slab thickening, and the approximate distribution of the material. For the absolute locations of the continental margins we considered their motions in the HS and MHS reference frames (see Figs. 5.3-5.4, pp. 109-110). However, the HS frame seems to predict locations for the
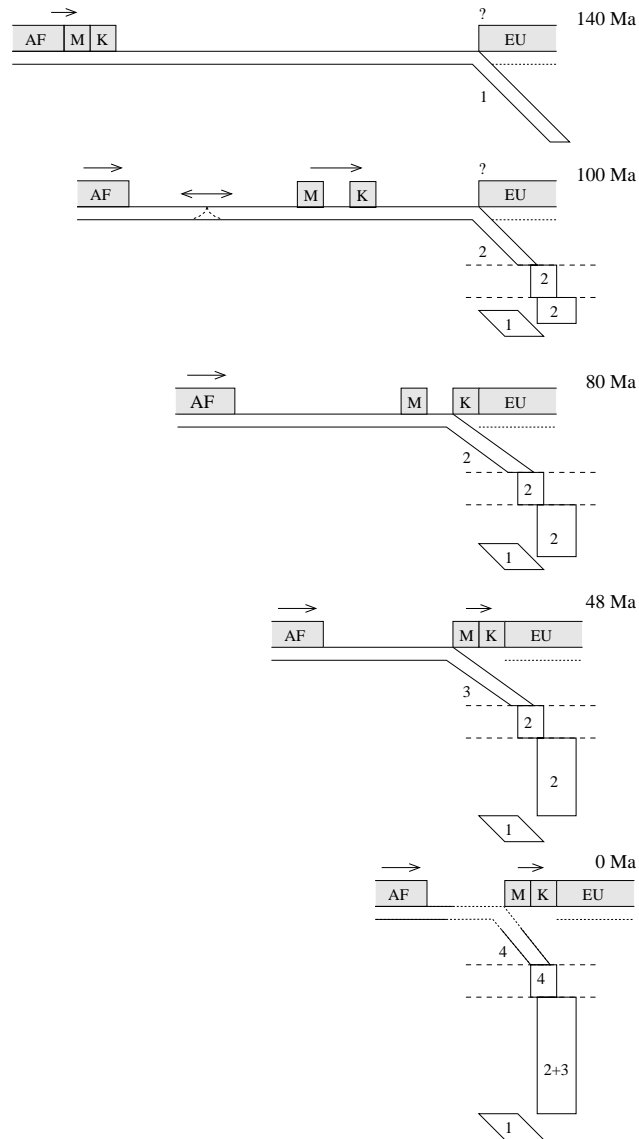
Figure 5.24: Schematic scenario for the subduction in the eastern Mediterranean as proposed by Exxon-Mobil, *Dercourt et al.* (1993) and *Şengör and Natal'in* (1996). The figures illustrate the accretion of continental fragments and the single, continuous subduction process of the underlying lithosphere. The evolution is shown for a section accross the present Hellenic arc in an absolute reference frame (prior to 80 Ma uncertain). The numbers indicate the four phases of subduction as discussed in the text. *Key*: A = Africa, M = Menderes, K = Kirşehir, EU = Eurasia. See text for alternative scenario proposed by *Stampfli and Borel* (2002, 2004).

trench systems that are too far south and east to explain the position of anomaly Gr. Therefore, we prefer the MHS frame in which the locations of the trenches appear to be at the appropriate latitudes, although probably somewhat too far west as discussed before (e.g. Section 5.6).

The four phases of subduction that were derived from the reconstruction of *Stampfli and Borel* (2002, 2004) would result in a different scenario than illustrated in Figure 5.24. For example, when comparing the 80-Ma situation with their Late Cretaceous reconstruction (Fig. 2.6, p. 25), fragment K would correspond to the just accreted Pelagonian zone and M to the Ionian zone, with the Pindos basin in between. Slab (1) would represent the detached Maliac basin, and slab (2) the subducted Vardar Ocean. Although significantly different from the scenario sketched above, the general conclusion that the continental fragments have been accreted during a single, continuous subduction process of the underlying lithosphere will hold.

Conclusions   When considering the separate rifting and accretion of intermediate continental fragments in the eastern Mediterranean, the decreasing lithospheric ages and especially residence times in the mantle are found to largely compensate the increasing subducted lithosphere. Our results indicate that the total thermal slab volume calculated for the westernmost Aegean region can be explained by the size of the single tomographic anomaly (Gr) underneath the present Hellenic trench system. This suggests that the subduction of the lithosphere underlying the various fragments and basins has been continuous in this area since at least Early Cretaceous times.

5.9   Conclusions

Three broadly accepted subduction scenarios for the Tethyan oceanic lithosphere and its spreading ridges, based on the reconstructions of *Norton* (1999), *Dercourt et al.* (1993), *Şengör and Natal'in* (1996), and *Stampfli and Borel* (2002, 2004), have been investigated by comparing the predicted thermal volumes of the subducted lithosphere to the tomographic mantle structure underneath the Tethyan region. We found that from the bulk volumes predicted by the three different subduction scenarios alone, we cannot distinguish the tectonic reconstructions underlying the scenarios.

To discriminate between the different reconstructions, we have predicted the subvolumes associated with the particular oceanic basins proposed in each subduction scenario. We compared these to the separate tomographic anomalous volumes in the Tethyan region by systematically analysing the amount, location and timing of subduction with the size, position and geometry of the tomographic anomalies. We found that the subduction scenario based on the reconstruction of *Stampfli and Borel* (2004), comprising the opening of large back-arc oceanic basins within the Eurasian margin, can best explain both the volumes and the positions of the anomalous volumes.

One of the key issues in evaluating the different subduction scenarios has appeared to be the absolute motions of the ancient trench systems in the past. Our results give the impression that the fixed hotspot reference frame considered here (*Müller et al.*, 1993) predicts locations of the continental margins that are too far south and east with respect to the relevant tomographic anomalies. The moving hotspot reference frame used (*O'Neill et al.*, 2003) results in absolute

positions that seem to be at the appropriate latitudes, but too far west with respect to the tomographic anomalies instead.

Our results further suggest that most lithosphere subducted in the Tethyan region has thickened by a factor of 3 in the mantle, which seems to be reasonable in view of the large amount of subducted material that entered the lower mantle. If this has been the case indeed, the differences between the predicted thermal volumes and tomographic volumes leave room for average spreading rates of about 1-1.5 cm/yr in the Arabian region, and 1.5-2.5 cm/yr in the Indian region, during subduction of the Neo-Tethys. Late Miocene slab break-off underneath the Zagros suture zone, and diachronous Eocene to Miocene break-off below the eastern to western Himalayas, has been found to best explain the associated slab volumes. Finally, Paleo-Tethyan lithosphere seems to be imaged in the lower mantle underneath the Himalayas, but the larger and older part of the Paleo-Tethys must have been subducted elsewhere or is no longer detectable as a separate anomalous volume today.

In spite of the limitations of our approach, we found that the method does enable us to successfully integrate the information contained in plate tectonic reconstructions and seismic tomographic models, and put further constraints on the subduction history of an ocean that is entirely lost today.

Chapter 6

Modelling active subduction in the easternmost Tethyan region

We have studied so far the evolution of the Tethyan region by investigating the subduction, and subsequent closure, of the Tethyan oceans in the Arabian and Indian regions. The Indonesian region, however, can be considered as Tethyan as well: The Paleo-Tethys disappeared with the accretion of continental fragments like Indochina and Sibumasu onto Eurasia, and subduction of the Neo-Tethys occurred along elongated trench systems that extended far eastwards to Southeast Asia (e.g. see Figs. 2.3-2.8 of Chapter 2, pp. 22-29). Moreover, the tomographic anomalies in the lowermost mantle underneath India, associated with subducted Tethyan lithosphere, appear to connect to the deep mantle anomalies beneath the Indonesian islands (e.g. Fig. 4.3, p. 71).

Whereas the larger part of the Tethyan region is at present marked by the continental collisions of Arabia and India with Eurasia, the Indonesian region is still characterised by the active subduction of various oceanic basins. As discussed in Chapter 3, such ongoing subduction is a good starting point for estimating parameters like the convergence velocity and the age of the oceanic lithosphere upon subduction. Instead of approximating the thermal volumes of the subducted material, as was necessarily done in Chapter 4 and 5, we are here capable of actually modelling the present thermal structure of the subduction zones. As in the previous, we will use seismic tomography to test tectonic reconstructions of the area, but now by comparing directly the predicted and tomographic models of the mantle structure.

6.1   Introduction

Southeast Asia is an actively deforming area located on the junction of the converging Eurasian, Indo-Australian and Philippine Sea plates (Fig. 6.1). In the last decade, several tectonic re-

constructions of the complex Cenozoic development of this region have been proposed, for example by *Rangin et al.* (1990a), *Daly et al.* (1991), *Lee and Lawver* (1995), and *Hall* (1996). Their descriptions of the tectonic processes are all based on extensive data sets that resulted from geological, paleomagnetic and shallow seismic studies. The very existence of the various reconstructions indicates that the currently incorporated data do not allow a definition of one single scenario for the tectonic evolution. Consequently, there are some important - as yet unresolved - differences between the reconstructed surface motions within the Southeast Asian region. In this study, we investigate whether we can contribute to a better understanding of the geodynamic evolution of the area by incorporating seismic tomography results into the analysis of the tectonic reconstructions.
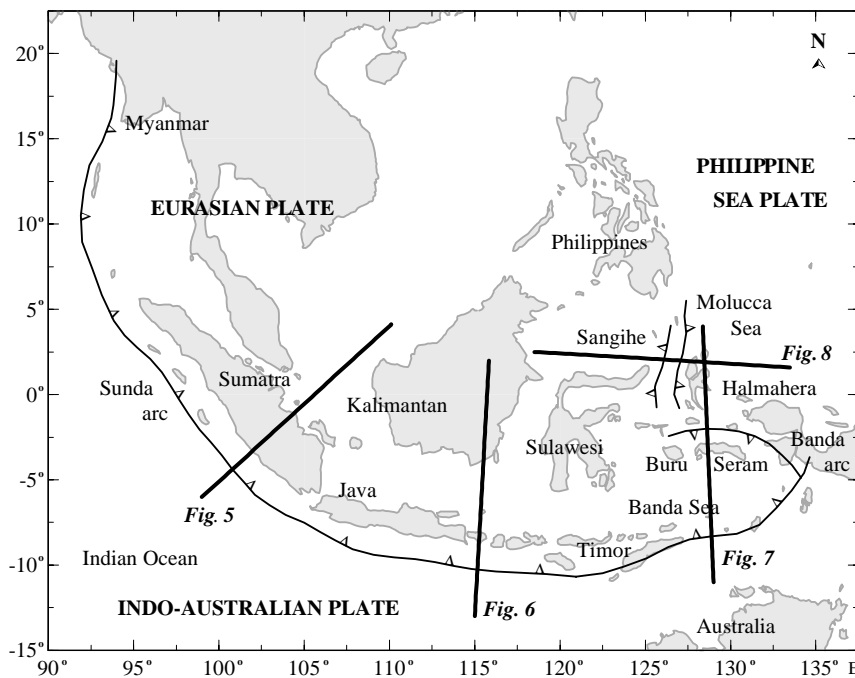
Figure 6.1: Location map of the Indonesian region. Barbed lines are the main active trenches from *Lee and Lawver* (1995). Straight lines indicate the vertical cross-sections that are shown in Figures 6.5-6.8.

The method we follow has been successfully applied to the Mediterranean region by *De Jonge et al.* (1993, 1994). This thermo-kinematic modelling procedure links the surface movements proposed in a tectonic reconstruction to the present seismic P-velocity structure of the underlying lithosphere and mantle. A fundamental assumption in the approach is that horizontal surface motions are always coupled to vertical displacement of material through plate subduction and isostatic compensation of extending lithosphere. Naturally, these processes significantly affect the temperature distribution in the mantle and, therefore, result in a change of the seismic velocity structure. A comparison of the calculated three-dimensional model of velocity anomalies with independently obtained seismic tomography results will enable us

158

to test the proposed tectonic reconstruction. Our approach fully acknowledges the value of the geological and other near-surface data that underlie the tectonic reconstruction and makes use of the fact that the reconstruction intrinsically represents a synthesis of geological and geophysical data on the larger regional scale involved.

We apply our procedure to the Indonesian part of the tectonic reconstructions proposed by *Rangin et al.* (1990a,b) and *Lee and Lawver* (1995). In the present Indonesian area (Fig. 6.1), the Indo-Australian plate subducts northward beneath the Indonesian islands along the Sunda arc. Continental collision processes are characteristic of the Banda arc and the Molucca Sea region. The two tectonic reconstructions show important differences in trench migration, rotations of the Indo-Australian and Philippine Sea plates, and the collision of the Eurasian and Australian continental margins (Fig. 6.2). The calculated models of the seismic P-velocity structure beneath Indonesia are compared with the global seismic velocity model of *Bijwaard et al.* (1998) which gives detailed tomographic images of the region.

6.2   The forward modelling procedure

To calculate the present seismic velocity structure from a tectonic reconstruction, we use the numerical modelling procedure developed by *De Jonge et al.* (1993, 1994) and *De Jonge* (1995). Three successive stages can be distinguished in this forward approach.

1) Quantification of kinematic model. The time-dependent kinematics of the region are derived from the surface motions proposed in a tectonic reconstruction. Relative convergence between plates is modelled by subduction, for which the velocities are determined from the reconstructed plate rotations and trench migrations. The dip of the subducting slab is held fixed and is estimated from the distribution of recent earthquake hypocentres (ISC data set). Extension of lithosphere is modelled as pure shear deformation (*McKenzie*, 1978). All motions within the timespan to be tested are translated into a kinematic model for narrow 2D vertical sections perpendicular to the plate boundaries. We note here that the relative convergence velocities between the different fragments are calculated from the information contained in the tectonic reconstructions. The total convergence along a trench segment can, therefore, be directly related to the reconstructions themselves. Our predicted velocity anomalies are influenced by assumptions made in the following modelling steps.

2) Calculation of thermal evolution. Based on the kinematic model, the thermal evolution of each 2D section in the region is calculated. First, the initial temperature distribution needs to be defined. Oceanic lithosphere is approximated by a cooling halfspace with the appropriate lithospheric ages. In continental regions, the crustal thicknesses are used in a steady-state approximation of a typical three-layer model (*Chapman*, 1986). The mantle temperatures are constrained by an adiabatic thermal gradient with temperature jumps at the 410- and 660-km discontinuities. Next, the thermal evolution within each section is modelled forward in small timesteps, starting from the initial structure. For each timestep, the temperatures are displaced as defined by the kinematic model, and the associated diffusion of heat is calculated (similar to *Minear and Toksöz* (1970) and *Sleep* (1973)). Relative to the dominant direction of heat transport in a subduction zone, which is perpendicular to the descending plate, conduction of heat in the direction parallel to the trench is negligible. When the total timespan has been modelled, the differences between the calculated temperatures and the average temperature

distribution for the region define the thermal perturbations that are combined into a 3D model.

3) Conversion to seismic velocity structure. The predicted temperature perturbations are converted into seismic P-wave velocity anomalies by using the depth-dependent temperature derivative of the seismic velocity determined by *De Jonge* (1995). Because the velocity anomalies in the lower lithosphere and upper part of the mantle appear to be primarily controlled by temperature (see for example *De Jonge*, 1995; *Ranalli*, 1996; *Goes et al.*, 2000), we believe that our predicted models will yield a reasonable representation of the anomaly distribution. Other contributions to seismic velocities, such as composition and partial melting, are neglected. At crustal depths and in the lower mantle, the effect of temperature may
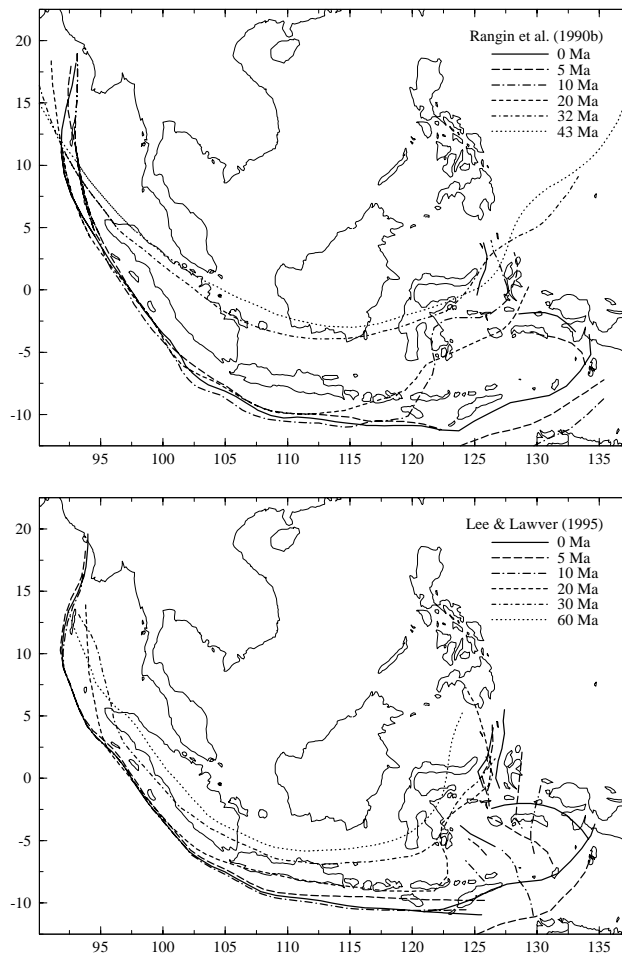
Figure 6.2: Stages in the evolution of the active Indonesian trench system according to the reconstruction of *Rangin et al.* (1990a,b) (top) and the reconstruction of *Lee and Lawver* (1995) (bottom). Present coastlines are given for reference only.

be less dominant, and therefore, we have to analyse the models with caution.

For further details and values of the standard modelling parameters, we refer to *De Jonge et al.* (1993, 1994) and *De Jonge* (1995).

6.3   Tectonic reconstructions

Rangin et al. (1990a) and *Lee and Lawver* (1995) have presented their reconstructions in a sequence of tectonic maps of the Southeast Asian region for the past 43 Myr and 60 Myr, respectively. In this section, we give a short outline of the differences between the two reconstructions within the Indonesian region. For a more detailed description, we refer to the original publications.

In both reconstructions, the present-day Sunda arc (Fig. 6.1) was the western part of an ancient subduction zone that once curved around the Eurasian plate from west of the Andaman Sea to northeast of Sulawesi (Fig. 6.2). Indian Ocean lithosphere has subducted northward along this trench system during the total reconstructed timespan. A similar history, as well as indications for earlier subduction, has also been proposed by others, e.g. *Audley-Charles et al.* (1988), *Daly et al.* (1991), and *Hall* (1996). In the two reconstructions, the location and horizontal extent of the ancient arc system differ. Compared to the evolution described by *Lee and Lawver* (1995), *Rangin et al.* (1990a) placed the earlier stages of the arc in a more northerly position, while the arc extended further to the northeast (Fig. 6.2). *Rangin et al.* (1990a) have used constant rotation poles for the lower Indo-Australian plate motions which differ from the variable poles of *Lee and Lawver* (1995).

During the Paleogene, the Indonesian trench system migrated southwards in both reconstructions (Fig. 6.2). In the Early Neogene, the eastern part of the trench was pushed north(west)ward again due to the collision with the first fragments of the Australian continental margin. As a result, the present southeast arm of Sulawesi accreted with the - Eurasian - north and west arms and large parts of the trench became inactive (Fig. 6.2). Today, active subduction only takes place beneath the Sangihe islands (see also Fig. 6.1). According to *Lee and Lawver* (1995), continent-continent collision started at 20 Ma and the larger part of the eastern trench became inactive before 14 Ma. *Rangin et al.* (1990a) placed these events about 5 Myr later (15 and 10 Ma, respectively). Nowadays, the Molucca Sea plate subducts westward beneath the Sangihe islands as well as eastward beneath Halmahera (Fig. 6.1). *Lee and Lawver* (1995) proposed that the eastward subduction has been active since 10 Ma, whereas *Rangin et al.* (1990a) indicated eastward subduction since 6 Ma. In the latter reconstruction, the present Halmahera trench has collided with the Sangihe trench (see Fig. 6.2).

The highly curved Banda arc is apparently continuous with the present Sunda arc (Fig. 6.1). The cause of the extreme curvature of the Banda arc is still a point of discussion. It has been suggested that the arc was constructed from two separate trench systems (e.g. *McCaffrey*, 1988; *Daly et al.*, 1991; *Hall*, 1996), or that the arc has been one continuous trench system that was bent into its present configuration (e.g. *Katili*, 1975; *Milsom et al.*, 1996). *Rangin et al.* (1990a,b) proposed an evolution of the Banda arc in which the southern trench (along Timor) and the northern trench (along the Buru-Seram islands) of the system lay separately in their present-day relative configuration. Lithospheric material subducted southward along the Buru-Seram part of the trench in the past 8 Myr. Northward subduction of a marginal basin

south of Timor was proposed since 20 Ma. *Lee and Lawver* (1995) also reconstructed the Banda arc from two separate trench systems, but they took into account a counterclockwise rotation ($\sim 90°$) of Buru-Seram in the past 18 Myr through which the underlying lithosphere was subducted southward beneath the islands. Only a short timespan of 4 Myr of northward subduction was proposed to have taken place beneath Timor.

6.4 Modelling results

We predict models of the seismic velocity distribution beneath Indonesia from both the reconstruction of *Rangin et al.* (1990a,b) and the reconstruction of *Lee and Lawver* (1995). The calculations for the 3D models are made within vertical 2D sections spaced at 50-100 km intervals, depending on the complexity of the trench structure. In this chapter, we will refer to the modelling results for the above two reconstructions as the R-model and LL-model which represent evolutions of the past 40 Myr and 60 Myr, respectively.

The predicted structures are compared with the global tomographic BSE-model of *Bijwaard et al.* (1998). The horizontal resolution of the BSE-model is good in the Indonesian region, where it gradually decreases from below 100 km in the subduction zone regions of the upper mantle to 250 km in the lower mantle. Vertical resolution can be poorer in the shallow parts of subduction zones when rays are travelling predominantly down dip, but is usually better than 200 km. We will restrict our analysis to the large-scale features in the model.

Generally we find that the amplitudes of imaged seismic velocities are smaller than those computed from forward modelling. The underestimation of the tomographic amplitudes can be inferred from tests with synthetic velocity models (*Bijwaard et al.*, 1998) and is due to a combination of model parameterisation, regularisation, and incomplete convergence in the tomographic inversion. Therefore, the shown amplitude range of the imaged velocity anomalies will be different from the range of the predicted anomalies.

6.4.1 General structure

Figures 6.3 to 6.8 show horizontal and vertical slices down to 1500 km depth through the R-, LL- and BSE-models (see also Fig. 6.1 for locations of the cross-sections). To allow for the identification of an approximate relationship between depth range and time window on the tectonic evolution, we indicate in Figures 6.3 and 6.4 the average time (in Myr) it took the predicted slabs to subduct down to the depth of 200 km and 500 km, respectively. We find that for the reconstructions used, the subduction-related high velocity anomalies in the upper 500 km are an expression of the modelled geodynamic evolution during the last 8 Myr (east of Java) to 40 Myr (under Myanmar (Burma)). With a minor exception for the southern Sulawesi region, a similar conclusion (about 10-40 Myr) holds for the entire upper mantle, i.e. down to 670 km depth. High velocity anomalies associated with earlier episodes - depending on the subregion - in the regional evolution are likely to be found in the lower mantle.

While our predicted slabs subduct at fixed dips, in some regions (for example beneath the Sunda arc, see Figs. 6.5 and 6.6) the tomographic anomalies lose their plate-like geometry in the lower mantle (see *Bijwaard et al.* (1998) for a discussion). This indicates that our current approach is not yet appropriate for a comparison between the models at lower mantle levels.
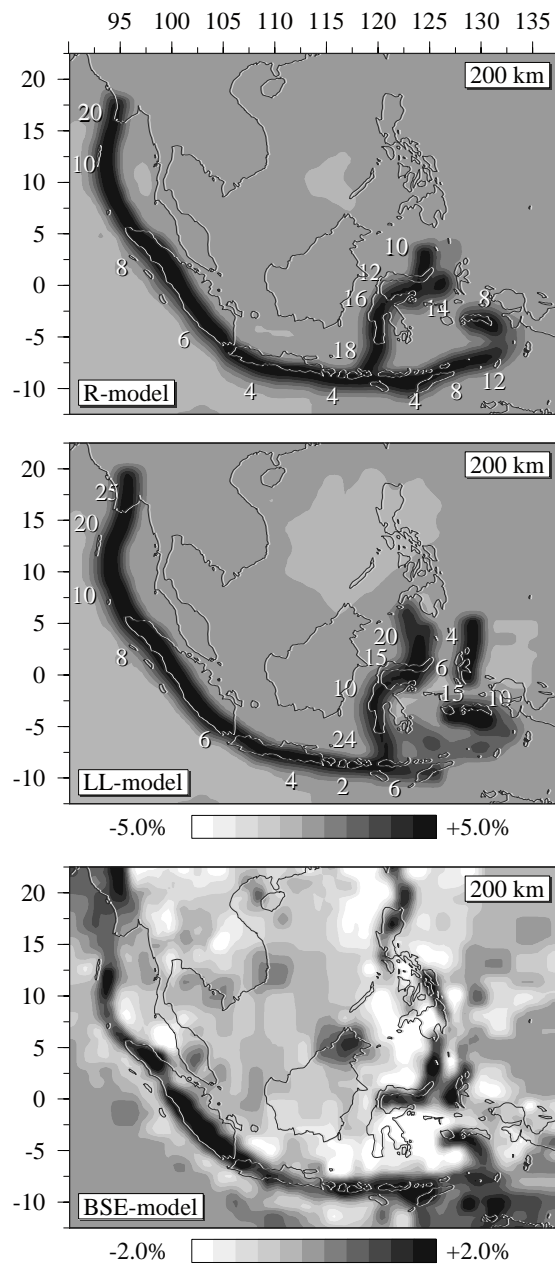
Figure 6.3: P-velocity anomaly structure at 200 km depth. From the top downward: The R-model (based on *Rangin et al.*, 1990a,b), LL-model (based on *Lee and Lawver*, 1995) and tomographic BSE-model (*Bijwaard et al.*, 1998). Numbers give an indication of the average time (Myr) it has taken for the predicted slab remnants to subduct down to the shown depth. For a colour version of this figure, see Figure A.10 in the Appendix.
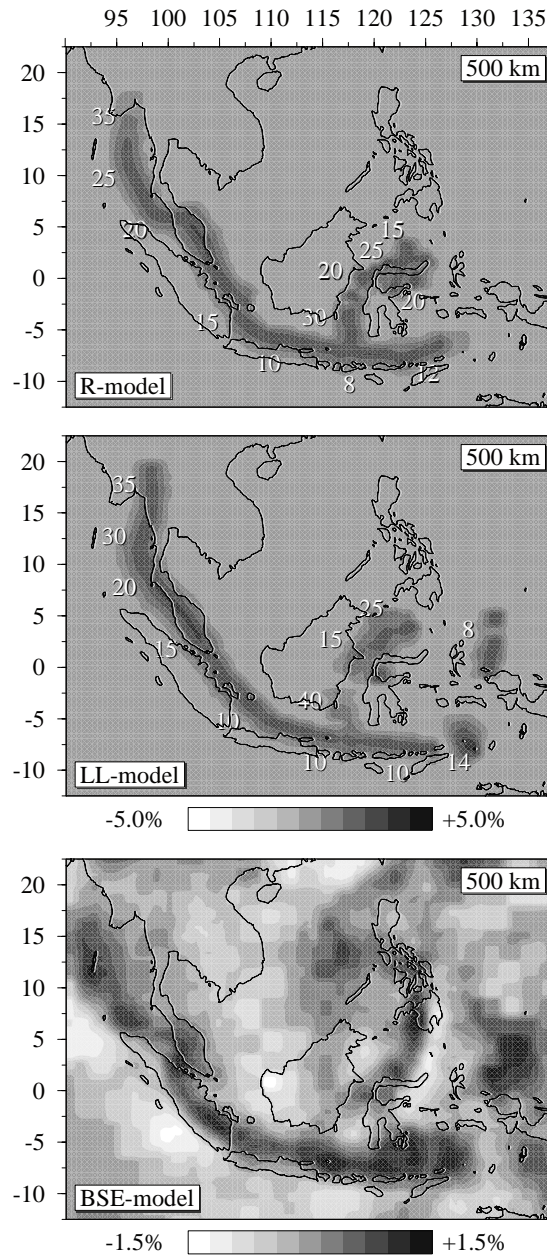
Figure 6.4: P-velocity anomaly structure at 500 km depth of the R-model (upper), LL-model (middle) and tomographic BSE-model (lower panel). Numbers as in Figure 6.3. For a colour version of this figure, see Figure A.11 in the Appendix.
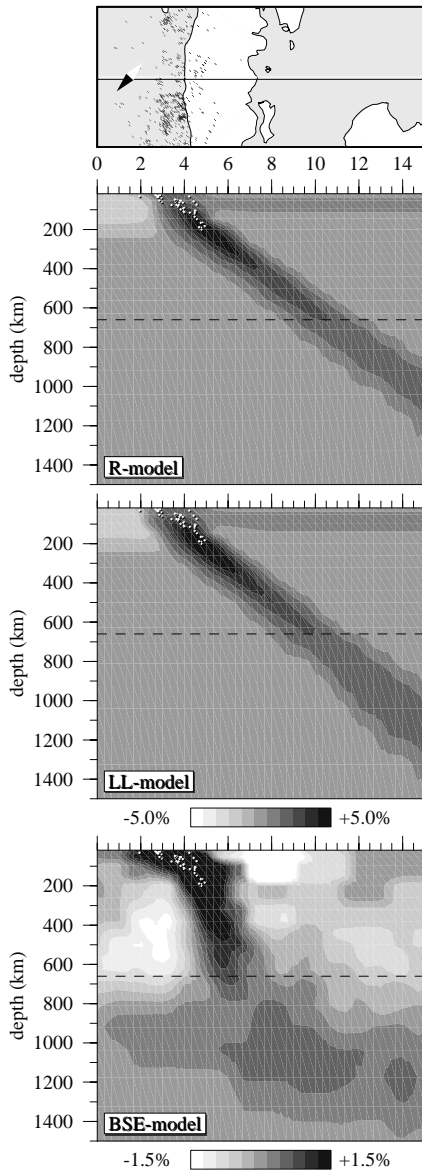
Figure 6.5: Vertical sections down to 1500 km depth across Sumatra through the P-velocity anomalies of the R-model (upper), LL-model (middle) and tomographic BSE-model (lower panel). The location of the section is indicated in the small map on top and in Figure 6.1. The dots represent earthquake hypocentres. For a colour version of this figure, see Figure A.12.
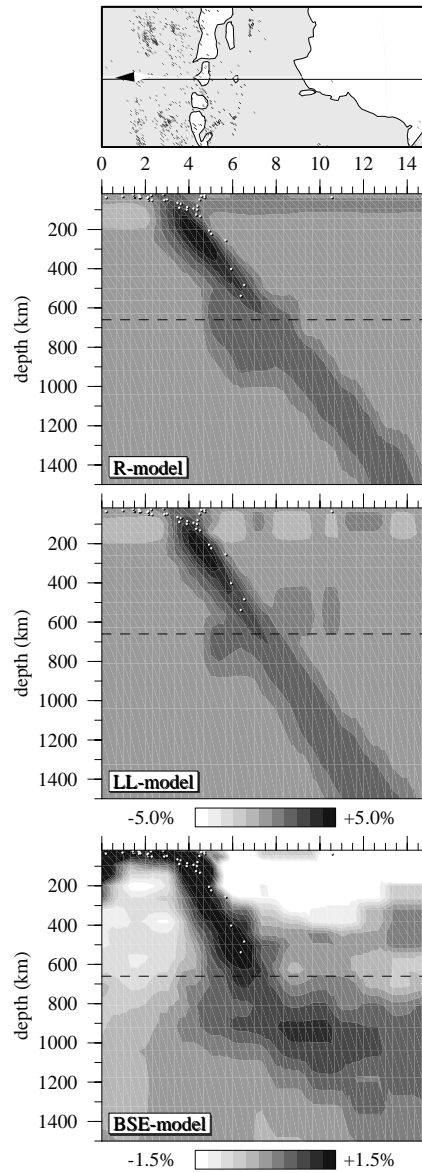
Figure 6.6: Vertical sections across Java through the R-model (upper), LL-model (middle) and tomographic BSE-model (lower panel). See Figure 6.1 for location of the section. For a colour version of this figure, see Figure A.13.
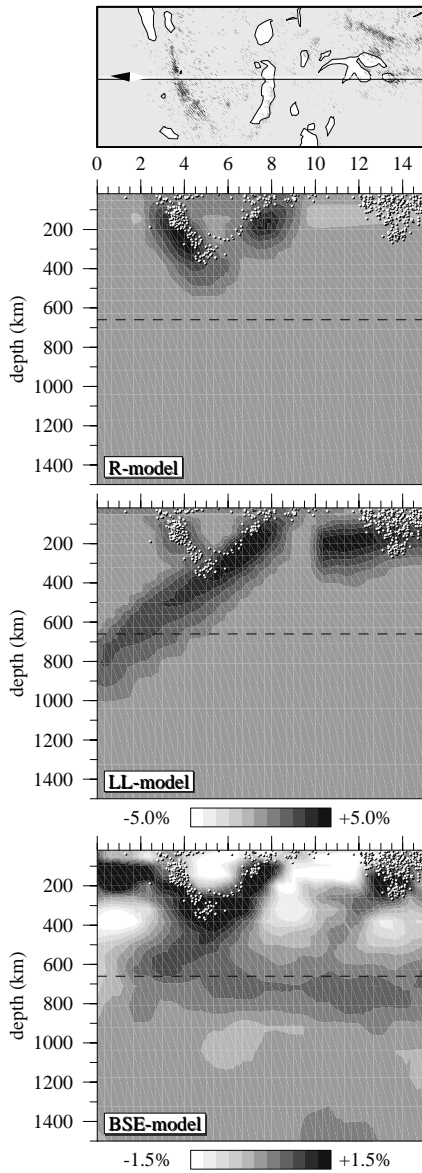
Figure 6.7: Vertical sections across the Banda arc through the R-model (upper), LL-model (middle) and tomographic BSE-model (lower panel). The shallow high velocity structure on the north side (right) of the LL-model subducted along the Halmahera trench system. See Figure 6.1 for location of the section. For a colour version of this figure, see Figure A.14.
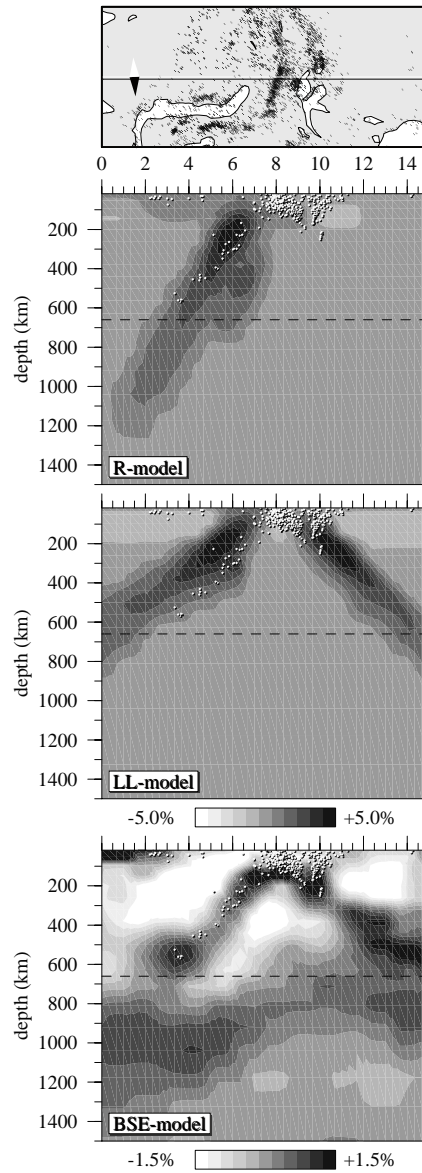
Figure 6.8: Vertical sections across the Molucca Sea through the R-model (upper), LL-model (middle) and tomographic BSE-model (lower panel). In the R- and LL-model, material that subducted along the Sulawesi trench system can be seen on the west side of the section (left). See Figure 6.1 for location of the section. For a colour version of this figure, see Figure A.15.

In this chapter, we will therefore concentrate on the upper mantle structure and only give an indication of possible similarities and dissimilarities between the lower mantle anomalies. Below, we will focus on sections through the Sunda arc, Banda arc, Molucca Sea and Sulawesi region (see Fig. 6.1 for locations).

6.4.2 Sunda Arc

The reconstructions proposed by *Rangin et al.* (1990a,b) and *Lee and Lawver* (1995) differ in the migration of the Sunda arc as well as in the rotation of the subducting Indo-Australian plate (Section 6.3). Nevertheless, we find that the amounts of Cenozoic convergence along the trench are comparable. During the total modelled timespan of 40 Myr (in the R-model) and 60 Myr (in the LL-model) lithosphere of up to 2,500 km to 3,000 km length, respectively, has descended into the mantle underneath Sumatra and about 500 km more beneath Java. Near Myanmar (Burma), about 700 km of convergence is predicted for the reconstruction of *Lee and Lawver* (1995) and an average 500 km of convergence for the reconstruction of *Rangin et al.* (1990a,b). The lithospheric subduction has resulted in a comparable positive velocity pattern beneath the present Sunda arc (Figs. 6.3 to 6.6). The predicted distributions show strong similarities with the tomographic images. In this case, the comparison between the predicted models and the tomography model lends support to both reconstructions. Because the eastern part of the Paleogene Indonesian trench system (mentioned above, in Section 6.3) is totally disconnected from the present Sunda arc, we prefer to discuss the results of this area in the section about the Sulawesi and Molucca Sea region.

According to *Bijwaard et al.* (1998) and *Van der Voo et al.* (1999), part of the lower mantle anomalies beneath the western Sunda arc of the BSE-model (Fig. 6.5) may represent lithospheric material of the Mesozoic Tethys Ocean. Since the continental margins of Greater India and Eurasia started to collide around 60 Ma, followed by a continent-continent collision after 45 Ma (e.g. *Audley-Charles et al.*, 1988; *Lee and Lawver*, 1995; *Van der Voo et al.*, 1999), most of the Tethys Ocean must have been subducted before the start of both reconstructions. The upper mantle anomalies of the BSE-model indicate a subduction of about 900 km of lithosphere. If the lower mantle anomalies do represent the remnants of the Tethys Ocean, then these upper mantle anomalies may be the result of processes of the past 45-60 Myr. Continuity between the upper mantle anomalies and the lower mantle reservoir is not very clear. The calculated convergence along this part of the trench (2,500 km in the R-model to 3,000 km in the LL-model) far exceeds the 900 km of tomographic upper mantle anomalies. This may indicate that for the modelled timespan, part of the subducted material did indeed accumulate into the lower mantle reservoirs or that the total amount of convergence that was predicted by the tectonic reconstructions is too large. Beneath Myanmar, the slab length that is predicted in the LL-model is larger than the maximum of 500 km that can be estimated from the tomography.

The positive velocity anomalies in the BSE-model (Fig. 6.6) merge into another huge high velocity pattern, situated at 800-1400 km depth beneath Java and Kalimantan up to the southern Philippines. From the total volume of this SW-NE oriented anomaly we arrive at an estimate of ancient convergence of up to 4,500 km in an approximately NW direction. The Indian Ocean lithospheric material subducted along the Java trench (Fig. 6.6) may have fed this huge eastern reservoir, and probably still does. The upper mantle slab of 900 km length

in the BSE-model increases the total convergence along this part of the trench to 5,400 km. This is much longer than the 3,000 to 3,500 km length of our calculated models and suggests an actual subduction of more material, probably prior to the modelled timespans.

6.4.3 Banda Arc

In the R-model, lithospheric material of about 250 km length subducted northward along the Timor trench, and some 150 km subducted southward along the Buru-Seram trench (Fig. 6.2). The counterclockwise rotation of Buru-Seram, proposed in the *Lee and Lawver* (1995) reconstruction, has resulted in a southward subduction of over 700 km of lithosphere under Seram which is significantly more than calculated for the R-model. Beneath Timor, the short timespan (4 Myr) of subduction has resulted in only 50-100 km of convergence. Because all reconstructed processes of subduction along the Banda arc took place within the modelled timespans, the comparison with the tomography results should be very meaningful.

Highly curved velocity anomalies can be seen clearly around the Banda Sea in the tomographic BSE-model (Figs. 6.3 and 6.4). Both the R-model and the LL-model show a similar u-shape geometry of subducted material, predicted from the two separate north and south trenches. The vertical cross-section of Figure 6.7 cuts both the north- and southward subducted material beneath the Banda arc. Across the arc, the positive velocity anomalies in the BSE-model represent subduction of approximately 300 km beneath Timor and nearly 800 km under Buru-Seram. In view of the tomographic anomalies, the subduction beneath Timor is underestimated in the LL-model, where the small amount of convergence beneath Timor has resulted in only minimal anomalies.

Although it is difficult to draw conclusions from the anomalies alone, the R-model seems to give a better estimate of the convergence along the trench. This would favour the suggestion for a longer duration of subduction beneath the southern Banda arc (e.g. *Richardson and Blundell*, 1996). Beneath the Buru-Seram islands, the predicted subducted material in the R-model is clearly less than the 800 km length that can be inferred from the tomographic slab remnants. In Figure 6.7, the LL-model seems to overestimate this amount.

6.4.4 Molucca Sea and Sulawesi region

The patterns of positive velocity anomalies in the upper mantle beneath Sulawesi that can be seen in our forward models (Figs. 6.3 and 6.4) result from the northward subduction of the oceanic lithosphere ahead of the Australian continent, and the eventual collision with its margins (Section 6.3). Under the region between Sulawesi and the Sunda arc, both the R-model and the LL-model show N-S oriented material that subducted along presently inactive trenches, so the anomalies represent relatively old material. In the Molucca region, the Molucca Sea plate has subducted both westward beneath the Sangihe islands and eastward beneath Halmahera. Along the Sangihe trench, both predicted mantle models reflect a total subduction of approximately 1,000 km (R-model) to over 1,500 km (LL-model) of lithospheric material. In the LL-model, the large anomalies beneath Halmahera represent a convergence of more than 900 km in 10 Myr of subduction with high convergence velocities. In the R-model, modest subduction beneath the Halmahera islands (6 Myr with an average convergence velocity of only 1.5 cm/yr) has resulted in minimal anomalies.

The BSE-model clearly shows a high velocity pattern associated with the double-sided subduction of the Molucca Sea plate (Figs. 6.3 and 6.8). The locations of the two trench systems are very close to each other and the plate seems to be subducted completely. Both slabs seem to connect up to larger positive velocity reservoirs in the mantle (Fig. 6.8). The Sangihe slab is continuous with the SW-NE oriented lower mantle reservoir (see above section) for which a 4,500 km of convergence in an approximately NW direction was derived above. Including the anomalies in this reservoir, the BSE slab remnants beneath the Sangihe islands represent a total length of about 5,500 km. The positive velocity reservoir beneath the Halmahera subduction zone can be interpreted as an accumulation of about 3,500 km of lithosphere subducted earlier along the Halmahera trench system.

The geometry of the subduction zones shown in the LL-model is similar to the BSE-model, although the modelled locations of the two trenches may be too far apart. The lack of a significant slab beneath Halmahera in the R-model is in clear contradiction with the tomography results. In the BSE-model, the total length of subducted material beneath the Sangihe islands is significantly longer than predicted from the reconstructions. Also the amounts under the Halmahera trenches exceed the predicted lengths. The results indicate that higher convergence velocities must have occurred during the reconstructed timespan of subduction, or that there has been subduction prior to the modelled period.

In contrast to the calculated models, the N-S pattern of positive velocity anomalies between Sulawesi and the Sunda arc cannot be seen in the BSE-model (Figs. 6.3 and 6.4). The only structure that could be identified as a continuity between the material subducted along the Sunda arc and the EW oriented pattern beneath Sulawesi (*Rangin et al.*, 1999) is the SW-NE oriented lower mantle reservoir below Kalimantan (discussed above). This would indeed imply a former connection of the trenches. In that case, however, the eastern part of the ancient arc system must have been in a more westward position (i.e. at lower longitudes) than proposed in both tectonic reconstructions.

6.5   Conclusions

We have presented models of the seismic P-velocity structure beneath Indonesia calculated from the tectonic reconstructions of *Rangin et al.* (1990a,b) and *Lee and Lawver* (1995). They have been compared to the tomographic BSE-model of *Bijwaard et al.* (1998). This comparison provides a tool for defining the merits and shortcomings of the different scenarios for the Cenozoic evolution that are proposed in the two reconstructions.

We conclude that both the R-model and LL-model predict positive velocity anomalies - associated with subducted material - in upper mantle regions that are characterised by high velocities in the BSE-model as well. The calculated upper mantle anomalies reflect the tectonic evolution of the past 10 to 40 Myr (depending on the subregion).

From both reconstructions, a similar pattern of subducted material is predicted beneath the Sunda arc. Along the southern part of this trench, the length of subducted material is much less than the length inferred from the upper and lower mantle anomalies of the tomography. The results suggest that more material must have been subducted along the trench system than was calculated, probably prior to the reconstructed timespan. The anomalies under Myanmar (Burma) that can be seen in the tomographic images indicate a convergence of at most 500

km which is less than the 700 km predicted in the LL-model.

Along the Banda arc, the curved geometry of anomalies in the predicted models is in agreement with the tomography results. This indicates that the tomographic Banda anomaly can be explained by subduction along the two separate trench systems that are proposed in both reconstructions. Beneath the southern side of the arc, the 250 km of subduction proposed for the R-model results in positive velocity anomalies that are comparable to the tomography, whereas the length for the LL-model is underestimated. Under the northern side, the R-model predicts less subduction than the 800 km inferred from the tomographic images. The counter-clockwise rotation of Buru-Seram as proposed for the LL-model results in a better estimate of the convergence along this trench.

The positive velocity anomalies between the Sunda arc and Sulawesi that were modelled from the reconstructions cannot be found in the tomographic images. The double-sided subduction of the Molucca Sea plate of the LL-model is in agreement with the tomography. In the R-model, the length of subducted material beneath the Halmahera islands (< 100 km) clearly is too small but also the 500 km of the LL-model is an underestimation. The large anomalies within the tomographic mantle model suggest that nearly 6,500 to 8,000 km lithospheric material may have subducted along the double trench system, either during or prior to the proposed subduction processes.

Our forward approach is limited by its kinematic properties, implying that dynamically related features like trench migration, convergence velocity, age and slab geometry are all pre-described. Strike-slip faulting and oblique subduction (or extension) cannot be modelled properly owing to our 2D calculations. Furthermore, the conversion into seismic P-velocity anomalies is simplified. In spite of these limitations, our results show that the method enables us to evaluate the qualities of the proposed tectonic reconstructions. Therefore, we expect that continued application and further development of our approach will significantly contribute to resolving major issues in the complex evolution of Southeast Asia.

References

Audley-Charles, M., P. Ballantyne, and R. Hall, Mesozoic-Cenozoic rift-drift sequence of Asian fragments from Gondwanaland, *Tectonophysics*, *155*, 317–330, 1988.

Becker, T. W., C. Faccenna, R. J. O'Connell, and D. Giardini, The development of slabs in the upper mantle: insights from numerical and laboratory experiments, *J. Geophys. Res*, *104*, 15,207–15,226, 1999.

Bercovici, D., Y. Ricard, and M. Richards, The relation between mantle dynamics and plate tectonics: A primer, in *The History and Dynamics of Global Plate Motions*, edited by M. A. Richards, R. G. Gordon, and R. D. van der Hilst, vol. 121 of *Geophysical Monograph*, pp. 5–46, Am. Geophys. Union, 2000.

Bertrand, G., C. Rangin, H. Maluski, H. Bellon, and GIAC Scientific Party, Diachronous cooling along the Mogok Metamorphic Belt (Shan scarp, Myanmar): the trace of the northward migration of the Indian syntaxis, *Journal of Asian Earth Sciences*, *19*, 649–659, 2001.

Bijwaard, H., *Seismic travel-time tomography for detailed global mantle structure*, Ph.D. Thesis, Utrecht University, the Netherlands, 1999.

Bijwaard, H., and W. Spakman, Nonlinear global P-wave tomography by iterated linearized inversion, *Geophys. J. Int.*, *141*, 71–82, 2000.

Bijwaard, H., W. Spakman, and E. R. Engdahl, Closing the gap between regional and global travel time tomography, *J. Geophys. Res*, *103*, 30,055–30,078, 1998.

Bowin, C., G. Purdy, C. Johnston, G. Shor, L. Lawver, H. Hartono, and P. Jezek, Arc-continent collision in Banda Sea region, *Am. Assoc. Petr. Geol. Bull.*, *64*, 868–915, 1980.

Bunge, H.-P., and S. P. Grand, Mesozoic plate-motion history below the northeast Pacific Ocean from seismic images of the subducted Farallon slab, *Nature*, *405*, 337–340, 2000.

Bunge, H.-P., M. Richards, C. Lithgow-Bertelloni, J. Baumgardner, S. Grand, and B. Romanowicz, Time scales and heterogeneous structure in geodynamic earth models, *Science*, *280*, 91–95, 1998.

Čadek, O., D. A. Yuen, V. Steinbach, A. Chopelas, and C. Matyska, Lower mantle thermal structure deduced from seismic tomography, mineral physics and numerical modelling, *Earth Planet. Sci. Lett.*, *121*, 385–402, 1994.

Cammarano, F., S. Goes, P. Vacher, and D. Giardini, Inferring upper-mantle temperatures from seismic velocities, *Phys. Earth Planet. Int.*, *138*, 197–222, 2003.

Carslaw, H. S., and J. C. Jaeger, *Conduction of heat in solids*, Clarendon Press, 1959.

Chapman, D. S., Thermal gradients in the continental crust, in *The Nature of the Lower Continental Crust*, edited by J. B. Dawson, vol. 24 of *Geol. Soc. Spec. Publ.*, pp. 63–70, Geological Society Publishing House, 1986.

Chopelas, A., and R. Boehler, Thermal expansivity in the lower mantle, *Geophys. Res. Lett.*, *19*, 1983–1986, 1992.

Christensen, U. R., The influence of trench migration on slab penetration into the lower mantle, *Earth Planet. Sci. Lett.*, *140*, 27–39, 1996.

Chung, S.-L., C.-H. Lo, T.-Y. Lee, Y. Zhang, Y. Xie, X. Li, K.-L. Wang, and P.-L. Wang, Diachronous uplift of the Tibetan plateau starting 40 Myr ago, *Nature*, *394*, 769–773, 1998.

Cox, A., and R. B. Hart, *Plate tectonics: How it works*, Blackwell Science, 1986.

Daly, M., M. Cooper, and I. Wilson, Cenozoic plate tectonics and basin evolution in Indonesia, *Mar. Pet. Geol.*, *8*, 2–21, 1991.

References

Daniel, A. J., N. J. Kusznir, and P. Styles, Thermal and dynamic modeling of deep subduction of a spreading center: Implications for the fate of the subducted Chile Rise, southern Chile, *J. Geophys. Res*, *106*, 4293 (1998JB900,028), 2001.

Danishwar, S., R. J. Stern, and M. A. Khan, Field relations and structural constraints for the Teru volcanic formation, northern Kohistan Terrane, Pakistani Himalayas, *Journal of Asian Earth Sciences*, *19*, 683–695, 2001.

Davies, J. H., and D. J. Stevenson, Physical model of the source region of subduction zone volcanics, *J. Geophys. Res*, *97*, 2037–2070, 1992.

Davies, J. H., and F. von Blanckenburg, Slab breakoff: A model of lithosphere detachment and its test in the magmatism and deformation of collisional orogens, *Earth Planet. Sci. Lett.*, *129*, 85–102, 1995.

De Jonge, M. R., *Geodynamic evolution and mantle structure*, Ph.D. Thesis, Utrecht University, the Netherlands, 1995.

De Jonge, M. R., M. J. R. Wortel, and W. Spakman, From tectonic reconstruction to upper mantle model: An application to the Alpine-Mediterranean region, *Tectonophysics*, *223*, 53–65, 1993.

De Jonge, M. R., M. J. R. Wortel, and W. Spakman, Regional scale tectonic evolution and the seismic velocity structure of the lithosphere and upper mantle: The Mediterranean region, *J. Geophys. Res*, *99*, 12,091–12,108, 1994.

Deal, M. M., G. Nolet, and R. D. van der Hilst, Slab temperature and thickness from seismic tomography 1. Method and application to Tonga, *J. Geophys. Res*, *104*, 28,789–28,802, 1999.

DeLong, S. E., W. M. Schwarz, and R. N. Anderson, Thermal effects of ridge subduction, *Earth Planet. Sci. Lett.*, *44*, 239–246, 1979.

DeMets, C., R. G. Gordon, D. F. Argus, and S. Stein, Effect of recent revisions to the geomagnetic reversal timescale on estimates of current plate motions, *Geophys. Res. Lett.*, *21*, 2191–2194, 1994.

Dercourt, J., L. E. Ricou, and B. Vrielynck (Eds.), *Atlas Téthys, Palaeoenvironmental Maps*, Gauthier-Villars, 1993.

Deschamps, F., and J. Trampert, Mantle tomography and its relation to temperature and composition, *Phys. Earth Planet. Int.*, *140*, 277–291, 2003.

Duffy, T., and D. Anderson, Seismic velocities in mantle minerals and the mineralogy of the upper mantle, *J. Geophys. Res*, *94*, 1895–1912, 1989.

Duncan, R., and M. Richards, Hotspots, mantle plumes, flood basalts, and true polar wander, *Reviews of Geophysics*, *29*, 31–50, 1991.

Dziewonski, A. M., and D. L. Anderson, Preliminary reference Earth model, *Phys. Earth Planet. Int.*, *25*, 297–356, 1981.

Ekström, G., and A. M. Dziewonski, The unique anisotropy of the Pacific upper mantle, *Nature*, *394*, 168–172, 1998.

Engdahl, E. R., R. van der Hilst, and R. Buland, Global teleseismic earthquake relocation with improved travel times and procedures for depth determination, *Bull. Seism. Soc. Am.*, *88*, 722–743, 1998.

Faccenna, C., L. Jolivet, C. Piromallo, and A. Morelli, Subduction and the depth of convection in the Mediterranean mantle, *J. Geophys. Res*, *108*, 2099 (2001JB001,690), 2003.

Forte, A. M., R. L. Woodward, and A. M. Dziewonski, Joint inversions of seismic and geodynamic data for models of three-dimensional mantle heterogeneity, *J. Geophys. Res*, *99*, 21,857–21,877, 1994.

Fournier, M., P. Patriat, and S. Leroy, Reappraisal of the Arabia-India-Somalia triple junction kinematics, *Earth Planet. Sci. Lett.*, *189*, 103–114, 2001.

Gahagan, L., C. Scotese, J.-Y. Royer, D. Sandwell, J. Winn, R. Tomlins, M. Ross, J. Newman, R. Müller, C. Mayes, L. Lawver, and C. Heubeck, Tectonic fabric map of the ocean basins from satellite altimetry data, *Tectonophysics*, *155*, 1–26, 1988.

Gaherty, J. B., and B. H. Hager, Compositional vs. thermal buoyancy and the evolution of subducted lithosphere, *Geophys. Res. Lett.*, *21*, 141–144, 1994.

Gealey, W. K., Plate tectonic evolution of the Mediterranean - Middle East region, *Tectonophysics*, *155*, 285–306, 1988.

Goes, S., and S. van der Lee, Thermal structure of the North American uppermost mantle inferred from seismic tomography, *J. Geophys. Res*, *107*, 2050 (2000JB000,049), 2002.

Goes, S., R. Govers, and P. Vacher, Shallow mantle temperatures under Europe from P and S wave tomography, *J. Geophys. Res*, *105*, 11,153–11,169, 2000.

Goes, S., F. Cammarano, and U. Hansen, Synthetic seismic signature of thermal mantle plumes, *Earth Planet. Sci. Lett.*, *218*, 401–417, 2004.

Goldstein, H., *Classical mechanics*, Addison-Wesley Press, 1950.

Gordon, R. G., and D. M. Jurdy, Cenozoic global plate motions, *J. Geophys. Res*, *91*, 12,389–12,406, 1986.

Griffiths, R. W., R. I. Hackney, and R. D. van der Hilst, A laboratory investigation of effects of trench migration on the descent of subducted slabs, *Earth Planet. Sci. Lett.*, *133*, 1–17, 1995.

Guillou-Frottier, L., J. Buttles, and P. Olson, Laboratory experiments on the structure of subducted lithosphere, *Earth Planet. Sci. Lett.*, *133*, 19–34, 1995.

Gurnis, M., and B. H. Hager, Controls on the structure of subducted slabs, *Nature*, *335*, 317–321, 1988.

Hall, R., Reconstructing Cenozoic SE Asia, in *Tectonic Evolution of Southeast Asia*, edited by R. Hall and D. Blundell, vol. 106 of *Geol. Soc. Spec. Publ.*, pp. 153–184, Geological Society Publishing House, 1996.

Hall, R., and W. Spakman, Subducted slabs beneath the eastern Indonesia-Tonga region: Insights from tomography, *Earth Planet. Sci. Lett.*, *201*, 321–336, 2002.

Hamilton, W., Tectonics of the Indonesian region, *US Geol. Surv. Prof. Pap.*, *1078*, 1979.

Han, L., and M. Gurnis, How valid are dynamic models of subduction and convection when plate motions are prescribed?, *Phys. Earth Planet. Int.*, *110*, 235–246, 1999.

Harrison, T. M., M. Grove, O. M. Lovera, and E. J. Catlos, A model for the origin of Himalayan anatexis and inverted metamorphism, *J. Geophys. Res*, *103*, 27,017–27,032, 1998.

Hauck, S. A., R. J. Phillips, and H. A. M., Variable conductivity: Effects on the thermal structure of subducting slabs, *Geophys. Res. Lett.*, *26*, 3257–3260, 1999.

Hofmeister, A. M., Mantle values of thermal conductivity and the geotherm from phonon lifetimes, *Science*, *283*, 1699–1706, 1999.

Houseman, G. A., and D. Gubbins, Deformation of subducted oceanic lithosphere, *Geophys. J. Int.*, *131*, 535–551, 1997.

Isaak, D. G., High-temperature elasticity of iron-bearing olivines, *J. Geophys. Res*, *97*, 1871–1885, 1992.

Jackson, I., and S. M. Rigden, Composition and temperature of the Earth's mantle: Seismological models interpreted through experimental studies of Earth materials, in *The Earth's mantle: Composition, structure, and evolution*, edited by I. Jackson, pp. 405–460, Cambridge University Press, 1998.

Jolivet, L., A comparison of geodetic and finite strain pattern in the Aegean, geodynamic implications, *Earth Planet. Sci. Lett.*, *187*, 95–104, 2001.

Jolivet, L., and C. Faccenna, Mediterranean extension and the Africa-Eurasia collision, *Tectonics*, *19*, 1095–1106, 2000.

Kárason, H., and R. D. van der Hilst, Constraints on mantle convection from seismic tomography, in *The History and Dynamics of Global Plate Motions*, edited by M. A. Richards, R. G. Gordon, and R. D. van der Hilst, vol. 121 of *Geophysical Monograph*, pp. 277–288, Am. Geophys. Union, 2000.

References

Karato, S.-I., Importance of anelasticity in the interpretation of seismic tomography, *Geophys. Res. Lett.*, *20*, 1623–1626, 1993.

Katili, J., Volcanism and plate tectonics in the Indonesian island arcs, *Tectonophysics*, *26*, 165–188, 1975.

Kellogg, L. H., B. H. Hager, and R. D. van der Hilst, Compositional stratification in the deep mantle, *Science*, *283*, 1881–1884, 1999.

Kennett, B. L. N., and E. R. Engdahl, Traveltimes for global earthquake location and phase identification, *Geophys. J. Int.*, *105*, 429–465, 1991.

Kennett, B. L. N., E. R. Engdahl, and R. Buland, Constraints on seismic velocities in the Earth from traveltimes, *Geophys. J. Int.*, *122*, 108–124, 1995.

Keskin, M., Magma generation by slab steepening and breakoff beneath a subduction-accretion complex: An alternative model for collision-related volcanism in eastern Anatolia, Turkey, *Geophys. Res. Lett.*, *30*, 8046 (2003GL018,019), 2003.

Kincaid, C., and P. Olson, An experimental study of subduction and slab migration, *J. Geophys. Res*, *92*, 13,832–13,840, 1987.

Klitgord, K., and H. Schouten, Plate kinematics of the central Atlantic, in *The Geology of North America, Volume M, The Western North Atlantic Region*, edited by P. Vogt and B. Tucholke, pp. 351–378, Geological Society of America, 1986.

Knipper, A., L.-E. Ricou, and J. Dercourt, Ophiolites as indicators of the geodynamic evolution of the Tethyan Ocean, *Tectonophysics*, *123*, 213–240, 1986.

Kohn, M. J., and C. D. Parkinson, Petrologic case for Eocene slab breakoff during the Indo-Asian collision, *Geology*, *30*, 591–594, 2002.

Lawver, L., R. Müller, S. Srivastava, and W. Roest, The opening of the Arctic Ocean, in *Geological History of the Polar Oceans: Arctic versus Antarctic*, edited by U. Bleil and J. Thiede, pp. 29–62, Kluwer Academic Press, 1990.

Lee, T.-Y., and L. Lawver, Cenozoic plate reconstruction of Southeast Asia, *Tectonophysics*, *251*, 85–138, 1995.

LePichon, X., and J.-M. Gaulier, The rotation of Arabia and the Levant fault system, *Tectonophysics*, *153*, 271–294, 1988.

Lévêque, J. J., L. Rivera, and G. Wittlinger, On the use of the checker-board test to assess the resolution of tomographic inversions, *Geophys. J. Int.*, *115*, 313–318, 1993.

Lips, A. L. W., D. Cassard, H. Sözbilir, H. Yilmaz, and J. R. Wijbrans, Multistage exhumation of the Menderes Massif, western Anatolia (Turkey), *Int. J. Earth Sc.*, *89*, 781–792, 2001.

Lithgow-Bertelloni, C., and M. A. Richards, The dynamics of Cenozoic and Mesozoic plate motions, *Reviews of Geophysics*, *36*, 27–78, 1998.

Mahéo, G., S. Guillot, J. Blichert-Toft, Y. Rolland, and A. Pêcher, A slab breakoff model for the Neogene thermal evolution of South Karakorum and South Tibet, *Earth Planet. Sci. Lett.*, *195*, 45–58, 2002.

McCaffrey, R., Active tectonics of the eastern Sunda and Banda arcs, *J. Geophys. Res*, *93*, 15,163–15,182, 1988.

McClusky, S., S. Balassanian, A. Barka, et al., Global Positioning System constraints on plate kinematics and dynamics in the eastern Mediterranean and Caucasus, *J. Geophys. Res*, *105*, 5695–5719, 2000.

McClusky, S., R. Reilinger, S. Mahmoud, D. Ben Sari, and A. Tealeb, GPS constraints on Africa (Nubia) and Arabia plate motions, *Geophys. J. Int.*, *155*, 126–138, 2003.

McKenzie, D. P., Some remarks on heat flow and gravity anomalies, *J. Geophys. Res*, *72*, 6261–6273, 1967.

McKenzie, D. P., Speculations on the consequences and causes of plate motion, *Geophys. J. R. Astr. Soc.*, *18*, 1–32, 1969.

McKenzie, D. P., Temperature and potential temperature beneath island arcs, *Tectonophysics*, *10*, 357–366, 1970.

McKenzie, D. P., Some remarks on the development of sedimentary basins, *Earth Planet. Sci. Lett.*, *40*, 25–32, 1978.

174

Milsom, J., K. S., and Sardjono, Extension, collision and curvature in the eastern Banda arc, in *Tectonic Evolution of Southeast Asia*, edited by R. Hall and D. Blundell, vol. 106 of *Geol. Soc. Spec. Publ.*, pp. 85–94, Geological Society Publishing House, 1996.

Minear, J. W., and M. N. Toksöz, Thermal regime of a downgoing slab and new global tectonics, *J. Geophys. Res*, *8*, 1397–1419, 1970.

Montagner, J. P., Can seismology tell us anything about convection in the mantle?, *Reviews of Geophysics*, *32*, 115–138, 1994.

Morelli, A., and A. M. Dziewonski, Body wave travel-times and a spherically symmetric P- and S-wave velocity model, *Geophys. J. Int.*, *112*, 178–194, 1993.

Morgan, W. J., Convection plumes in the lower mantle, *Nature*, *230*, 42–43, 1971.

Morris, A., and D. H. Tarling, Palaeomagnetism and tectonics of the Mediterranean region: an introduction, in *Palaeomagnetism and Tectonics of the Mediterranean Region*, edited by A. Morris and D. H. Tarlin, vol. 105 of *Geol. Soc. Spec. Publ.*, pp. 1–18, Geological Society Publishing House, 1996.

Müller, R., J.-Y. Royer, and L. Lawver, Revised plate motions relative to the hotspots from combined Atlantic and Indian Ocean hotspot tracks, *Geology*, *21*, 275–278, 1993.

Norton, I. O., Global plate reconstruction model, *Tech. rep.*, ExxonMobil Exploration, Houston, Texas, USA, 1999.

Norton, I. O., Global hotspot reference frames and plate motion, in *The History and Dynamics of Global Plate Motions*, edited by M. A. Richards, R. G. Gordon, and R. D. van der Hilst, vol. 121 of *Geophysical Monograph*, pp. 339–357, Am. Geophys. Union, 2000.

O'Connor, J. M., and A. P. le Roex, South Atlantic hotspot-plume systems: 1. Distribution of volcanism in time and space, *Earth Planet. Sci. Lett.*, *113*, 343–364, 1992.

Okay, A. I., Was the Late Triassic orogeny in Turkey caused by the collission of an oceanic plateau?, in *Tectonics and Magmatism in Turkey and the Surrounding Area*, edited by E. Bozkurt, J. A. Winchester, and J. D. A. Piper, vol. 173 of *Geol. Soc. Spec. Publ.*, pp. 25–41, Geological Society Publishing House, 2000.

Olbertz, D., M. Wortel, and U. Hansen, Trench migration and subduction zone geometry, *Geophys. Res. Lett.*, *24*, 221–224, 1997.

O'Neill, C., D. Müller, and B. Steinberger, Geodynamic implications of moving Indian Ocean hotspots, *Earth Planet. Sci. Lett.*, *215*, 151–168, 2003.

Parsons, B., and J. G. Sclater, An analysis of the variation of ocean floor bathymetry and heat flow with age, *J. Geophys. Res*, *82*, 803–827, 1977.

Peacock, S. M., Thermal and petrologic structure of subduction zones, in *Subduction: Top to Bottom*, edited by G. E. Bebout, D. W. Scholl, S. H. Kirby, and J. P. Platt, vol. 96 of *Geophysical Monograph*, pp. 119–133, Am. Geophys. Union, 1996.

Pollack, H. N., S. J. Hurter, and J. R. Johnson, Heat flow from the Earth's interior: Analysis of the global data set, *Reviews of Geophysics*, *31*, 267–280, 1993.

Ponko, S. C., and S. M. Peacock, Thermal modeling of the southern Alaska subduction zone: Insight into the petrology of the subducting slab and overlying mantle wedge, *J. Geophys. Res*, *100*, 22,117–22,128, 1995.

Pysklywec, R. N., J. X. Mitrovica, and M. Ishii, Mantle avalanche as a driving force for tectonic reorganization in the southwest Pacific, *Earth Planet. Sci. Lett.*, *209*, 29–38, 2003.

Ranalli, G., Seismic tomography and mineral physics, in *Seismic modelling of the Earth structure*, edited by E. Boschi, G. Ekström, and A. Morelli, pp. 443–461, Instituto Nazionale di Geofisica, 1996.

Rangin, C., L. Jolivet, M. Pubellier, et al., A simple model for the tectonic evolution of Southeast Asia and Indonesian region for the past 43 m.y., *Bull. Soc. géol. France*, *8*, 889–905, 1990a.

References

Rangin, C., M. Pubellier, J. Azéma, A. Briais, P. Chotin, H. Fontaine, P. Huchon, L. Jolivet, R. Maury, C. Müller, J. Rampnoux, J. Stephan, J. Tournon, N. Cottereau, J. Dercourt, and L. Ricou, The quest for Tethys in the western Pacific: 8 paleogeodynamic maps for Cenozoic time, *Bull. Soc. géol. France*, *8*, 907–913, 1990b.

Rangin, C., D. Dahrin, R. Quebral, and the Modec Scientific Party, Collision and strike-slip faulting in the northern Molucca Sea, in *Tectonic Evolution of Southeast Asia*, edited by R. Hall and D. Blundell, vol. 106 of *Geol. Soc. Spec. Publ.*, pp. 29–46, Geological Society Publishing House, 1996.

Rangin, C., W. Spakman, M. Pubellier, and H. Bijwaard, Tomographic and geological constraints on subduction along the eastern Sundaland continental margin (South-East Asia), *Bull. Soc. géol. France*, *170*, 775–788, 1999.

Ribe, N. M., Seismic anisotropy and mantle flow, *J. Geophys. Res*, *94*, 4213–4223, 1989.

Richards, M. A., and D. C. Engebretson, Large-scale mantle convection and the history of subduction, *Nature*, *355*, 437–440, 1992.

Richardson, A., and D. Blundell, Continental collision in the Banda arc, in *Tectonic Evolution of Southeast Asia*, edited by R. Hall and D. Blundell, vol. 106 of *Geol. Soc. Spec. Publ.*, pp. 47–60, Geological Society Publishing House, 1996.

Robertson, A., and M. Searle, The northern Oman Tethyan continental margin: stratigraphy, structure, concepts and controversis, in *The Geology and Tectonics of the Oman Region*, edited by A. Robertson, M. Searle, and A. Ries, vol. 49 of *Geol. Soc. Spec. Publ.*, pp. 213–224, Geological Society Publishing House, 1990.

Röhm, A. H. E., R. Snieder, S. Goes, and J. Trampert, Thermal structure of continental upper mantle inferred from S-wave velocity and surface heat flow, *Earth Planet. Sci. Lett.*, *181*, 395–407, 2000.

Saltzer, R. L., R. D. van der Hilst, and H. Kárason, Comparing P and S wave heterogeneity in the mantle, *Geophys. Res. Lett.*, *28*, 1335–1338, 2001.

Schmid, C., S. Goes, S. van der Lee, and D. Giardini, Fate of the Cenozoic Farallon slab from a comparison of kinematic thermal modeling with tomographic images, *Earth Planet. Sci. Lett.*, *204*, 17–32, 2002.

Sella, G. F., T. H. Dixon, and A. Mao, REVEL: A model for recent plate velocities from space geodesy, *J. Geophys. Res*, *107*, 2081 (2000JB000,033), 2002.

Şengör, A. M. C., and B. A. Natal'in, Paleotectonics of Asia: fragments of a synthesis, in *The Tectonic Evolution of Asia*, edited by A. Yin and T. M. Harrison, pp. 486–640, Cambridge University Press, 1996.

Sleep, N. H., Teleseismic P-wave transmission through slabs, *Bull. Seism. Soc. Am.*, *63*, 1349–1373, 1973.

Spakman, W., Delay time tomography of the upper mantle below Europe, the Mediterranean, and Asia Minor, *Geophys. J. Int.*, *107*, 309–332, 1991.

Spakman, W., and H. Bijwaard, Optimization of cell parameterizations for tomographic inverse problems, *Pure appl. geophys.*, *158*, 1401–1423, 2001.

Spakman, W., and G. Nolet, Imaging algorithms, accuracy and resolution in delay time tomography, in *Mathematical Geophysics: a survey of recent developments in seismology and geodynamics*, edited by N. Vlaar, G. Nolet, M. Wortel, and S. Cloetingh, pp. 155–188, Reidel, 1988.

Spakman, W., S. van der Lee, and R. D. van der Hilst, Travel-time tomography of the European-Mediterranean mantle down to 1400 km, in *Recent Advances in Geosciences*, pp. 3–74, Elsevier Sci., 1993.

Srivastava, S., and W. Roest, Seafloor spreading history ii-iv: Map sheets l17,2-l17,6, in *East Coast Basin Atlas Series: Labrador Sea*, edited by J. Bell, Atlantic Geoscience Centre, Geologic Survey of Canada, 1989.

176

Stampfli, G. M., Tethyan oceans, in *Tectonics and Magmatism in Turkey and the Surrounding Area*, edited by E. Bozkurt, J. A. Winchester, and J. D. A. Piper, vol. 173 of *Geol. Soc. Spec. Publ.*, pp. 1–23, Geological Society Publishing House, 2000.

Stampfli, G. M., and G. D. Borel, A plate tectonic model for the Paleozoic and Mesozoic constrained by dynamic plate boundaries and restored synthetic oceanic isochrons, *Earth Planet. Sci. Lett.*, *196*, 17–33, 2002.

Stampfli, G. M., and G. D. Borel, The TRANSMED transects in space and time: Constraints on the paleotectonic evolution of the Mediterranean domain, in *The TRANSMED Atlas: the Mediterranean Region from Crust to Mantle*, edited by W. Cavazza, F. Roure, W. Spakman, G. M. Stampfli, and P. A. Ziegler, Springer Verlag, 2004.

Stein, C. A., and S. Stein, A model for the global variation in oceanic depth and heat flow with lithospheric age, *Nature*, *359*, 123–129, 1992.

Steinberger, B., Slabs in the lower mantle – results of dynamic modelling compared with tomographic images and the geoid, *Phys. Earth Planet. Int.*, *118*, 241–257, 2000.

Tackley, P. J., Effects of strongly variable viscosity on three-dimensional compressible convection in planetary mantles, *J. Geophys. Res*, *101*, 3311–3332, 1996.

Tarduno, J. A., and J. Gee, Large scale motion between Pacific and Atlantic hotspots, *Nature*, *378*, 477–480, 1995.

Toksöz, M. N., J. W. Minear, and B. R. Julian, Temperature field of a downgoing slab, *J. Geophys. Res*, *76*, 1113–1139, 1971.

Toksöz, M. N., N. H. Sleep, and A. T. Smith, Evolution of the downgoing lithosphere and the mechanics of deep focus earthquakes, *Geophys. J. R. Astr. Soc.*, *35*, 285–310, 1973.

Torsvik, T. H., R. van der Voo, and T. F. Redfield, Relative hotspot motions versus true polar wander, *Earth Planet. Sci. Lett.*, *202*, 185–200, 2002.

Trampert, J., and H. J. van Heijst, Global azimuthal anisotropy in the transition zone, *Science*, *296*, 1297–1299, 2002.

Trampert, J., P. Vacher, and N. Vlaar, Sensitivities of seismic velocities to temperature, pressure and composition in the lower mantle, *Phys. Earth Planet. Int.*, *124*, 255–267, 2001.

Turcotte, D., and G. Schubert, *Geodynamics*, Cambridge University Press, 2002.

Turcotte, D. L., and E. R. Oxburgh, Finite amplitude convective cells and continental drift, *J. Fluid Mech.*, *28*, 29–42, 1967.

Van de Zedde, D. M. A., and M. J. R. Wortel, Shallow slab detachment as a transient source of heat at midlithospheric depths, *Tectonics*, *20*, 868–882, 2001.

Van den Beukel, J., Break up of young oceanic lithosphere in the upper part of a subduction zone: Implications for the emplacement of ophiolites, *Tectonics*, *9*, 825–844, 1990.

Van den Beukel, J., Some thermomechanical aspects of the subduction of continental lithosphere, *Tectonics*, *11*, 316–329, 1992.

Van den Beukel, J., and R. Wortel, Temperature and shear stresses in the upper part of a subduction zone, *Geophys. Res. Lett.*, *14*, 1057–1060, 1988.

Van der Hilst, R., Complex morphology of subducted lithosphere in the mantle beneath the Tonga trench, *Nature*, *374*, 154–157, 1995.

Van der Hilst, R. D., and H. Kárason, Compositional heterogeneity in the bottom 1000 kilometers of Earth's mantle: Toward a hybrid convection model, *Science*, *283*, 1885–1888, 1999.

Van der Voo, R., *Paleomagnetism of the Atlantic, Tethys and Iapetus Oceans*, Cambridge University Press, 1993.

Van der Voo, R., W. Spakman, and H. Bijwaard, Tethyan subducted slabs under India, *Earth Planet. Sci. Lett.*, *171*, 7–20, 1999.

Van Hunen, J., A. P. van den Berg, and N. J. Vlaar, The impact of the South-American plate motion and the Nazca Ridge subduction on the flat subduction below south Peru, *Geophys. Res. Lett.*, *29*, 1690 (2001GL014,004), 2002.

References

Van Wijk, J. W., R. Govers, and K. P. Furlong, Three-dimensional thermal modeling of the California upper mantle: a slab window vs. stalled slab, *Earth Planet. Sci. Lett.*, *186*, 175–186, 2001.

Wen, L., and D. L. Anderson, The fate of slabs inferred from seismic tomography and 130 million years of subduction, *Earth Planet. Sci. Lett.*, *133*, 185–198, 1995.

Wong A Ton, S. Y. M., and M. J. R. Wortel, Slab detachment in continental collision zones: An analysis of controlling parameters, *Geophys. Res. Lett.*, *24*, 2095–2098, 1997.

Yang, K., A plate reconstruction of the eastern Tethyan orogen in Southwestern China, in *Mantle Dynamics and Plate Interactions in East Asia*, edited by M. F. J. Flower, S.-L. Chung, C.-H. Lo, and T.-Y. Lee, vol. 27 of *Geodynamics*, pp. 269–287, Am. Geophys. Union, 1998.

Appendix A

Colour figures

Figure A.1: Topography of the Tethyan region, cf. Fig. 1.1.
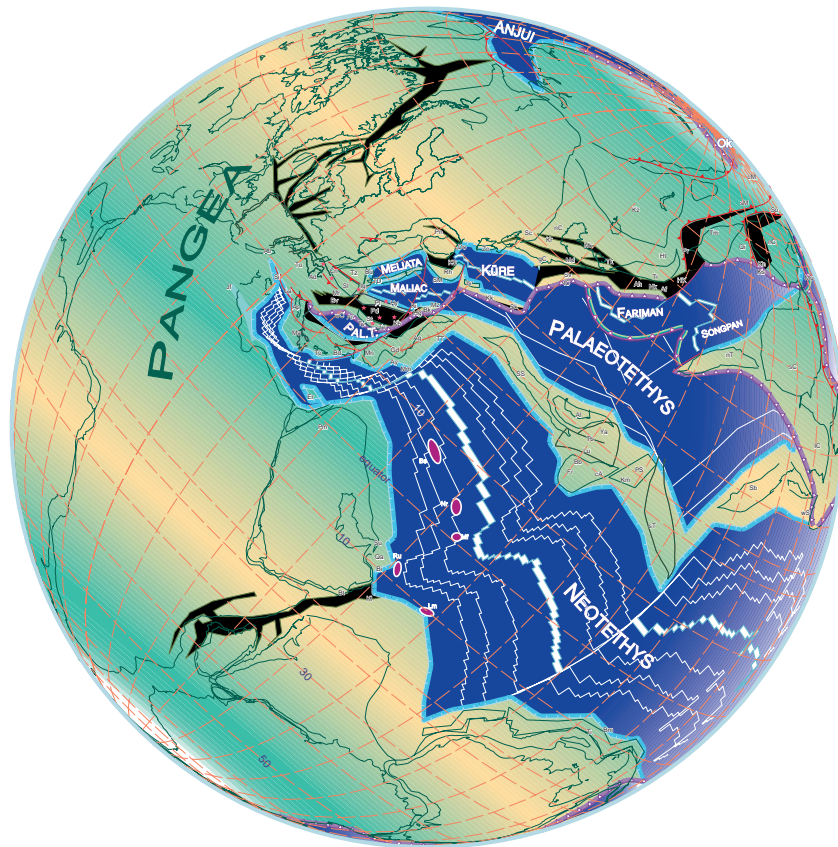
230 Ma - Ladinian

Figure A.2: Triassic reconstruction of *Stampfli and Borel* (2004), cf. Fig. 2.3.
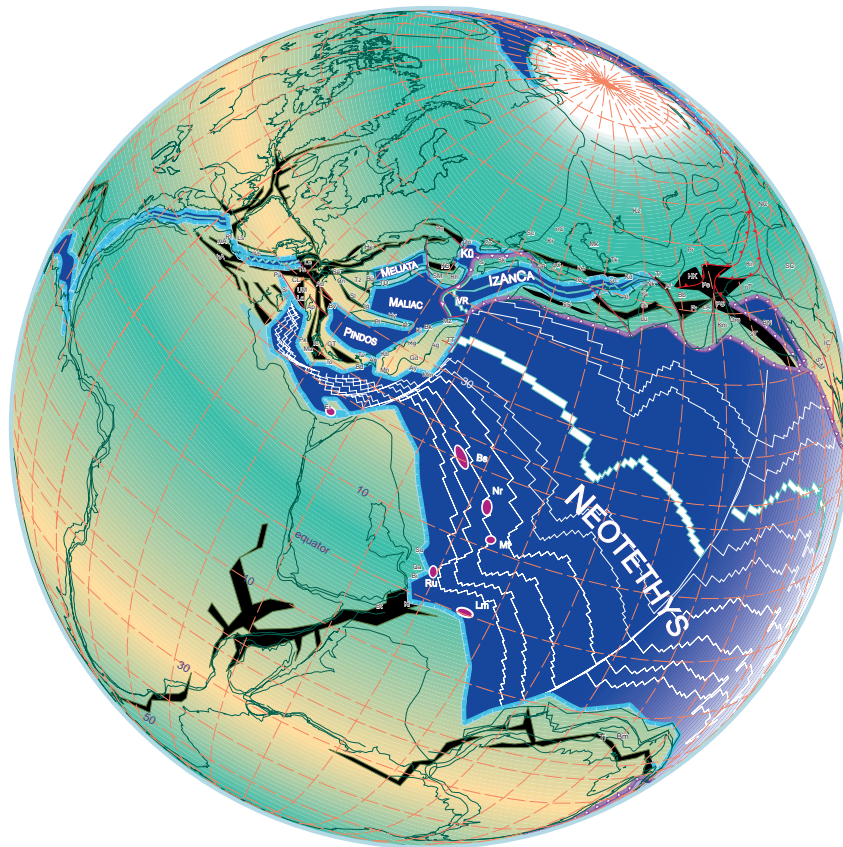
180 Ma - Toarcian-Aalenian

Figure A.3: Jurassic reconstruction of *Stampfli and Borel* (2004), cf. Fig. 2.4.
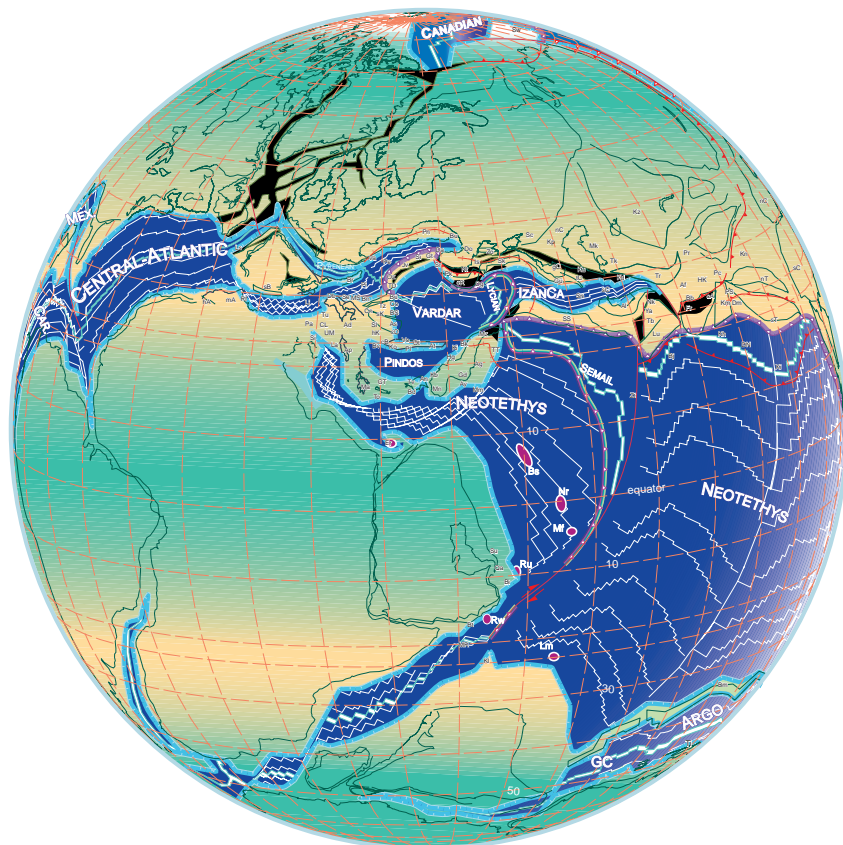
121Ma - Barremian-Aptian (an. M0)

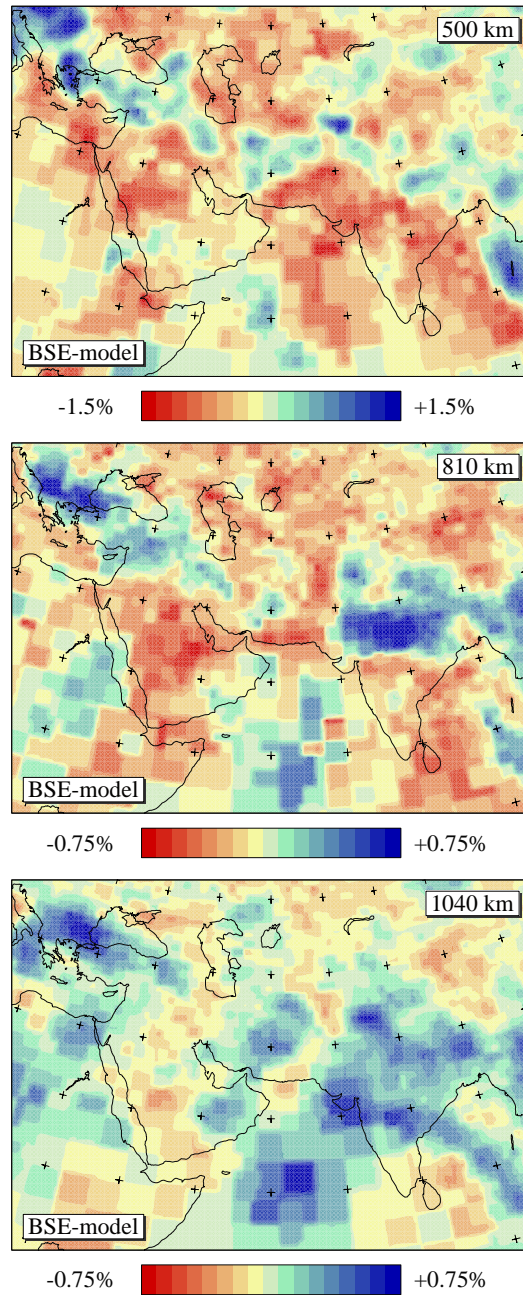**Figure A.4:** Early Cretaceous reconstruction of *Stampfli and Borel* (2004), cf. Fig. 2.5.
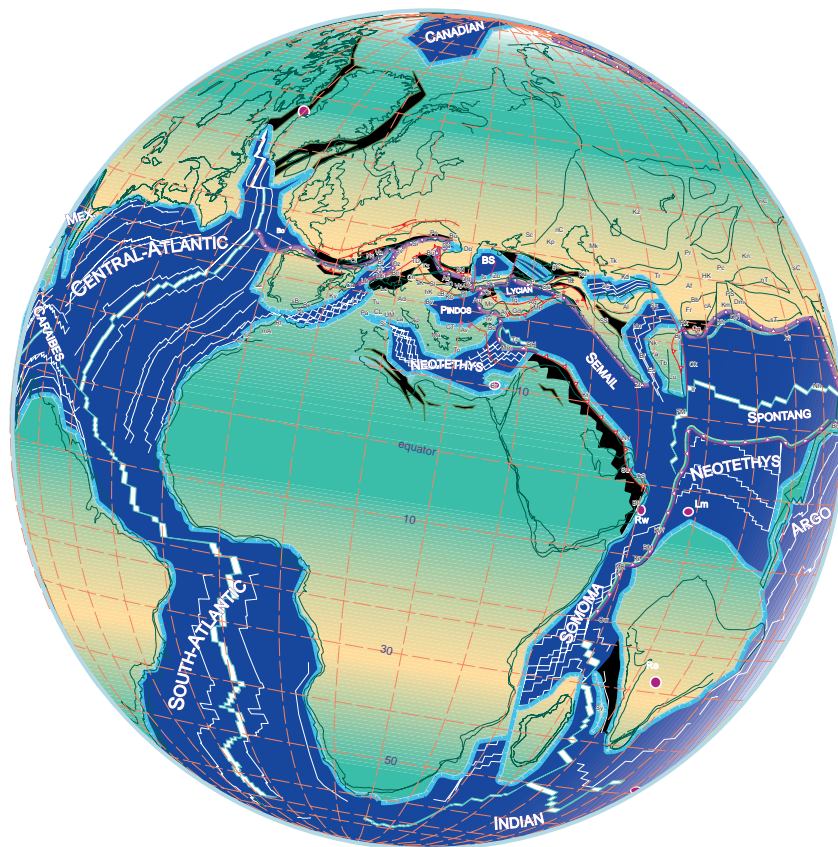
70 Ma - Early Maastrichtian (an. 31)

Figure A.5: Late Cretaceous reconstruction of *Stampfli and Borel* (2004), cf. Fig. 2.6.

Figure A.6: Horizontal sections through the tomographic BSE-model of *Bijwaard et al.* (1998) at 500, 810 and 1040 km depth (cf. Fig. 4.2).
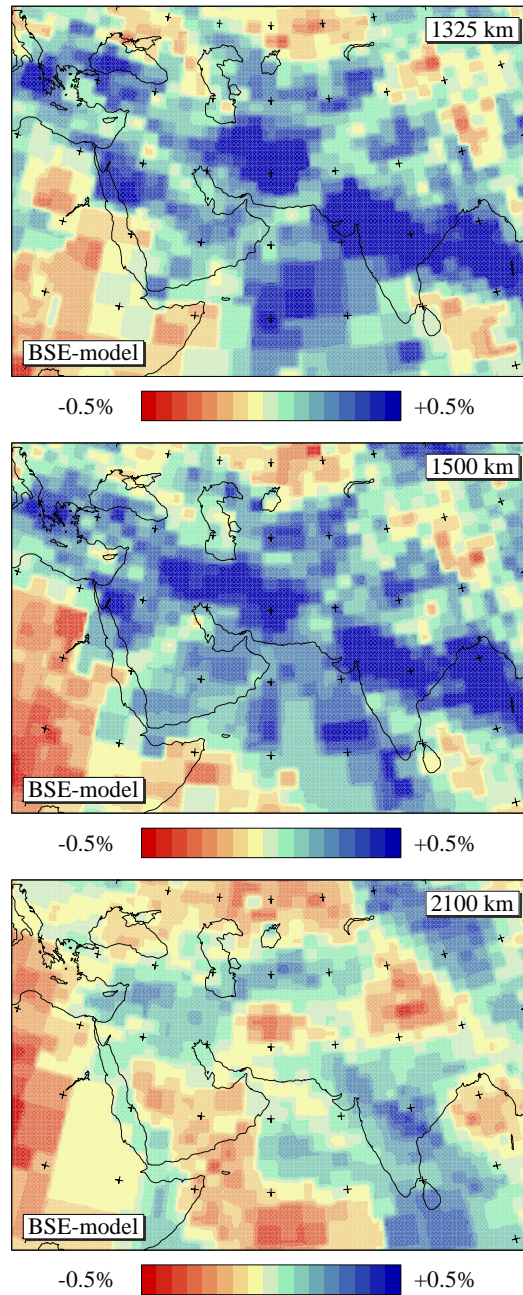
Figure A.7: Horizontal sections through the tomographic BSE-model of *Bijwaard et al.* (1998) at 1325, 1500 and 2100 km depth (cf. Fig. 4.3).
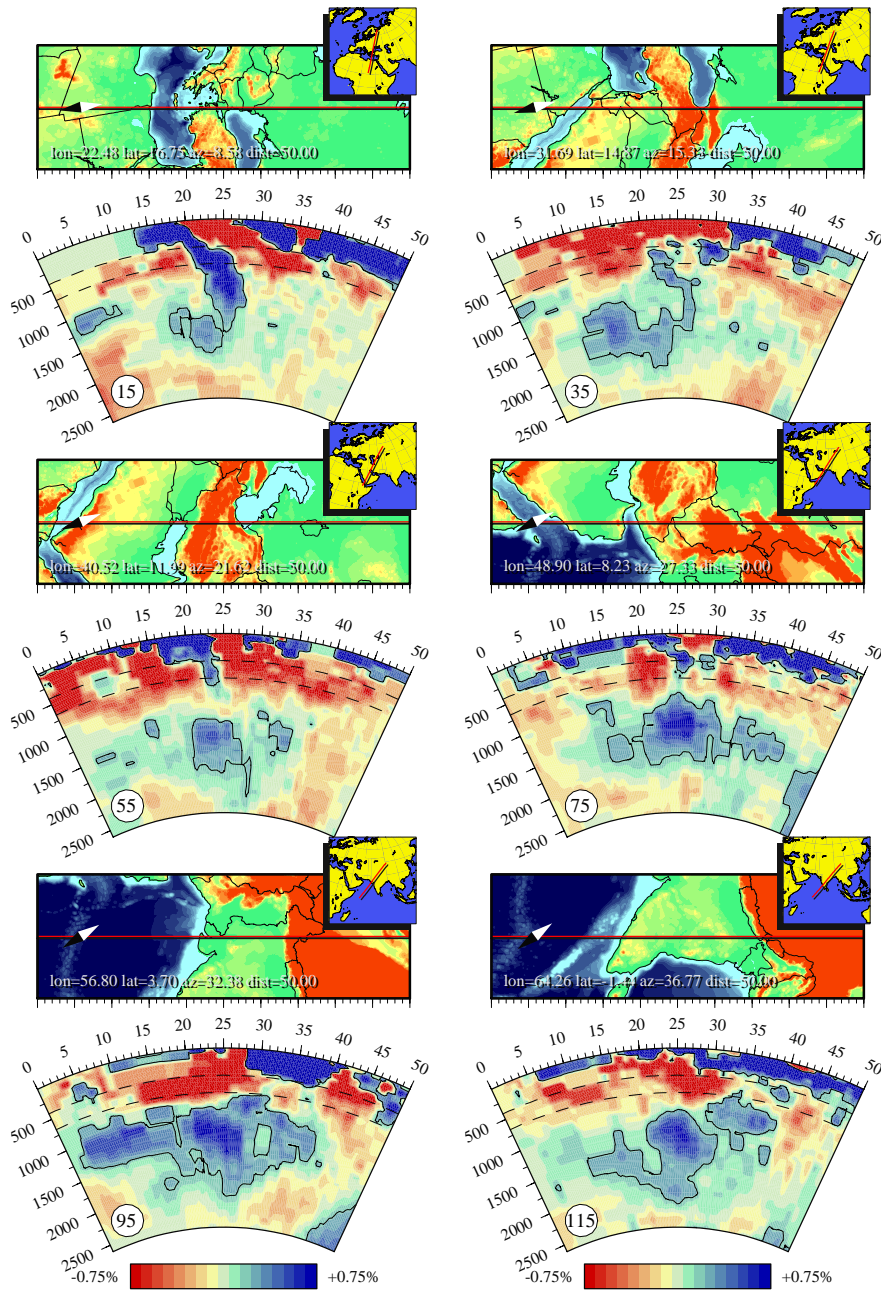
Figure A.8: Vertical sections through the tomographic model of *Bijwaard et al.* (1998) down to 2600 km depth. The sections are indicated in Figures 4.4-4.6 (pp. 73-75), cf. Fig. 4.7.
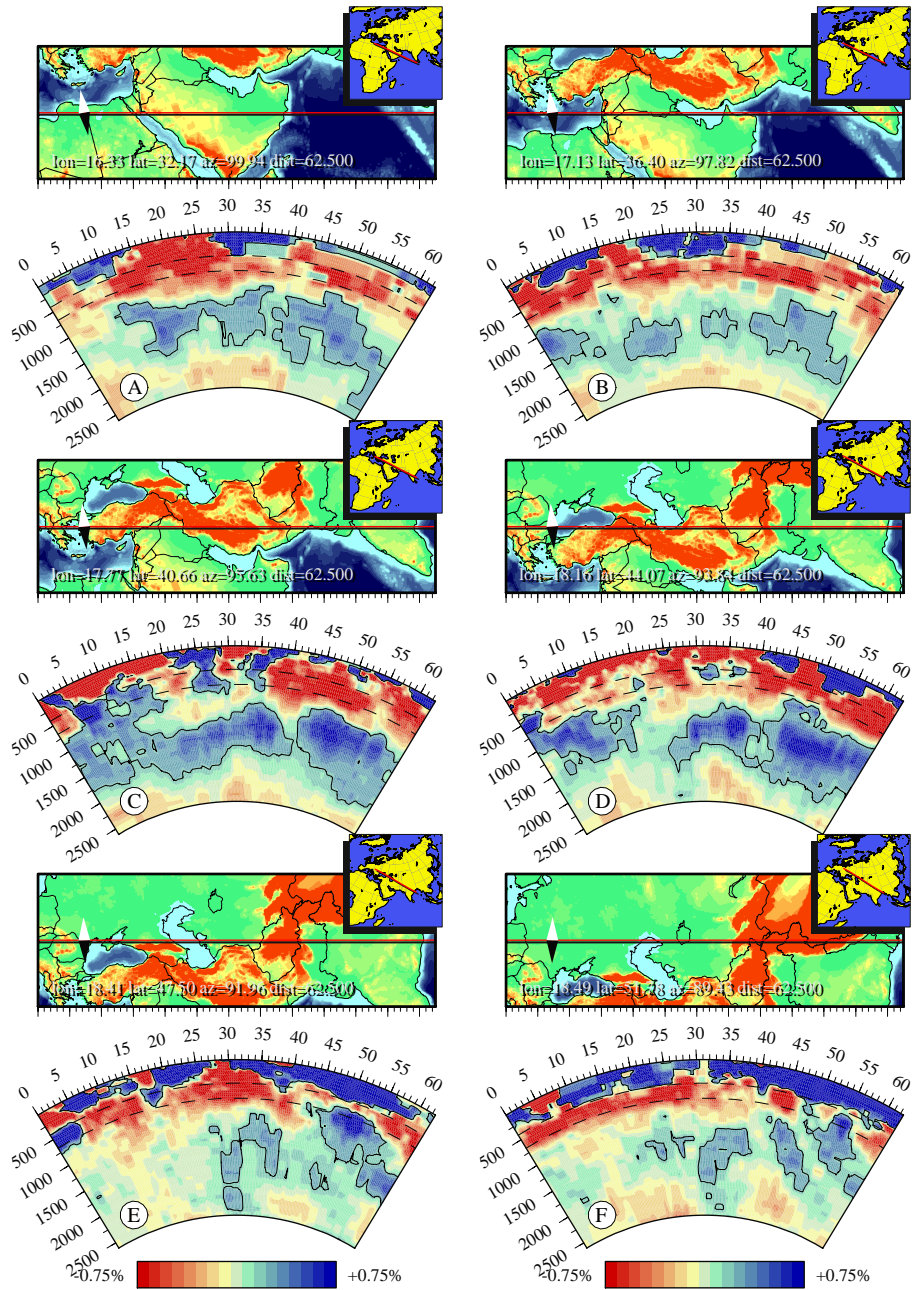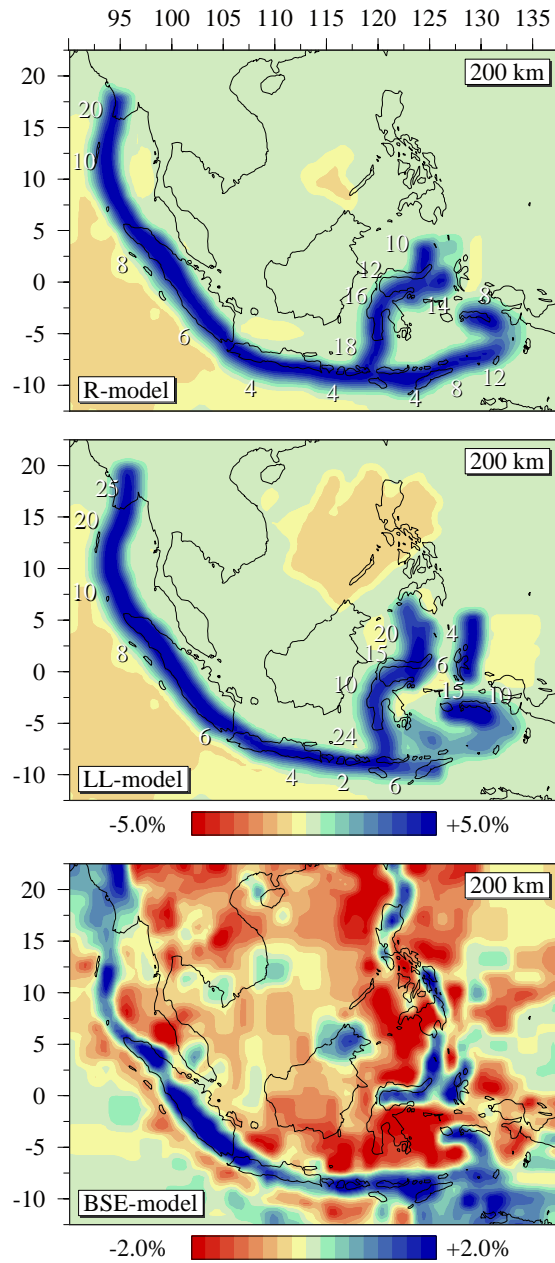
Figure A.9: Vertical sections through the tomographic model of *Bijwaard et al.* (1998) down to 2600 km depth. The sections are indicated in Figures 4.4-4.6 (pp. 73-75), cf. Fig. 4.8.

187

Figure A.10: P-velocity anomaly structure at 200 km depth. From the top downward: The R-model (based on *Rangin et al.*, 1990a,b), LL-model (based on *Lee and Lawver*, 1995) and tomographic BSE-model (*Bijwaard et al.*, 1998). Numbers give an indication of the average time (Myr) it has taken for the predicted slab remnants to subduct down to the shown depth (cf. Fig. 6.3).
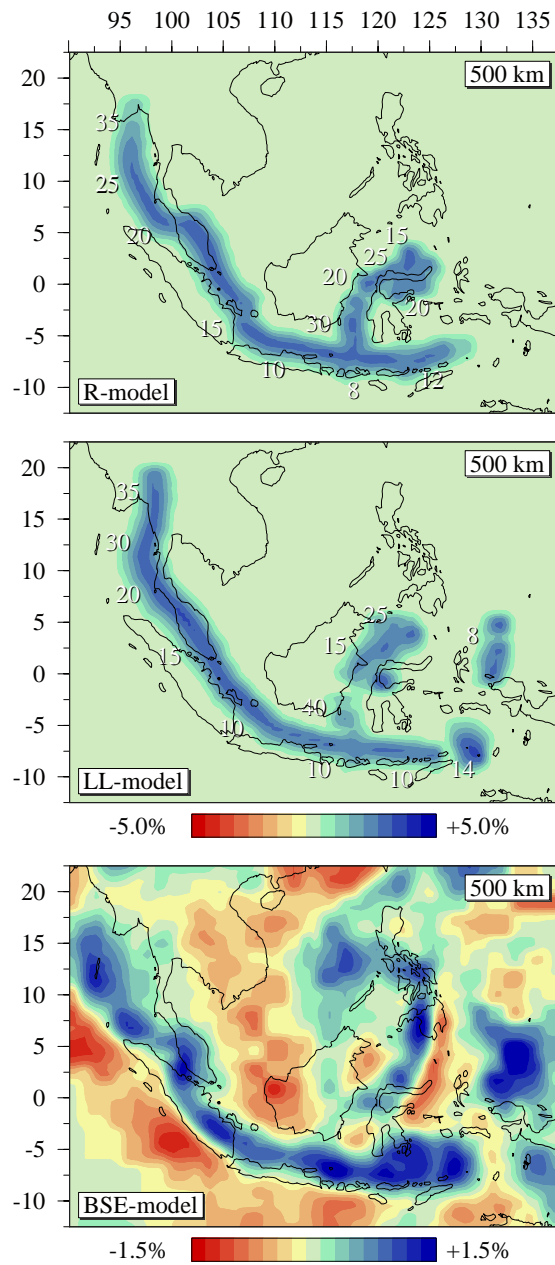
Figure A.11: P-velocity anomaly structure at 500 km depth of the R-model (upper), LL-model (middle) and tomographic BSE-model (lower panel), cf. Fig. 6.4.
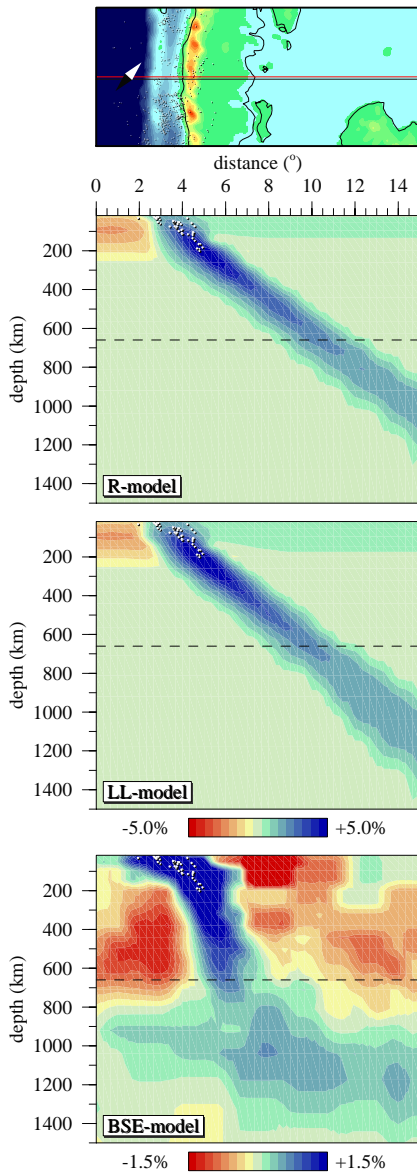
Figure A.12: Vertical sections down to 1500 km depth across Sumatra through the P-velocity anomalies of the R-model (upper), LL-model (middle) and tomographic BSE-model (lower panel), cf. Fig. 6.5.
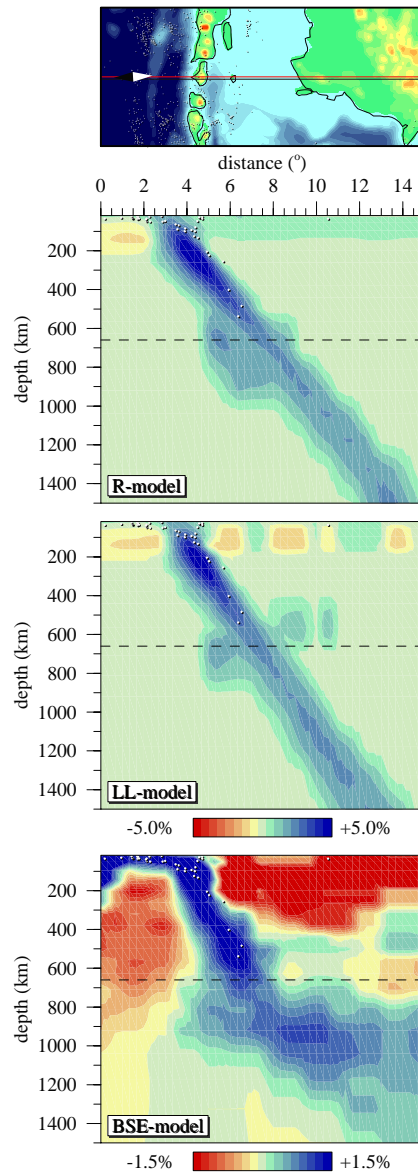
Figure A.13: Vertical sections across Java through the R-model (upper), LL-model (middle) and tomographic BSE-model (lower panel), cf. Fig. 6.6.
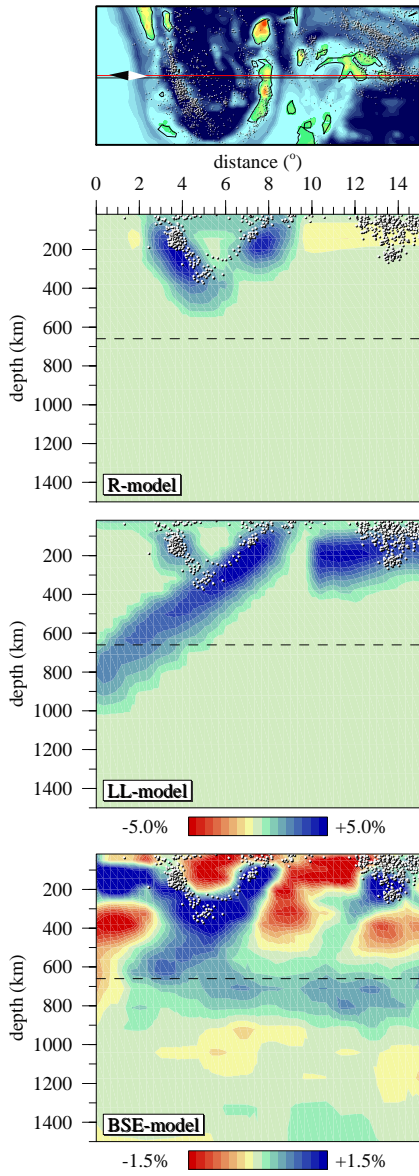
Figure A.14: Vertical sections across the Banda arc through the R-model (upper), LL-model (middle) and tomographic BSE-model (lower panel), cf. Fig. 6.7.
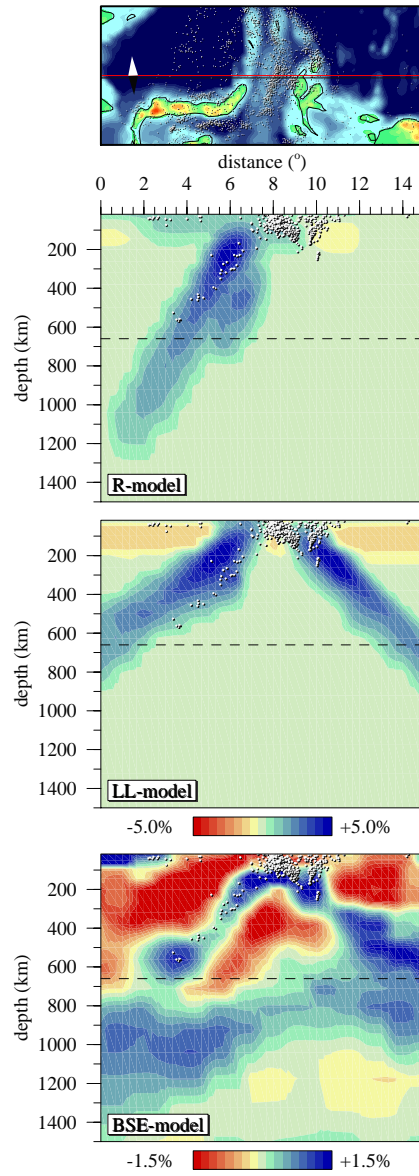
Figure A.15: Vertical sections across the Molucca Sea through the R-model (upper), LL-model (middle) and tomographic BSE-model (lower panel), cf. Fig. 6.8.

Samenvatting (Summary in Dutch)

Aardwetenschappers kijken naar de structuur van het oppervlak en inwendige van de aarde, en de processen die zich daar afspelen. De aarde lijkt op het eerste gezicht nogal hard en vast, maar alles beweegt: het binnenste van de aarde koelt langzaam af, het aardmagneetveld verandert de hele tijd, continenten schuiven over het aardoppervlak, er vinden aardbevingen en vulkaanuitbarstingen plaats, enzovoort. Inmiddels is er veel bekend over dit soort processen, maar nog lang niet alles. Het blijft lastig dat we alleen datgene hebben wat op dit moment aan het aardoppervlak waargenomen kan worden. Hoe de aarde er heel vroeger uitzag, en hoe het er in het binnenste van de aarde uitziet, zullen we nooit rechtstreeks kunnen nagaan.

Plaatbewegingen

Wat we van de aarde kunnen zien is de koude bovenlaag, de korst (zie figuur 1). De korst van continenten is relatief dik en licht van gewicht, terwijl de korst van oceaanbodems juist dun is en wat zwaarder. Onder de korst ligt de mantel, de warme laag die om de kern van de aarde ligt en bijna 2900 kilometer dik is. De bovenste laag van de mantel is vrij koud en wat stijver dan de rest. Deze laag wordt de lithosfeer genoemd en is gemiddeld 100 kilometer dik.
De korst en lithosfeer vormen samen de platen die langzaam (een paar centimeter per jaar) over de diepere mantel bewegen. Daar waar de stijve platen langs of over elkaar schuiven, komen aardbevingen en vulkaanuitbarstingen voor en worden gebergtes opgebouwd. De platen bewegen doordat het binnenste van de aarde erg heet is en de buitenkant juist koud. Het mantel-materiaal is hard gesteente, tenminste in onze ogen, maar toch kan het stromen (zoals het harde ijs van een gletsjer dat ook kan) - als de krachten die er op spelen maar groot genoeg zijn en je lang genoeg blijft wachten (bijvoorbeeld een paar miljoen jaar). Het hete mantel-materiaal komt vanuit de diepte omhoog, koelt af aan het aardoppervlak en zakt vervolgens weer naar beneden. Dit proces noemen we convectie.
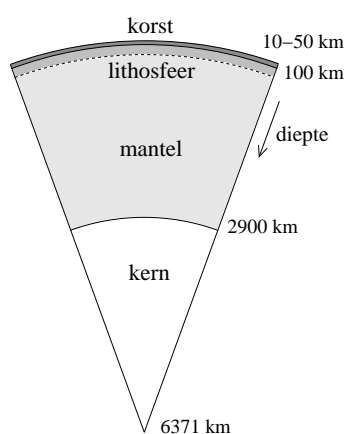
Figuur 1: Schematische doorsnede van de aarde

Samenvatting

Door het convectie-proces in de aarde worden de korst en lithosfeer van oceaanbodems continu opnieuw gevormd en weer vernietigd. Bij oceanische ruggen komt het mantel-materiaal omhoog terwijl de oceaanbodem aan beide kanten van de rug opzij schuift (zie figuur 2). Het materiaal dat aan het oppervlak is gekomen koelt af en vormt zo een nieuw deel van de oceaanbodem. Om het aangroeien te compenseren schuift op andere plekken oude, sterk afgekoelde oceaanbodem weer de aarde in. Bij diepe troggen duikt koude oceanische lithosfeer (en het meeste van de korst) de mantel in en verdwijnt van het aardoppervlak. Dit proces wordt subductie genoemd. De korst en lithosfeer van continenten worden niet op dezelfde manier gerecycled, maar juist steeds weer uit elkaar gedreven (als er nieuwe oceaanbodem tussen komt) en op elkaar geduwd (als alle oceaanbodem tussen continenten verdwenen is).
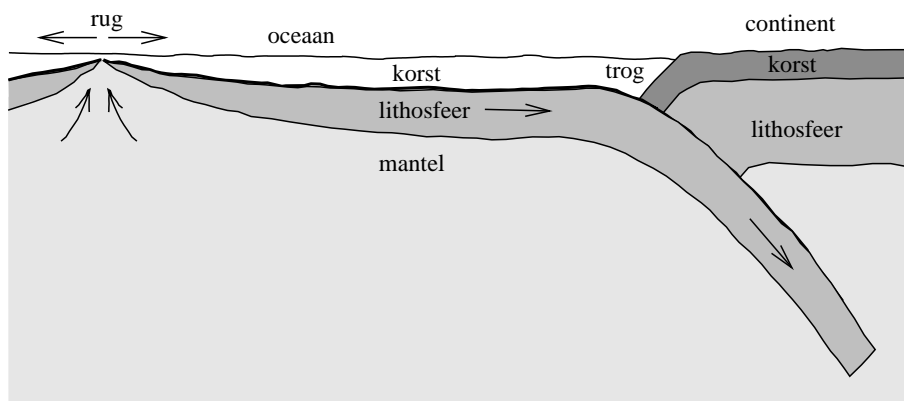
Figuur 2: Het aanmaken en subduceren van oceanische lithosfeer

Mantel-tomografie

Wat gebeurt er met de oceaanbodem die in de aarde is verdwenen? Hoe snel zinkt de lithosfeer naar beneden? Blijft het een stijve plaat of gaat het vervormen? Zou het materiaal kunnen afbreken van het oppervlak of blijft het er aan vast zitten? Zoals gezegd kunnen we helaas niet in de aarde kijken (met boringen komen we nu tot maar 10 van de 6371 kilometer). Om toch meer over het subductie-proces te weten te komen, kunnen we het wel nabootsen. Dit kan bijvoorbeeld met computer-modellen van de aarde. Of in laboratoria, waar alles in de juiste verhoudingen wordt nagemaakt. Uit dat soort studies blijkt onder andere dat subducerende lithosfeer helemaal van vorm kan veranderen, en dat het koude materiaal in de hete mantel weer langzaam opwarmt.

Veel informatie over het inwendige van de aarde krijgen we via aardbevingsgegevens. Aardbevingen veroorzaken seismische golven die dwars door de aarde heen reizen en zo door verschillende stations, verspreid over de hele wereld, worden geregistreerd. Door bijvoorbeeld de reistijden van alle aardbevingen naar alle stations bij elkaar te nemen, kunnen we een beeld krijgen van de variatie van de reissnelheid in de aarde. Met deze techniek, seismische tomografie, kunnen dus een soort scans van de interne structuur van de aarde gemaakt worden (ongeveer vergelijkbaar met de computer-scans uit ziekenhuizen die het inwendige van het menselijk lichaam afbeelden).

De seismische tomografie-beelden laten ons zien waar in de aarde de aardbevingsgolven sneller kunnen reizen dan normaal. De snelheid waarmee de golven zich voortbewegen hangt af van het soort materiaal waar ze doorheen gaan, de temperatuur, de druk, de kristalstructuur, enzovoort. Hoewel een afwijking in snelheid dus van verschillende factoren kan afhangen, blijkt dat temperatuur het grootste effect heeft als er gekeken wordt naar gesubduceerde oceanische lithosfeer. Hoewel de koude lithosfeer weer opwarmt in de mantel, gaat dit proces erg langzaam. Ook platen die lang geleden zijn verdwenen, zijn nu nog steeds kouder dan de omliggende mantel. Omdat seismische golven relatief snel door koud materiaal reizen, kan gesubduceerde lithosfeer dus met tomografie in beeld gebracht worden.

Tethys Oceaan

Ongeveer 200 miljoen jaar geleden (Dinosaurus-tijdperk) lagen Afrika, Arabië, India en Australië vast aan Antarctica (zie bijvoorbeeld figuren A.2-A.5 in de bijlage). Tussen deze continenten en het grote Europese/Aziatische continent lag in die tijd de Tethys Oceaan: een grote oceaan die op sommige plekken net zo breed was als de Pacifische Oceaan nu. Toen de continenten naar elkaar toe gingen bewegen, begon de tussenliggende oceanische lithosfeer te subduceren. Ook braken in dezelfde periode steeds weer stukken van de grote continenten af waardoor er tijdelijk kleinere oceanen bij kwamen (daarom wordt er vaak over Tethys Ocean*en* gesproken). Toen uiteindelijk alle oceanische lithosfeer was verdwenen, botsten de continenten zelf op elkaar en ontstond de lange gordel van gebergtes tussen het Middellandse-Zeegebied en Indonesië (zie figuur A.1).

Reconstructies van de plaatbewegingen in het verleden worden tektonische reconstructies genoemd. Ze worden gemaakt aan de hand van informatie die we nu aan het aardoppervlak vinden, zoals gesteentes, breukstructuren, fossielen, en achtergebleven stukken korst van de gesubduceerde platen. Vooral grootschalige reconstructies zoals die van het Tethys-gebied kunnen nuttig zijn voor andere aardwetenschappelijke onderzoeksdisciplines. Zo zijn bijvoorbeeld de posities van continenten belangrijk om het klimaat en de oceaanstromingen in het verleden te kunnen bepalen. Omdat in het Tethys-gebied veel bewijsmateriaal op elkaar gepropt is in het gebergte, blijkt het moeilijk om er achter te komen wat er precies gebeurd is. Tektonische reconstructies van dit gebied verschillen daarom soms nogal van elkaar, ookal voldoen ze wel allemaal aan de beschikbare informatie.

Gegevens over het binnenste van de aarde, zoals tomografie-beelden van de mantel, kunnen helpen om de reconstructies verder te verbeteren. We kunnen bijvoorbeeld uitzoeken of (en waar) de gesubduceerde lithosfeer van de Tethys Oceanen is terug te vinden in de aarde. De tomografie-beelden van de mantel onder het Tethys-gebied laten enorm grote gebieden zien waar aardbevingsgolven relatief snel doorheen gaan (zie de blauwgekleurde vlakken in de figuren A.6-A.8). Deze volumes zouden heel goed de restanten van de gesubduceerde lithosfeer kunnen zijn.

Dit onderzoek

In mijn onderzoek koppel ik de informatie van a) het oppervlak en b) het inwendige van de aarde aan elkaar, met als doel de verschillende tektonische reconstructies en het subductieproces in het Tethys-gebied te testen.

Samenvatting

Uit de reconstructies kan berekend worden hoe groot het oorspronkelijke oppervlak van de oceaanbodem is geweest, en uit de tomografie-beelden kan bepaald worden hoe groot de relatief snelle (en dus koude) volumes in de mantel zijn. Maar het is duidelijk dat een bodem-oppervlak niet direct te vergelijken is met een 'hoge-snelheid volume'. Om te kijken of de gesubduceerde lithosfeer inderdaad is terug te vinden in de mantel moet ik eigenlijk weten hoeveel relatief koud materiaal er nu nog zichtbaar zou moeten zijn (volgens de reconstruc-ties) en hoeveel materiaal er daadwerkelijk is (volgens de tomografie). Daarom ga ik in mijn onderzoek zowel het bodemoppervlak als de tomografische volumes omrekenen naar 'lage-temperatuur volumes'.

Voor het omrekenen van de volumes uit de tomografie-beelden kan ik informatie gebruiken over de relatie tussen afwijkingen in seismische golfsnelheid en afwijkingen in temperatuur. Om de thermische volumes uit de reconstructies te bepalen, moeten meer tussenstappen gemaakt worden (zie het schema in figuur 1.2). Zoals eerder gezegd is de lithosfeer het afgekoelde bovenlaagje van de mantel, en als deze subduceert dan wordt het materiaal in de mantel weer gewoon opgewarmd. Ten eerste bereken ik daarom voor het hele bodem-oppervlak wat de oorspronkelijke dikte van de koude lithosfeer was. Zo krijg ik het *oor-spronkelijke* thermische volume van de oceaanbodem, dus voordat het subduceerde. Ten tweede wil ik weten in hoeverre dit oorspronkelijke koude volume inmiddels weer is opge-warmd. Met computer-modellen bereken ik daarvoor wat er kan gebeuren met de tem-peraturen in de lithosfeer als deze op een bepaalde manier subduceert Door de mogelijke subductie-scenario's op een rijtje te zetten, kan ik voorspellen wat het *huidige* thermische volume van de gesubduceerde oceaanbodem zou moeten zijn.

In elke tektonische reconstructie is het oceaanoppervlak, de oorspronkelijke dikte, èn de manier van subduceren anders geweest. Daardoor krijg ik voor iedere reconstructie ook een andere voorspelling van de huidige thermische volumes. De plek en het tijdstip van sub-ductie zijn ook afhankelijk van de gebruikte reconstructie. In mijn onderzoek zal ik dus de verschillende reconstructies kunnen testen door de voorspelde hoeveelheid, plek en tijdstip van subductie te vergelijken met de grootte, lokatie (plek en diepte) en vorm van de tomo-grafische volumes.

Dit proefschrift

In dit proefschrift begin ik in hoofdstuk 2 met het geven van een overzicht van de verschil-lende tektonische reconstructies die er van het Tethys-gebied zijn. Daarna behandel ik in hoofdstuk 3 de theoriën en methodes die ik nodig heb in mijn onderzoek.

Vervolgens bekijk ik eerst het oostelijke Middellandse-Zeegebied, het Midden Oosten, en het Himalaya-gebied. In hoofdstuk 4 bereken ik de totale (voorspelde èn tomografische) volumes voor het hele gebied in één keer. Daaruit blijkt dat de *totale* volumes vrijwel hetzelfde zijn. Dit wijst erop dat de gesubduceerde lithosfeer van de Tethys Oceanen inderdaad is terug te vinden in de mantel. Helaas helpt het ons niet om de verschillen in de tektonische recon-structies te testen. In hoofdstuk 5 kijk ik daarom meer gedetailleerd naar de lokatie en vorm van de volumes in de tomografie-beelden, en naar de volumes die we zouden verwachten op grond van de verschillende reconstructies. Daardoor kan ik concluderen dat sommige tektonische reconstructies, en de bijbehorende subductie-processen, duidelijk beter kloppen met de beelden van de mantel dan andere. De subductie-scenario's die uiteindelijk het best

blijken te passen voor het Midden Oosten en het Himalaya-gebied zijn te zien in figuur 5.20 en 5.21 (pagina 146 en 147). Een goedpassend scenario voor de subductie in het oostelijke Middellandse-Zeegebied is geschetst in figuur 5.24 (pagina 153).

Tot slot onderzoek ik in hoofdstuk 6 het Indonesische gebied. Omdat in Indonesië geen continenten op elkaar zijn gebotst maar nog steeds oceanische lithosfeer subduceert, pak ik het hier anders aan dan in de eerdere hoofdstukken. In dit geval voorspel ik, weer voor verschillende tektonische reconstructies, hoe de tomografie-beelden eruit zouden moeten zien als de reconstructies kloppen. Deze voorspelde beelden (te zien in de bovenste twee plaatjes in figuren A.10-A.15) kan ik direct vergelijken met de èchte tomografie-beelden (zie de onderste plaatjes in dezelfde figuren). Hieruit blijkt opnieuw dat sommige voorspellingen beter overeenkomen met de mantel-tomografie dan andere.

Het is lastig om kort en in woorden uit te leggen wat de belangrijkste conclusies van mijn onderzoek zijn. Het is wat dat betreft beter om zelf eens goed te kijken naar de verschillende figuren die ik hierboven heb genoemd. Het is in ieder geval wèl duidelijk geworden dat het met mijn aanpak inderdaad lukt om de informatie van het oppervlak en inwendige van de aarde te koppelen, en om daarmee de subductie-geschiedenis van de verdwenen Tethys Oceanen te reconstrueren.

Dankwoord (Acknowledgments)

Iedereen die me heeft geholpen tijdens mijn promotietijd wil ik hiervoor graag bedanken.

Rinus Wortel en Wim Spakman, bedankt voor jullie enthousiasme, goede ideeën en adviezen, voor de hulp bij het op papier krijgen van alle lastige analyses en discussies, en voor het kritische maar altijd opbouwende commentaar op mijn werk.

I thank ExxonMobil Exploration for the use of their reconstruction, for which the data were compiled by the PLATES project at the University of Texas. Pinar Yilmaz and Ian Norton, your enthusiasm and help on the plate rotation program were very much appreciated.

The members of my dissertation committee, Sierd Cloetingh, Cor Langereis, Gérard Stampfli and Reinoud Vissers are thanked for reading the manuscript. Your comments and suggestions have certainly helped improve my thesis.

Vele collega's hebben voor wetenschappelijke, praktische en morele steun gezorgd.

Paul, bedankt voor het constructieve meedenken en discussiëren over mijn rotatieproblemen. Antonio, *muchas gracias* for helping me with the tomographic images. Susanne en Harmen, dank voor jullie eerdere bijdrage aan hoofdstuk zes. Theo en Joop, bedankt voor het regelen van alle computergerelateerde zaken.

Menno, ik ben erg blij dat ik jou steeds als kamergenoot heb gehad - mijn promotietijd was anders niet half zo leuk en relaxed geweest. Bedankt dus voor alle nuttige discussies over subduceren, modelleren, promoveren en andere interessante problemen. Maar vooral bedankt voor de koffie en gezelligheid, en voor de vele gesprekken over de wetenschappelijk gezien wat minder relevante onderwerpen.

All other colleagues and former colleagues from Utrecht, Delft, Amsterdam and abroad - many thanks for all the useful and not-so-useful conversations during lunch and coffee breaks, the Betics excursion, several conferences and workshops, bijeenkomsten van het promovendi-platform, borrels & barbecues, uitreikingen van vergulde stoelpoten, etc. Ook de adviezen van mijn oud-collega's, variërend van 'het is maar een proefschrift' tot 'oogkleppen voor en vol gas vooruit', hebben hun nut inmiddels wel bewezen.

En tot slot natuurlijk mijn familie en vrienden: Juist jullie hebben - door het aanhoren van mijn frustraties, met gevraagd en ongevraagd advies, via losse opmerkingen, tijdens vakanties en weekendjes weg, of simpel door het gezellig samen sporten, spelletjes doen, tv-kijken, eten of even een terrasje pakken - enorm bijgedragen aan de voortgang van mijn onderzoek. Vooral de vele aanmoedigingen in de laatste maanden hebben me er absoluut doorheen geholpen. Bedankt voor alle steun de afgelopen jaren!!!

Curriculum Vitae

30 March 1974	Born in Leiderdorp, the Netherlands
1986 - 1992	Secondary school, Montessori Lyceum Herman Jordan, Zeist, the Netherlands
1992 - 1999	Study of Geophysics, Utrecht University, the Netherlands
1999 - 2004	Ph.D. Student in the Tectonophysics research group, Faculty of Geosciences, Utrecht University, the Netherlands